

HIGH ENERGY NEUTRINO ANALYSIS AT KAMLAND
AND APPLICATION TO DARK MATTER SEARCH

A DISSERTATION SUBMITTED TO THE GRADUATE DIVISION OF THE
UNIVERSITY OF HAWAII AT MĀNOA IN PARTIAL FULFILLMENT
OF THE REQUIREMENTS FOR THE DEGREE OF
DOCTOR OF PHILOSOPHY

IN

PHYSICS

MAY 2016

By
Michinari Sakai

Dissertation Committee:

John G. Learned, Chairperson
Stephen T. Dye
Jason Kumar
Gary S. Varner
Brent R. Tully

For everyone in the world.

Acknowledgements

Firstly I want to express my sincere gratitude to my advisor Prof. John Learned for his continuous support and patience during my studies despite all of my shortcomings and procrastination. His wisdom, frank honesty, and relentless pursuit of new ideas have been an influential part of my education that I will try to carry on and emulate.

I would also like to thank Prof. Kunio Inoue for his warm hospitality during my visits to Japan and for supporting my studies and travels to RCNS and Kamioka. My thanks also go to all of the scientists, students, and staff in the KamLAND collaboration who have just been a pleasure to work with. I don't think I will ever find a group of people more friendlier and more dedicated to science. I want to especially extend my gratitude to Prof. Itaru Shimizu whom I have consulted with questions and emails numerous times. His dedication to his work and prompt answers have been an invaluable asset for my studies that I could not have accomplished without. I would like to mention Prof. Hiroko Watanabe who helped me with my topic and how to get about when I first visited RCNS in Sendai. My thanks also go to Prof. Kyoko Tamae who has tirelessly listen to my requests to maintain the computing servers at RCNS, and to Prof. Haruo Ikeda who despite his seemingly strict and terse demeanor is extremely kind and knowledgeable. I would like to acknowledge Prof. Masayuki Koga and Prof. Kengo Nakamura who have always warmly welcomed my stay at Mozumi and made me feel at home during my shifts at KamLAND. I cannot forget Mrs. Katsuko Shimizu who took care of me and made sure that I was well fed during my stay in Mozumi when I was alone taking shifts through the new year periods. I will dearly miss the Wednesday English club that she would so kindly invited me over to and the interesting range of topics we covered in the conversations we had together. My thanks also go to Prof. Sanshiro Enomoto for his input in improving the event reconstruction algorithms in this work and for the intriguing chats we have had together on trips to some of the local hot springs in the Gifu area.

I am also grateful to my dissertation committee members. Prof. Jason Kumar who helped me immensely with many of the calculations during the early stages of this work and for his patience. Prof. Stephen Dye who's input I value greatly because he always quick to point out the most relevant and practical issues. Prof. Gary Varner the electronics

wizard of our department who is amazing at what he does and whom I regret not having had more time to work with. And Prof. Brent Tully who is an inspiration to everyone through his work with galaxies.

Sincere thanks also go to my local mTC lab members at the University of Hawaii at Manoa. I want to thank Prof. Shigenobu Matsuno who is incredibly knowledgeable and helpful with almost anything I can throw at him. In fact, he is akin to a human magnet that people seeking help are attracted to with all sorts of questions. I am guilty of being one of those people. My thanks also go to Stephanie Smith whom I have worked together with and have had the opportunity for many constructive discussions throughout the years. Our engineer Marc Rosen whom I have been lucky to meet and learn from about designing and building mechanical systems. Viacheslav Li who has been our driving force to publish papers on the mTC and my driving force to go to the gym, Sergey Negrashov for being my computer science guru/consultant for many of my computing needs and his wife Lisa Ritter. They are a very sweet couple and I wish them many more years together to come. Ryan Dorill for initially being my guinea pig to test out event reconstruction techniques in the mTC and now for handling most of the mTC data acquisition software. Mark Duvall for his helpful insights about simulations and interesting conversations about esoteric musical instruments. I want to also acknowledge our mTC project manager Andrew Druetzler for keeping our agenda organized and for encouraging us to clean our lab at least once in a while with delicious pastries and coffee. Jan Bruce who has always helped me with my travel issues with incredible efficiency. I cannot forget the friendly chats I've had from time to time with Prof. Robert Morse and his bubbling enthusiasm for the fascinating topic of musical scale theory.

I owe my gratitude to my parents Philip and Kyoko Sakai who have raised me from a young age to seek the truth and live for the sake of others. I cannot express how deeply indebted I am to my wife Chiharu Sakai who has been constantly supporting me throughout my studies despite all of my neglect for her wellbeing.

This work was supported by the U.S. Department of Energy (DOE) Grant DE-SC0010504, and the Japan Society for the Promotion of Science Grant K15K217470.

ABSTRACT

There are currently two active detector technologies for neutrino detection, namely Cherenkov and scintillator detectors. In the past, scintillator detectors have traditionally been used much like calorimeters to analyze neutrinos at lower energies of $\sim\text{MeV}$, whereas neutrino directionality and flavor discrimination at higher energy scales have been greatly pursued by Cherenkov detectors. In this work, we will introduce a novel analysis technique to resolve the directionality of $\sim\text{GeV}$ scale neutrinos in scintillator with data taken at the Kamioka Liquid Scintillator Antineutrino Detector (KamLAND), the world's largest scintillator neutrino detector located in Kamioka, Japan. Studies suggest that the directional resolution using this new method may be better than that of the Cherenkov method by $\sim 10^\circ$ in this energy regime. We will also explore track reconstruction and flavor discrimination techniques that were initially developed for R&D in the Low Energy Neutrino Astronomy (LENA) detector, and apply these techniques for the first time using real data. Finally we will employ the methods introduced to conduct an indirect dark matter search by looking for neutrino signals originating from dark matter annihilation in the Sun and Earth.

Contents

Acknowledgements	v
Abstract	vii
List of Tables	xii
List of Figures	xiii
Acronyms	xix
1 Dark Matter	1
1.1 Introduction	1
1.2 Weakly interacting massive particles (WIMPs)	8
1.3 The WIMP miracle	9
1.4 Halo models	13
1.5 Dark matter capture rate	15
2 Neutrino Oscillation	23
2.1 Overview	23
2.2 Theory	24
3 The Detector	38
3.1 Introduction	38
3.2 Detector construction	38
3.2.1 Overview	38
3.2.2 Inner detector	41
3.2.3 Outer detector	47
3.2.4 Chimney and dome area	47
3.2.5 Photomultiplier tubes	48
3.3 Electronics and data acquisition	54
3.3.1 Overview	54
3.4 Purification systems	61

3.4.1	Overview	61
3.4.2	First purification system	62
3.4.3	Second purification system	63
4	Detector Calibration and Event Reconstruction	66
4.1	Signal waveform processing	66
4.2	Timing calibration	67
4.3	Charge calibration	69
4.4	Cosmic ray muons	72
4.4.1	Muon identification	72
4.4.2	Muon fitter	78
4.4.3	Residual charge	80
4.4.4	Muon veto contribution to dead time	84
4.5	Bad channels	84
4.6	Energy calibration	86
4.7	Vertex reconstruction	95
4.8	Neutrino directionality	102
4.8.1	Overview	102
4.8.2	Neutrino-nucleon interaction	102
4.8.3	Photomultiplier tube (PMT) pre-pulsing	109
4.8.4	Neutrino directionality algorithm	111
4.8.5	Validation of neutrino directionality	117
4.9	Track reconstruction and particle identification	127
4.9.1	Hellgartner’s algorithm	127
4.9.2	Particle identification	142
5	Signal and Background Models	145
5.1	Atmospheric neutrinos	145
5.2	Weakly interacting massive particle (WIMP) annihilation induced neutrinos from the Sun or Earth	158
6	Analysis	186
6.1	Event rate equation	186
6.2	Statistical methods for setting upper limits	190
6.2.1	The frequentist method	191
6.2.2	The Bayesian method	193
6.3	WIMP-nucleon cross section bound calculation	195
6.4	Event selection	196
6.4.1	Run selection	196
6.4.2	Noise event rejection	197
6.4.3	Fiducial volume selection	198

6.4.4	Vertex <i>point-likeness</i> estimation using χ_{time}^2	199
6.4.5	Reconstructed energy of candidate events	201
6.4.6	Event distribution with respect to time	203
6.5	Fitting data to the model	203
6.6	Live time calculation	206
6.6.1	Dead time	206
6.6.2	Veto time	207
6.6.3	Live time	208
6.7	Number of target nuclei	208
6.8	Detector efficiency for events to be fully contained	212
6.9	WIMP-nucleon cross section bounds	215
7	Summary and Discussion	222
7.1	Summary	222
7.2	Future outlook	224
7.3	Issues with high energy particle simulations in scintillator	227
8	Conclusion	229
A	Friedmann Equations	231
B	Isotopes and Natural Abundances	236
C	Bayesian Priors	237
D	NFPA Flammability Rating	241
	Glossary	243
	Bibliography	253

List of Tables

1.1	Dark matter halo profile models and their respective parameters	14
1.2	DarkSUSY parameters for WIMP capture rate calculation	18
1.3	Ratio of WIMP capture rate in the Earth and WIMP-nucleon scattering cross section	21
1.4	Ratio of WIMP capture rate in the Sun and WIMP-nucleon scattering cross section	22
2.1	Neutrino oscillation parameters (2014)	37
3.1	Properties of the KamLAND liquid scintillator (LS)	43
3.2	Chemical composition of the KamLAND liquid scintillator (LS)	44
3.3	Properties of the KamLAND buffer oil (BO)	45
3.4	Properties of components for liquid scintillator (LS) and buffer oil (BO)	46
3.5	photomultiplier tubes (PMTs) used in the detector	48
4.1	Calibration sources for the KamLAND vertex fitter	101
4.2	Simulation parameters for Hellgartner’s muon track reconstruction	130
4.3	Simulation parameters for neutrino event reconstruction in the KamLAND Geant4 Simulation (KLG4Sim)	133
7.1	NFPA 704 safety ratings for liquid scintillator (LS) used in existing or proposed neutrino experiments	226
B.1	Isotopes and natural abundances relevant to the LS in KamLAND.	236
D.1	NFPA 704 safety rating codes for flammable material	242

List of Figures

1.1	Rotation curve for spiral galaxy NGC6503	2
1.2	Galaxy cluster 1E 0657-56	3
1.3	CMB radiation intensity sky-map	4
1.4	CMB anisotropy spectrum	5
1.5	Ratio of various mass-energy content of the universe	6
1.6	WIMP number density in the early universe	10
1.7	Spatial distribution of matter in the typical galaxy	14
1.8	Dark matter capture rate in the Earth	19
1.9	Dark matter capture rate in the Sun	19
2.1	Sun composition densities	32
2.2	Earth composition densities	33
2.3	Survival and oscillation probabilities for 0.1 GeV ν_e in Earth	34
2.4	Survival and oscillation probabilities for 1 GeV ν_e in Earth	35
2.5	Survival and oscillation probabilities for 10 GeV ν_e in Earth	36
3.1	Schematic of KamLAND	39
3.2	Illustration of the KamLAND detector in the Kamioka mine tunnel	40
3.3	Schematics of photomultiplier tubes (PMTs)	49
3.4	Quantum efficiency (QE) and radiant sensitivity of photomultiplier tubes (PMTs)	50
3.5	Time response of photomultiplier tubes (PMTs)	52
3.6	Signal gain of photomultiplier tubes (PMTs)	53
3.7	front-end electronics (FEE) and its components	55
3.8	Data acquisition (DAQ) system and data flow	56
3.9	Diagram of front-end electronics (FEE) circuitry	57
3.10	Schematic of the first purification system	63
3.11	Flux spectrum of natural and human-made reactor neutrinos	64
3.12	Schematic of the second purification system	65
4.1	Photomultiplier tube (PMT) pulse time slewing effects	68

4.2	Photomultiplier tube (PMT) timing resolution	69
4.3	Charge calibration of 17-inch photomultiplier tubes (PMTs)	70
4.4	Single photoelectron (p.e.) charge distribution	71
4.5	Correlation of 20-inch PMT charge to mean of surrounding 17-inch PMTs .	73
4.6	Frequency of cosmic ray muons	75
4.7	Cosmic ray muon rate versus time	76
4.8	Charge deposit of cosmic ray muons	77
4.9	Schematic of a cosmic ray muon traversing the KamLAND inner detector (ID)	79
4.10	Charge deposition of cosmic ray muons with respect to impact parameter . .	81
4.11	Charge deposition of cosmic ray muons per unit track length	82
4.12	Charge deposition of cosmic ray muons with respect to track length	83
4.13	Time evolution of number of bad PMT channels	87
4.14	Mean excitation energy of various elements	89
4.15	Stopping power of positive muons in copper	90
4.16	Energy loss per thickness of positive muons in silicon	91
4.17	Stopping power of positive muons in the KamLAND liquid scintillator (LS)	93
4.18	Charge deposition per unit track length of cosmic ray muons (data from run 3001)	94
4.19	Charge deposition per energy loss of cosmic ray muons (data from run 3001)	95
4.20	Time evolution of charge deposition per unit energy loss of muons in the LS and buffer oil (BO)	96
4.21	Time evolution of charge deposition per unit energy loss of scintillation muons traversing the ID	97
4.22	Spatial resolution of KamLAND vertex fitter	99
4.23	Spatial bias of the KamLAND vertex fitter	100
4.24	Cherenkov ring pattern	103
4.25	Feynman diagram of inverse beta decay (IBD)	104
4.26	Feynman diagrams for high energy ν_μ interaction with proton and neutron .	105
4.27	Neutrino total charged current scattering cross sections for nucleons in the LS	106
4.28	Neutrino cross sections for scattering processes on protons	107
4.29	Neutrino cross sections for scattering processes on Carbon nucleons	108
4.30	Photomultiplier tube (PMT) pre-pulsing versus muon charge	109
4.31	Photomultiplier tube (PMT) pre-pulsing versus PMT angle with respect to muon track	110
4.32	Schematic of fully contained charged lepton track in the ID	112
4.33	Example of center of gravity calculation	113
4.34	Example of center of charge and time calculation	115
4.35	Comparison between neutrino and muon directional fitters on muon data .	118
4.36	Comparison between the fitted and true neutrino direction in Monte Carlo .	119

4.37	Reconstructed directional resolution of ν_e undergoing charged current interaction on ^1H and ^{12}C nuclei taking into account outer detector (OD) inefficiencies.	121
4.38	Reconstructed directional resolution of $\bar{\nu}_e$ undergoing charged current interaction on ^1H and ^{12}C nuclei taking into account OD inefficiencies.	122
4.39	Reconstructed directional resolution of ν_μ undergoing charged current interaction on ^1H and ^{12}C nuclei taking into account OD inefficiencies.	123
4.40	Reconstructed directional resolution of $\bar{\nu}_\mu$ undergoing charged current interaction on ^1H and ^{12}C nuclei taking into account OD inefficiencies.	124
4.41	Geographic location of the KamLAND detector and Japan Proton Accelerator Research Complex (J-PARC)	125
4.42	Energy spectrum of Tokai to Kamioka (T2K) neutrinos	126
4.43	Energy spectrum of T2K neutrinos per flavor	127
4.44	Reconstructed direction of T2K neutrinos	128
4.45	Hellgartner track reconstruction for simulated muon tracks.	131
4.46	Hellgartner track reconstruction for simulated 2 GeV ν_e event	132
4.47	quantum efficiency (QE) used in the KamLAND Geant4 Simulation (KLG4Sim)	134
4.48	Reconstructed T2K event image 1	135
4.49	Reconstructed T2K event image 2	135
4.50	Reconstructed T2K event image 3	136
4.51	Reconstructed T2K event image 4	136
4.52	Reconstructed T2K event image 5	137
4.53	Reconstructed T2K event image 6	137
4.54	Reconstructed T2K event image 7	138
4.55	Reconstructed T2K event image 8	138
4.56	Reconstructed T2K event image 9	139
4.57	Reconstructed T2K event image 10	139
4.58	Reconstructed T2K event image 11	140
4.59	Reconstructed T2K event image 12	140
4.60	Reconstructed T2K event image 13	141
4.61	Reconstructed T2K event image 14	141
4.62	Ellipsoids symmetric about the z -axis	143
4.63	Particle identification of 1 GeV leptons in the KamLAND Geant4 Simulation (KLG4Sim)	143
4.64	Reconstructed ellipticity of fully contained T2K events	144
5.1	Production and detection scheme of atmospheric neutrinos	146
5.2	Pre-oscillated atmospheric neutrino flux at the Kamioka mine	147
5.3	Models for atmospheric neutrino flux spectrum	148
5.4	Raw survival and oscillation probabilities of atmospheric neutrinos ν_e and ν_μ	150

5.5	Effective survival and oscillation probabilities of atmospheric neutrinos ν_e and ν_μ	151
5.6	Raw survival and oscillation probabilities of atmospheric neutrinos $\bar{\nu}_e$ and $\bar{\nu}_\mu$	152
5.7	Effective survival and oscillation probabilities of atmospheric neutrinos $\bar{\nu}_e$ and $\bar{\nu}_\mu$	153
5.8	Pure unoscillated and oscillated ν_e and $\bar{\nu}_e$ flux spectrum with respect to zenith angle at the Kamioka mine	154
5.9	Pure unoscillated and oscillated ν_μ and $\bar{\nu}_\mu$ flux spectrum with respect to zenith angle at the Kamioka mine	155
5.10	Effective atmospheric ν_e , $\bar{\nu}_e$, ν_μ , and $\bar{\nu}_\mu$ flux spectrum with respect to polar angle from the direction toward the Sun's core at the Kamioka mine	156
5.11	Effective atmospheric ν_e , $\bar{\nu}_e$, ν_μ , and $\bar{\nu}_\mu$ flux spectrum with respect to zenith angle at the Kamioka mine	157
5.12	Production and detection scheme of WIMP annihilation induced neutrinos	158
5.13	Directional flux spectra for ν_e , $\bar{\nu}_e$ from 1 GeV WIMPs (XX) annihilating in the Earth through sample channels.	161
5.14	Directional flux spectra for ν_μ , $\bar{\nu}_\mu$ from 1 GeV WIMPs (XX) annihilating in the Earth through sample channels.	162
5.15	Directional flux spectra for ν_e , $\bar{\nu}_e$ from 10 GeV WIMPs (XX) annihilating in the Earth through sample channels.	163
5.16	Directional flux spectra for ν_μ , $\bar{\nu}_\mu$ from 10 GeV WIMPs (XX) annihilating in the Earth through sample channels.	164
5.17	Directional flux spectra for ν_e , $\bar{\nu}_e$ from 100 GeV WIMPs (XX) annihilating in the Earth through sample channels.	165
5.18	Directional flux spectra for ν_μ , $\bar{\nu}_\mu$ from 100 GeV WIMPs (XX) annihilating in the Earth through sample channels.	166
5.19	Directional flux spectra for ν_e , $\bar{\nu}_e$ from 1 GeV WIMPs (XX) annihilating in the Sun through sample channels.	167
5.20	Directional flux spectra for ν_μ , $\bar{\nu}_\mu$ from 1 GeV WIMPs (XX) annihilating in the Sun through sample channels.	168
5.21	Directional flux spectra for ν_e , $\bar{\nu}_e$ from 10 GeV WIMPs (XX) annihilating in the Sun through sample channels.	169
5.22	Directional flux spectra for ν_μ , $\bar{\nu}_\mu$ from 10 GeV WIMPs (XX) annihilating in the Sun through sample channels.	170
5.23	Directional flux spectra for ν_e , $\bar{\nu}_e$ from 100 GeV WIMPs (XX) annihilating in the Sun through sample channels.	171
5.24	Directional flux spectra for ν_μ , $\bar{\nu}_\mu$ from 100 GeV WIMPs (XX) annihilating in the Sun through sample channels.	172
5.25	Directional flux spectra for ν_e , $\bar{\nu}_e$ from 1 GeV WIMPs (XX) annihilating in the Earth through sample channels with detector effects taken into account.	174

5.26	Directional flux spectra for $\nu_\mu, \bar{\nu}_\mu$ from 1 GeV WIMPs (XX) annihilating in the Earth through sample channels with detector effects taken into account.	175
5.27	Directional flux spectra for $\nu_e, \bar{\nu}_e$ from 10 GeV WIMPs (XX) annihilating in the Earth through sample channels with detector effects taken into account.	176
5.28	Directional flux spectra for $\nu_\mu, \bar{\nu}_\mu$ from 10 GeV WIMPs (XX) annihilating in the Earth through sample channels with detector effects taken into account.	177
5.29	Directional flux spectra for $\nu_e, \bar{\nu}_e$ from 100 GeV WIMPs (XX) annihilating in the Earth through sample channels with detector effects taken into account.	178
5.30	Directional flux spectra for $\nu_\mu, \bar{\nu}_\mu$ from 100 GeV WIMPs (XX) annihilating in the Earth through sample channels with detector effects taken into account.	179
5.31	Directional flux spectra for $\nu_e, \bar{\nu}_e$ from 1 GeV WIMPs (XX) annihilating in the Sun through sample channels with detector effects taken into account.	180
5.32	Directional flux spectra for $\nu_\mu, \bar{\nu}_\mu$ from 1 GeV WIMPs (XX) annihilating in the Sun through sample channels with detector effects taken into account.	181
5.33	Directional flux spectra for $\nu_e, \bar{\nu}_e$ from 10 GeV WIMPs (XX) annihilating in the Sun through sample channels with detector effects taken into account.	182
5.34	Directional flux spectra for $\nu_\mu, \bar{\nu}_\mu$ from 10 GeV WIMPs (XX) annihilating in the Sun through sample channels with detector effects taken into account.	183
5.35	Directional flux spectra for $\nu_e, \bar{\nu}_e$ from 100 GeV WIMPs (XX) annihilating in the Sun through sample channels with detector effects taken into account.	184
5.36	Directional flux spectra for $\nu_\mu, \bar{\nu}_\mu$ from 100 GeV WIMPs (XX) annihilating in the Sun through sample channels with detector effects taken into account.	185
6.1	Neyman construction of the confidence interval	192
6.2	Distribution of reconstructed vertices	198
6.3	Linear correlation between the first photon hit time on a PMT and the distance between the vertex and the PMT	200
6.4	Vertex point-likeness versus radial distance from detector center	201
6.5	Reconstructed energy spectrum of candidate events	202
6.6	Atmospheric neutrino event distribution with respect to time	202
6.7	Angular distribution of signal and background neutrino model fitted to data with respect to angle from the direction toward the Earth's core	204
6.8	Angular distribution of signal and background neutrino model fitted to data with respect to angle from the direction toward the Sun's core	205
6.9	Simulated detector efficiency for ν_e and $\bar{\nu}_e$	216
6.10	Simulated detector efficiency for ν_μ and $\bar{\nu}_\mu$	217
6.11	WIMP-nucleon spin independent scattering cross section upper bounds at 90 % confidence level for WIMP annihilations in the Earth	218
6.12	WIMP-nucleon spin independent scattering cross section upper bounds at 90 % confidence level for WIMP annihilations in the Sun	219

6.13	WIMP-proton spin dependent scattering cross section upper bounds at 90 % confidence level for WIMP annihilations in the Sun	221
7.1	Projected absorption length achievable by water based liquid scintillators and comparison to that of purified water in Super-Kamiokande (SK)	225
A.1	Two-dimensional analog of the 3 different types of metric spaces with constant curvatures. (a) shows the analog of a closed universe, (b) shows the analog of a flat universe, and (c) shows the analog of an open universe.	234

Acronyms

- ADC** analog-to-digital converter 61, 66, 67, 70, 71, 85
- ATWD** analog transient waveform digitizer 54–57, 60, 61, 67, 69, 73, 85
- BO** buffer oil xii, xiv, 41, 44–46, 48, 62, 74, 78, 80–82, 92–98, 118, 188, 190, 210–212,
Glossary: buffer oil
- CMB** cosmic microwave background xiii, 4, 5
- DAQ** data acquisition xiii, 54, 56, 60, 61
- FEE** front-end electronics xiii, 54–58, 61, 68, 85, 207
- FLRW metric** Friedmann-Lemaître-Robertson-Walker metric 231, 234, *Glossary:* Friedmann-Lemaître-Robertson-Walker metric
- FPGA** field programmable gate array 55, 57
- FWHM** full width at half maximum 51
- GENIE** Generates Events for Neutrino Interaction Experiments 106, 118, 127, 128, 130, 223, *Glossary:* Generates Events for Neutrino Interaction Experiments
- GPS** Global Positioning System 58, 60
- GPU** graphics processing unit 228
- IBD** inverse beta decay xiv, 84, 104, *Glossary:* inverse beta decay

IceCube IceCube Neutrino Observatory 224, *Glossary:* IceCube Neutrino Observatory

ICRU International Commission on Radiation Units and Measurements 89

ID inner detector xiv, 38, 41, 47–49, 51, 55, 59, 60, 72, 74, 78–80, 85–88, 95, 97, 102, 109, 111, 112, 120, 132, 142, 188, 190, 197, 199, 203, 206, 208, 212–214, 227

ISA International Standard Atmosphere 149, *Glossary:* 1976 International Standard Atmosphere

J-PARC Japan Proton Accelerator Research Complex xv, 125, 126, 128, 134, 251, *Glossary:* Japan Proton Accelerator Research Complex

JST Japan Standard Time 96, *Glossary:* Japan Standard Time

KamLAND Kamioka Liquid Scintillator Antineutrino Detector vii, xii, xiii, xv, 39–41, 44, 106, 117, 118, 125, 126, 142, 145, 208–210, 223, 224, 226, 227, 229, 230, 236, 243, 246, 247, 249–251, *Glossary:* Kamioka Liquid Scintillator Antineutrino Detector

KL KamLAND *Acronym:* KamLAND

KLG4Sim KamLAND Geant4 Simulation xii, xv, 118, 126, 128, 130, 133, 134, 142, 143, 208, 213, 223

K-S test Kolmogorov-Smirnov test 127, *Glossary:* Kolmogorov-Smirnov test

LAB linear alkylbenzene 130, 226, *Glossary:* linear alkylbenzene

LAPPD Large Area Picosecond Photodetector 226, *Glossary:* Large Area Picosecond Photodetector

LENA detector Low Energy Neutrino Astronomy detector vii, 127, *Glossary:* Low Energy Neutrino Astronomy detector

LS liquid scintillator xii, xiv, 41–48, 59–63, 65, 67, 74, 78, 80–82, 92–98, 104, 106, 111, 118, 119, 126, 128, 130, 133, 142, 188, 190, 197–199, 208–210, 212, 225–227, 230, 236, 243, 247, *Glossary:* liquid scintillator

MACHO massive astrophysical compact halo object 8, 248, *Glossary*: massive astrophysical compact halo object

MOND modified Newtonian dynamics 8, 251, *Glossary*: modified Newtonian dynamics

MSW effect Mikheyev-Smirnov-Wolfenstein effect 24, 149, 156, 157, 223, 248, *Glossary*: Mikheyev-Smirnov-Wolfenstein effect

mwe meter water equivalent 38, 72, 78, *Glossary*: meter water equivalent

NFPA 704 National Fire Protection Association Standard System for the Identification of the Hazards of Materials for Emergency Response xi, xii, 225, 226, 241, 242, *Glossary*: NFPA 704

NSum digital sum across all 125 ns long gates, of which each gate is produced by a single PMT tube that registered a hit by photons 58–61, 70

OD outer detector xv, 38, 47, 48, 59, 60, 72, 74, 86, 87, 120–124, 199, 213, 227

PC personal computer 58

PCA principal component analysis 142, *Glossary*: principal component analysis

PDF probability distribution function 193, 194, 237

PDG Particle Data Group 194, *Glossary*: Particle Data Group

p.e. photoelectron xiv, 71, *Glossary*: photoelectron

PMT photomultiplier tube x, xii–xiv, xvii, xxi, 41, 42, 44, 47–61, 66–74, 78, 80, 82, 84–88, 94–99, 102, 109–117, 120, 129, 130, 132, 133, 142, 197–200, 206, 224–227, 243, 249, 252, *Glossary*: photomultiplier tube

PPO 2,5-Diphenyloxazole 41, 46, 133, 250, *Glossary*: 2,5-Diphenyloxazole

PPS pulse per second 58, 60

PREM preliminary reference Earth model 31, 33, 149, 150, 152, 223, *Glossary*: preliminary reference Earth model

QE quantum efficiency xiii, xv, 50, 130, 133, 134, 224, 225, *Glossary*: quantum efficiency

RAMBO robust association of massive baryonic objects 8, 250, *Glossary*: robust association of massive baryonic objects

SCA switched capacitor array 54

SK Super-Kamiokande 149, 251, *Acronym*: Super-K

Super-K Super-Kamiokande xviii, 102, 103, 125–127, 215, 220, 224, 225, *Glossary*: Super-Kamiokande

T2K Tokai to Kamioka xv, 125–128, 134, 144, 229, *Glossary*: Tokai to Kamioka

TeVS tensor-vector-scalar gravity 8, *Glossary*: tensor-vector-scalar gravity

TTS transit-time spread 51, 52, *Glossary*: transit-time spread

VME Versa Module Europa 56–58

WbLS water-based liquid scintillator 225, 226, *Glossary*: water-based liquid scintillator

WILP weakly interacting light particle 7

WIMP weakly interacting massive particle ix–xiii, xvi–xviii, 8–10, 13, 15–18, 21, 22, 158–187, 195, 203–205, 215, 218–221, 223, 243, 244, 252

WMAP Wilkinson Microwave Anisotropy Probe 4

Chapter 1

Dark Matter

1.1 Introduction

Dark matter is a postulated type of matter that seems to constitute most of the matter in the present universe but does not interact with (neither emits nor absorbs) light or any other electromagnetic radiation. The first robust evidence for the existence of dark matter was discovered in the 1960s and 1970s through the inconsistency between galaxy rotation curves and that predicted by the visible matter in galaxies [69, 70]. This phenomenon can readily be seen in examples such as that shown in Figure 1.1. Subsequently, there have been numerous observations indicating the presence of dark matter. Some of which include gravitational lensing of background objects by galaxy clusters such as the Bullet Cluster as shown in Figure 1.2; the temperature distribution of hot gas in galaxies and galaxy clusters; and the anisotropies in the cosmic microwave background pattern as shown in Figure 1.3.

The existence of dark matter is also extremely crucial to the widely popular and successful Big Bang model of cosmology. It is believed from observations that the structure formation in the universe proceeded hierarchically where material to form smaller structures coagulated and collapsed first followed by larger scale structures such as galaxies and eventually clusters of galaxies in what is called the *bottom-up* formation structure [22]. Ordinary (baryonic) matter is thought to have been too high in temperature with too much pressure after the Big Bang to have contributed to the formation of the smaller structures

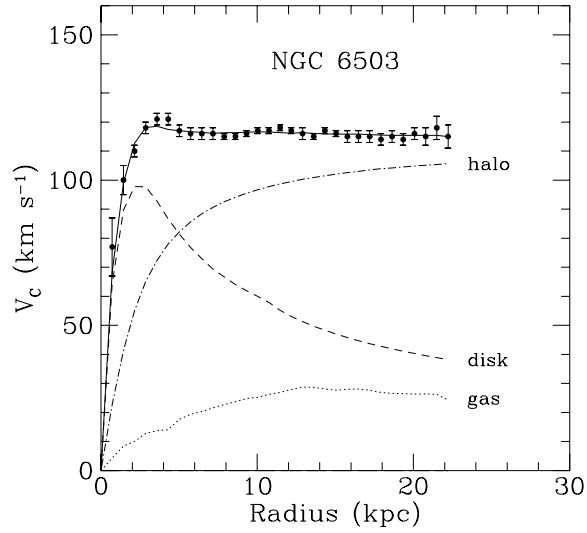


Figure 1.1: Rotation curve for the spiral galaxy NGC6503. The data points are the measured magnitudes of the circular rotation velocities with respect to the distance from the center of the galaxy. The dashed curve represents the contribution to the rotational velocity due to the observed galaxy disk, and the dotted curve that of the galaxy gas. The dot-dash curve represents that of the supposed dark matter halo to make up for the difference between the data and contributions from observed sources. This is one of the leading evidences for the existence of dark matter. Figure taken from [58].

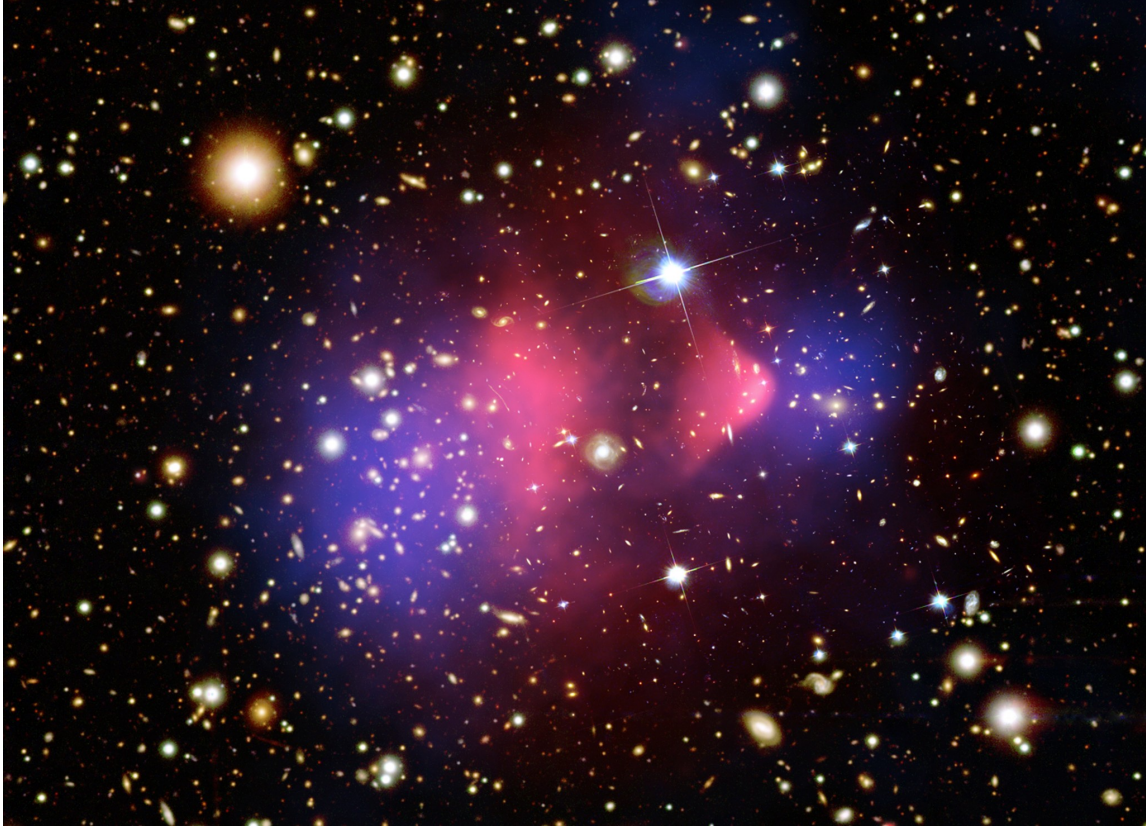


Figure 1.2: The matter in galaxy cluster 1E 0657-56, also known as the *bullet cluster*, is shown in this composite image. The bullet cluster's individual galaxies are seen in the optical image data. The cluster's two clouds of hot x-ray emitting gas is shown in red and representing even more mass than the optical galaxies and x-ray gas combined, the blue hues show the distribution of dark matter in the cluster. The dark matter was mapped by observations of gravitational lensing of background galaxies. The clear separation of dark matter and gas clouds is often considered to be direct evidence for the existence of dark matter. Image taken from [64].

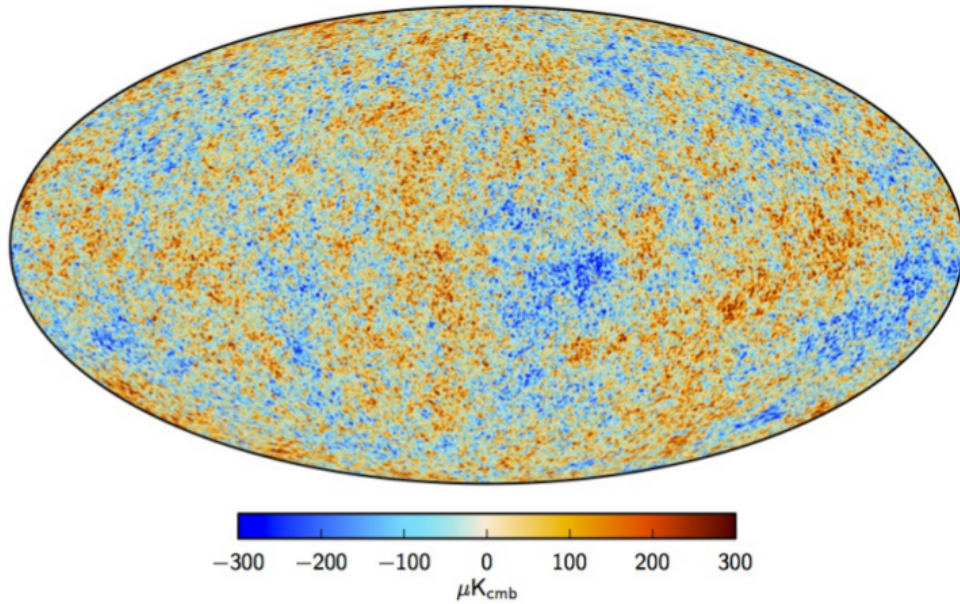


Figure 1.3: The cosmic microwave background (CMB) radiation intensity sky-map at $5'$ resolution derived from the joint analysis of Planck, Wilkinson Microwave Anisotropy Probe (WMAP), and 408 MHz observations. The temperature is measured in units of μK with respect to 2.7 K . The distribution is isotropic to roughly one part in 10^5 . Figure taken from [4].

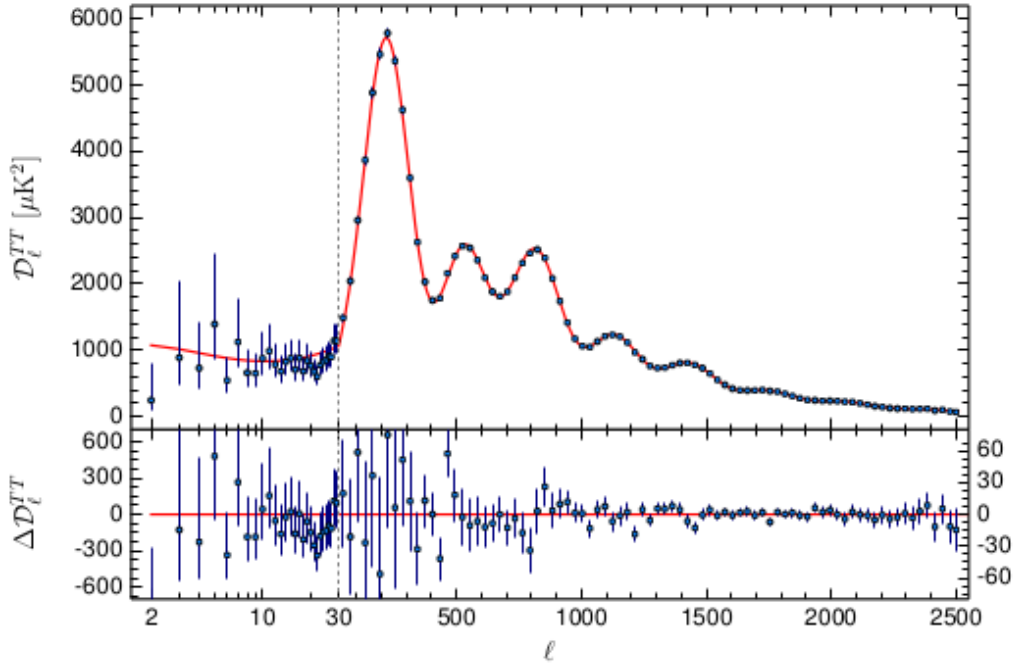


Figure 1.4: The CMB anisotropy spectrum with respect to a multi-pole expansion in parameter l where $\mathcal{D}_l^{TT} = l(l+1)C_l/(2\pi)$. The best-fit base theoretical spectrum is fitted to the data in the upper panel. Residuals with respect to this model are shown in the lower panel. The error bars show $\pm 1\sigma$ uncertainties. The first peak determines the curvature of the universe. The second peak determines the reduced baryon density. The third peak can be used to get information about the dark matter density. Figure taken from [4].

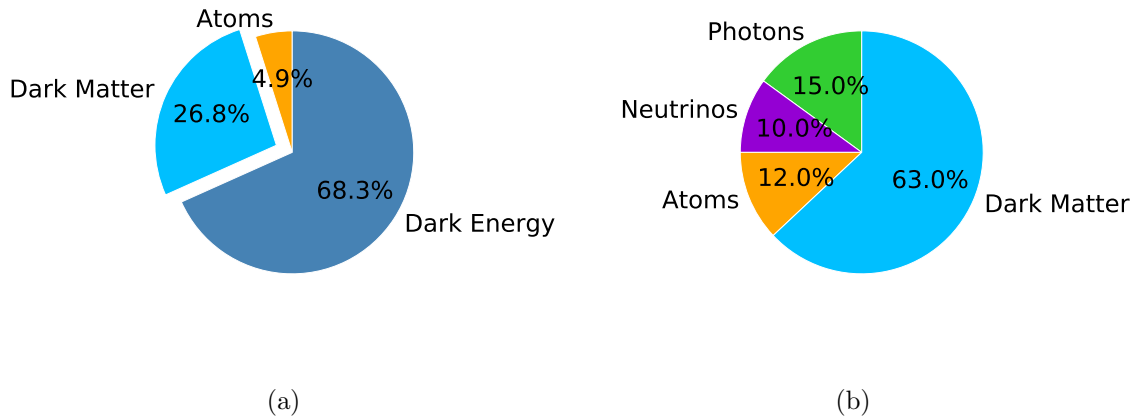


Figure 1.5: Ratio of dark matter to other components that comprise the total mass-energy content of the universe in (a) the present day at about 13.798×10^9 years after the Big Bang, and (b) the early universe at approximately 380 000 years old.

single-handedly. The postulated dark matter serves as a compactor of structure in this scenario while at the same time being consistent with predictions made by the cosmic microwave background.

The current best estimate of the matter and energy composition of the present day universe is that dark matter makes up 26.8% of the mass-energy content of the observable universe. Dark energy composes 68.3% and the left over 4.9% is the contribution from ordinary baryonic matter [66]. This translates to the premise that dark matter may very well comprise an astonishing 84.5% of the total matter in the universe. The contribution of the different constituents of the universe is shown in Figure 1.5.

The hypothesis that most of the matter in the universe may not be visible to us is one of the greatest mysteries in physics and is under intense investigation by cosmologists and various research groups. According to consensus among cosmologists, dark matter is composed primarily of a not yet characterized type of subatomic particle [19, 30] and the search for this particle is one of the major efforts in particle physics today.

Dark matter in the form of a particle can be classified into the three types of *cold*, *warm*, and *hot* dark matter [75]. They are classified in this way depending on the how fast

the particles were moving and thus how far they were able to travel due to random motions just after the Big Bang before they began to slow down as the universe expanded. The approximate dividing line is that warm dark matter particles were able to travel distances or had free-streaming lengths on the scale of the size of protogalaxies in the early universe. They became non-relativistic when the universe was about 1 year old and 1 millionth the size of what it is today. This roughly translates to a mass scale of ~ 250 eV for warm dark matter. Dark matter with masses much less than this and consequently with free-streaming lengths much larger than a protogalaxy is called *hot* dark matter, and those with masses much greater, such as on the GeV to TeV scale, are called *cold* dark matter.

- Cold dark matter: mass \sim GeV or \sim TeV, free-streaming length \ll protogalaxy size [84].
- Warm dark matter: mass ~ 250 eV, free-streaming length \sim protogalaxy size.
- Hot dark matter: mass $< \sim 250$ eV, free-streaming length \gg protogalaxy size [83].

The only known form of hot dark matter is neutrinos, although other forms are speculated to exist. Neutrinos only interact with normal matter through gravity and the weak force making them ideal candidates for dark matter. Neutrinos being light in mass at around less than an eV are a type of weakly interacting light particle (WILP).

There is currently no theoretically well motivated candidate for warm dark matter in the mass range of ~ 300 eV to 3000 eV, although there is a postulated candidate called the sterile neutrino. Sterile neutrinos are proposed to be a heavier version of the typical three flavors of neutrinos and thus move slower, but does not interact through the weak force. At present there is yet no proof of the existence of sterile neutrinos.

Today, candidate models proposing a mixed form of various forms of dark matter as well as those that employ a warm or hot dark matter dominated scenario are considered to be unlikely due to comparisons with cosmological simulations or to a lack of particles candidates provided by theory. In particular, simulations running a hot dark matter dominated cosmology suffer from severe problems when attempting to recreate galaxy-size density fluctuations in a consistent way with the bottom-up galaxy formation structure. Currently, the cold dark matter dominated scenario is the most elegant explanation for

many cosmological observations, but the exact identity of what makes up these cold dark matter particles is still illusive. Some possible candidates may include relatively large baryonic objects such as black holes [51] or neutron stars (collectively called massive astrophysical compact halo object (MACHO)s or smaller sized objects such as brown dwarfs or white dwarfs (collectively called robust association of massive baryonic objects (RAMBO), although these objects have not been found in the abundance required by the Hubble telescope [30] [28]. However, much of the evidence provided by multiple sources such as galaxy rotation curves, gravitational lensing, structure formation, and studies of baryon densities indicate that 85 % to 90 % of the mass content in the universe does not interact electromagnetically and thus cannot be baryonic [68].

This leads to the most favorable candidate being the so-called weakly interacting massive particles (WIMPs) [30] that interact only through gravity and the weak force. This work will focus on the search for WIMPs and their neutrino signals due to their interactions.

It should also be noted here that although there is a general consensus within the community for the existence of dark matter, there exists other alternative theories and ongoing efforts to solve this missing mass problem from other perspectives such as modified Newtonian dynamics (MOND) and tensor-vector-scalar gravity (TeVeS).

1.2 Weakly interacting massive particles (WIMPs)

Weakly interactive massive particles or WIMPs are one of the popular particle physics candidates for cold dark matter. WIMPs are postulated to interact only through gravity and the nuclear weak force or any other type of yet unknown force similar in magnitude to the weak force. The popularity of WIMPs is due to the fact that their properties seem to naturally agree well with that predicted for relic dark matter particles from the early universe.

When the universe was young and hot at extremely high temperatures, particles were energetic enough to create other energetic or massive particles. In this environment, particles were in a state of thermal equilibrium where they and their antiparticle partners would have been constantly forming into and from lighter particles and vice versa. In

particular, dark matter particles would also be involved in this primordial *soup* undergoing the same creation and annihilation processes just like any other type of particle. In this state of equilibrium, the average number of a given type of particles would be more or less constant with respect to time. However, as the universes expanded, the temperatures and thus the kinetic energies of the particles decreased leading to a disruption in this equilibrium. Lighter particles would no longer have enough kinetic energy to produce heavier dark matter particles while the dark matter particles and antiparticles would still be annihilating into the lighter particles. Furthermore, with the expansion of the universe the particle densities became more diluted such that their interactions occurred less frequently until eventually a point was reached when the number of dark matter particles became almost constant in time. This is referred to as *freeze-out* and happens when the reaction rate given by

$$\Gamma = \langle \sigma v \rangle n, \quad (1.2.1)$$

becomes roughly equal to the Hubble parameter $H = 67.80 \text{ (km/s)/Mpc} \sim 10^{-42} \text{ GeV}$. Here $\langle \sigma v \rangle$ is the thermally averaged value of the total cross section for annihilation of dark matter particles χ and antiparticles $\bar{\chi}$ into lighter particles multiplied by the relative velocity v , and n is the dark matter number density. The approximate density of a specific particle type at the time of freeze-out is known as the *relic density*. The relic densities for dark matter with different annihilation cross-sections is shown in Figure 1.6.

1.3 The WIMP miracle

Now let us see how WIMPs have the necessary properties to be good candidates for dark matter. The Friedmann equations (see Appendix A for a derivation and more details) state

$$\frac{\dot{a}^2 + kc^2}{a^2} = \frac{8\pi G\rho + \Lambda c^2}{3}, \quad (1.3.1)$$

$$\frac{\ddot{a}}{a} = -\frac{4\pi G}{3} \left(\rho + \frac{3p}{c^2} + \frac{\Lambda c^2}{3} \right), \quad (1.3.2)$$

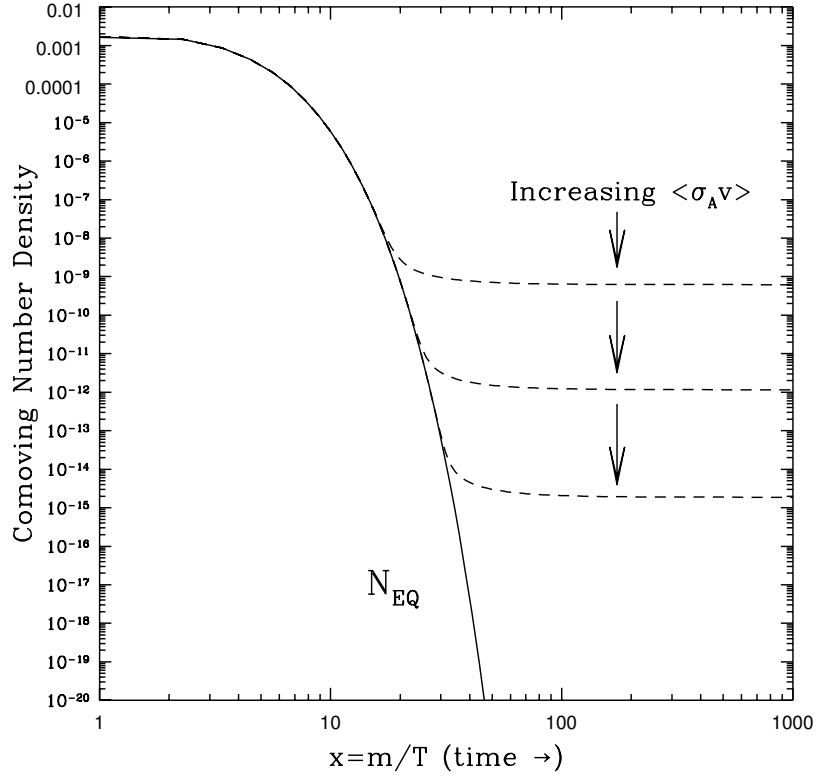


Figure 1.6: Number density of WIMPs in the early universe co-moving with the volume of the universe where m denotes the WIMP mass and T denotes its temperature. The value m/T monotonically increases with the age of the universe. An increase in the WIMP annihilation cross section σ_A , and hence also in $\langle \sigma_A v \rangle$ which denotes the thermally averaged annihilation cross section multiplied by its relative velocity v , induces the WIMPs to stay in thermal equilibrium for a longer period of time, thus resulting in a smaller relic abundance. Dashed curves represent actual abundances, and the solid curve represents that of the case of thermal equilibrium N_{EQ} for all time. Figure taken from [58].

where $a = a(t)$ is the scale factor of the universe as a function of the age of the universe t , and $\dot{a} \equiv \frac{da(t)}{dt}$ and $\ddot{a} \equiv \frac{d^2a(t)}{dt^2}$ are respectively its first and second derivatives with respect to t . $k = +1, 0$, or -1 is a constant depending on the shape of the universe.

- $k = +1$: universe is a closed 3-sphere or three-dimensional surface of a hypersphere.
- $k = 0$: universe is flat or a Euclidean space.
- $k = -1$: universe is an open 3-hyperboloid.

c is the constant speed of light in vacuum, and $G \approx 6.674 \text{ N m}^2/\text{kg}^2$ is Newton's gravitational constant. $\Lambda = 8\pi(G/c^2)\rho_{\text{vac}}$ is the cosmological constant with ρ_{vac} being the energy density of vacuum. ρ is the mass-energy density and p is the hydrostatic pressure.

Assuming that the local spatial geometry is always flat ($k = 0$) and the cosmological constant to be 0 ($\Lambda = 0$), Equation (1.3.1) can be used to define what is called the critical energy density

$$\rho_c \equiv \frac{3H^2}{8\pi G}, \quad (1.3.3)$$

where $H \equiv \dot{a}/a$ is called the Hubble parameter. We can also define the total mass-energy density parameter

$$\Omega_{\text{total}} \equiv \frac{\rho_{\text{total}}}{\rho_c}, \quad (1.3.4)$$

which relates the total mass-energy density of the universe ρ_{total} to that for the case of a locally flat geometry ρ_c . The contribution to Ω_{total} coming solely from mass alone Ω_{mass} has long been studied by various groups yielding approximate bounds

$$0.1 \lesssim \Omega_{\text{mass}} \lesssim 0.4. \quad (1.3.5)$$

The methods for these studies have included application of the virial theorem to galaxy cluster dynamics, gravitational lensing of background galaxies, temperature anisotropies of X-ray gas, and a myriad of others [82]. However, ordinary baryonic matter is known to be insufficient to account for the allowed matter density range coming from these observations. Current best estimates on the baryonic matter density [67] [72] reveal values of only around

$$\Omega_{\text{baryonic}} = 0.04 \pm 0.02, \quad (1.3.6)$$

hence the need for dark matter to make up for the *missing* mass.

If we let the mass-energy density of dark matter be symbolized by ρ_{DM} and its density parameter as

$$\Omega_{\text{DM}} = \frac{\rho_{\text{DM}}}{\rho_c}, \quad (1.3.7)$$

we can roughly estimate a *natural* value for Ω_{DM} . We now know that dark matter is most likely cold and this implies that the dark matter particles were non-relativistic by the time they froze-out and chemically decoupled from other particles in the early Universe. Their mass-energy density today would then be

$$\rho_{\text{DM}} \simeq m_{\text{DM}} n_{\text{DM}}, \quad (1.3.8)$$

where m_{DM} is the mass of the dark matter particle and n_{DM} is its number density. Numerical integration of the Boltzmann equation for n_{DM} gives

$$n_{\text{DM}}(T < T_{\text{freeze-out}}) \sim \frac{n_\gamma}{\sigma m_{\text{DM}} m_{\text{p}}}, \quad (1.3.9)$$

where T and $T_{\text{freeze-out}}$ are respectively the temperatures of dark matter at the time of evaluation and freeze-out, n_γ is the present photon number density, σ is the dark matter annihilation cross-section, and

$$m_{\text{p}} \equiv \sqrt{\hbar c / G} \quad (1.3.10)$$

is the Planck mass. Combining Equations (1.3.7) to (1.3.9) we arrive at the following approximate expression

$$\Omega_{\text{DM}} = \frac{\rho_{\text{DM}}}{\rho_c} \sim \frac{8\pi}{3} \frac{n_\gamma}{\sigma m_{\text{p}}^3 H^2}. \quad (1.3.11)$$

Substituting in the relevant parameters

$$\begin{aligned} \hbar &= c \equiv 1, \\ n_\gamma &\sim 10^{-39} / \text{GeV}^3, \\ H &\sim 10^{-42} \text{ GeV}, \\ m_{\text{p}} &\sim 10^{18} \text{ GeV}, \end{aligned} \quad (1.3.12)$$

and ignoring the constant factor of $8\pi/3$, we obtain

$$\Omega_{\text{DM}} \sim \frac{1}{\sigma(10^9 \text{ GeV})}. \quad (1.3.13)$$

If we assume that dark matter particles are weakly interacting, its annihilation cross-section should be on the order of

$$\sigma \sim \alpha_W^2 G_F \sim 10^{-9}/\text{GeV}^2, \quad (1.3.14)$$

where $\alpha_W \sim 10^{-2}$ is the weak coupling constant and $G_F \sim (300 \text{ GeV})^2$ is the Fermi constant. Substituting these values results in a dark matter density parameter of

$$\Omega_{\text{DM}} \sim 1, \quad (1.3.15)$$

which is roughly the value we need to account for the *missing* matter in the universe. The seemingly remarkable coincidence of weakly interacting cold dark matter particles naturally lending the correct order-of-magnitude density in the universe is the reason why WIMPs are such a favorable candidate. This is sometimes referred to as the *WIMP miracle*.

1.4 Halo models

All observations for detection of existing dark matter, whether it be direct or indirect, depends to varying degrees on the properties of the dark matter halo in the Milky Way. This includes the spatial distribution of the dark matter density. The spatial mass density profile in the Milky Way is broken down into three main components called the *bulge*, the *disk*, and the *halo* depicted in Figure 1.7. The dark matter component is typically assumed to be more or less spherically symmetric and extend well beyond the visible galaxy. The presence of dark matter in the halo is inferred from its gravitational effect on the rotation curve of spiral galaxies.

The dark matter halo profile is typically presented in literature in the form

$$\rho(r) \propto \frac{1}{\left(\frac{r}{a}\right)^\gamma \left[1 + \left(\frac{r}{a}\right)^\alpha\right]^{\left(\frac{\beta-\gamma}{\alpha}\right)}}. \quad (1.4.1)$$

It should be noted that this form can give rise to profiles that are very steep at the center of the galaxy which is in tension with available observations, and this is a currently actively debated topic that will not be addressed further here. Some models with their respective parameters for Equation (1.4.1) are listed in Table 1.1.

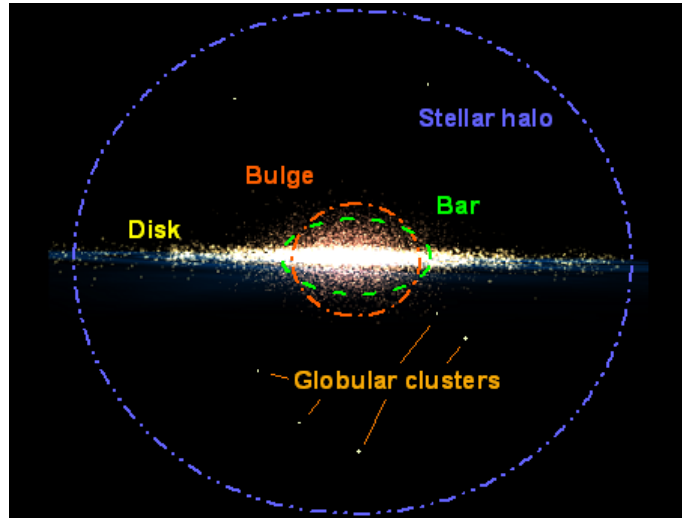


Figure 1.7: Artist’s impression depicting the typical breakdown of the spatial distribution of matter in a galaxy such as the Milky Way. The bulge and bar describe the bulk of matter located at around the central region of the galaxy. The disk extends outward in a flat disk-like profile with the most sparse halo component encompassing the other features. The spatial profile of the dark matter not shown here is typically assumed to be more or less spherically symmetric and extend well beyond the edge of the visible components of the galaxy.

Table 1.1: Dark matter halo profile models with their respective parameters.

Model	(α, β, γ)	$a(\text{kpc})$
Isothermal sphere	(2, 2, 0)	3.5 – 5.0
Kravtsov et al.	(2, 3, 0.2 – 0.4)	–
Navarro, Frenk and White	(1, 3, 1)	20
Moore et al.	(1.5, 3.0, 1.5)	28

Some uncertainties exist in simulations and calculations concerned with dark matter. Namely our galactocentric distance R_0 is not exactly known and is estimated to range within about 7.1 kpc to 8.5 kpc. Furthermore, it is unknown how the black hole at the center of our galaxy would have interacted with the dark matter. Another issue is that the normalization of the dark matter halo profile needs to be set. This is arbitrarily done through the halo density value ρ_0 at our galactocentric distance R_0 and in our calculation this is set to be

$$\rho_0 = 0.3 \text{ GeV}/\text{cm}^3. \quad (1.4.2)$$

1.5 Dark matter capture rate

Dark matter is thought to interact dominantly through the weak and gravitational interactions. It is thought that dark matter particles that are low enough in energy will be *captured* by the gravitational potential well created by astronomical bodies such as our Sun or Earth. Various studies on this have already been conducted since the 1980's and a succinct explanation will be presented here.

Following the customary calculation of dark matter capture in astronomical bodies, we assume radial symmetry of the body with respect to mass density as well as the density of the elemental composition of the body. Then the capture rate of dark matter per unit time Γ_C can be calculated for each element type i in an infinitesimal spherical shell volume of the body according to [46] such that

$$\frac{d\Gamma_{C,i}}{dV} = \int_0^{u_{\max}} du \frac{f(u)}{u} w \Omega_{v_{\text{esc},i}}^-(w), \quad (1.5.1)$$

where u is the magnitude of the WIMP velocity at an infinite distance away from the body $f(u)$ is the velocity distribution normalized such that $\int_0^\infty f(u) = \rho_X$ where ρ_X is the local WIMP density at the body. u has the relation to local velocity w at a given shell through

$$w = \sqrt{u^2 + v_{\text{esc}}^2}, \quad (1.5.2)$$

where v_{esc} is the escape velocity at the shell. The expression $\Omega_{v_{\text{esc},i}}^-(w)$ is the rate of WIMP scatter from velocity w to below v_{esc} due to elements of type i . $\Omega_{v_{\text{esc},i}}^-(w)$ is calculated by

multiplying the WIMP scatter rate on element i , $\sigma_i \rho_i w$, with the conditional probability that a given scatter will leave the WIMP with a velocity less than the escape velocity. If it is assumed that the shell is at zero temperature and the scattering cross section σ_i is isotropic with respect to the scattering deflection angle and velocity independent, this can be written as

$$w \Omega_{v_{\text{esc}},i}^-(w) = \sigma_i \rho_i \left(v_{\text{esc}}^2 - \frac{\mu_-^2}{\mu} u^2 \right) \theta \left(v_{\text{esc}} - \frac{\mu_-}{\mu} u \right), \quad (1.5.3)$$

where we have introduced some new parameters

$$\mu = \frac{m_X}{m_i}, \quad \mu_{\pm} = \frac{\mu \pm 1}{2}. \quad (1.5.4)$$

The Heaviside step function θ makes sure that we only include the WIMPs that scatter to a velocity lower than the escape velocity v_{esc} . m_X is the WIMP mass and m_i is the mass of the i -th element nucleus. In the more general case where the cross section σ_i may be *anisotropic* and *velocity dependent*, this can be expressed as

$$w \Omega_{v_{\text{esc}},i}^-(w) = \sigma_i \rho_i \frac{\mu_+^2}{\mu} 2E_0 \left[\exp \left(-\frac{m_X u^2}{2E_0} \right) - \exp \left(-\frac{\mu}{\mu_+} m_X \frac{u^2 + v_{\text{esc}}^2}{2E_0} \right) \right] \theta \left(\frac{\mu}{\mu_+} - \frac{u^2}{u^2 + v_{\text{esc}}^2} \right), \quad (1.5.5)$$

where

$$E_0 = \frac{3\hbar^2}{2m_X r_i^2} \quad (1.5.6)$$

is what is known as the characteristic coherence energy and r_i is the nuclear radius of the i -th element that can be estimated from [33] as

$$r_i \sim \left[0.91 \left(\frac{m_i}{\text{GeV}} \right)^{\frac{1}{3}} + 0.3 \right] \times 10^{-13} \text{ cm}. \quad (1.5.7)$$

The scattering cross section on the i -th element can be expressed as

$$\sigma_i = \sigma_p A_i^2 \frac{(m_X m_i)^2}{(m_X + m_i)^2} \frac{(m_X + m_p)^2}{(m_X m_p)^2}, \quad (1.5.8)$$

where A_i is the atomic number of the element, m_p is the proton mass, and σ_p is the scattering cross section on protons.

This now gives us everything that is required to calculate the WIMP capture rate. The velocity distribution of WIMPs at an infinite distance $f_0(u)$ is usually taken to be a Maxwell-Boltzmann distribution,

$$f_0(u) du = \rho_X \frac{4}{\sqrt{\pi}} \left(\frac{3}{2}\right)^{\frac{3}{2}} \frac{u^2}{\bar{v}^3} e^{-\frac{3}{2} \frac{u^2}{\bar{v}^2}} du, \quad (1.5.9)$$

where \bar{v} is the three-dimensional velocity dispersion defined in [46] as

$$\bar{v}^2 \equiv \frac{3kT_X}{m_X}, \quad (1.5.10)$$

and k is the Boltzmann constant with T_X being the temperature of the WIMP distribution. However, the solar system moves through the WIMP halo with some non-zero velocity, say v_B . Then an observer with this velocity will experience a distribution such as

$$\begin{aligned} f_B(u) &= f_0(u) \exp\left(-\frac{3}{2} \frac{v_B^2}{\bar{v}^2}\right) \frac{\sinh\left(\frac{3uv_B}{\bar{v}^2}\right)}{\frac{3uv_B}{\bar{v}^2}} \\ &= \rho_X \sqrt{\frac{3}{2\pi}} \left[\exp\left(-\frac{3}{2} \frac{(u - v_B)^2}{\bar{v}^2}\right) - \exp\left(-\frac{3}{2} \frac{(u + v_B)^2}{\bar{v}^2}\right) \right]. \end{aligned} \quad (1.5.11)$$

This expression is correct for an observer on the Sun moving through *free space*, but is not exactly correct for the case of the Earth which itself lies deep in the gravitational potential well of the Sun. There are two competing effects which arise for the case of the Earth in the Sun's potential well that differs from that of if the Earth were in free space. The first is that the *direct* capture of WIMP particles in unbounded orbits is reduced because the incoming WIMPs have a higher speed being accelerated by the Sun's potential well by the time they reach the Earth, and thus are more unlikely to be captured. The second effect is that WIMPs may be *indirectly* captured in the sense that those that scatter off from nuclei in the Earth, may not lose enough energy to be captured by the Earth, but may lose enough energy to be bounded by the Sun's gravitational well, thus potentially enable a recaptured by the Earth at a later time. It turns out that the combined effect of direct capture by the Earth from bound and unbounded WIMPs is similar to that of the case if the Earth were in free space within about 10% [47]. Moreover, due to gravitational diffusion of the WIMPs toward the center of the Sun, the effect from indirect capture is estimated to be

Table 1.2: Default parameters used by DarkSUSY for calculating WIMP capture in the Sun and Earth.

Parameter	Value
Three-dimensional velocity dispersion	$\bar{v} = 270 \text{ km/s}$
Galactocentric speed of Sun	$v_{\odot} = 220 \text{ km/s}$
Galactic escape velocity	$v_{\text{esc,galaxy}} = 600 \text{ km/s}$
Sun escape velocity at Sun surface	$v_{\text{esc},\odot} = 617.57 \text{ km/s}$
Earth escape velocity at Earth surface	$v_{\text{esc},\oplus} = 11.2 \text{ km/s}$
Yearly averaged Earth velocity with respect to halo	$v_{\oplus,\text{halo}} = 264 \text{ km/s}$
Earth velocity with respect to solar system	$v_{\oplus} = 29.78 \text{ km/s}$
Galactocentric distance of Sun	$R_0 = 8 \text{ kpc}$
Local dark matter halo density	$\rho_X = \rho_0 = 0.3 \text{ GeV/cm}^3$
Shape of halo	spherical
Halo profile	Navarro-Frenk-White

negligible [47]. It has been shown that all of these approximations hold true even for the case of WIMP masses m_X outside of the so called resonance range of

$$10 \text{ GeV} \lesssim m_X \lesssim 75 \text{ GeV} , \quad (1.5.12)$$

where m_X is close to the nucleus mass of at least one of the elements in the Earth.

Now using Equation (1.5.1) with our chosen velocity distribution $f_B(u)$, we can integrate over the radius of the body and sum over the different elements comprising the body

$$\Gamma_C = \int_0^{R_B} dr \sum_i \frac{d\Gamma_{C,i}}{dV} 4\pi r^2 . \quad (1.5.13)$$

The actual calculation for WIMP capture on the Sun and Earth in this study is conducted using the DarkSUSY numerical simulation software [43]. Table 1.2 shows the default parameters used by DarkSUSY for the calculation.

Figures 1.8 and 1.9 show the dark matter capture rates in the Earth and Sun for identical dark matter-nucleon scattering cross sections for both spin-independent and

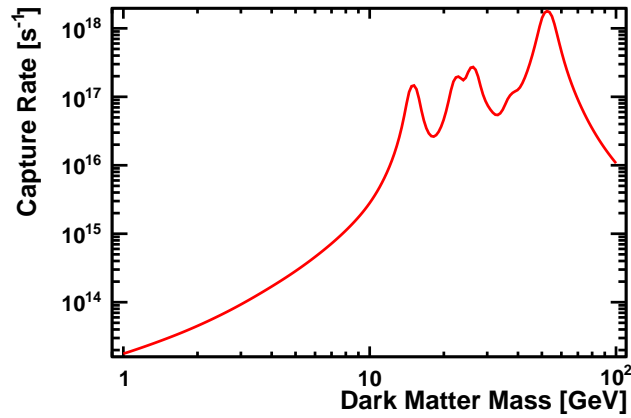


Figure 1.8: Dark matter capture rate in the Earth for spin-independent dark matter-nucleon scattering cross-section $\sigma_{\text{SI}} = 1 \times 10^{-40} \text{ cm}^2$. Four resonance peaks in the capture rate are seen due to enhancements from matching of the dark matter mass with that of the Earth elements. The first peak is due to ^{16}O , the second to ^{24}Mg , the third to ^{28}Si and ^{32}S , and the fourth to ^{56}Fe – ^{58}Ni .

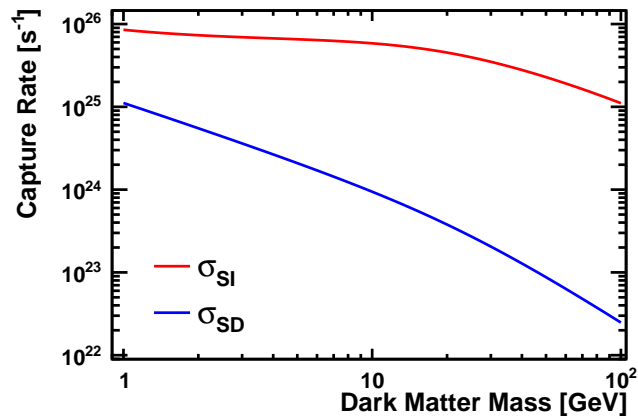


Figure 1.9: Dark matter capture rate in the Sun for spin-dependent and spin-independent dark matter-nucleon scattering cross-sections, σ_{SD} and σ_{SI} , both set at identical values such that $\sigma_{\text{SD}} = \sigma_{\text{SI}} = 1 \times 10^{-40} \text{ cm}^2$.

spin-dependent cases such that $\sigma_{\text{SI}} = \sigma_{\text{SD}} = 10^{-40} \text{ cm}^2$. Also Shown are the two commonly assumed cases of isospin-invariant and isospin-violating dark matter where the ratios between the coupling strengths to protons and neutrons were respectively chosen to be $f_n/f_p = 1$ and $f_n/f_p = -0.7$.

It is convenient in our analysis as will be shown later in Section 6.3 to define a dark matter mass dependent parameter that represents the ratio of dark matter capture rate Γ_C over the dark matter-nucleon scattering cross section σ_{XN} such as

$$C_0(m_X) \equiv \frac{\Gamma_C(m_X)}{\sigma_{XN}}. \quad (1.5.14)$$

All dependence on the cross section is effectively taken out of both sides of the equation and we can calculate $C_0(m_X)$ using DarkSUSY with some arbitrary cross section for the range of dark matter masses we are interested in. This is tabulated in Tables 1.3 and 1.4 using $\sigma_{XN} = 10^{-40} \text{ cm}^2$.

Table 1.3: Ratio $C_0 = \Gamma_C/\sigma$ of WIMP capture rate in the Earth Γ_C over WIMP-nucleon scattering cross section σ with respect to WIMP mass m_X . SI indicates *spin independent* scattering. Units for the ratio C_0 are in $\text{s}^{-1} \text{pb}^{-1}$.

$\log_{10}(m_X/\text{GeV})$	$m_X[\text{GeV}]$	$C_0^{\text{SI}}(f_n/f_p = 1)$	$C_0^{\text{SI}}(f_n/f_p = -0.7)$
0.00	1.0000	1.7697×10^{17}	2.7420×10^{15}
0.05	1.1220	2.0281×10^{17}	3.1476×10^{15}
0.10	1.2589	2.3408×10^{17}	3.6332×10^{15}
0.15	1.4125	2.7201×10^{17}	4.2157×10^{15}
0.20	1.5849	3.1838×10^{17}	4.9237×10^{15}
0.25	1.7783	3.7616×10^{17}	5.8118×10^{15}
0.30	1.9953	4.4949×10^{17}	6.9595×10^{15}
0.35	2.2387	5.4316×10^{17}	8.4565×10^{15}
0.40	2.5119	6.6393×10^{17}	1.0421×10^{16}
0.45	2.8184	8.2142×10^{17}	1.3034×10^{16}
0.50	3.1623	1.0304×10^{18}	1.6578×10^{16}
0.55	3.5481	1.3080×10^{18}	2.1398×10^{16}
0.60	3.9811	1.6779×10^{18}	2.7958×10^{16}
0.65	4.4668	2.1757×10^{18}	3.6962×10^{16}
0.70	5.0119	2.8660×10^{18}	4.9573×10^{16}
0.75	5.6234	3.8486×10^{18}	6.7556×10^{16}
0.80	6.3096	5.2855×10^{18}	9.3978×10^{16}
0.85	7.0795	7.4468×10^{18}	1.3429×10^{17}
0.90	7.9433	1.0873×10^{19}	1.9979×10^{17}
0.95	8.9125	1.6729×10^{19}	3.1520×10^{17}
1.00	10.000	2.8122×10^{19}	5.4836×10^{17}
1.05	11.220	5.5713×10^{19}	1.1354×10^{18}
1.10	12.589	1.4792×10^{20}	3.1566×10^{18}
1.15	14.125	8.0266×10^{20}	1.7769×10^{19}
1.20	15.849	9.4332×10^{20}	2.0797×10^{19}
1.25	17.783	2.7690×10^{20}	5.3486×10^{18}
1.30	19.953	4.5924×10^{20}	8.6939×10^{18}
1.35	22.387	1.9184×10^{21}	3.6782×10^{19}
1.40	25.119	2.3030×10^{21}	4.6270×10^{19}
1.45	28.184	1.4346×10^{21}	2.8654×10^{19}
1.50	31.623	5.8679×10^{20}	9.6668×10^{18}
1.55	35.481	7.7062×10^{20}	1.1012×10^{19}
1.60	39.811	1.2536×10^{21}	1.3927×10^{19}
1.65	44.668	3.0567×10^{21}	2.4988×10^{19}
1.70	50.119	1.4285×10^{22}	1.1393×10^{20}
1.75	56.234	1.1543×10^{22}	8.6750×10^{19}
1.80	63.096	2.4789×10^{21}	1.8325×10^{19}
1.85	70.795	8.3154×10^{20}	6.2868×10^{18}
1.90	79.433	3.6181×10^{20}	2.7724×10^{18}
1.95	89.125	1.8588×10^{20}	1.4396×10^{18}
2.00	100.00	1.0721×10^{20}	8.3687×10^{17}

Table 1.4: Ratio $C_0 = \Gamma_C/\sigma$ of WIMP capture rate in the Sun Γ_C over WIMP-nucleon scattering cross section σ with respect to WIMP mass m_X . SI indicates *spin independent* and SD indicates *spin dependent* scattering. Units for the ratio C_0 are in $\text{s}^{-1} \text{pb}^{-1}$.

$\log_{10}(m_X/\text{GeV})$	$m_X[\text{GeV}]$	C_0^{SD}	$C_0^{\text{SI}}(f_n/f_p = 1)$	$C_0^{\text{SI}}(f_n/f_p = -0.7)$
0.00	1.0000	1.1132×10^{29}	8.5234×10^{29}	1.2783×10^{29}
0.05	1.1220	9.9166×10^{28}	8.2573×10^{29}	1.1530×10^{29}
0.10	1.2589	8.8296×10^{28}	8.0225×10^{29}	1.0410×10^{29}
0.15	1.4125	7.8580×10^{28}	7.8156×10^{29}	9.4088×10^{28}
0.20	1.5849	6.9897×10^{28}	7.6335×10^{29}	8.5136×10^{28}
0.25	1.7783	6.2140×10^{28}	7.4730×10^{29}	7.7133×10^{28}
0.30	1.9953	5.5212×10^{28}	7.3312×10^{29}	6.9979×10^{28}
0.35	2.2387	4.9026×10^{28}	7.2051×10^{29}	6.3582×10^{28}
0.40	2.5119	4.3503×10^{28}	7.0920×10^{29}	5.7858×10^{28}
0.45	2.8184	3.8574×10^{28}	6.9894×10^{29}	5.2735×10^{28}
0.50	3.1623	3.4175×10^{28}	6.8945×10^{29}	4.8144×10^{28}
0.55	3.5481	3.0249×10^{28}	6.8052×10^{29}	4.4026×10^{28}
0.60	3.9811	2.6747×10^{28}	6.7190×10^{29}	4.0327×10^{28}
0.65	4.4668	2.3623×10^{28}	6.6336×10^{29}	3.6998×10^{28}
0.70	5.0119	2.0836×10^{28}	6.5466×10^{29}	3.3995×10^{28}
0.75	5.6234	1.8351×10^{28}	6.4557×10^{29}	3.1279×10^{28}
0.80	6.3096	1.6134×10^{28}	6.3584×10^{29}	2.8814×10^{28}
0.85	7.0795	1.4158×10^{28}	6.2519×10^{29}	2.6569×10^{28}
0.90	7.9433	1.2396×10^{28}	6.1337×10^{29}	2.4515×10^{28}
0.95	8.9125	1.0826×10^{28}	6.0010×10^{29}	2.2626×10^{28}
1.00	10.000	9.4284×10^{27}	5.8512×10^{29}	2.0881×10^{28}
1.05	11.220	8.1845×10^{27}	5.6823×10^{29}	1.9258×10^{28}
1.10	12.589	7.0793×10^{27}	5.4926×10^{29}	1.7742×10^{28}
1.15	14.125	6.0993×10^{27}	5.2815×10^{29}	1.6320×10^{28}
1.20	15.849	5.2324×10^{27}	5.0491×10^{29}	1.4981×10^{28}
1.25	17.783	4.4682×10^{27}	4.7971×10^{29}	1.3717×10^{28}
1.30	19.953	3.7974×10^{27}	4.5281×10^{29}	1.2524×10^{28}
1.35	22.387	3.2115×10^{27}	4.2458×10^{29}	1.1399×10^{28}
1.40	25.119	2.7024×10^{27}	3.9548×10^{29}	1.0340×10^{28}
1.45	28.184	2.2629×10^{27}	3.6599×10^{29}	9.3476×10^{27}
1.50	31.623	1.8858×10^{27}	3.3660×10^{29}	8.4209×10^{27}
1.55	35.481	1.5643×10^{27}	3.0775×10^{29}	7.5599×10^{27}
1.60	39.811	1.2919×10^{27}	2.7982×10^{29}	6.7639×10^{27}
1.65	44.668	1.0626×10^{27}	2.5310×10^{29}	6.0318×10^{27}
1.70	50.119	8.7078×10^{26}	2.2782×10^{29}	5.3614×10^{27}
1.75	56.234	7.1110×10^{26}	2.0412×10^{29}	4.7505×10^{27}
1.80	63.096	5.7889×10^{26}	1.8208×10^{29}	4.1959×10^{27}
1.85	70.795	4.6994×10^{26}	1.6173×10^{29}	3.6946×10^{27}
1.90	79.433	3.8052×10^{26}	1.4306×10^{29}	3.2431×10^{27}
1.95	89.125	3.0743×10^{26}	1.2605×10^{29}	2.8379×10^{27}
2.00	100.00	2.4788×10^{26}	1.1061×10^{29}	2.4757×10^{27}

Chapter 2

Neutrino Oscillation

2.1 Overview

There is ample experimental evidence for the theory of the oscillation of neutrino flavor [39, 44]. This phenomenon is seen in a plethora of different types of neutrinos such as those originating from the Sun, the atmosphere of the Earth, and human-made sources such as nuclear reactors and neutrino beams. The phenomenon of the oscillation of neutrino flavor or more simply referred to as *neutrino oscillation* or *neutrino mixing* arises from the mixture between flavor and mass eigenstates of the neutrinos. Here the neutrino flavor states that interact through the weak interaction with a charged lepton such as an electron, tau, or muon are not proportional to but are superpositions of the neutrino states of definite mass. Neutrinos are created in their flavor eigenstates through the weak interaction but the quantum mechanical phases of the mass eigenstates that comprise the flavor state, each advance at slightly different rates due to the slight differences in the neutrino masses. As the neutrino propagates, it evolves to become a different mixture of mass states from that of what it initially started as and in effect also becomes a different mixture of flavor states. An observer who detects the neutrino at some later time, again using the same weak interaction mechanism, has a finite probability to observe a different neutrino flavor from what it had originally started out as.

2.2 Theory

According to the current standard model, there are three types of neutrino flavors and three different masses of neutrinos that are known to exist. It may very well be the case that there are even more neutrino states than what is currently known and these if any are aptly coined *sterile neutrinos* by the community. However we will ignore the existence of sterile neutrinos for the time being and assume the standard three flavor and three mass eigenstates for the duration of this chapter.

In the following, we will develop the full theory of three flavor neutrino oscillation and the effects of the ambient matter, known as the Mikheyev-Smirnov-Wolfenstein (MSW) effect, for the case of when neutrinos travel through normal matter such as those that comprise the Sun or Earth. Let us begin by defining the notation for the three neutrinos of different flavors to be ν_e, ν_μ, ν_τ , and the three neutrinos of different masses to be ν_1, ν_2, ν_3 with masses m_1, m_2, m_3 respectively.

The three neutrino flavors are mixed states of the three mass states such that

$$\nu_\alpha = \sum_{k=1,2,3} U_{\alpha k} \nu_k, \quad (2.2.1)$$

where $\alpha = e, \mu, \tau$ and U is a unitary three-by-three mixing matrix ($UU^\dagger = U^\dagger U = 1$). When the neutrino is first produced through a charged-current weak interaction process with a charged lepton, say any one of the particles e, μ, τ , it carries a certain definite momentum p

$$|\nu_\alpha(p)\rangle = \sum_{k=1,2,3} U_{\alpha k}^* |\nu_k(p)\rangle. \quad (2.2.2)$$

Here $|\nu_k(p)\rangle$ denotes the state of a neutrino with definite mass m_k , momentum p , and energy $E_k = \sqrt{p^2 + m_k^2}$ that satisfies the energy eigenvalue equation

$$\mathcal{H}_0 |\nu_k(p)\rangle = E_k |\nu_k(p)\rangle, \quad (2.2.3)$$

where \mathcal{H}_0 is the Hamiltonian of the neutrino in vacuum. The neutrino having an extremely small mass and in addition being very relativistic, at least for those that are currently

detectable in feasible experiments, allows us to make the approximation

$$E_k \simeq p + \frac{m_k^2}{2p}. \quad (2.2.4)$$

For the case of neutrinos propagating through matter such as the Sun or the Earth, the full Hamiltonian is no longer \mathcal{H}_0 but

$$\mathcal{H} = \mathcal{H}_0 + \mathcal{H}_1, \quad (2.2.5)$$

where \mathcal{H}_1 is the effective contribution of the weak interaction of the neutrino with electrons, protons, or neutrons in the medium. Here the neutrino flavor states are eigenstates of \mathcal{H}_1 :

$$\mathcal{H}_1 |\nu_\alpha(p)\rangle = V_\alpha |\nu_\alpha(p)\rangle, \quad (2.2.6)$$

with

$$V_e = V_{\text{CC}} + V_{\text{NC}}, \quad V_\mu = V_\tau = V_{\text{NC}}, \quad (2.2.7)$$

or equivalently

$$V_\alpha = V_{\text{NR}} + V_{\text{CC}}\delta_{\alpha e}. \quad (2.2.8)$$

V_{CC} and V_{NC} are the effective potentials for the charged-current and neutral-current interactions respectively:

$$V_{\text{CC}} = 2G_{\text{F}}N_e, \quad V_{\text{NC}} = -\frac{\sqrt{2}}{2}G_{\text{F}}N_n, \quad (2.2.9)$$

where $G_{\text{F}} = 1.16637 \times 10^{-5} \text{ GeV}^{-2}$ is the Fermi constant and N_e and N_n are, respectively, the electron and neutron number densities of the medium. The corresponding effective potentials of the anti-neutrinos have the same value but are opposite in sign: $\bar{V}_{\text{CC}} = -V_{\text{CC}}$, $\bar{V}_{\text{NC}} = -V_{\text{NC}}$.

Let us consider a neutrino with momentum p produced at some time $t = 0$ by a charged current weak interaction process involving a charged lepton α ($\alpha = e, \mu, \tau$). In the Schrödinger picture, at some later point in time $t \neq 0$, this neutrino is described by the state

$$|\varphi^{(\alpha)}(p, t)\rangle = \sum_{\beta} \varphi_{\beta}^{(\alpha)}(p, t) |\nu_{\beta}(p)\rangle. \quad (2.2.10)$$

This state is a superposition of flavor states $|\nu_\beta(p)\rangle$ with amplitudes $\varphi_\beta^{(\alpha)}(p, t)$ which depend on time and have the initial value $\varphi_\beta^{(\alpha)}(p, t) = \delta_{\alpha\beta}$.

The time evolution of this state is given by the Schrödinger equation

$$\begin{aligned}
i \frac{d}{dt} |\varphi^{(\alpha)}(p, t)\rangle &= \mathcal{H} |\varphi^{(\alpha)}(p, t)\rangle \\
&= \sum_{\rho} \varphi_{\rho}^{(\alpha)}(p, t) (\mathcal{H}_0 + \mathcal{H}_1) |\nu_{\rho}(p)\rangle \\
&= \sum_{\rho} \varphi_{\rho}^{(\alpha)}(p, t) \left(\sum_k U_{\rho k}^* E_k |\nu_k(p)\rangle + V_{\rho} |\nu_{\rho}(p)\rangle \right) \\
&= \sum_{\sigma, \rho} \varphi_{\rho}^{(\alpha)}(p, t) \left(\sum_k U_{\rho k}^* E_k U_{\sigma k} + V_{\rho} \delta_{\rho\sigma} \right) |\nu_{\sigma}(p)\rangle .
\end{aligned} \tag{2.2.11}$$

Projecting this equation on $\langle \nu_{\beta}(p) |$ and taking into account that $\langle \nu_{\beta}(p) | \nu_{\rho}(p) \rangle = \delta_{\beta\rho}$, we obtain

$$i \frac{d}{dt} \varphi_{\beta}^{(\alpha)}(p, t) = \sum_{\rho} \left(\sum_k U_{\beta k} E_k U_{\rho k}^* + V_{\rho} \delta_{\beta\rho} \right) \varphi_{\rho}^{(\alpha)}(p, t) . \tag{2.2.12}$$

This is the evolution equation for the flavor amplitudes $\varphi_{\beta}^{(\alpha)}(p, t)$, whose modulus-square give the probability of $\nu_{\alpha} \longrightarrow \nu_{\beta}$ transition, $P_{\nu_{\alpha} \rightarrow \nu_{\beta}}(p, t) = |\varphi_{\beta}^{(\alpha)}(p, t)|^2$. Using Equation (2.2.4) for the approximation of relativistic neutrinos and Equation (2.2.8) for the effective potentials

of neutrinos propagating through matter, we can rewrite this as

$$\begin{aligned}
i \frac{d}{dt} \varphi_\beta^{(\alpha)}(p, t) &= \sum_\rho \left(\sum_k U_{\beta k} \left(p + \frac{m_k^2}{2p} \right) U_{\rho k}^* + (V_{\text{NC}} + V_{\text{CC}} \delta_{\rho e}) \delta_{\beta \rho} \right) \varphi_\rho^{(\alpha)}(p, t) \\
&= \sum_\rho \left(p \sum_k U_{\beta k} U_{\rho k}^* + V_{\text{NC}} \delta_{\beta \rho} \right) \varphi_\rho^{(\alpha)}(p, t) \\
&\quad + \sum_\rho \left(\sum_k U_{\beta k} \frac{m_k^2}{2p} U_{\rho k}^* + V_{\text{CC}} \delta_{\rho e} \delta_{\beta \rho} \right) \varphi_\rho^{(\alpha)}(p, t) \\
&= \sum_\rho (p \delta_{\beta \rho} + V_{\text{NC}} \delta_{\beta \rho}) \varphi_\rho^{(\alpha)}(p, t) \\
&\quad + \sum_\rho \left(\sum_k U_{\beta k} \frac{m_k^2}{2p} U_{\rho k}^* + V_{\text{CC}} \delta_{\rho e} \delta_{\beta e} \right) \varphi_\rho^{(\alpha)}(p, t) \\
&= (p + V_{\text{NC}}) \varphi_\beta^{(\alpha)}(p, t) \\
&\quad + \sum_\rho \left(\sum_k U_{\beta k} \frac{m_k^2}{2p} U_{\rho k}^* + V_{\text{CC}} \delta_{\beta e} \delta_{\rho e} \right) \varphi_\rho^{(\alpha)}(p, t),
\end{aligned} \tag{2.2.13}$$

where we have separated the contribution of the neutral-current effective potential V_{NC} , which is the same for all three neutrino flavors, from the contribution of the charged-current effective potential V_{CC} , which solely affects only the electron neutrino component. Redefining the flavor amplitudes $\varphi_\beta^{(\alpha)}$ to accommodate for an extra phase factor that leaves the observable transition probabilities unaltered, we can define

$$\psi_\beta^{(\alpha)}(p, t) \equiv \varphi_\beta^{(\alpha)} \exp \left(ipt + i \int_0^1 V_{\text{NC}}(t') dt' \right), \tag{2.2.14}$$

where the integral of V_{NC} over time takes into account the fact that V_{NC} in general may not be constant along the neutrino trajectory. This yields for relativistic neutrinos the following equation for the evolution of the flavor transition amplitudes $\psi_\beta^{(\alpha)}$:

$$i \frac{d}{dt} \psi_\beta^{(\alpha)}(p, t) = \sum_\rho \left(\sum_k U_{\beta k} \frac{m_k^2}{2p} U_{\rho k}^* + V_{\text{CC}} \delta_{\beta e} \delta_{\rho e} \right) \psi_\rho^{(\alpha)}(p, t). \tag{2.2.15}$$

We can substitute $V_{\text{CC}} = 0$ for the case of neutrino oscillation in vacuum as well as $V_{\text{CC}} \neq 0$ for the case of oscillation in matter. The solution to this evolution Equation (2.2.15) in

vacuum is given by

$$\psi_\beta^{(\alpha)}(p, t) = \sum_k U_{\alpha k}^* U_{\beta k} \exp\left(-i \frac{m_k^2}{2p} t\right), \quad (2.2.16)$$

and observable probability of detecting a given neutrino of flavor β after some time $t \simeq L/c$ where L is the distance traversed, is given by

$$P_{\nu_\alpha \rightarrow \nu_\beta}(p, t) = \left| \varphi_\beta^{(\alpha)}(p, t) \right|^2 = \left| \psi_\beta^{(\alpha)}(p, t) \right|^2. \quad (2.2.17)$$

If we work out the transition probabilities explicitly, we have

$$\begin{aligned} P_{\nu_\alpha \rightarrow \nu_\beta}(p, t) &= \left| \psi_\beta^{(\alpha)}(p, t) \right|^2 \\ &= \left| \sum_k U_{\alpha k}^* U_{\beta k} \exp\left(-i \frac{m_k^2}{2p} t\right) \right|^2 \\ &= \sum_k U_{\alpha k}^* U_{\beta k} \exp\left(-i \frac{m_k^2}{2p} t\right) \sum_j U_{\alpha j} U_{\beta j}^* \exp\left(i \frac{m_j^2}{2p} t\right) \\ &= \sum_k \sum_j U_{\alpha k}^* U_{\alpha j} U_{\beta k} U_{\beta j}^* \exp\left(-i \frac{m_k^2 - m_j^2}{2p} t\right). \end{aligned} \quad (2.2.18)$$

Noticing the feature that the final double sum is over elements of a three-by-three Hermitian matrix, we can rewrite this to be a sum over the diagonal and non-diagonal elements separately giving us

$$\begin{aligned} P_{\nu_\alpha \rightarrow \nu_\beta}(p, t) &= \sum_{k=j} U_{\alpha k}^* U_{\alpha j} U_{\beta k} U_{\beta j}^* \exp\left(-i \frac{m_k^2 - m_j^2}{2p} t\right) \\ &\quad + \sum_{k \neq j} U_{\alpha k}^* U_{\alpha j} U_{\beta k} U_{\beta j}^* \exp\left(-i \frac{m_k^2 - m_j^2}{2p} t\right). \end{aligned} \quad (2.2.19)$$

Simplifying and rewriting this gives us the famous formula for flavor oscillation probabilities in vacuum,

$$P_{\nu_\alpha \rightarrow \nu_\beta}(p, t) = \sum_k |U_{\alpha k}|^2 |U_{\beta k}|^2 + 2\Re \sum_{k>j} U_{\alpha k}^* U_{\beta k} U_{\alpha j} U_{\beta j}^* \exp\left(-i \frac{\Delta m_{kj}^2}{2p} t\right), \quad (2.2.20)$$

where we have defined $\Delta m_{kj}^2 \equiv m_k^2 - m_j^2$.

Let us now turn our attention to the solution to the flavor evolution Equation (2.2.15) for the case of neutrino propagation in matter. For convenience, writing this equation in matrix form, we have

$$i\frac{d}{dt}\Psi_W^{(\alpha)}(p,t) = \frac{1}{2p} \left(UM^2U^\dagger + A_W \right) \Psi_W^{(\alpha)}(p,t), \quad (2.2.21)$$

where we have defined

$$\Psi_W^{(\alpha)}(p,t) \equiv \begin{pmatrix} \psi_e^{(\alpha)}(p,t) \\ \psi_\mu^{(\alpha)}(p,t) \\ \psi_\tau^{(\alpha)}(p,t) \end{pmatrix}, \quad (2.2.22)$$

and

$$M \equiv \begin{pmatrix} m_1 & 0 & 0 \\ 0 & m_2 & 0 \\ 0 & 0 & m_3 \end{pmatrix}, \quad A_W \equiv \begin{pmatrix} A_{CC} & 0 & 0 \\ 0 & 0 & 0 \\ 0 & 0 & 0 \end{pmatrix}, \quad A_{CC} \equiv 2pV_{CC}. \quad (2.2.23)$$

For anti-neutrinos, A_{CC} must be replaced by $\bar{A}_{CC} = -A_{CC}$.

The three-by-three mixing matrix U is popularly parameterized as

$$U = V_{23} \left(D_{13} V_{13} D_{13}^\dagger \right) V_{12} D(\lambda), \quad (2.2.24)$$

with the following three orthogonal rotation matrices in the Hilbert space spanned by the neutrino mass states

$$\begin{aligned} V_{23} &= \begin{pmatrix} 1 & 0 & 0 \\ 0 & \cos \theta_{23} & \sin \theta_{23} \\ 0 & -\sin \theta_{23} & \cos \theta_{23} \end{pmatrix}, \\ V_{13} &= \begin{pmatrix} \cos \theta_{13} & 0 & \sin \theta_{13} \\ 0 & 1 & 0 \\ -\sin \theta_{13} & 0 & \cos \theta_{13} \end{pmatrix}, \\ V_{12} &= \begin{pmatrix} \cos \theta_{12} & \sin \theta_{12} & 0 \\ -\sin \theta_{12} & \cos \theta_{12} & 0 \\ 0 & 0 & 1 \end{pmatrix}, \end{aligned} \quad (2.2.25)$$

and

$$D_{13} = \begin{pmatrix} 1 & 0 & 0 \\ 0 & 1 & 0 \\ 0 & 0 & e^{i\delta} \end{pmatrix}, \quad D(\lambda) = \begin{pmatrix} 1 & 0 & 0 \\ 0 & e^{i\lambda_1/2} & 0 \\ 0 & 0 & e^{i\lambda_2/2} \end{pmatrix}. \quad (2.2.26)$$

This is also often times written out fully in the form

$$U = \begin{pmatrix} c_{12}c_{13} & s_{12}c_{13} & s_{13}e^{-i\delta} \\ -s_{12}c_{23} - c_{12}s_{23}s_{13}e^{i\delta} & c_{12}c_{23} - s_{12}s_{23}s_{13}e^{i\delta} & s_{23}c_{13} \\ s_{12}s_{23} - c_{12}c_{23}s_{13}e^{i\delta} & -c_{12}s_{23} - s_{12}c_{23}s_{13}e^{i\delta} & c_{23}c_{13} \end{pmatrix} \begin{pmatrix} 1 & 0 & 0 \\ 0 & e^{i\lambda_1/2} & 0 \\ 0 & 0 & e^{i\lambda_2/2} \end{pmatrix}, \quad (2.2.27)$$

where $c_{ij} \equiv \cos \theta_{ij}$ and $s_{ij} \equiv \sin \theta_{ij}$. Here θ_{23} , θ_{13} , and θ_{12} are the three mixing angles, δ is the Dirac CP -violating phase, and λ_1 and λ_2 are the two Majorana CP -violating phases. The matrix V_{ab} represents a rotation of an angle θ_{ab} in the ν_a - ν_b plane. In the case neutrinos are Dirac particles, the matrix $D(\lambda)$ containing the two Majorana CP -violating phases can be eliminated with a suitable redefinition of the arbitrary phases of the Dirac neutrino fields. On the other hand, in the case they are Majorana neutrinos, this is not possible. However, the presence of the matrix $D(\lambda)$ does not have any effect on neutrino oscillation in vacuum nor in matter [24, 31, 60]. We can see this explicitly in that the only place the Majorana CP -violating phases appear in the flavor evolution Equation (2.2.21) is

$$\begin{aligned} UM^2U^\dagger &= V_{23} \left(D_{13} V_{13} D_{13}^\dagger \right) V_{12} D(\lambda) M^2 D(\lambda)^\dagger V_{12}^\dagger \left(D_{13} V_{13}^\dagger D_{13}^\dagger \right) V_{23}^\dagger \\ &= V_{23} \left(D_{13} V_{13} D_{13}^\dagger \right) V_{12} M^2 V_{12}^\dagger \left(D_{13} V_{13}^\dagger D_{13}^\dagger \right) V_{23}^\dagger, \end{aligned} \quad (2.2.28)$$

where we have utilized the fact that the two matrices $D(\lambda)$ and M^2 both being diagonal, commute with each other.

The evolution Equation (2.2.21) can further be simplified by noticing that the matrix A_W has only one non-zero element $(A_W)_{11} = A_{CC}$ implying that

$$V_{23}^\dagger A_W V_{23} = A_W. \quad (2.2.29)$$

This lets us conveniently define a new column matrix of flavor amplitudes

$$\tilde{\Psi}^{(\alpha)}(p, t) \equiv V_{23}^\dagger \Psi_W^{(\alpha)}(p, t). \quad (2.2.30)$$

Then the evolution Equation (2.2.21) can be rewritten as

$$\begin{aligned}
i \frac{d}{dt} \Psi_W^{(\alpha)}(p, t) &= \frac{1}{2p} \left(U M^2 U^\dagger + A_W \right) \Psi_W^{(\alpha)}(p, t), \\
i \frac{d}{dt} V_{23}^\dagger \Psi_W^{(\alpha)}(p, t) &= \frac{1}{2p} \left(V_{23}^\dagger U M^2 U^\dagger V_{23} + V_{23}^\dagger A_W V_{23} \right) V_{23}^\dagger \Psi_W^{(\alpha)}(p, t), \\
i \frac{d}{dt} \tilde{\Psi}^{(\alpha)}(p, t) &= \frac{1}{2p} \left((D_{13} V_{13} D_{13}^\dagger) V_{12} M^2 V_{12}^\dagger (D_{13} V_{13}^\dagger D_{13}^\dagger) + A_W \right) \tilde{\Psi}^{(\alpha)}(p, t), \\
i \frac{d}{dt} \tilde{\Psi}^{(\alpha)}(p, t) &= \frac{\tilde{M}^2}{2p} \tilde{\Psi}^{(\alpha)}(p, t),
\end{aligned} \tag{2.2.31}$$

with the definition

$$\tilde{M}^2 \equiv \left(D_{13} V_{13} D_{13}^\dagger \right) V_{12} M^2 V_{12}^\dagger \left(D_{13} V_{13}^\dagger D_{13}^\dagger \right) + A_W. \tag{2.2.32}$$

The amplitudes in the new column matrix $\tilde{\Psi}^{(\alpha)}(p, t)$ do not have a definite neutrino flavor or mass. They are introduced solely as a convenience for solving the evolution Equation (2.2.21).

For constant matter density or for a medium whose density changes slowly along the path of the neutrino trajectory, the effective squared-mass matrix \tilde{M}^2 can be diagonalized or an adiabatic approximation technique can be employed. However for the more general case of arbitrary variations in matter density, the transition probabilities must be computed numerically as was done by the author. The WIMP Monte-Carlo simulation package WimpSim [25, 34] was used for the propagation of neutrinos and for the calculation of flavor oscillation probabilities based on the density profiles of the Earth given in the Preliminary Reference Earth Model (PREM) [32] and the 2014 best fit neutrino oscillation and mass parameters shown in Table 2.1.

Figures 2.1 and 2.2 show the compositional densities, as well as the mass densities, and the electron and neutron number densities N_e and N_n of the Sun and Earth respectively as per calculated by DarkSUSY [42, 43]. Figures 2.3 to 2.5 show the neutrino oscillation probabilities for various flavors depending on where they are produced in the Earth. Full formulation of oscillation with matter effects is taken into account.

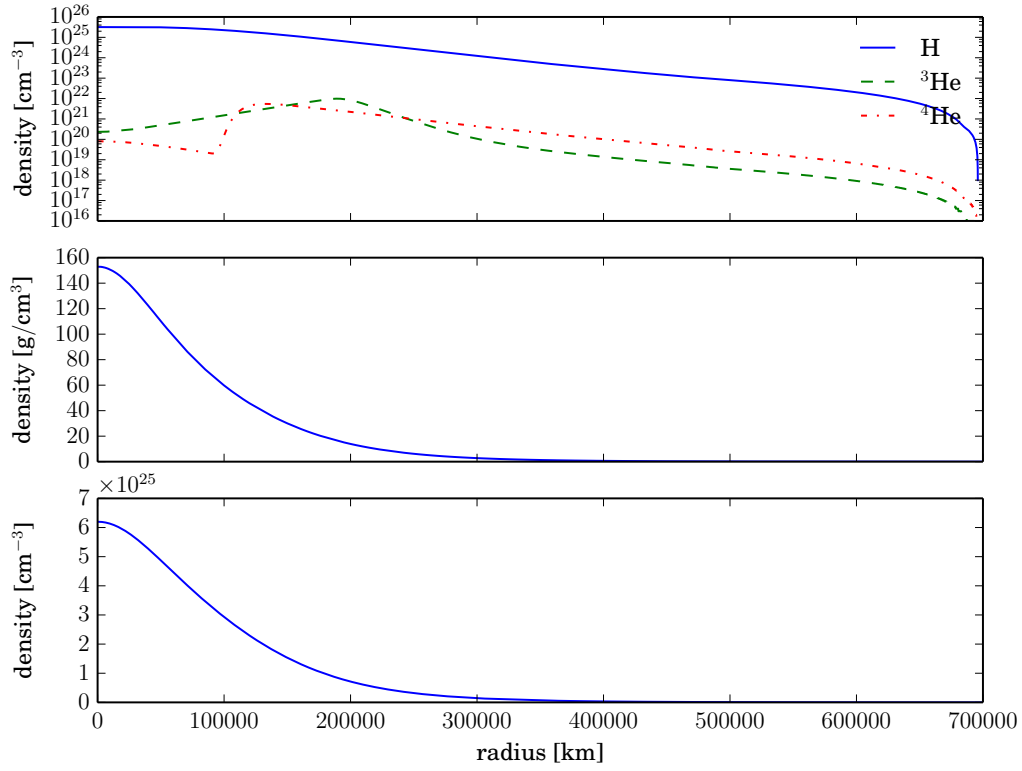


Figure 2.1: Here the various density figures of the Sun are plotted. The top figure shows the compositional densities of Hydrogen, Helium-3, and Helium-4. The middle figure shows the mass density. The bottom figure shows the electron number density. All figures are shown with respect to the radius extending outward from the center of the Sun. Calculations performed using DarkSUSY [42, 43].

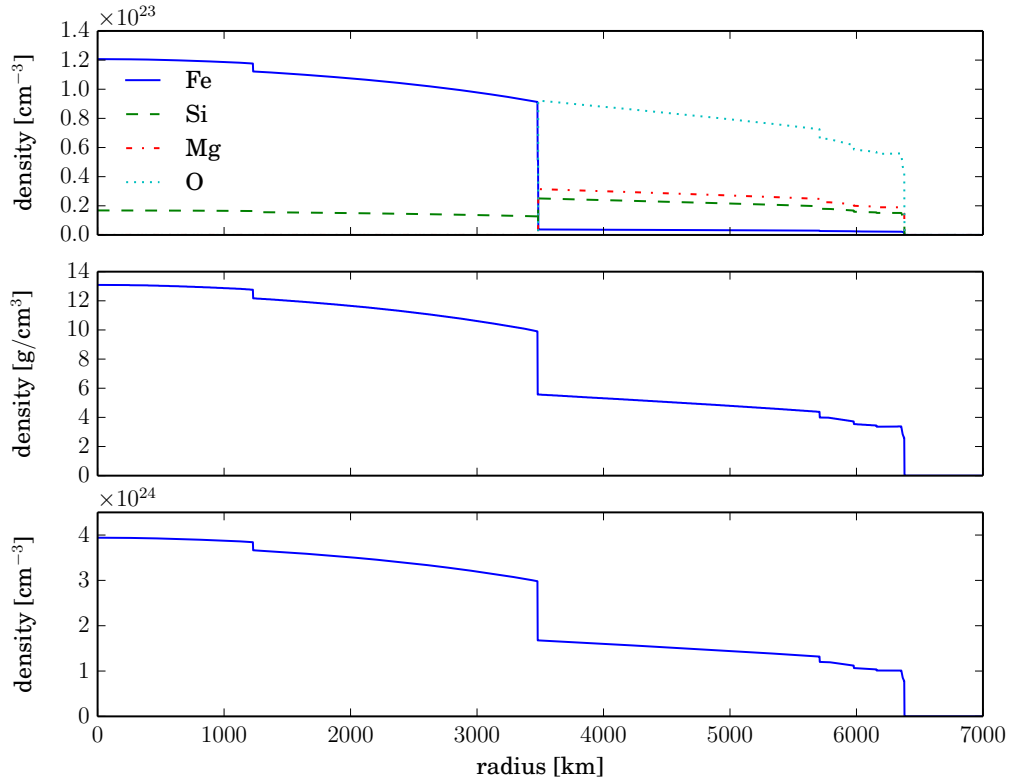
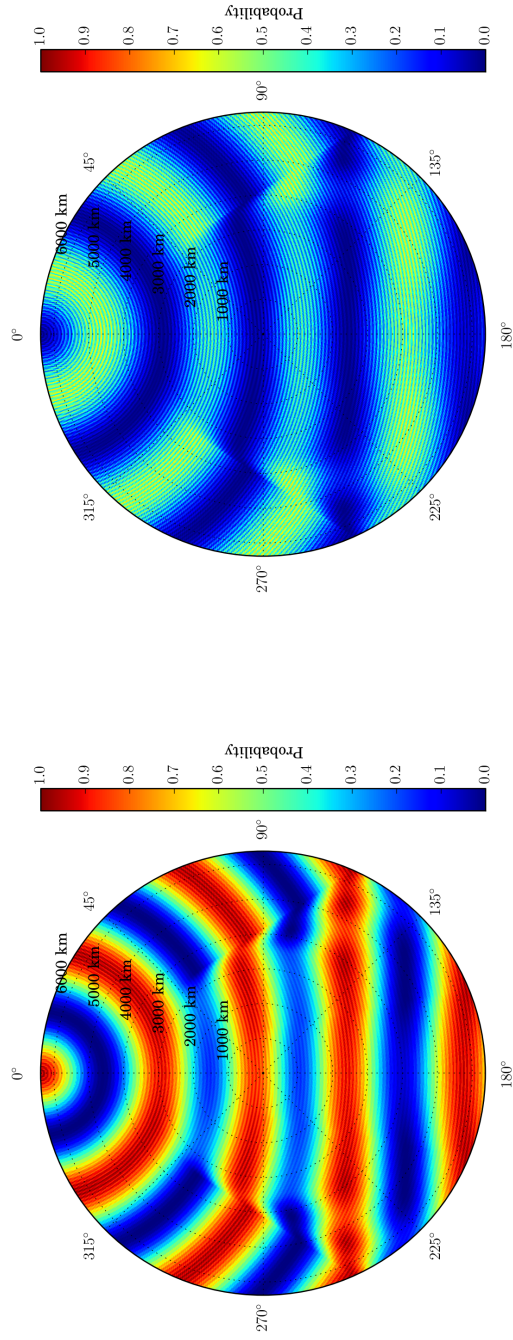


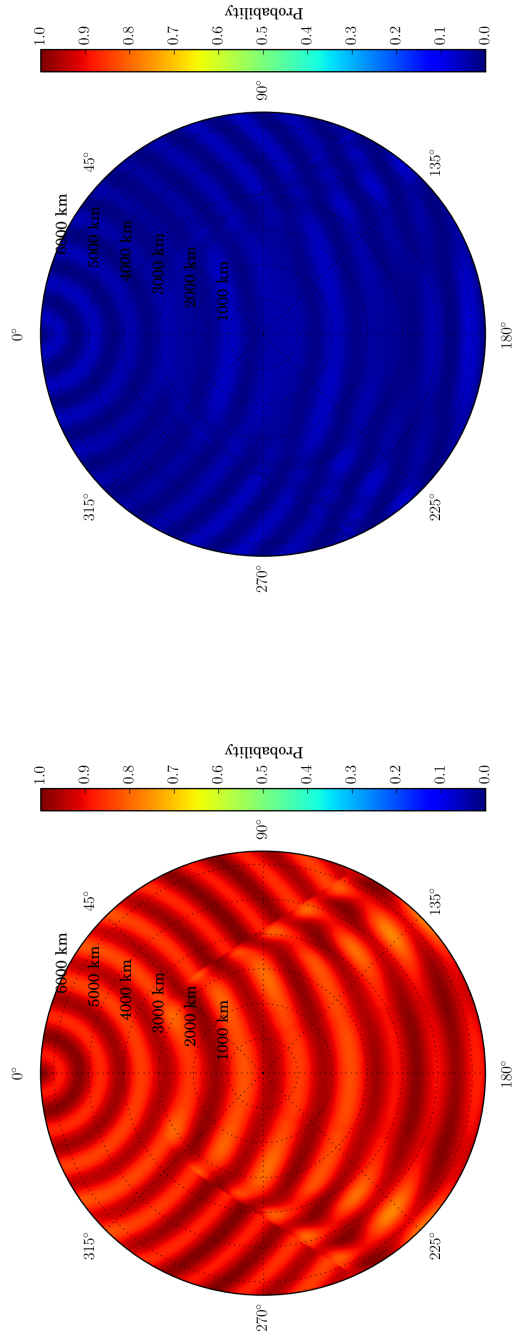
Figure 2.2: Here the various density figures of the Earth are plotted. The top figure shows the compositional densities Iron, Silicon, Magnesium, and Oxygen. The middle figure shows the mass density. The bottom figure shows the electron number density. All figures are shown with respect to the radius extending outward from the center of the Earth. Calculations performed with DarkSUSY [42, 43] using PREM [32].



(a) Probability of survival $\nu_e \longrightarrow \nu_e$.

(b) Probability of oscillation $\nu_e \longrightarrow \nu_\mu$.

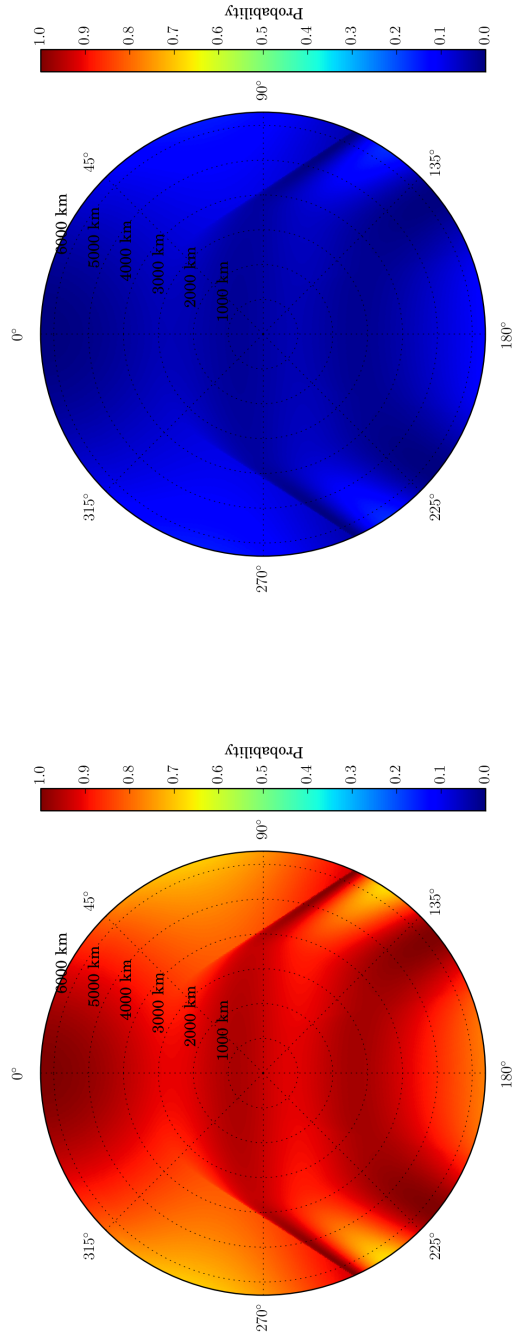
Figure 2.3: Probability distributions for the survival or oscillation of a 0.1 GeV ν_e created in the Earth to be detected as a neutrino of flavor (a) ν_e , (b) ν_μ . KamLAND is located on the surface of the Earth at a radius of 6378.14 km, at 0°.



(a) Probability of survival $\nu_e \longrightarrow \nu_e$.

(b) Probability of oscillation $\nu_e \longrightarrow \nu_\mu$.

Figure 2.4: Probability distribution for the survival or oscillation of a 1 GeV ν_e created in the Earth to be detected as a neutrino of flavor (a) ν_e , (b) ν_μ . KamLAND is located on the surface of the Earth at a radius of 6378.14 km, at 0° .



(a) Probability of survival $\nu_e \longrightarrow \nu_e$.

(b) Probability of oscillation $\nu_e \longrightarrow \nu_\mu$.

Figure 2.5: Probability distributions for the survival or oscillation of a 10 GeV ν_e created in the Earth to be detected as a neutrino of flavor (a) ν_e , (b) ν_μ . KamLAND is located on the surface of the Earth at a radius of 6378.14 km, at 0° .

Table 2.1: The 2014 best-fit neutrino oscillation and mass parameters taken from [36].

Parameter	Value
$\sin^2(2\theta_{12})$	0.846 ± 0.021
θ_{12}	33.45° (best fit)
$\sin^2(2\theta_{13})$	$(9.3 \pm 0.8) \times 10^{-2}$
θ_{13}	8.88° (best fit)
$\sin^2(2\theta_{23})$	$0.999^{+0.001}_{-0.018}$
θ_{23}	44.09° (best fit)
Δm_{21}^2	$7.53 \pm 0.18 \times 10^{-5}$ eV
Δm_{31}^2	$2.52 \pm 0.06 \times 10^{-3}$ eV

Chapter 3

The Detector

3.1 Introduction

KamLAND is situated in a rock cavern at the Kamioka Observatory, a neutrino physics laboratory located underground in the Mozumi Mine in the Japanese Alps near Hida city, Gifu Prefecture, Japan. The detector is overburdened by about 1000 m of mountain rock under the summit of Ikenoyama (Ike Mountain, 36.42°N , 137.31°E). This translates to about 2700 meter water equivalent (mwe) of shielding from cosmic ray muons which reduces the rate by roughly a factor of 1×10^{-5} to about 0.34 Hz in the apparatus. [79]

3.2 Detector construction

3.2.1 Overview

KamLAND consists of a 9 m radius stainless steel spherical containment vessel that physically defines the two major components of the detector; the inner detector (ID) which resides inside the containment vessel and the outer detector (OD) which resides outside the containment vessel. The ID and OD are both contained in a cylindrical cavity inside the Kamioka mines capped with a hemispherical dome overhead.

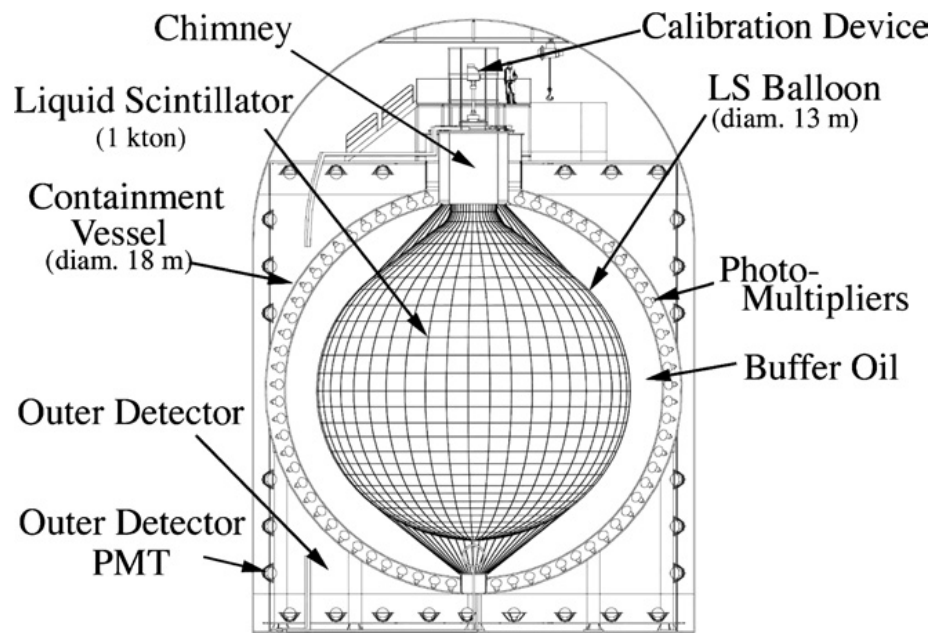


Figure 3.1: Schematic of the Kamioka Liquid Scintillator Antineutrino Detector (KamLAND).

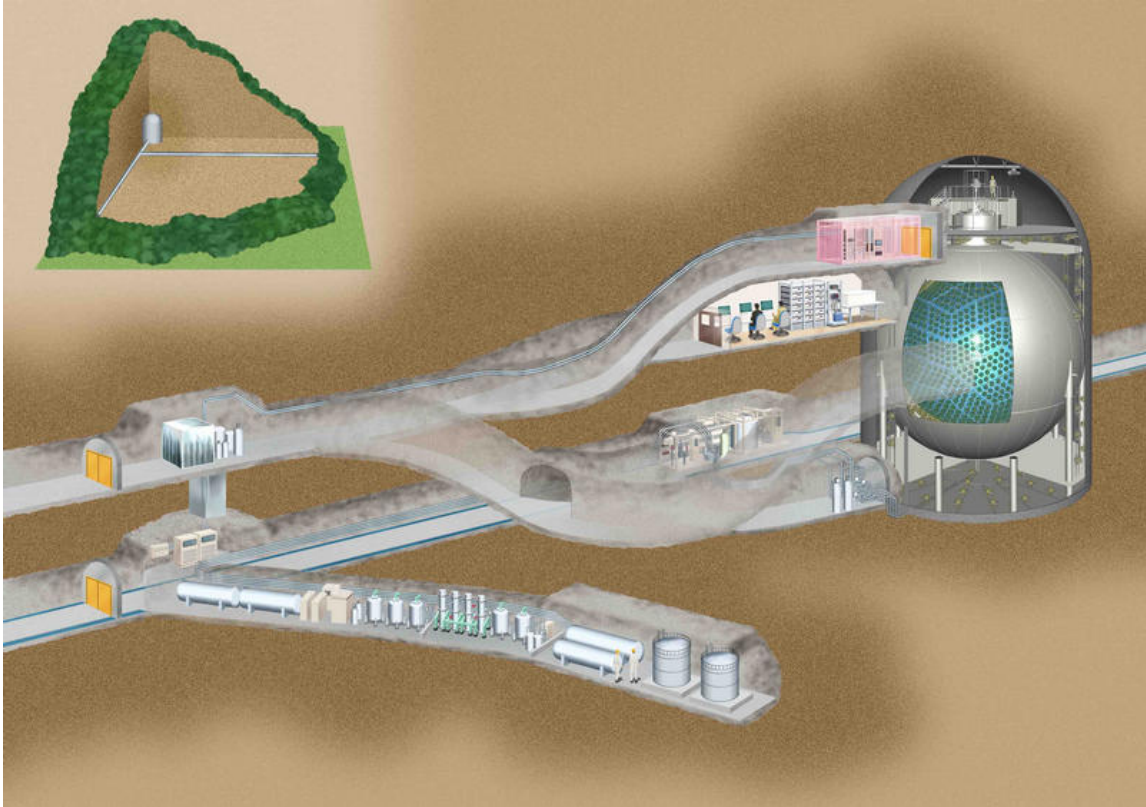


Figure 3.2: Illustration of the KamLAND detector in the Kamioka mine tunnel.

3.2.2 Inner detector

Overview

The ID houses 1879, 50 cm diameter, Hamamatsu photomultiplier tubes (PMTs) that are mounted on the inner surface of the 9 m radius spherical stainless steel containment vessel facing inward toward the center of the detector. Among these, 1325 are of Hamamatsu model R7250 dubbed *17-inch* PMTs and the remaining 554 are of Hamamatsu model R3600 dubbed *20-inch* PMTs.

There is a 8.5 m radius spherical layer of opaque black acrylic called the *black sheet* just inside the inner surface of the containment vessel. The black sheet optically defines the ID and has 25.4 cm radius circular cutouts to fit the widest equatorial region of the PMTs. The PMTs are physically held in position outside of the black sheet by the containment vessel but effectively *look into* the optically isolated ID through these cutouts.

Concentric to the containment vessel and black acrylic sheet, there is an approximately spherical, 13 m diameter, balloon supported by a network of 44 lateral and 30 longitudinal braided Kevlar support ropes inside of this vessel. The optical occlusion of the balloon and the support ropes is $\sim 5\%$ for light arriving at PMTs near the equatorial region and $\sim 10\%$ for light arriving at PMTs near the top or bottom of the ID.

This balloon consists of a 135- μm -thick transparent nylon/EVOH (ethylene vinyl alcohol) copolymer composite film. The balloon is filled with the liquid scintillator (LS) detector medium.

Liquid scintillator (LS) and buffer oil (BO)

Inside the 13 m diameter balloon is KamLAND's ultra-pure LS which consists of about a 1000 t ($1176.71 \pm 22.00 \text{ m}^3$) mixture of 80.2% Dodecane ($\text{CH}_3(\text{CH}_2)_{10}\text{CH}_3$) and 19.8% Pseudocumene (1,2,4-Trimethylbenzene, $\text{C}_6\text{H}_3(\text{CH}_3)_3$) by volume, doped with $1.36 \pm 0.03 \text{ g/L}$ of 2,5-Diphenyloxazole (PPO) (2,5-Diphenyloxazole, $\text{C}_{15}\text{H}_{11}\text{NO}$). The Pseudocumene serves as the solvent for the PPO solute which acts as the primary scintillating fluor. This binary mixture of Pseudocumene and PPO is diluted with Dodecane in order to obtain certain desirable physical properties. The large volume is necessary to acquire

high statistics and KamLAND is the largest scintillator experiment in the world as of this date. The different ratios of the components used in the LS mixture depended upon several desirable factors. These include a high light output, a very small amount of radioactive contaminants, a high Hydrogen-to-Carbon ratio, particle identification performance, alpha particle quenching factor, long term chemical stability, low toxicity, high flash point, and cost. The net light output recorded by the PMTs is effectively determined not only by the light output of the LS itself but also by its optical transparency. The composition of the LS was optimized for high light yield for central events [80] with Dodecane being chosen as the diluter due to several factors among which is its good optical transparency. Dodecane is a paraffin oil that has a high Hydrogen-to-Carbon ratio and excellent chemical stability due to its saturated compound structure having no unsaturated bonds nor any Benzene rings. Dodecane (flash point 83°C) also serves to raise the flash point of Pseudocumene (flash point 54°C) as well as to reduce the overall toxicity of the mixture. These two features are of utmost importance for the safety of personnel in the Kamioka mine. The LS was prepared at Tohoku University [80] [81] to contain cost as much as possible.

The density of the LS is measured to be $0.77754 \pm 0.00020 \text{ g/cm}^3$ at 15°C and projected to be $0.78013 \pm 0.00100 \text{ g/cm}^3$ at the actual temperature of the LS deployed on site of $11.5 \pm 1.0^{\circ}\text{C}$. The Hydrogen-to-Carbon ratio was measured to be $\text{H/C} = 1.969 \pm 2\%$ using chemical analysis [81]. The light yield is $\sim 300 \text{ p.e./MeV}$ using only the 17-inch PMTs and $\sim 500 \text{ p.e./MeV}$ using both 17-inch and 20-inch PMTs. The fractional area of coverage by the photocathode is $\sim 22\%$ when only 17-inch PMTs are considered and $\sim 34\%$ for both 17-inch and 20-inch PMTs combined. The attenuation length of the LS was measured to be 10 m at 400 nm using a dye-laser. [80] The LS has a light yield of 48% Anthracene or 8300 photons/MeV where 100% Anthracene corresponds to 17400 photons/MeV. Some properties of the LS are listed in Table 3.1. The elemental composition of the LS is listed in Table 3.2 and the natural abundances of each element is shown in Table B.1 in Appendix B

The LS converts the kinetic energy of charged particles into photons through ionization and de-excitation of molecules. The range of wavelengths of these scintillation photons is $\sim 350 \text{ nm}$ to 400 nm . The total number of visible photons produced is proportional

Table 3.1: Some properties of the KamLAND LS [74].

Property	Design Value	Actual Value
total volume at 12.45 °C [m ³]	—	1176.71 ± 22.00
volume within spherical part of balloon [m ³]	—	1154.22 ± 25.00
temperature [°C]	~12	11.5 ± 1.0
measured density at 15 °C [g/cm ³]	0.778	0.777 54 ± 0.000 20
projected density at 11.5 °C [g/cm ³]	—	0.780 13 ± 0.001 00
temperature dependence of density [g/(cm ³ K)]	—	0.000 741
Hydrogen-Carbon ratio [H/C]	1.902	1.969
index of refraction at $\lambda = 590$ nm, 14 °C	1.44	1.440 87 ± 0.000 15
light yield [p.e./MeV]		
17-inch	~ 250	~ 300 @ center
20-inch	~ 400	~ 500 @ center
time response $R(t) = a/\tau_a \exp(-t/\tau_a) + b/\tau_b \exp(-t/\tau_b)$		
a [ns]	0.86	0.69
b [ns]	0.14	0.31
τ_a [ns]	6.9	4.0
τ_b [ns]	8.8	8.6
neutron capture time [μ s]	~ 212	211.2 ± 2.6
radiation length [cm]	18	—
flash point [°C]	64	—
thermal expansion coefficient [1/°C]	-0.00095	—
kinematic viscosity @ 30 °C [mm ² /s]	1.4	—

Table 3.2: Chemical composition of the KamLAND LS [3].

Element	Stoichiometry	Number of Targets (per kiloton)
Hydrogen	1.97	8.47×10^{31}
Carbon	$\equiv 1$	4.30×10^{31}
Nitrogen	1×10^{-4} to 6×10^{-4}	5×10^{27} to 3×10^{28}
Oxygen	1×10^{-4}	5×10^{27}

to the kinetic energy lost by a charge particle inside of the LS with some corrections due to what is known as *quenching*.

The space between the balloon film and the containment vessel is filled with transparent, non-scintillating mineral oil called the buffer oil (BO). The BO serves to support the LS containing balloon and in addition provides shielding from external gamma rays from radioactive impurities such as ^{208}Tl and ^{40}K in the stainless-steel tank, PMTs and cavern rock as well as fast-neutrons from cosmic-ray showers. The BO was developed using a mixture of Dodecane and isoparaffin with a density $0.036 \pm 0.006\%$ lower than the LS in order to maintain the shape of the balloon. The density of the BO was measured to be $0.77732 \pm 0.00200 \text{ g/cm}^3$ at 15°C and is projected to be $0.78033 \pm 0.00100 \text{ g/cm}^3$ at the in situ temperature of $10.7 \pm 1.0^\circ\text{C}$. The mixture ratio is 53% Dodecane to 47% isoparaffin by volume. The excess weight of the LS is supported by the balloon which is itself supported by the Kevlar ropes. The BO is again divided into two sections by a 3 mm thick spherical acrylic shell at a diameter of 16.7 m separating the BO into what is known as the inner BO and outer BO. This was done so as to segregate the inner BO region and the LS from the PMTs effectively better limiting the diffusion of ^{222}Rn into the active LS volume. ^{222}Rn is produced from decay chains of ^{283}U and ^{232}Th minutely present in the glass housing structure of the PMTs. Some properties of the BO are listed in Table 3.3. Properties of the chemical components for the LS and BO are listed in Table 3.4.

Table 3.3: Properties of the BO.

Property	Design value	Actual value
total volume at 11.85 °C [m ³]	—	1795.58 ± 22.00
temperature [°C]	—	10.7 ± 1.0
measured density at 15 °C [g/cm ³]	0.778	0.777 32 ± 0.000 20
projected density at 10.7 °C [g/cm ³]	—	0.780 33 ± 0.001 00
temperature dependence of density [g/(cm ³ K)]	—	0.000 699
density difference with respect to the LS [%]	< 0.1	0.036 ± 0.006
index of refraction at $\lambda = 590$ nm, 14 °C	1.44	1.435 32 ± 0.000 13
flash point [°C]	≥ 78	—

Balloon and Support Cables

The KamLAND LS is contained in an approximately spherical 13 m diameter plastic balloon. This balloon meets several requirements for the experiment, namely to be optically transparent as possible, thin, radioactively clean, of high mechanical strength, and gas-tight in order to shield the LS from external contaminants such as ²²²Rn from the BO. The film material of the balloon was designed to be a 5-fold layer of EVOH (25 μ m)/Nylon (15 μ m)/Nylon (15 μ m)/Nylon (15 μ m)/EVOH (25 μ m) having a total thickness of 135 μ m at its thickest point. Nylon was used as a strength reinforcement material and the number of Nylon layers were decided based on the best compromise between mechanical strength and total thickness. EVOH is chemically tolerant and has a high gas-tightness to effectively block permeation of ²²²Rn. The mechanical strength of the balloon film was measured to be 8 kg/cm, well above the target value of 2.1 kg/cm which corresponds to a 1 % difference in the density of LS and BO amounting in a net load of \sim 10 t on the balloon and support cables. The balloon material and support cables were also soak-tested in 60 °C LS for two months to verify its long-term chemical stability and its optical transparency was measured to be 93 % at $\lambda = 400$ nm. The film was also observed to maintain a ²²²Rn density ratio of up to 1.8×10^{-6} across the material. The radioactive contamination of Uranium, Thorium,

Table 3.4: Properties of components for LS and BO [81].

Property	Pseudocumene	Dodecane	isoparaffin	PPO
molecular structure	C_9H_{12}	$C_{12}H_{26}$	C_nH_{2n+2} ($n \sim 15$)	$C_{15}H_{11}NO$
density at 15 °C [g/cm^3]	0.8796	0.7526	—	—
density at 20 °C [g/cm^3]	0.8758	0.7487	—	—
flash point [°C]	54	83	78	—
melting point [°C]	-43.78	-10.0 to -9.3	< -50	72
index of refraction at 15 °C, $\lambda = 589$ nm	1.5049	1.4217	1.4410	—
kinematic viscosity at 15 °C [mm^2/s]	1.108	2.379	4.754	—

and ^{40}K was measured to be 0.018 ppb, 0.014 ppb, and 0.27 ppb respectively. These figures were sufficiently within the design goals for the KamLAND balloon.

3.2.3 Outer detector

The OD is designated as the volume outside of the stainless-steel tank to the rock walls of the cavern and capped overhead by a stainless steel plate that serves as the floor for the Dome Area above. The OD is filled with approximately 3.2 kt of highly pure water and serves both as a water-Cherenkov veto detector for incoming cosmic-ray particles and a buffer zone to shield the ID from external gamma rays and fast neutrons. 225 of 20-inch PMTs (Hamamatsu model R3600) are mounted along the outer perimeter of this volume looking inward. The water in the OD is constantly circulated to regulate a stable environmental temperature by carrying away excess heat produced by all the PMTs in the ID and OD. The OD volume is partitioned into four optically isolated sub-volumes; top, upper, lower, and bottom, each fully lined with light reflecting Tyvek sheets for better light collectivity. The PMTs in the top and bottom sub-volumes; each amounting to a count of 50 and 60 respectively are placed in concentric circles along the ceiling and floor of the cylindrically shaped OD. The PMTs in the top sub-volume face downward whereas those in the bottom sub-volume face upward. The PMTs in the upper and lower sub-volumes; each with a count of 60 and 55 respectively are attached uniformly along the side of the cavern wall facing toward the cylindrical axis of the OD.

3.2.4 Chimney and dome area

The top portion of the ID and structures that segregate sub-volumes inside the ID taper off into concentric cylindrical structures which as a whole is called the *Chimney*. There are 6 5-inch PMTs attached to a plate that covers the Chimney and isolates the detector from the Dome Area above. The Chimney also contains a 16-inch diameter stainless-steel vertical pipe with a gate valve that serves as the sole connection from the LS inside of the detector to a glove-box in the Dome Area. This glove-box is used as a clean-space for preparing calibration sources that may be lowered into the detector through this stainless

Table 3.5: Number of PMTs per type used in the detector.

PMT type	ID	OD	Chimney region	Sum per PMT type
20-inch	554	225	—	779
17-inch	1325	—	—	1325
8-inch	—	—	16	16
5-inch	—	—	6	6
Sum per region	1879	225	22	2126

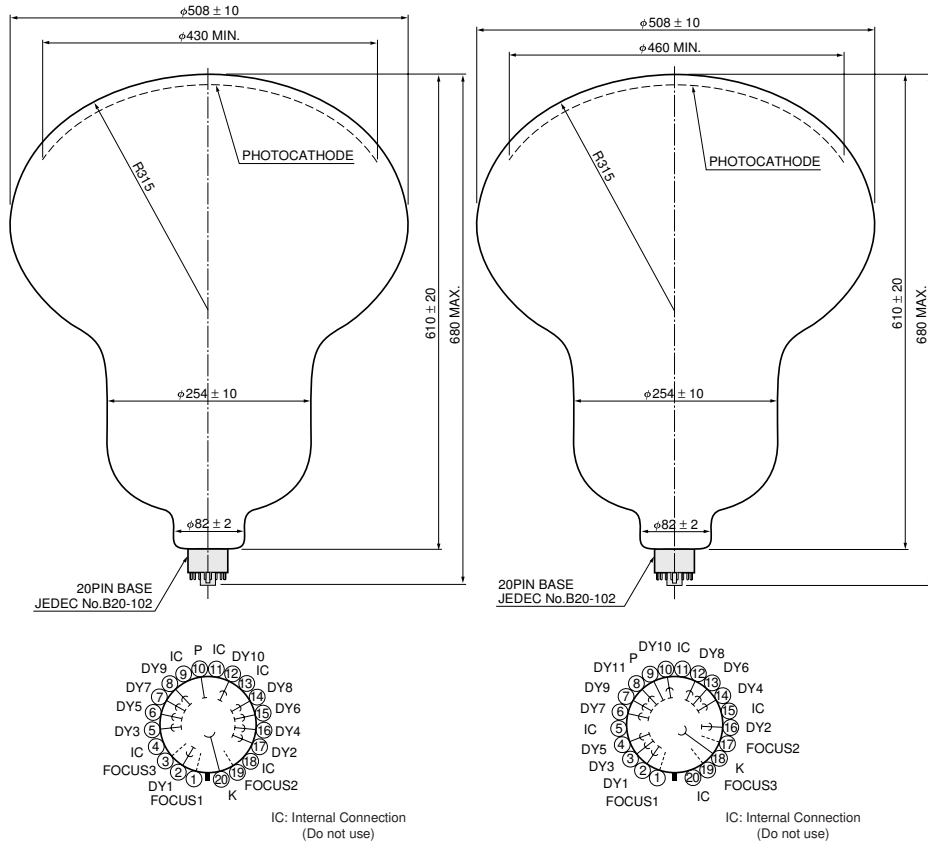
steel pipe. Housed in the Chimney are also LS/BO level sensors, load monitors for the cables that support the LS balloon, thermo-hygrometers, and pressure sensors, along with various other pipes that carry LS/BO and nitrogen gas into the detector. The cables feeding into the PMTs are also brought into the detector through the Chimney.

The Dome Area is where various other facilities are placed. Among them are the E-Hut which houses the data acquisition electronics and a clean-room for storing and preparing calibration sources. The Dome Area is designated as a clean-room where filtered air is brought in from outside the mine. Tyvek clean-suits are strictly mandated in this area.

3.2.5 Photomultiplier tubes

There are a total of 2126 PMTs deployed in the KamLAND detector. Different model PMTs are used in several regions of the detector due to constraints such as the imminent physical space and cost of the individual PMTs. Table 3.5 shows which type of PMT is installed in which regions of the detector.

When KamLAND was build, an internal coordinate system was decided based on the direction of the magnetic north pole. The positions of all the PMTs and CCD cameras that look into the ID or are placed in the OD are designated using this internal coordinate system. The y -axis is aligned with the direction toward magnetic north which at the time of construction was 8° westward of true north with respect to the detector location. The



(a) 17-inch PMT (model R7250) (b) 20-inch PMT (model R3600)

Figure 3.3: Schematic diagrams of Hamamatsu PMTs deployed in KamLAND. [50]

x -axis points in the direction rotated 90° clockwise from magnetic north. And the z -axis is taken to be pointing directly overhead forming a right-handed Cartesian coordinate system.

There are 1879 PMTs used in the ID of KamLAND among of which 1325 are of Hamamatsu model R7250 dubbed *17-inch* PMTs and the remaining 554 are of Hamamatsu model R3600 dubbed *20-inch* PMTs. A schematic of these two types of PMT models are depicted in Figure 3.3.

Both models have a quantum efficiency of $\sim 20\%$ in the desired photon spectrum of approximately 350 nm to 400 nm. This is shown in Figure 3.4.

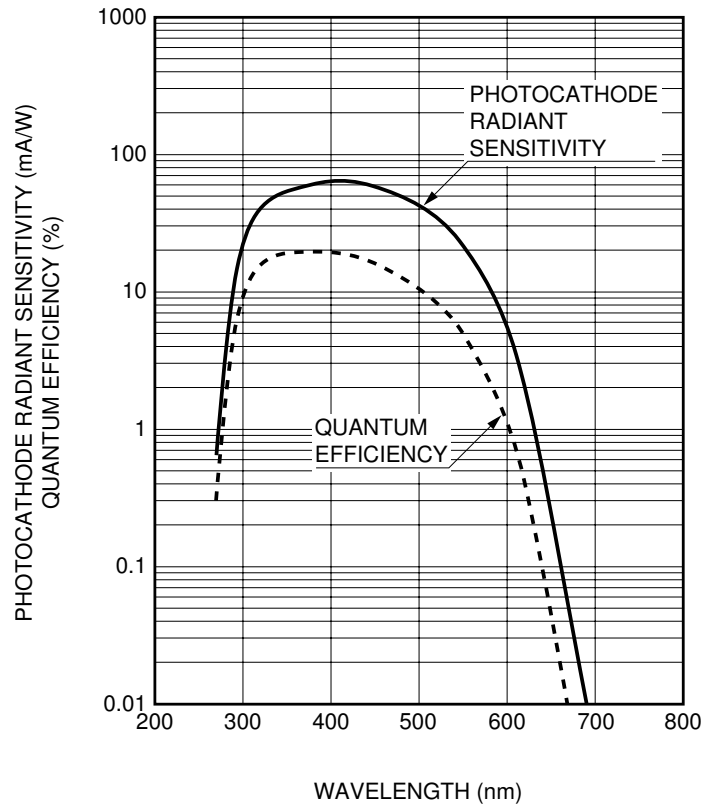


Figure 3.4: Photo cathode radiant sensitivity and quantum efficiency (QE) for both 20-inch and 17-inch PMTs as measured by Hamamatsu. [50]

The 20-inch PMTs are of an older model which was originally designed for the Kamiokande experiment [49]. They were refurbished and redeployed for KamLAND. The newer 17-inch PMTs were specifically developed for KamLAND with the goal to improve upon the energy and time response in comparison to the original 20-inch PMTs. This was achieved through several modifications to the existing design of the 20-inch PMTs. A black plastic ring-shaped mask was placed over the outer perimeter of the photo-cathode surface which was known to have a relatively poor energy and time resolution compared to the inner region closer to the cylindrical axis of the PMT because of effects from geometry. This mask effectively shrunk the photo-cathode area limiting the photon acceptance region to the central 17-inch diameter and hence the name *17-inch* PMTs. Another improved feature was a change in the cascade electron multiplying dynode structure. The 20-inch PMTs had utilized a Venetian Blind type dynode which was more suitable for a large area photo-cathode scheme. In contrast, the 17-inch PMTs were equipped with the newer so-called *line-focus* dynode which had a comparatively better energy and time response.

Through these modifications, the transit-time spread (TTS) of the PMT signal improved from ~ 5.5 ns (full width at half maximum (FWHM)) to ~ 3 ns a (FWHM), and the peak-to-valley ratio (P/V ratio) for the distribution of 1 p.e. pulse height was improved from ~ 1.5 to ~ 3 , Figure 3.5.

The high voltage for the PMTs are supplied at about 2000 V to maintain a gain of 1×10^7 . Figure 3.6 shows the relation between the supplied voltage and signal gain of both PMT models.

A stable gain value independent of PMT orientation is desirable, however this can be adversely affected by external influences such as the Earth's geomagnetic field which can range approximately anywhere between 250 mG to 650 mG. To mitigate this problem, magnetic compensation coils are used around the entire detector to regulate this field strength to well below 50 mG at which variations in the 1 p.e. pulse height were measured to be less than 20%.

The photo-cathode coverage for the ID is about 22% when only the 17-inch PMTs are taken into account whereas that of both 17-inch and 20-inch PMTs is about 34%.

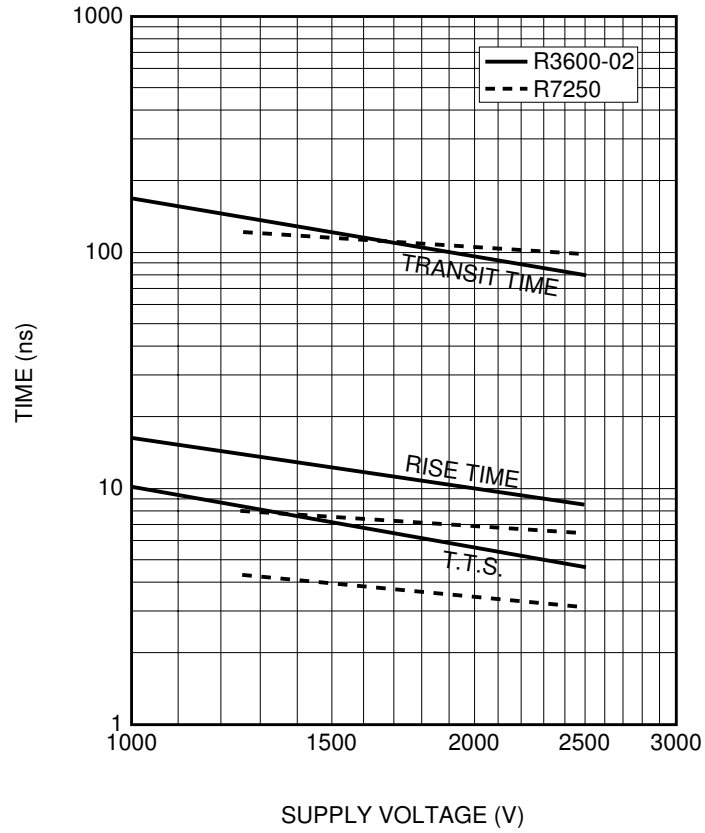


Figure 3.5: Time response curves for the transit time, pulse rise time, and TTS verses supply high-voltage for the 20-inch (R3600) and 17-inch (R7250) PMTs as measured by Hamamatsu. [50]

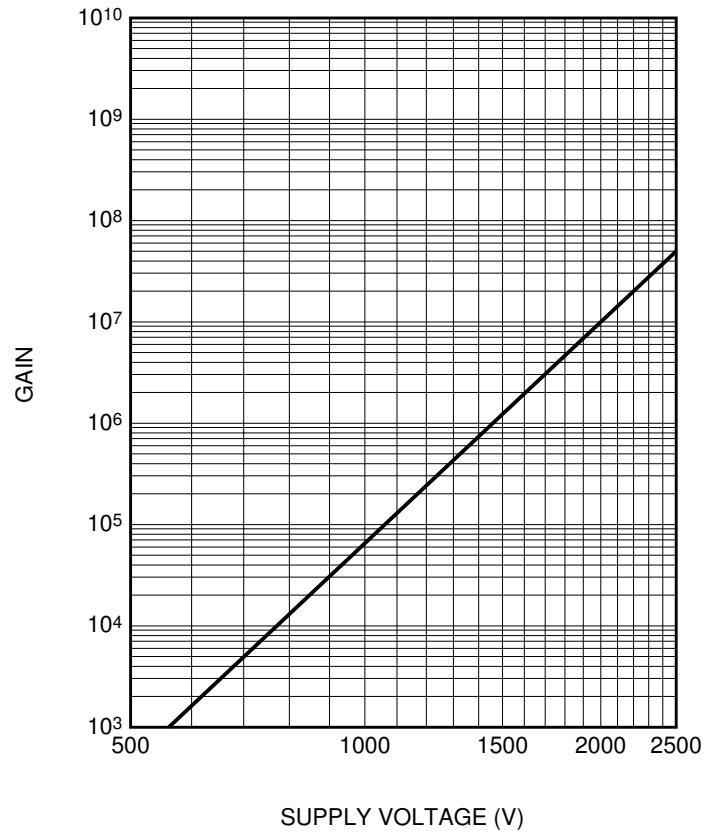


Figure 3.6: Signal gain versus the supply voltage for both 20-inch and 17-inch PMTs as measured by Hamamatsu. [50]

3.3 Electronics and data acquisition

3.3.1 Overview

The primary purpose of the KamLAND experiment is to detect low energy neutrinos with energies on the order of a few MeV. At these energies, most PMTs receive around 1 p.e./MeV. With a gain of 10^7 , 1 p.e. is amplified to ~ 1.6 pC which corresponds to an output signal pulse height of a few millivolts. On the other hand, the KamLAND electronics need to be able to handle very high-energy cosmic ray muons that may deposit over 1000 p.e./PMT necessitating the need for accommodating a dynamic range of more than 4 orders of magnitude. KamLAND is also designed to be sensitive to supernovae that may occur at the center of the Milky Way Galaxy which could induce 1 kHz of neutrino events and proton-decay events that produce multiple signals from cascade decays, over ~ 10 s.

There are three main components that comprise the KamLAND electronics; 200 front-end electronics (FEE) boards, the trigger system, and the data acquisition (DAQ) system. The PMT cables carrying raw charge pulses are grouped into bunches of 12 and assigned to one FEE board. Also the different PMT types, 17-inch, 20-inch, and OD PMTs are assigned to different FEE boards. The FEE boards are responsible for acquiring and digitizing these PMT waveforms. The trigger system decides whether to digitize and record the acquired waveforms on the FEE boards. The DAQ system reads out the digitized waveforms, and stores them for analysis at a later time.

Front-End Electronics

Each FEE board is connected to 12 PMTs. Figure 3.7 shows a picture of the actual board along with its components. The central piece of technology on the FEE board is the analog transient waveform digitizer (ATWD) which is responsible for storing the analog waveforms coming from the PMTs and digitizing them. Signal waveforms coming from the PMTs are continuously and cyclically stored in analog format in a switched capacitor array (SCA) inside the ATWD chip which can hold 128 10-bin samples in a configurable step size that is currently set at 1.5 ns letting it hold ~ 200 ns long records. A designated

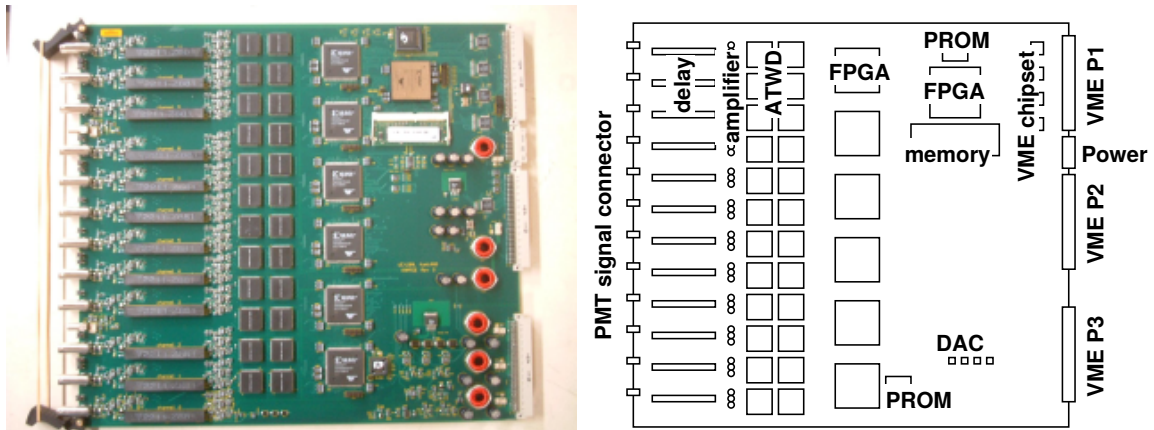


Figure 3.7: KamLAND FEE and its components. Figure taken from [35].

local discriminator is assigned for each PMT for which the signal threshold is set at 0.5 mV corresponding to 1/3 p.e.. When the amplitude of the PMT signal exceeds this threshold value, this is considered a *hit* for the particular PMT and the on-board field programmable gate array (FPGA) chip issues a *capture* signal which prompts the ATWD to halt its sampling process and the current waveform information existing on the switched capacitor array is temporarily held for 175 ns and the ATWD sits until further instructions from the FPGA during this time. Meanwhile the number of PMTs that registered a hit is compiled on a controller circuitry implemented on the FPGA and sent out to the trigger circuitry as a *hit-sum* signal that encodes the number of PMTs that registered a hit on the given FEE board. Based on the 'hit-sum' signals received from all 200 FEE boards, the trigger circuitry makes a decision whether the event is of interest or not. The period of 175 ns during the time when the analog waveform is held, roughly corresponds to the time it takes for a single photon to traverse a distance of twice the diameter of the ID, so in principle should provide enough time for the trigger circuitry to collect hit-sum information from all PMTs and make the decision. If the event is deemed of interest, the trigger circuitry sends a global trigger to all FEE boards to acquire this data prompting the on-board FPGAs to issue a *digitize* signal to the ATWD chips which proceed to digitize the held waveform. Waveforms that are digitized are subsequently copied to and stored in a large

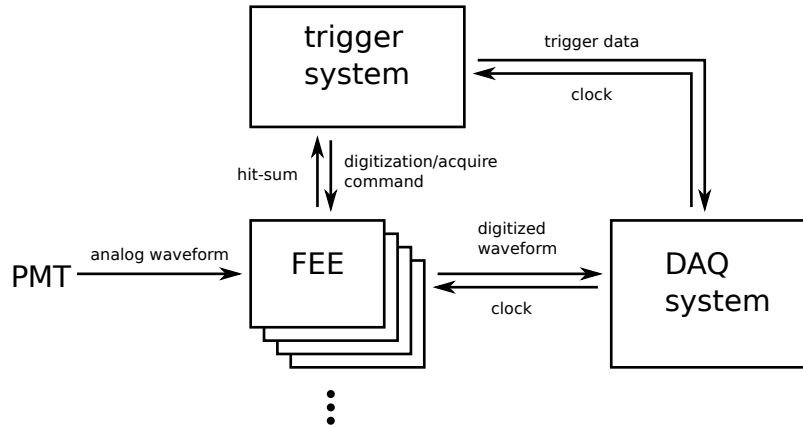


Figure 3.8: Diagram showing the direction of data flow and communication between the PMTs and various components of the DAQ system.

on-board buffer memory on FEE board that can be read out at a later time in leisure. This digitization and copy process takes $\sim 25 \mu\text{s}$. If the event is deemed to be of no interest, the held waveform is disposed of and the ATWD chip resumes waveform sampling as before. The data stored in the buffer memory is read out by the DAQ software running on the front-end computers via the Versa Module Europa (VME) bus interface. A diagram of the data-flow and communication between the PMTs and various components of the DAQ system is shown in Figure 3.8.

There are three gain channels per PMT to realize a large dynamic range. Each channel receives a copy of the original signal pulse and amplifies it by an associated factor; high-gain ($20\times$ amplification for single photo-electron signals), mid-gain ($4\times$ amplification in case the high-gain channel saturates), and low-gain ($0.5\times$ amplification for very high energy events that saturate the mid-gain channel). The highest gain factor that does not saturate the signal is chosen at the time of digitization and the other remaining two are discarded. Each ATWD chip has a dedicated 128-element switched capacitor array for all four input channels to be recorded simultaneously. In addition, every PMT channel has two digitizer channels coined *ATWD-A* and *ATWD-B*. This configuration of having identical dual processing lines reduces the overall dead-time of signal processing where one ATWD

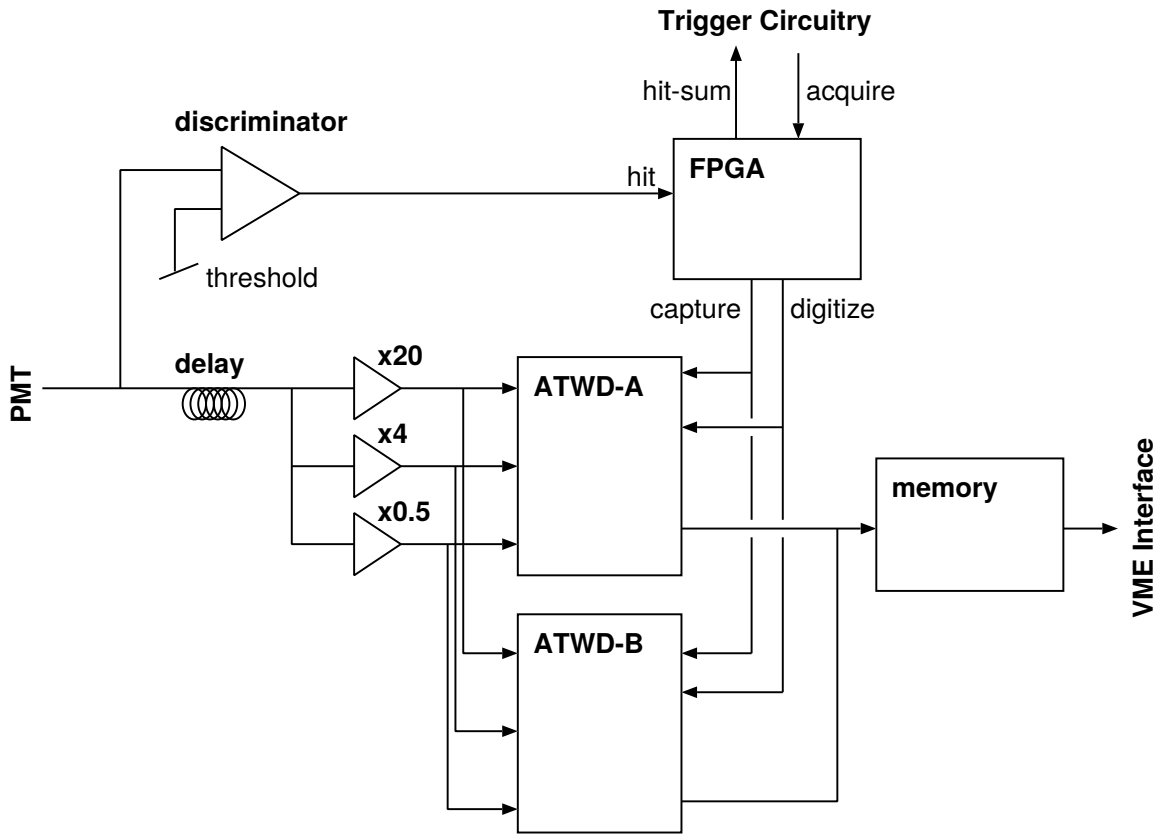


Figure 3.9: Diagram of the KamLAND FEE circuitry taken from [35]. The direction of arrows depict the flow of PMT pulse waveforms and processed data. Also shown is the flow of commands given to and received from the trigger circuitry.

chip can take over in the case that the other is busy. They are launched alternately by control of the FPGA chip. Each ATWD chip has four input channels of which three are designated for the PMT signal gain channels and the remaining one is left for the 40 MHz clock input line used for calibration of the sampling time interval. The dimension of the FEE board is a 9U size VME card.

Trigger System

Figure 3.9 shows a diagram of the trigger system. The trigger system makes a decision on whether an event is interesting based on the number of PMTs *hit* within a certain time window. 4-bit *hit-sum* signals are collected from each of the 200 FEE boards that encode how many of the 12 PMTs attached to each FEE board were hit. Each PMT that registered a hit produces a 125 ns long gate that is digitally summed across all PMTs into a value called the *N_{Sum}*. The trigger circuitry compares the *N_{Sum}* to a preset threshold value for which if exceeded will issue an *acquire* command to the FEE boards. This acquire command leads to waveform digitization and read out as described above. The timing between all FEE boards and the trigger board is synchronized using an on-board 40 MHz oscillator clock. The number of ticks from this clock since the beginning of the run is known as the *time-stamp*. In addition, the absolute time of the timestamps and hence any given event characterized by this time-stamp can be known to an accuracy of better than 1 μ s through one pulse per second (PPS) pulses that come from a Global Positioning System (GPS) module located outside of the entrance of the . The trigger system is configured to record both the GPS time-code and the time-stamp every 32 s. This allows for any event in KamLAND to be identified and compared to any other observations for which a valid GPS time is available. Information regarding the trigger type, time-stamp, and *N_{Sum}* is compiled and sent through a dedicated data stream called the *trigger data stream* and passed on to online software running on the front-end personal computer (PC) through the VME bus. The online software is also used to set trigger system settings such as trigger threshold, pre-scaling rate, enabling/disabling specific trigger types, supernovae criteria, prior to data taking.

There are two important groups of triggers called the *global acquisition triggers* and the *forced acquisition triggers*. The global acquisition trigger is a trigger command issued by the trigger circuitry to acquire PMTs waveforms based on the hit coincidences of several PMTs whereas the forced acquisition trigger is a trigger command meant to accomplish the same task but on the basis of external factors other than physical events that produce a signal at the PMTs.

Important types of triggers are listed below.

Global Acquisition Triggers

ID Singles Trigger

This trigger is based on the value of NSum for 17-inch PMTs in the ID. The threshold was originally set at $\text{NSum} \geq 200$ which corresponds to an electron equivalent energy deposit of ~ 1 MeV at the center of the detector. The threshold value was subsequently modified to be 70 after the purification campaigns which lowered the background levels in the LS.

ID Prompt Trigger

Identical to the ID Singles Trigger but used in conjunction with the ID Delayed Trigger for searching coincident events.

ID Delayed Trigger

This trigger is based on the value of NSum for 17-inch PMTs in the ID. It is designed to trigger on lower energy events that are correlated with an ID Prompt Trigger. This trigger is active and hence can only be triggered during a 1000 μs time window following an ID Prompt Trigger. The threshold was previously set at $\text{NSum} \geq 120$ which corresponds to an electron equivalent energy deposit of ~ 0.5 MeV at the center of the detector. This trigger was originally introduced to study low energy background events such as heavily quenched alpha particles from ^{238}U and ^{232}Th decay chains. The threshold value was subsequently changed to 70 after the purification campaigns which lowered the background levels in the LS.

OD NSum Triggers

These four triggers correspond to the four optically isolated sub-volumes of the OD. The OD NSum threshold values are 6 for the top, 5 for the upper, 6 for the lower, and 7 for the bottom.

ID-OD Trigger

This trigger is issued to acquire OD and chimney PMT waveforms if an ID Trigger is issued. This can be useful for studying correlated low energy events

in the OD that would otherwise not be observable in a Water-Cherenkov veto detector.

OD-ID Trigger

This trigger is issued to acquire the waveform of ID PMTs if any of the four OD triggers are issued. This was designed to be able to monitor and characterize ID activity associated with OD events such as cosmic ray muons that pass through the entire detector or fast neutrons produced from showers associated with these events that may sneak into the LS with no other obvious signal.

Pre-scale Trigger

This trigger is based on the NSum of 17-inch PMTs in the ID similar to other ID triggers, but introduces an artificial DAQ duty cycle to control excessive data rates. The fraction of time the DAQ is active is called the *pre-scale fraction*. This trigger is used when collecting data from calibration sources that may have excessive high event rates in the LS.

Forced Acquisition Triggers

Snapshot Trigger (1 PPS Trigger)

Every PPS signal from the GPS module triggers a forced global acquisition trigger. This trigger is not correlated with any physical events in the detector. The low occupancy of the PMTs for these snapshots is useful in monitoring the dark hit rate of the PMTs. The stable frequency of this trigger can also be used to measure and monitor deviations in the DAQ oscillator frequency.

GPS trigger

A forced acquisition trigger is issued every 32 s where the GPS time-code is saved in data record.

Clock and Pedestal Triggers

There are 50 forced acquisition triggers at start of every run. These are issued for the purpose of calibrating the ATWD sampling interval for each run. The waveforms recorded on the three ATWD PMT signal input channels during these

triggers are called *pedestals*. These are not correlated to any physical events and they are used as a measurement of the average analog-to-digital converter (ADC) offset of ATWDs.

Data Acquisition and Event Building

Trigger data and waveform data of PMT pulses are read out separately by the DAQ software. The trigger data includes three pieces of information; the time-stamp of the trigger digitize command, the type of trigger, and the NSum value that was triggered on. The waveform data includes information such as the time-stamp of digitize command issued by the trigger system, the ATWD launch offset, PMT channel number, which of the two ATWD channels were used (A or B), the ATWD input channel that was digitized (high-gain, mid-gain, low-gain, or clock-channel), and 128 pulse-height samples. As mentioned before, the waveform data is temporarily stored in an on-board memory buffer on the FEE board and read out at a later time in convenient chunks for efficiency. The event builder software that runs in parallel with the DAQ software is responsible to sort the trigger and waveform record data according to their timestamps such that photons arriving within a ~ 350 ns window will be grouped into a single event with one time-stamp. If multiple physics events occur within the same time window, the events are considered as a single event and this is said that the events *pile up*. Data that is processed in this way by the event builder is finally compressed and transferred to a mass storage facility in Tohoku University in Sendai, Japan.

3.4 Purification systems

3.4.1 Overview

The KamLAND LS mainly consists of paraffin oils of which due to their non-ionic molecular composition, intrinsically carry a very low level of ionic impurities. In fact, natural paraffin-based crude oils carry the smallest Uranium content of any type of crude oil [18] and the radioactive contamination of the KamLAND LS was measured to be 10^{-13} g/g, 10^{-12} g/g, 7×10^{-11} g/g for Uranium, Thorium, and Potassium respectively without any

purification. However, in order to observe anti-neutrinos which were estimated to be seen at a rate of about 1 event/day, the radioactive backgrounds had to be reduced to below 0.1 event/day. KamLAND commissioned in the year 2002 with 1 kt of LS that was purified for this purpose with what is known as the *1st purification system*. This reduced the radioactive trace elements of Uranium, Thorium, and Potassium to 10^{-14} g/g, 10^{-14} g/g, and 10^{-15} g/g respectively. Although this was adequate for observing neutrinos originating from nuclear reactors, the very low energy solar-neutrinos and geo-neutrinos required the LS to be purified even further. For this purpose, the *second purification system* along with a dedicated high-purity nitrogen gas generator was constructed in the Fall of 2006. The time periods of when the LS was being purified are coined *purification campaigns* and they lasted during March 2007 through August 2007 and June of 2008 through February of 2009.

3.4.2 First purification system

During the initial construction of KamLAND, the LS and BO were purified independently using identical processes. There are three major steps to the purification process; water extraction, nitrogen purging, and filtering. In the water extraction process, ionic impurities such as Uranium, Thorium, Potassium are removed by utilizing the difference between their solubilities in ionic molecules of water and non-ionic molecules in paraffin oils. The impurities are preferentially extracted out into the water and the water is discarded leaving behind a purified LS. This procedure is performed at normal room temperature and pressure for a few seconds.

Next, the LS is sent to be purged with nitrogen gas. Nitrogen gas is bubbled in the LS extracting contaminants such as dissolved water and oxygen effectively increasing its light yield and transparency. The purge process also removes excess traces of radioactive radon that is produced in the decay chains of other radioactive elements contained in the environment.

Finally, 0.1 μm mesh filters are used to remove dust and large molecular impurities.

The final product of the purification process was measured to contain radioactive contamination of Uranium, Thorium, and Potassium with densities of 3.5×10^{-18} g/g,

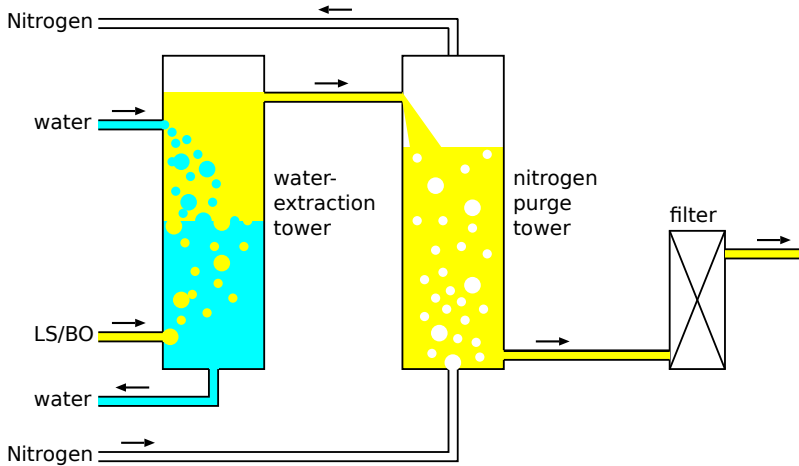


Figure 3.10: Schematic of the first purification system.

5.2×10^{-17} g/g, and $<2.7 \times 10^{-16}$ g/g respectively. Figure 3.10 shows a diagram of the process.

In conclusion the first purification campaign reduced radioactive backgrounds in the LS by about five orders of magnitude.

3.4.3 Second purification system

Neutrinos originating from solar processes such as ${}^7\text{Be}$ decays from fusion chains, Carbon-Nitrogen-Oxygen (CNO) cycles and Proton-Electron-Proton (PEP) decays as well as neutrinos produced by natural radionuclide in the Earth carry energies much lower than neutrinos produced by human-made nuclear reactors. The energy range of neutrinos and their fluxes depending on source is shown in Figure 3.11. Detection of these neutrinos coined *solar-neutrinos* and *geo-neutrinos* requires extremely low background levels of ${}^{85}\text{Kr}$, ${}^{210}\text{Pb}$. The second purification system was constructed for this purpose. Figure 3.12 shows a diagram of this process.

First the LS is extracted from the top portion of the balloon and sent to a buffer tank for temporary storage.

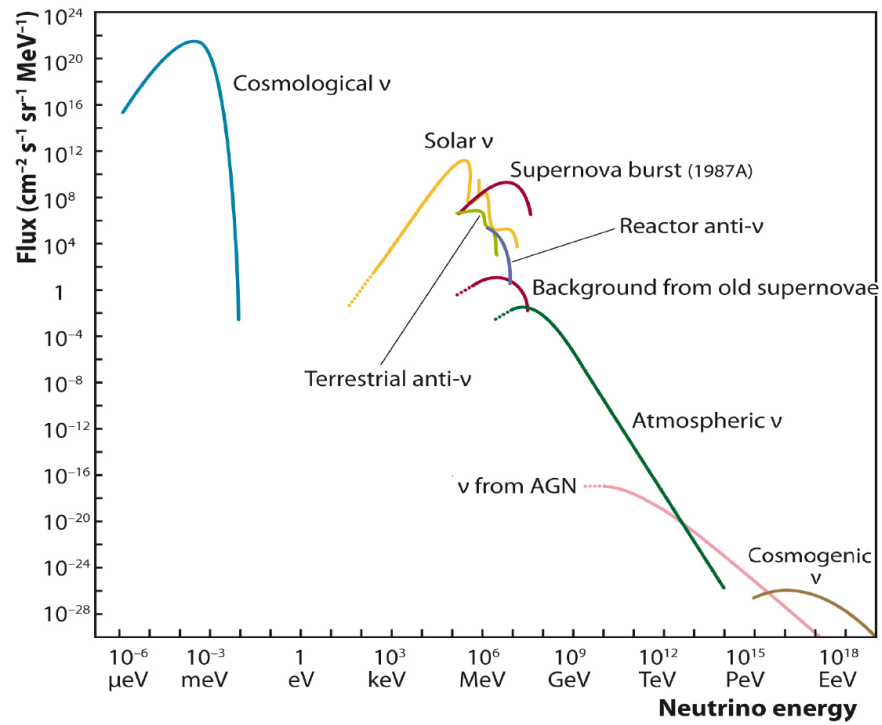


Figure 3.11: Expected fluxes and energies of natural and human-made reactor neutrinos. [77]

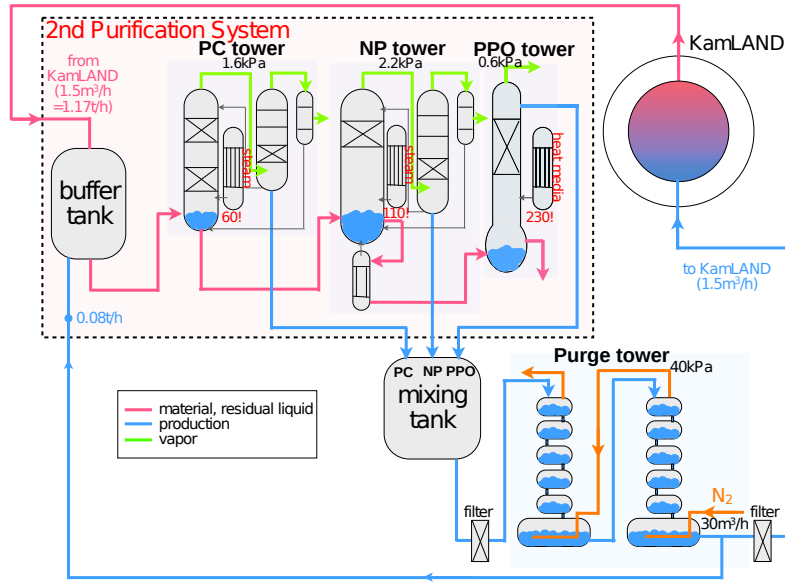


Figure 3.12: Schematic of the second purification system. [85]

It is then fed into a process where the components of the LS are distilled individually in designated distillation towers effectively removing any residual contaminants.

Finally the distilled components are remixed in a mixing tank and the LS density is readjusted and sent through a nitrogen purging process. The flow rate of the nitrogen gas is set at 30 m³/h, 20 times higher than that of the LS and the environment is de-pressurized to 400 hPa to expedite the extraction of the dissolved contaminants. The completed LS is resent to the KamLAND balloon.

Chapter 4

Detector Calibration and Event Reconstruction

4.1 Signal waveform processing

Analysis of physical events taking place in the detector is conducted using the information provided by photons arriving at the photomultiplier tubes (PMTs). The photons that produce a photo-electron at the cathode surface of a PMT induces an electric signal that is amplified by the dynode structure. The resulting electronic signal waveform is subsequently captured by the analog-to-digital converter (ADC) in the form of 128 consecutive 10-bit samples, with each sample being a width of about 1.49 ns in time. The whole waveform is digitized into a total time window of about 190 ns. However, the raw signal waveforms that are digitized in this way cannot be used as is, but must be processed in order to accurately extract useful information such as photon arrival time and charge. This is due to numerous factors that affect the raw waveforms other than just the amplification of photoelectrons in the PMT dynode structure. The waveforms are slightly different for individual PMTs and even for different numbers of photons arriving at the same PMT due to intrinsic non-linear characteristics of the PMT response, the electronics circuitry processing the signals, signal attenuation in different cable lengths, and overall aging effects.

At the beginning of every data taking run, extra calibration waveforms are taken for all signal channels. These include 50 pedestal waveforms, 50 test-pulsar waveforms, and

50 of the 40 MHz clock pulses. These are taken for both analog transient waveform digitizer (ATWD) channels A and B for every PMT. The online waveform analyzer software then uses these waveforms to process all future PMT waveforms in the given run.

The procedure in which the software processes the waveform is the following. First, the pedestal waveform is subtracted from the raw signal waveform. Second, the waveform is smoothed in order to reduce statistical fluctuations due to high frequency noise. Next, the overall baseline of the waveform is adjusted. It is often the case that the baseline may not stay at zero ADC counts after the smoothing process, and this needs to be corrected to stay at zero in order to retain accurate values for pulse arrival time and charge. The difference between the average ADC counts for the 128 pre-smoothed and post-smoothed samples is used for this adjustment. Finally, the pulse time is determined by fitting the leading edge of the earliest peak found by employing the first and second derivatives of the waveform. The pulse charge is defined as the integrated area of the smoothed pulse within the pulse window.

The vertical scale of the resulting waveform, which corresponds to voltage, is determined by the test-pulsar waveforms. The time interval between neighboring ADC waveform samples is about 1.49 ns. This value is calibrated for each channel at the beginning of every run using the 40 MHz clock pulses.

4.2 Timing calibration

Every PMT channel has an intrinsic transit time in processing a photon signal. This is due to various contributions from the different hardware that the signal passes through by the time it is processed. These include intrinsic transit times of the PMTs themselves, varying cable lengths that carry the signals, and any other systematic errors. Therefore the photon arrival time which is inferred from the rising edge of a PMT signal pulse needs to be calibrated and synchronized across different PMTs. In KamLAND, a pulsed dye laser tuned to 500 nm in wavelength with a pulse width of 1.2 ns is used as the light source for this calibration. The absorption wavelength of the liquid scintillator (LS) is less than 400 nm, effectively making the LS transparent to the laser light. The photons in

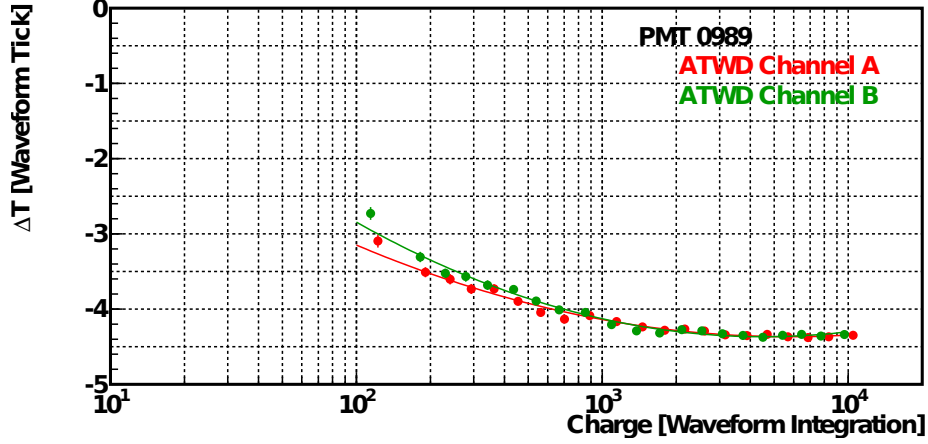


Figure 4.1: The slewing effect showing the correlation between relative pulse time ΔT in units of waveform sample ticks and waveform integrated charge in units of ADC counts. Data and fitted polynomials are shown for both ATWD channels *A* and *B* for a single PMT channel 989. Figure taken from [35].

the laser pulse are introduced through a 230 m long optical fiber which is terminated with a diffuser ball at the center of the detector and spread uniformly across the PMTs. The laser pulse is pre-filtered with a neutral density filter which enables the calibration system to provide controlled intensities from low occupancy single photo-electron level light up to about 5000 p.e. level light to the PMTs. In addition to this optical fiber, there is a duplicate fiber, identical in length, running from the dye laser to a reference PMT connected to a reference front-end electronics (FEE) channel. The trigger system is designed to issue an FEE global acquisition trigger command on signals coming from this reference PMT.

Every PMT has a unique intrinsic correlation between the signal pulse time and charge due to its unique gain. This is called the *slewing* effect and is shown in Figure 4.1 This effect which is a function of pulse charge is fitted with a second order polynomial function $\Delta T(Q)$ where

$$\Delta T(Q) = P_0 + P_1 (\log_{10} Q) + P_2 (\log_{10} Q)^2, \quad (4.2.1)$$

and P_0 , P_1 , P_2 are free parameters, and Q is the integrated pulse charge. P_0 represents the effective absolute timing offset introduced by the overall combined effect of the PMT

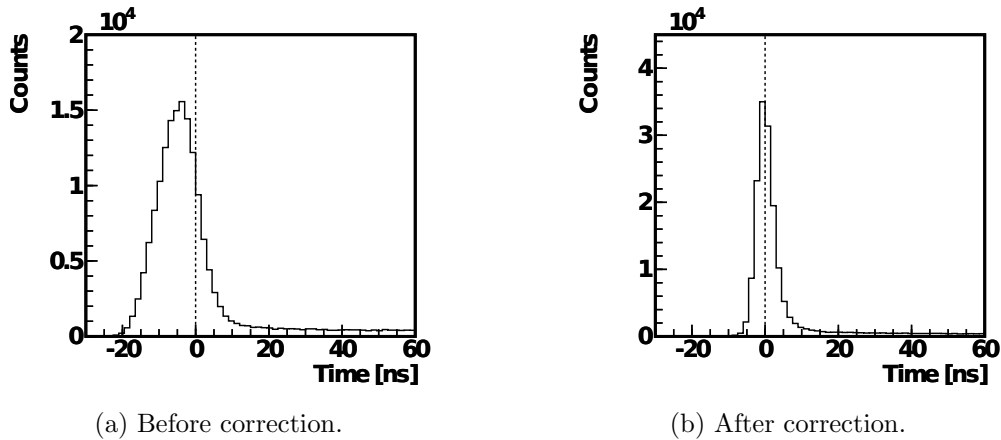


Figure 4.2: Distribution of PMT hit times of single photo-electron pulses with respect to that of the reference PMT for (a) before timing corrections are applied and (b) after timing corrections are applied. The timing resolution is improved from 6.7 ns to 2.0 ns. Figure taken from [35].

response and cable length along with any other factors that may apply. P_1 and P_2 represent the slewing effect. This fit is conducted for each ATWD channel for every PMT.

Figure 4.2 shows the distribution of the hit times of the single photo-electron pulses from the PMTs before and after the correction for slewing effects. The timing resolution is improved from 6.7 ns to 2.0 ns.

4.3 Charge calibration

Every PMT has a unique intrinsic gain value for charge multiplication. This and other factors such as signal attenuation in cables of varying lengths and nonlinear response characteristics of any processing electronics necessitates a charge calibration in order to be able to accurately measure the signal pulse charge in units of photoelectrons in a consistent manner across different signal channels. This is done through determining the integrated pulse area corresponding to one photoelectron for each channel individually. Furthermore, PMT gain is known to be time dependent so this calibration must be conducted run by run.

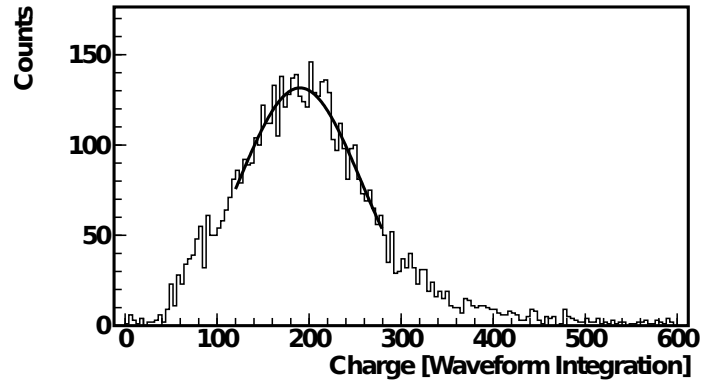


Figure 4.3: Charge calibration for a typical signal channel for a 17-inch PMT. The histogram shows the number of low occupancy events in counts versus the integrated signal waveform charge in units of ADC counts. The Gaussian peak is fitted to calibrate the integrated waveform charge that corresponds to one photoelectron. Figure taken from [35].

In the case of 17-inch PMTs, the integrated pulse area corresponding to one photoelectron is determined by finding the most probable integrated pulse area among signals coming from low occupancy events. Low occupancy events tend to populate PMTs with single photoelectron level light. These type of events are found by looking for events using the following cut conditions.

- Post-muon veto for 2 ms.
- Noise event removal.
- Search among events with a low occupancy determined by the NSum value where $120 \leq \text{NSum} \leq 180$ before purification, and $120 \leq \text{NSum} \leq 230$ after purification.
- Distance from the reconstructed vertex to the PMT in question must be greater than 6.0 m.
- Signal pulse must be a waveform containing a single peak.

Figure 4.3 shows an example distribution of integrated waveform charge for signals coming from low occupancy events. The distribution is fitted with a Gaussian peak

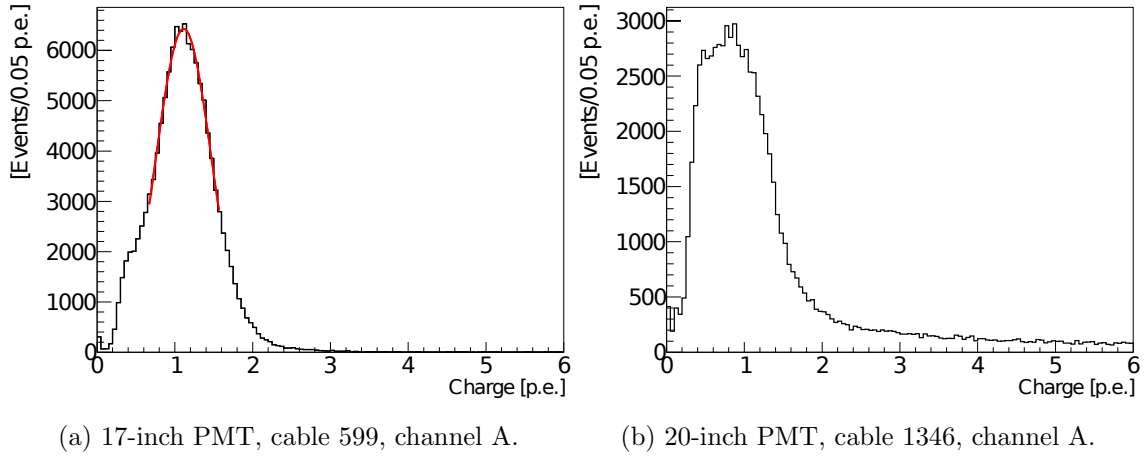


Figure 4.4: Distribution of charge for single photoelectron (p.e.) pulses in the case of (a) a typical 17-inch PMT, and (b) a typical 20-inch PMT. There is a clear Gaussian peak fitted with a red line in the distribution for a 17-inch PMT but this peak is ill defined in the case of a 20-inch PMT. Gain calibration using the peak in a single photoelectron charge distribution works well for 17-inch PMTs but a different approach must be used for 20-inch PMTs. Figure taken from [85].

which determines the charge scale corresponding to a single photoelectron. Once the conversion from charge to photoelectrons is known, all charge can be expressed in terms of photoelectrons (p.e.) rather than ADC counts.

On the other hand, this method of charge calibration is difficult to carry out in the case of 20-inch PMTs. This is due to the fact that the most probable charge corresponding to one photoelectron is not well defined in the case of 20-inch PMTs as can be readily seen in Figure 4.4. A different approach is employed for the case of 20-inch PMTs. Using events with a large number of photons, such as muon events, where the 20-inch PMT in question and eight of the closest neighboring 17-inch PMTs receive similar amounts of photons, the charge of the 20-inch PMT signal is compared to the average charge of the 17-inch PMTs

via a charge ratio R defined as

$$R \equiv \frac{Q_{20\text{-inch}}}{\left(\frac{1}{8} \sum_{i=1}^8 Q_{17\text{-inch}}\right)}, \quad (4.3.1)$$

where $Q_{20\text{-inch}}$ is the charge of the 20-inch PMT in question, and $Q_{17\text{-inch}}$ is the charge of the eight immediate neighboring 17-inch PMTs. The ratio is shown in Figure 4.5.

4.4 Cosmic ray muons

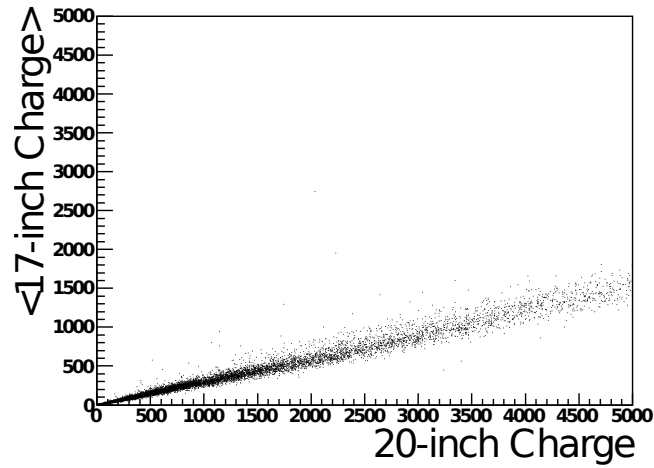
Overview

The 2700 meter water equivalent (mwe) rock overburden above shields the KamLAND detector from cosmic ray muons reducing the flux by about a factor of 10^{-5} compared with that of the surface of the Earth. This effectively reduces the flux down to $J_\mu = 5.37 \pm 0.41/(\text{m h}^2)$ [3] or to a rate of about 0.34 Hz through the detector. Although the flux is significantly diminished, the muons are a constant background for neutrino analysis because they can by themselves mimic neutrino events or produce secondary spallation products and radioactive isotopes that are mistakenly identified in a similar fashion. A specific muon reconstruction algorithm was developed by the KamLAND group to identify, classify, and reconstruct muon events.

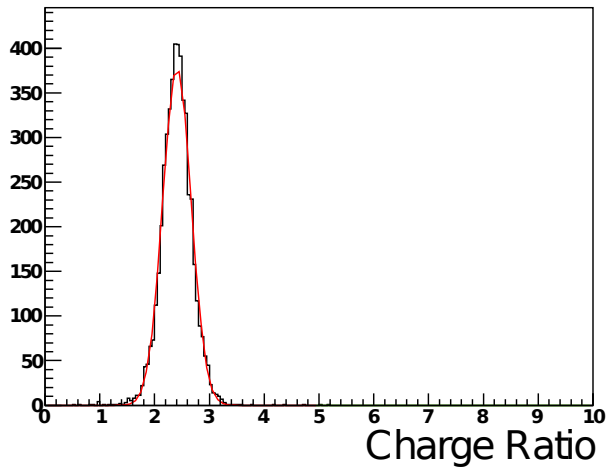
4.4.1 Muon identification

Cosmic ray muons are a constant background for neutrino analysis and it is vital to reliably identify them. Cosmic-ray muons are recognized either by the large amount of scintillation and Cherenkov light detected by the 17-inch inner detector (ID) PMTs or by the Cherenkov light detected by the outer detector (OD) PMTs. Events that satisfy either or both of the following two conditions are designated as a *muon* event:

- $Q_{\text{ID}, 17\text{-inch}} \geq 10\,000$ p.e. (~ 30 MeV).
- $Q_{\text{ID}, 17\text{-inch}} \geq 500$ p.e. and $N_{\text{OD}, 200\text{-ns}} \geq 5$ hits.



(a)



(b)

Figure 4.5: The 20-inch PMT charge is calibrated using the ratio of the 20-inch PMT charge to the mean charge of eight of the immediately neighboring 17-inch PMTs. (a) shows the correlation of the mean charge of the 17-inch PMTs versus the 20-inch PMT charge. (b) shows a histogram tallying this ratio. Both figures are for PMT cable number 1346 and ATWD channel A. Figure taken from [85].

Here $Q_{\text{ID}, 17\text{-inch}}$ is the total charge of all 17-inch PMTs in the ID in units of photoelectrons (p.e.), and $N_{\text{OD}, 200\text{-ns}}$ is the number of PMT hits in the OD within a 200 ns time window. This time window was optimized to remove accidental OD PMT hits and to improve the overall efficiency of muon tagging.

The events that are identified as being due to muons are further categorized as being either *scintillation* muons or *Cherenkov* muons depending on whether the muon track travels through the LS portion or solely the buffer oil (BO) region inside the ID. Tracks that travel only through the BO produce photons by the Cherenkov process alone and are referred to as *Cherenkov* muons. On the other hand, those that traverse the LS stimulate the medium and produce scintillation photons through ionization in addition to Cherenkov photons are referred to as *scintillation* muons. Scintillation muons generally produce around 20 to 40 times more photoelectrons per event compared to Cherenkov muons. The frequency of these events along with a distribution of their deposited charge is shown in Figure 4.6.

Scintillation muons are further categorized into *showering* and *non-showering* muons depending on whether or not the muons produce many secondary shower particles. This is parameterized by a variable called the *residual charge* ΔQ defined in Section 4.4.3 and utilized as shown in the following:

Showring muon A scintillation muon with $\Delta Q \geq 10^6$ p.e.. These are very energetic muons that often times produce radioactive isotopes in secondary particle showers.

Non-showering muon A scintillation muon with $\Delta Q < 10^6$ p.e.. These are less energetic muons that do not produce as many secondary particles. These are more common and are the majority.

The muon rate in KamLAND has been very stable ever since the beginning of data taking as shown in Figure 4.7. However, the average charge deposited in the ID for scintillation and Cherenkov muons has not been stable as shown in Figure 4.8. This can be attributed to various reasons. The sudden changes are due to *purification* campaigns and electronics upgrades conducted by the KamLAND group in the past, while the more slowly varying trends may possibly be attributed to gradual changes in the LS and BO properties themselves. There exists the possibility of minute leakage of the LS into the BO

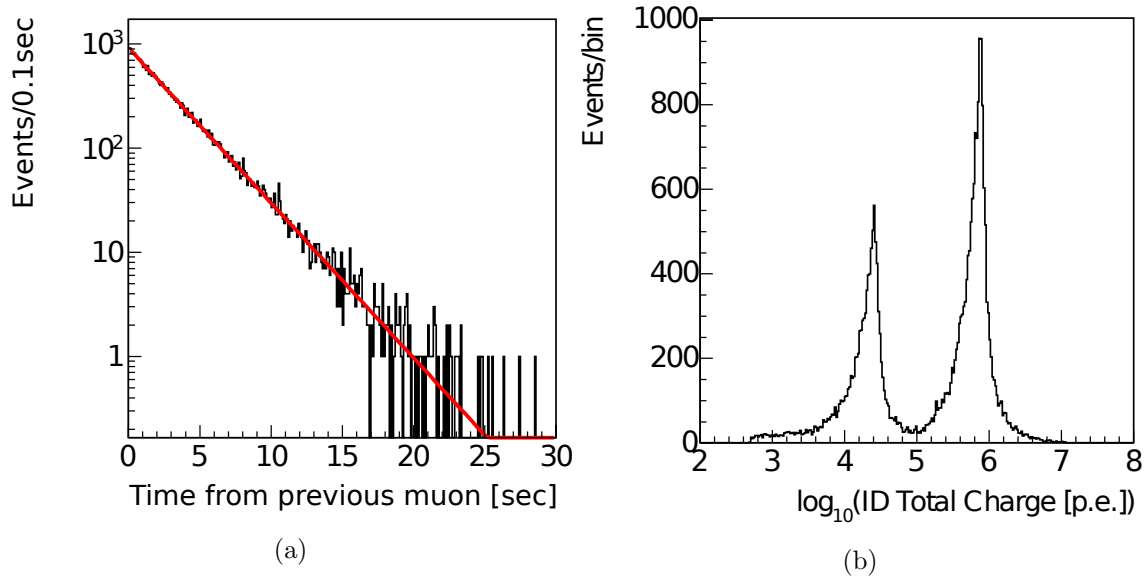


Figure 4.6: The muon event interval is shown in (a). The interval is calculated by measuring the elapsed time between subsequent muons. The average value is 3 s. (b) shows the total charge deposited by muon events. A clear distinction between the two types of through-going muons, scintillation and Cherenkov muons, can be seen. Scintillation muons deposit about 20 to 40 times more charge compared to Cherenkov muons. Figure taken from [85].

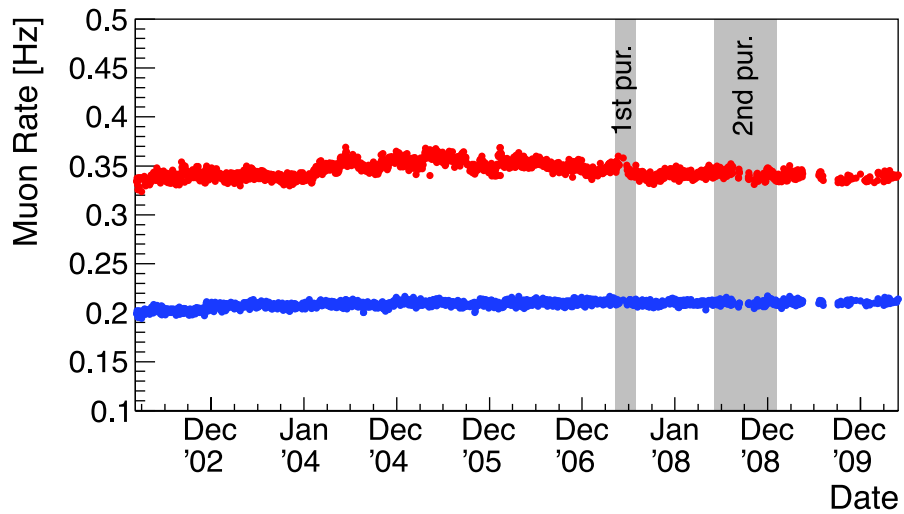
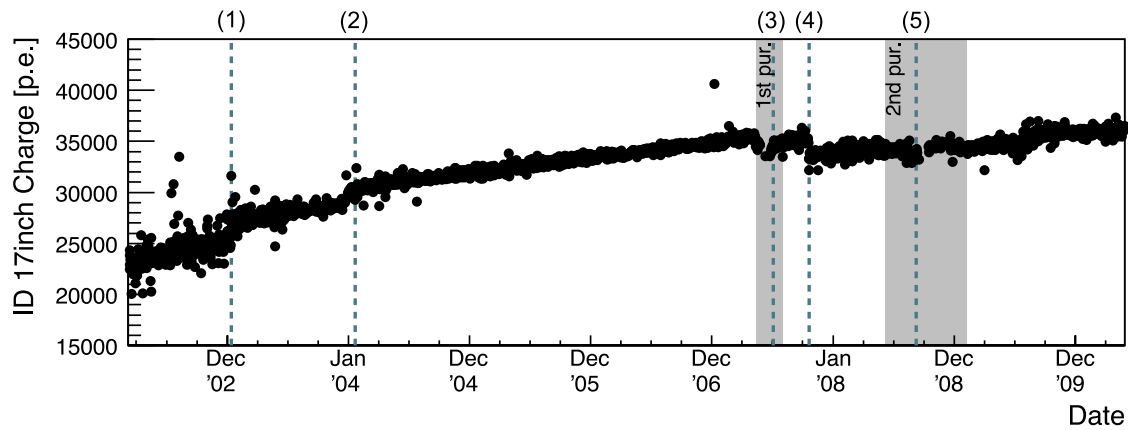
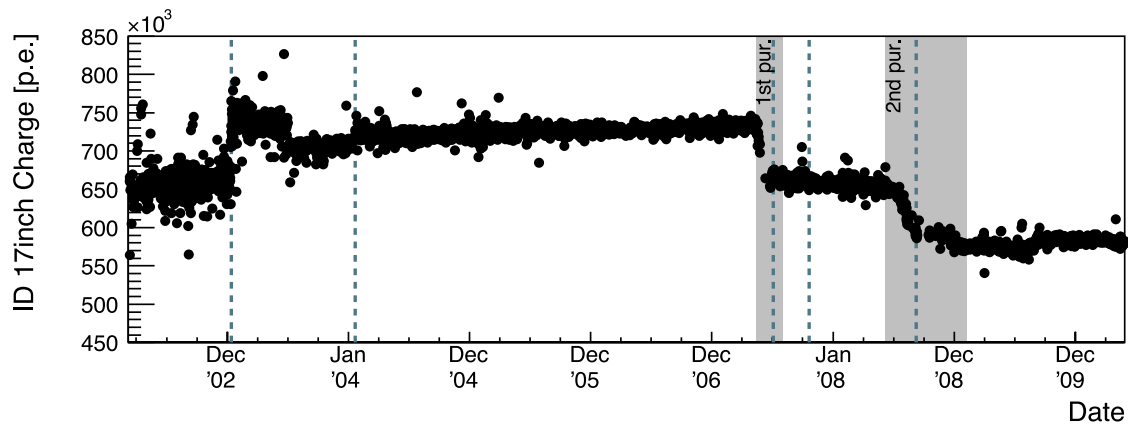


Figure 4.7: The muon rate versus time. The red colored points show the time variation of the total muon rate. Its value is stable at about 0.34 Hz. The blue colored points show the rate of only scintillation muons. Its rate is also stable at about 0.20 Hz. The gray shaded bands show the time periods for the two purification campaigns in KamLAND. Figure taken from [85].



(a) Cherenkov muon.



(b) Scintillation muon.

Figure 4.8: Average charge deposited in the inner detector using only 17-inch PMTs for the case of (a) Cherenkov muons, and (b) scintillation muons. Sudden changes with respect to time can be attributed to various *purification* campaigns and electronics modifications conducted by the KamLAND group as can be seen below. Figure taken from [85].

- (1) Electronics (FEE) upgrade (January 13, 2003).
- (2) High-voltage module replacement (January 21, 2004).
- (3) End of high dark-rate period during first purification (September 7, 2008).
- (4) Electronics (FEE) upgrade (October 20, 2008).
- (5) All crates turned on (September 7, 2008).

over time. However, this hypothesis is not confirmed and resolving the exact cause requires further study. The effects that these may have for energy reconstruction of events in the ID is compensated by conducting energy calibrations on a per-run basis as will be explained in more detail in Section 4.6.

4.4.2 Muon fitter

Charged particles traveling through a medium at a speed faster than that of light radiate Cherenkov photons. In the case that a cosmic-ray muon traverses the ID, the muon track can be reconstructed by utilizing the earliest Cherenkov photons emanating from the muon track. As the muon travels through the LS or BO regions, Cherenkov photons are emitted at a muon velocity dependent angle θ known as the *Cherenkov angle* with respect to the track as shown in Figure 4.9. As opposed to the mean muon energy of about 4 GeV on the surface of the Earth at sea-level, the 2700 mwe rock overburden of KamLAND shields the detector from the majority of the lower energy muons yielding a mean muon energy at the detector of 260 ± 8 GeV. Muons at these energies travel at about 99.99999% of the speed of light in vacuum. Therefore the earliest photon arrival time t for a given PMT can be written as

$$\begin{aligned} t &= t_0 + \frac{l}{c} + \left(\frac{n_{\text{eff}}}{c}\right) \left(\frac{z-l}{\cos\theta}\right) \\ &= t_0 + \frac{l}{c} + \left(\frac{n_{\text{eff}}}{c}\right) \sqrt{(z-l)^2 + \rho^2}, \end{aligned} \tag{4.4.1}$$

where t_0 denotes the time at which the muon enters the ID, and l , z , and ρ are respectively the distance the muon travels inside the ID before photon emission, the distance from the point of entry to the PMT parallel to the muon track, and the perpendicular distance of the PMT from the muon track. Also we have taken the muon velocity to be equal to the speed of light in vacuum c . Here n_{eff} is the effective overall index of refraction for both the LS and BO. The actual index of refraction varies within the range of about 1.44 to 1.47 for various wavelengths in the LS and BO. n_{eff} is tuned to give an average value that includes all such effects. The Cherenkov angle is determined by calculating the fastest possible

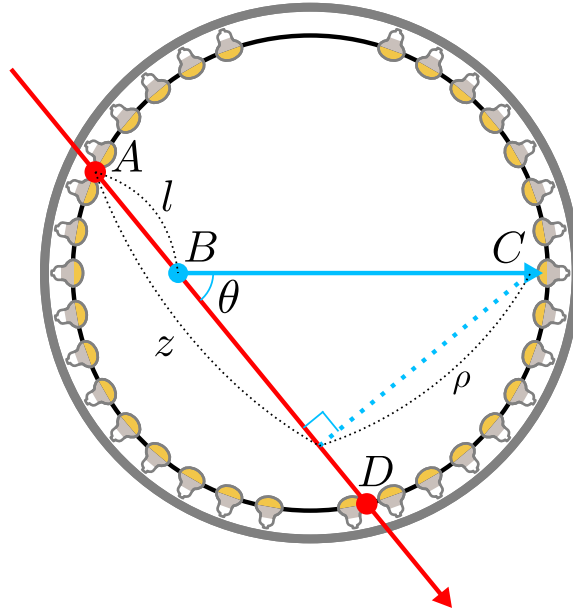


Figure 4.9: Schematic of a cosmic ray muon traversing the ID of KamLAND. The muon track is represented by the arrow-head tipped red line. Points A and B respectively represent the entry and exit points of the muon with respect to the ID. The solid blue line represents the path traveled by the earliest photons originating along the muon track at point B and arriving at a PMT at point C . The Cherenkov angle between the muon track and the photon path is denoted by θ . The black solid circle that coincides with the equator of the PMTs represents the 8.5 m radius opaque black acrylic sheet that optically defines the ID. The outermost gray solid circle represents the 9 m radius stainless steel containment vessel.

photon arrival time by setting

$$\begin{aligned}
0 = \frac{dt}{dl} &= \frac{1}{c} - \frac{n_{\text{eff}}}{c} \left(\frac{z-l}{\sqrt{(z-l)^2 + \rho^2}} \right) \\
&= \frac{1}{c} - \frac{n_{\text{eff}}}{c} \cos \theta,
\end{aligned}
\tag{4.4.2}$$

giving the Cerenkov angle as

$$\cos \theta = \frac{1}{n_{\text{eff}}}.
\tag{4.4.3}$$

The muon track is reconstructed by finding the track that best reproduces the earliest photon arrival signature.

This reconstruction algorithm is designed for muons of which the track completely traverses the ID (*through-going muons*). However, it is not appropriate for events where the muon stops inside the ID (*stopping muon*) or those that have multiple muons in the same event (*multi-muon events*). In addition, muon events associated with too small a charge sum are classified as *mis-reconstructed muon* events. Mis-reconstructed through-going muons comprise about 0.2% of all muons. Muons with extremely large charge sums are classified as *showering muons* and these make up about 1.5% of all muons.

4.4.3 Residual charge

Figure 4.10 shows the total charge from 17-inch PMTs versus the impact parameter of cosmic ray muon tracks traversing the ID. The impact parameter of these tracks is defined as the shortest distance from the muon track to the center of the ID of KamLAND. A clear boundary can be seen at a radius of 650 cm for which muons with an impact parameter less than this are mostly scintillation muons traveling through the LS containing balloon, and for those greater are generally Cherenkov muons that only *clip* the BO.

A ratio between total 17-inch PMT charge and track length for both Cherenkov muons and scintillation muons can be derived as

$$\begin{aligned}
\left(\frac{dQ}{dx} \right)_{\text{Cherenkov}} &= \frac{Q_{\text{ID}}}{L_{\text{BO}}}, \\
\left(\frac{dQ}{dx} \right)_{\text{scintillation}} &= \frac{Q_{\text{ID}} - L_{\text{BO}} \left(\frac{dQ}{dx} \right)_{\text{Cherenkov}}}{L_{\text{ID}}},
\end{aligned}
\tag{4.4.4}$$

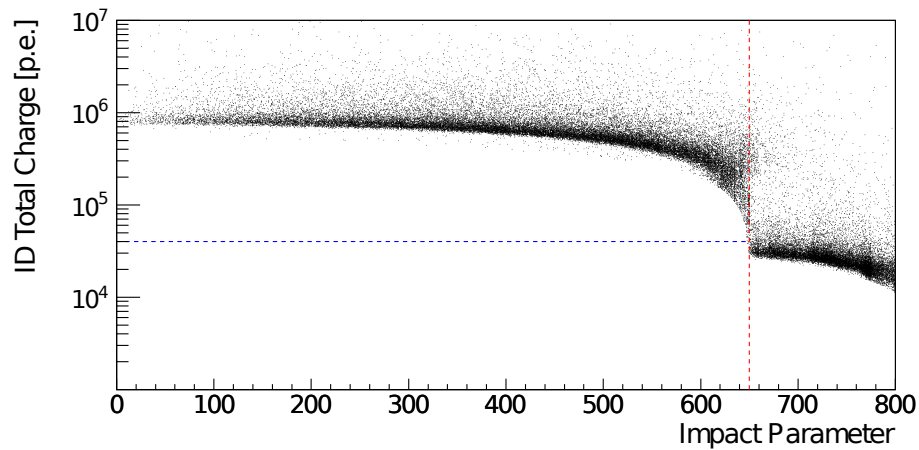


Figure 4.10: Scatter plot showing total charge of 17-inch PMTs with respect to the perpendicular distance from the muon track to the center of the inner detector (impact parameter) in units of cm. The vertical dashed line represents the physical boundary between the LS and BO regions at a radius of 650 cm. There is a clear distinction between scintillation and Cherenkov muons that can be seen at this this radius. The horizontal dashed line corresponds to 4×10^4 p.e. for which most of the total charge for scintillation muons resides above. Figure taken from [85].

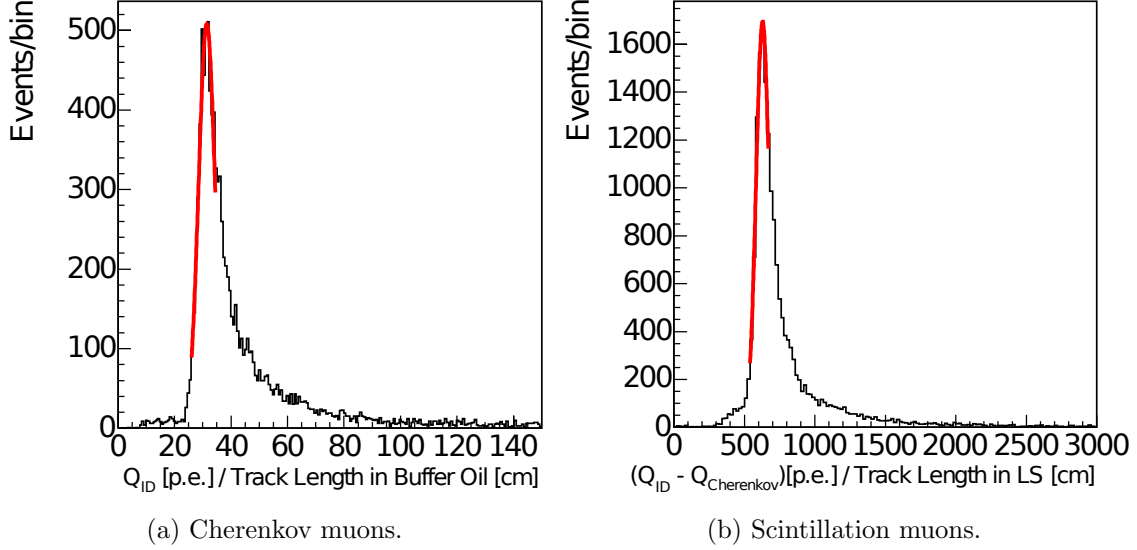
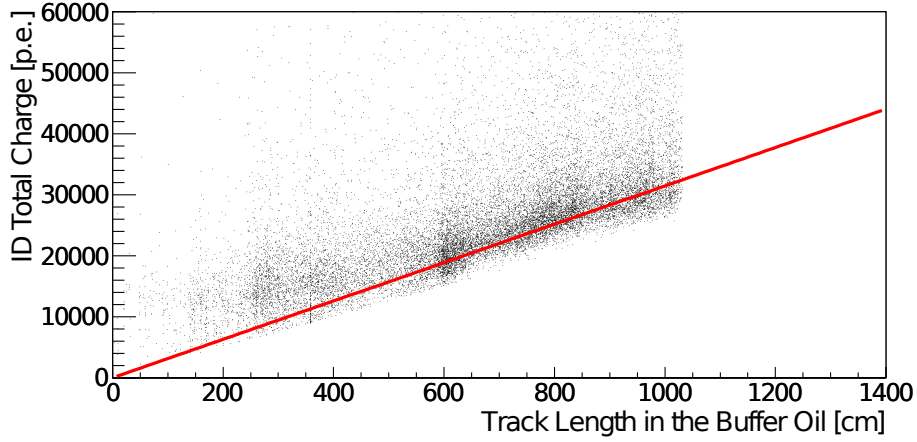


Figure 4.11: Histograms showing the distribution of the total 17-inch PMT charge per reconstructed muon track length for the case of (a) Cherenkov muons, and (b) scintillation muons. Both distributions are in the form of Landau distributions for which the peak can be fitted to obtain best fit values of $(dQ/dx)_{\text{Cherenkov}} = 31.45 \text{ p.e./cm}$ and $(dQ/dx)_{\text{scintillation}} = 629.4 \text{ p.e./cm}$ Figure taken from [85].

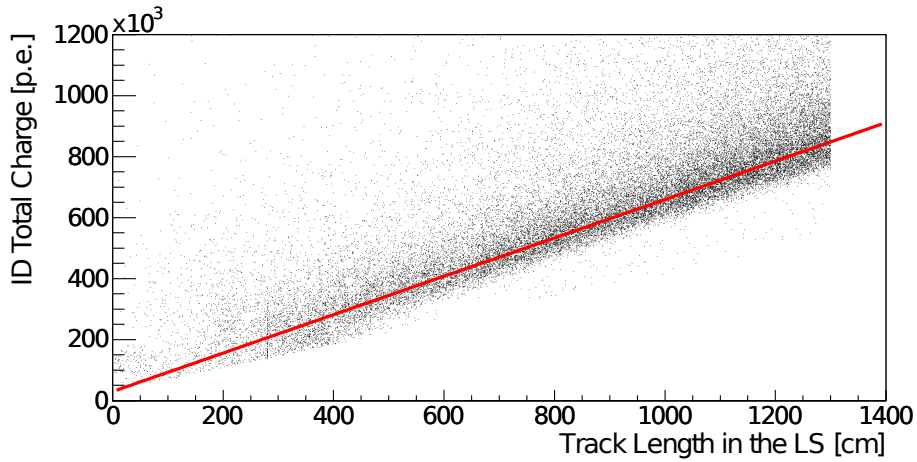
where Q_{ID} is the total charge of the 17-inch PMTs, and L_{ID} and L_{BO} are respectively the portions of the reconstructed track length overlapping with only the LS and BO regions. Here $(dQ/dx)_{\text{scintillation}}$ includes the contribution from the Cherenkov component of light created in the LS. The best fit values for these ratios are obtained by fitting the corresponding correlation distributions as shown in Figure 4.11 resulting in

$$\begin{aligned} \left(\frac{dQ}{dx}\right)_{\text{Cherenkov}}^{\text{fit}} &= 31 \pm 2 \text{ p.e./cm}, \\ \left(\frac{dQ}{dx}\right)_{\text{scintillation}}^{\text{fit}} &= 629 \pm 47 \text{ p.e./cm}. \end{aligned} \tag{4.4.5}$$

Correlations between the total charge of the 17-inch PMTs and the muon track length is shown in Figure 4.12. A clear linear correlation between the baseline of deposited charge and track length is apparent in the case of both Cherenkov and scintillation muons. These trends corresponds to minimum ionizing muons and the slope of this baseline



(a) Cherenkov muons.



(b) Scintillation muons.

Figure 4.12: Correlation scatter plots between the total 17-inch PMT charge and the reconstructed track length for (a) Cherenkov muons, and (b) scintillation muons. The solid lines represent the fitted ratios of charge per unit length dQ/dx in the respective medium. Muon tracks that are ill reconstructed with a badness parameter greater than 100 are not plotted in these figures. Figure taken from [85].

indicates the charge deposit per unit track length. However, there are also events that have considerably higher charge deposits than those of the fitted baselines. These muon events are more likely to involve secondary particles produced in showers. Using this guideline, we can define the *residual charge* as follows:

$$\Delta Q = Q_{\text{ID}} - L_{\text{BO}} \left(\frac{dQ}{dx} \right)_{\text{Cherenkov}}^{\text{fit}} - L_{\text{LS}} \left(\frac{dQ}{dx} \right)_{\text{scintillation}}^{\text{fit}}. \quad (4.4.6)$$

4.4.4 Muon veto contribution to dead time

In the traditional low-energy analysis of KamLAND, a 2 s post-muon veto is applied to reduce backgrounds due to muon induced spallation products along with a 2 ms veto for those related with post-muon noise events. These two timing cuts were applied depending on the type of muon that was observed as follows. A muon with a residual charge of ΔQ greater than 10^6 p.e. was classified as a *showering* muon for which a subsequent 2 s veto was applied to the whole detector volume to reduce inverse beta decay (IBD) backgrounds associated with secondary particle production. On the other hand, a muon with a residual charge of ΔQ less than 10^6 p.e. was classified as a *non-showering* muon for which only a 2 ms whole volume veto was applied, albeit a 2 s veto was still applied to a 3 m-radius cylindrical volume concentric with the muon track.

However, in this analysis we analyze event with energies greater than a GeV. Spallation products are known to deposit energies below around 20 MeV effectively letting us relax the 2 s veto. Therefore we will solely apply a 2 ms global post-muon veto to the whole detector volume for any muon event regardless of the its classification. This modified veto ultimately contributes a dead time equal to 0.2 % of the total run time, and 18.1 % of the total dead time of this analysis.

4.5 Bad channels

There exist 1879 PMTs in the inner detector and 225 PMTs in the outer detector. Not all of the PMT channels are reliable enough at any given time for their signals to be used in physics analysis. They may be faulty for a number of different reasons. The

gain may be unstable resulting in an abnormally high or low hit rate in comparison with a typical PMT. In addition, there may be problems with the high-voltage power supply channel or the cable connection along with any other electronics component failure that can lead to strange effects in the PMT signals. Unreliable PMTs need to be identified and masked during physics analysis in order to prevent systematic biases. These are referred to as *bad channels* and are searched for during every run. The following lists a number of conditions of which any single one is sufficient for a given PMT channel in the inner detector to be designated as a bad channel.

- Channels with an abnormally low hit response rate:
hit rate < 1000 hits/10 000 events.
- Channels with an abnormally high rate of no-hit events:
no-hit rate > 1000 no-hit events/10 000 events
- Channels with excessively low gain:
hit rate < 80 hits/100 high-charge muon events, where a high-charge muon event is defined as a muon event with a total ID charge of $Q_{\text{ID}} > 10^{5.5}$ p.e.
- Channels for which the ping-pong scheme that alternates between the two ATWD channels in the FEE is not working properly:
the difference in hit rate between ATWD channels A and B within a 10 000 event sample is greater than 22 %.
- Channels with an abnormally high or low integrated ADC waveform charge corresponding to one photoelectron:
 $Q_{\text{ADC}} < (1/4) \times \bar{Q}_{\text{ADC}}$ or $Q_{\text{ADC}} > 4 \times \bar{Q}_{\text{ADC}}$, where Q_{ADC} is the 1 p.e. ADC charge and \bar{Q}_{ADC} is the average over that of all PMTs.
- Channels with an anomalous charge compared to that of physically neighboring PMTs in high-charge muon events with a total ID charge of $Q_{\text{ID}} > 10^{5.5}$ p.e.:

$$\frac{1}{N} \sum_{i=1}^N \frac{(Q - Q_i)^2}{Q_i} > 400 \text{ p.e.}, \quad (4.5.1)$$

where Q is the charge of the PMT in question, Q_i is that of a neighboring PMT, and N is the total number of neighboring PMTs.

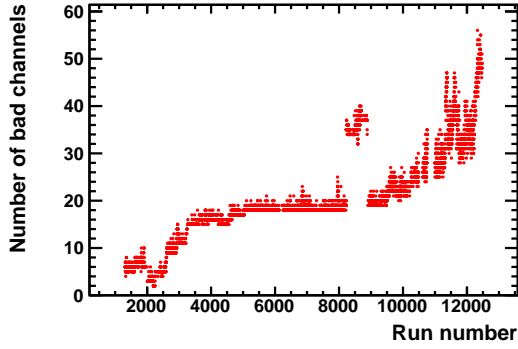
Only the first criterion is applied to PMT channels in the outer detector. Figure 4.13 shows the time evolution of the total number of bad channels for PMTs in the ID and OD. The ID houses both 17-inch and 20-inch type PMTs, whereas the OD only has 20-inch PMTs.

The actual PMT channels used in the analysis differs on a run-by-run basis depending on which channels were designated as being bad. During any given run, it is possible for an individual channel to be bad or even a whole group of channels, say all the ID 20-inch PMTs, to be bad and thus be unsuitable for data analysis. This can occur for instance if one of the high voltage systems that had been providing power specifically to only the 20-inch PMTs had had a malfunction. Since the 17-inch PMTs comprise the majority of the ID PMTs, analysis in this work is restricted to runs in which much of the 17-inch PMT channels are good. Energy calibration is conducted using only the 17-inch PMTs on a run-by-run basis to accommodate for the variable number of usable channels as well as any time dependent systematics that may affect energy reconstruction. Event reconstruction is also conducted using only the 17-inch PMT channels.

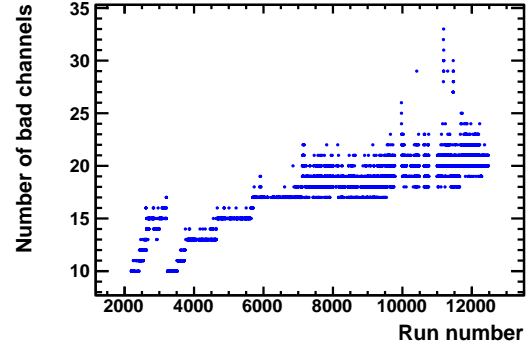
4.6 Energy calibration

The KamLAND detector has been utilized to observe neutrinos originating from nuclear processes in the Sun, Earth or human-made reactors. The energies of neutrinos from these sources are typically in the range of about 0.1 MeV to 10 MeV. Within this region, KamLAND has mainly conducted analyses within energies of about 1 MeV to 10 MeV. However, in order to observe neutrinos originating from dark matter annihilation, we must be able to resolve energies comparable to the proposed dark matter masses of around 1 GeV to 20 GeV. This is three orders of magnitude greater in energy relative to the conventional energy regime of KamLAND, necessitating a separate energy calibration on these scales.

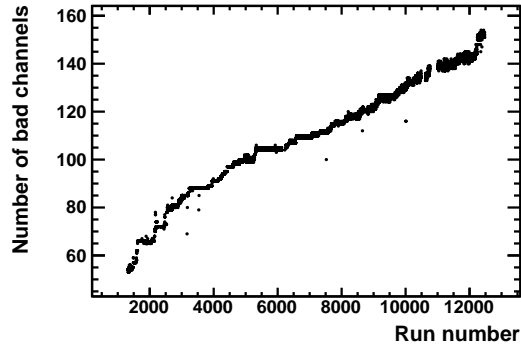
It was decided to take advantage of cosmic-ray muons as the calibration source due to their ample abundance and relatively well-known track energy deposition in media. The general idea is to use through-going muons to determine a run dependent relation



(a) ID 17-inch PMTs.



(b) ID 20-inch PMTs.



(c) OD 20-inch PMTs.

Figure 4.13: Time evolution of the number of bad PMT channels during the live time of the detector. (a) shows the number of bad 17-inch PMT channels and (b) that of bad 20-inch channels both for those in the ID. (c) shows the corresponding number for the OD PMTs which are all of the 20-inch type.

between the number of photoelectrons detected by the 17-inch ID PMTs and how much energy was lost by the muon in the inner detector. In order to do this, we must know how much energy is deposited by a muon track per unit track length.

The rate of energy-loss by a charged particle is known as the *stopping power* denoted by the positive function

$$S(E) = -\frac{dE}{dx}, \quad (4.6.1)$$

where E is the energy of the incident particle and x is the distance traveled in the medium. The mean stopping power of a relativistic charged particle with speed v , charge z , and energy E , traveling a distance of x , follows a well known formula called the *Bethe* equation,

$$\begin{aligned} \langle S(E) \rangle &= -\left\langle \frac{dE}{dx} \right\rangle \\ &= Kz^2 \frac{Z\rho}{AM_u} \frac{1}{\beta^2} \left(\frac{1}{2} \ln \frac{2m_e c^2 \beta^2 \gamma^2 T_{\max}}{I^2} - \beta^2 - \frac{\delta(\beta\gamma)}{2} \right), \end{aligned} \quad (4.6.2)$$

where

$$\begin{aligned} K &= 4\pi N_A r_e^2 m_e c^2 = 0.307\,075 \text{ MeV cm/g}, \\ r_e &= \frac{e^2}{4\pi\epsilon_0 m_e c^2} = 2.817\,940\,325 \pm 0.000\,000\,028 \text{ fm}, \\ \beta &= \frac{v}{c}, \\ \gamma &= \frac{1}{\sqrt{1 - \beta^2}}, \end{aligned} \quad (4.6.3)$$

and ρ , Z , and A are respectively the mass-density, atomic number, and atomic mass of the medium, $M_u = 1 \text{ g/mol}$ is the molar mass constant, N_A is Avogadro's number, m_e is the electron mass, r_e is the classical electron radius, $\delta(\beta\gamma)$ is the density effect correction computed using Sternheimer's parameterization [78], and e and c are respectively the typical values for the elementary charge and the speed of light in vacuum. Here, T_{\max} is the maximum energy transfer possible in a single collision of the incident particle with the medium, and I is the mean excitation energy as shown in Figure 4.14. $-\langle dE/dx \rangle$ is typically expressed in energy-loss per unit mass-density per unit track-length so ρ is usually divided on both sides of the equation and absorbed into E .

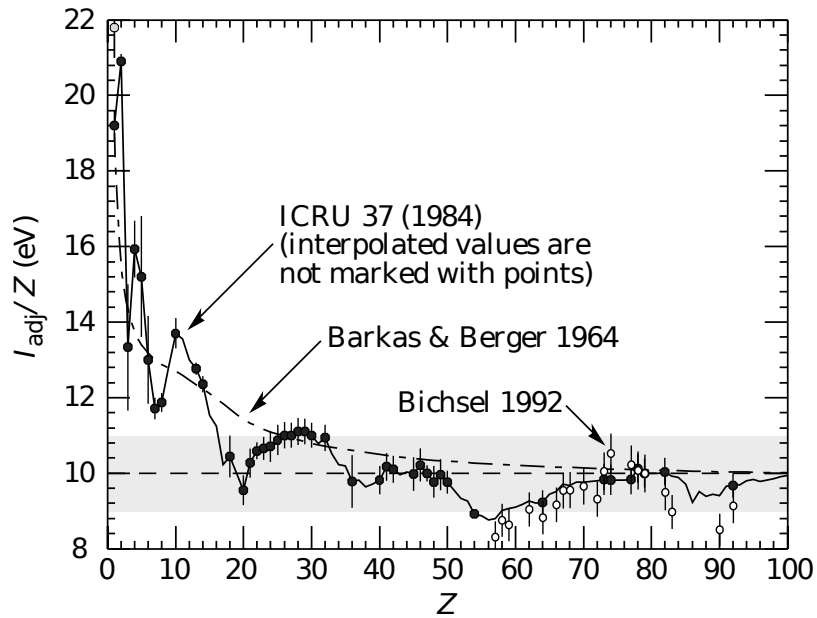


Figure 4.14: Mean excitation energies divided by atomic number Z adopted from the International Commission on Radiation Units and Measurements (ICRU) 37 [55] (filled points). Experimental measurements are depicted by symbols with error bars and the interpolated values are simply joined. The black and gray points at the lower end of Z is respectively for H_2 in the form of gas and liquid. The open circles show data from Bichsel [23]. The dotted curve is from theoretical approximations from Barks and Berger [14]. Figure taken from [48].

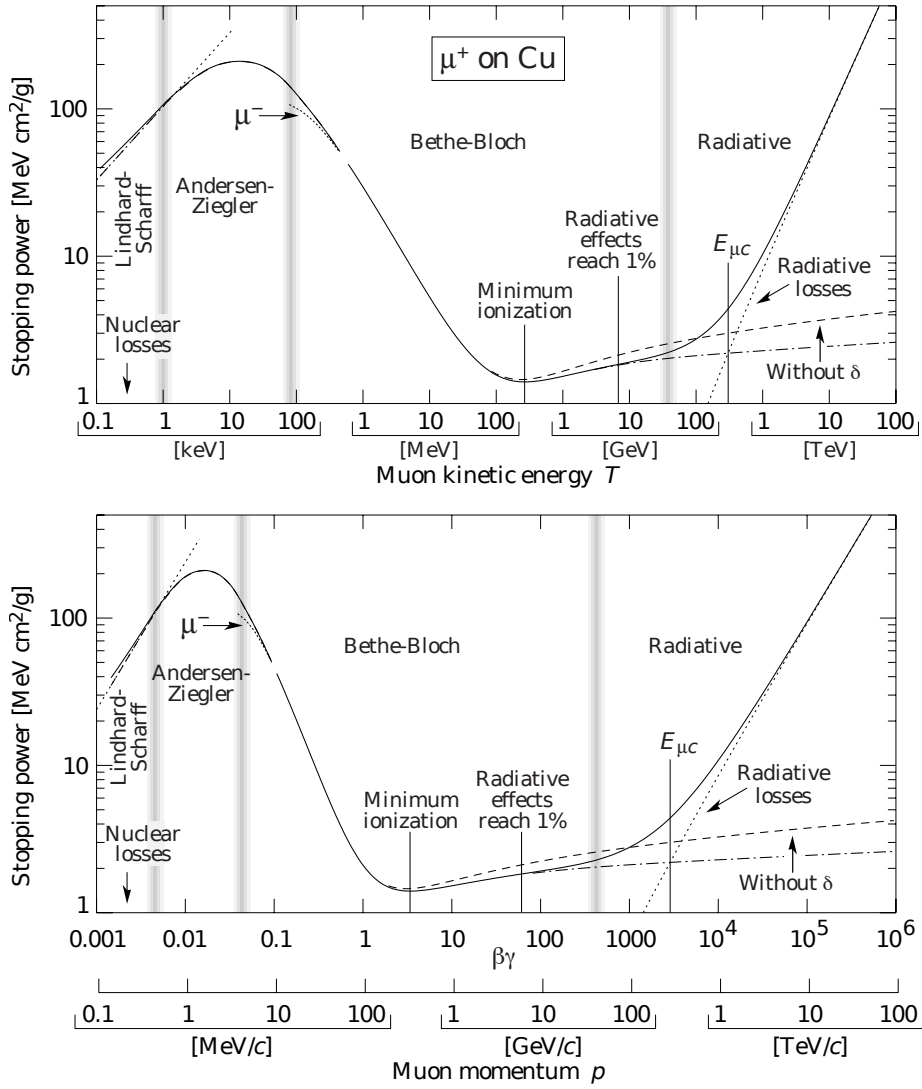


Figure 4.15: Stopping power $\langle -dE/dx \rangle$ for positive muons in copper as a function of kinetic energy T (top figure) and as a function of relativistic momentum p (bottom figure). Solid curves indicate the total stopping power. Data below the break in the solid line at $T \approx 0.5$ MeV are scaled from data for π^- . Vertical gray bands indicate boundaries between different theoretical approximations or dominant physics processes. Figure taken from [48].

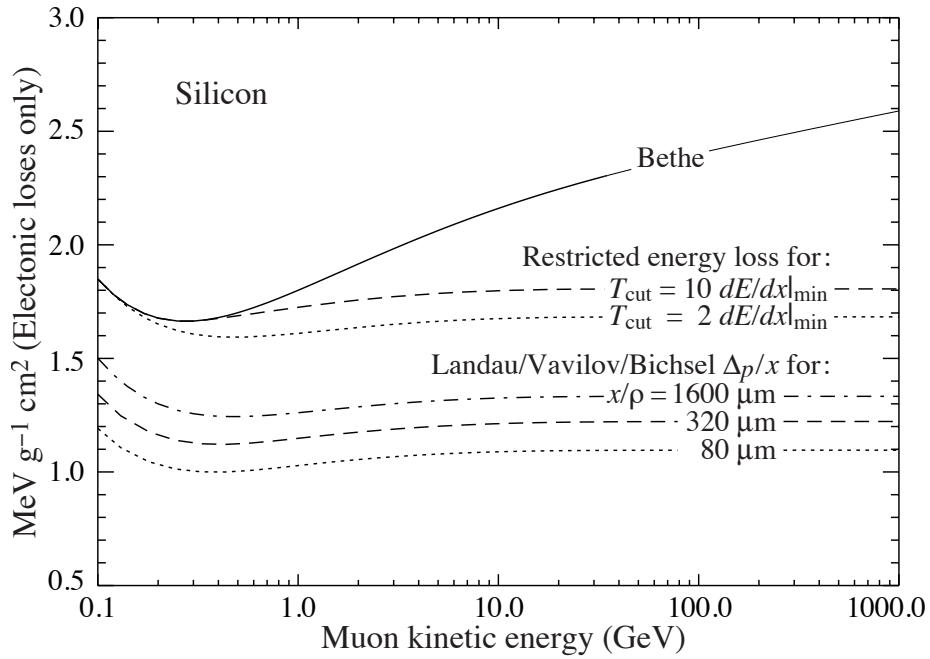


Figure 4.16: Bethe dE/dx , two examples of restricted energy loss, and the Landau most probable energy loss per unit thickness Δ_p/x in silicon. The change of Δ_p/x with thickness x illustrates its $a \log x + b$ dependence. Minimum ionization corresponds to $(dE/dx)_{\min} = 1.664 \text{ MeV cm/g}$. Radiative losses are excluded. The incident particles are muons. Figure taken from [20].

Figure 4.16 shows an example of the muon stopping power as a function of kinetic energy for the case of silicon. The Bethe curve is shown together with several other cases of *restricted energy-loss* for which the maximum energy-loss per collision was restricted to arbitrary cuts of $T_{\text{cut}} = 10 \times (dE/dx)_{\text{min}}$ and $T_{\text{cut}} = 2 \times (dE/dx)_{\text{min}}$, where $(dE/dx)_{\text{min}}$ is the stopping power for minimum-ionizing muons.

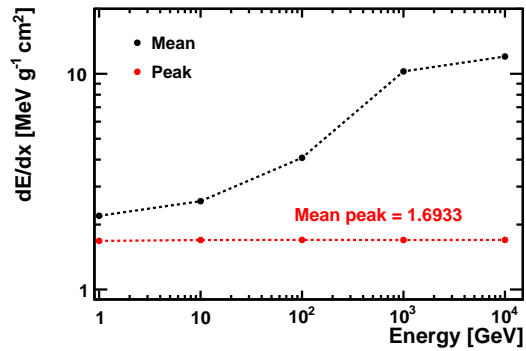
However, it is very easy to misuse the mean stopping power due to the fact that it is an average value that may include very rare events with large single-collision energy deposits that bias the mean toward the tail of the distribution. Even with samples of a few hundred events, the mean value can fluctuate substantially depending on whether these rare events exist in the sample or not making it an ill-defined value. Although the concept of restricted energy-loss alleviates this problem to some degree, it is much more reliable and consistent between different sample ensembles to use the most probable energy-loss. The most probable energy-loss is considerably lower than the mean energy-loss as can be seen in the Landau-Vavilov-Bichsel curves of the most probable energy loss Δ_p per medium thickness x in Figure 4.16.

Figure 4.17 shows the mean and most probable stopping powers for μ^+ particles in the KamLAND LS and BO simulated using the KLG4Sim Monte Carlo. The most probable peak values were fitted using a Landau distribution function which appears incredibly stable across a very large energy range of four orders of magnitude. The overall peak values were fitted as $(dE/dx)_{\text{LS}} = 1.6933 \pm 0.0076 \text{ MeV cm}^2/\text{g}$ for the LS and $(dE/dx)_{\text{BO}} = 1.7055 \pm 0.0076 \text{ MeV cm}^2/\text{g}$ for the BO.

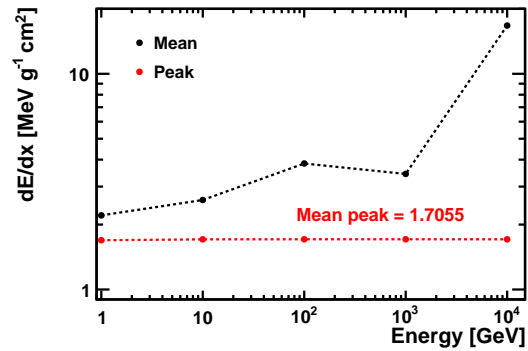
Using these peak dE/dx stopping power values, we can find the corresponding peak photoelectron yield per travel length $d(\text{p.e.})/dx$ of cosmic ray muons on a per-run basis to conduct an energy calibration. A muon track traversing a maximal distance through the KamLAND balloon loses energy ΔE of about

$$\Delta E = \left(\frac{dE}{dx} \right)_{\text{LS}} \rho_{\text{LS}} \phi_{\text{balloon}} \approx 1.7 \text{ GeV}, \quad (4.6.4)$$

where we used the most probable stopping power through the LS $(dE/dx)_{\text{LS}} = 1.6933 \text{ MeV cm}^2/\text{g}$, the LS density $\rho_{\text{LS}} \approx 0.778 \text{ g/cm}^3$, and the diameter of the balloon $\phi_{\text{balloon}} =$

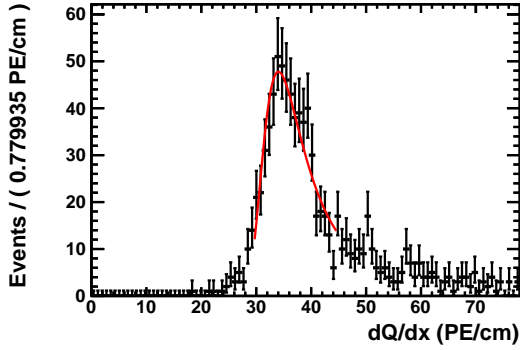


(a) Liquid scintillator (LS).

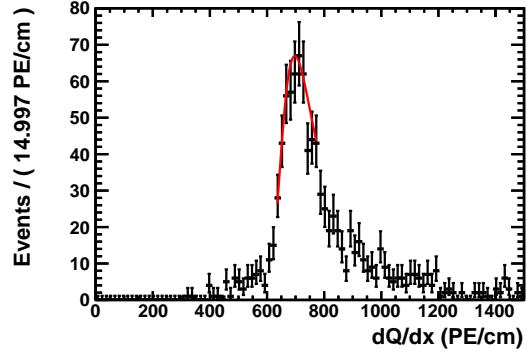


(b) Buffer oil (BO).

Figure 4.17: The mean and most probable peak values of the stopping power dE/dx for μ^+ simulated with Monte Carlo in the KamLAND (a) LS and (b) BO. The simulation was done only for five discrete energies indicated by the point markers, each using 10^5 events. The mean peak is the average of the five peak values which was determined to be $(dE/dx)_{\text{LS}} = 1.6933 \pm 0.0076 \text{ MeV cm}^2/\text{g}$ for the LS and $(dE/dx)_{\text{BO}} = 1.7055 \pm 0.0076 \text{ MeV cm}^2/\text{g}$ for the BO. The lines connecting the markers are shown solely for visual aid.



(a) Photon yield in the BO.



(b) Photon yield in the scintillator.

Figure 4.18: Distribution of charge deposition per track length dQ/dx in units of p.e./cm of 1000 cosmic ray muons traversing the BO (a) and scintillator (b) for a sample run using only the 17-inch PMTs. Both scintillation and Cherenkov components for photons emitted from inside the balloon are included in (b). Clear peaks can be seen for the respective fits that were done using Landau curves.

13 m. We are interested in energies of around 1 GeV to 20 GeV so this is fortunately at the energy scale of interest.

Figure 4.18 shows the distributions of charge per track length inside the scintillator and BO for scintillation and Cherenkov muons respectively. Both scintillation and Cherenkov components are included for the photon yield inside the balloon for scintillation muons. Figure 4.19 shows the distribution of charge per energy loss for the same sample of cosmic ray muon events. The muon energy loss was estimated using the reconstructed length of the muon track that overlaps with the BO or scintillator regions and their respective most probable stopping powers in the two media as shown in Figure 4.17.

Figure 4.20 shows the time evolution of the 17-inch PMT charge per muon energy loss for the distinct cases of when the muon is either in the LS or BO. This was calculated using the most probable photoelectron yield per track length similar to those shown in Figure 4.18 and the most probable muon stopping power as shown in Figure 4.17. Figure 4.21 shows a similar plot for scintillation muons traversing the balloon using the total estimated

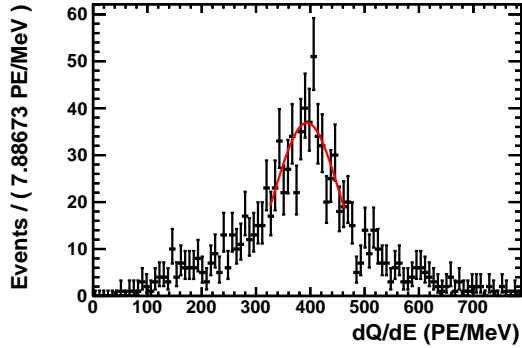
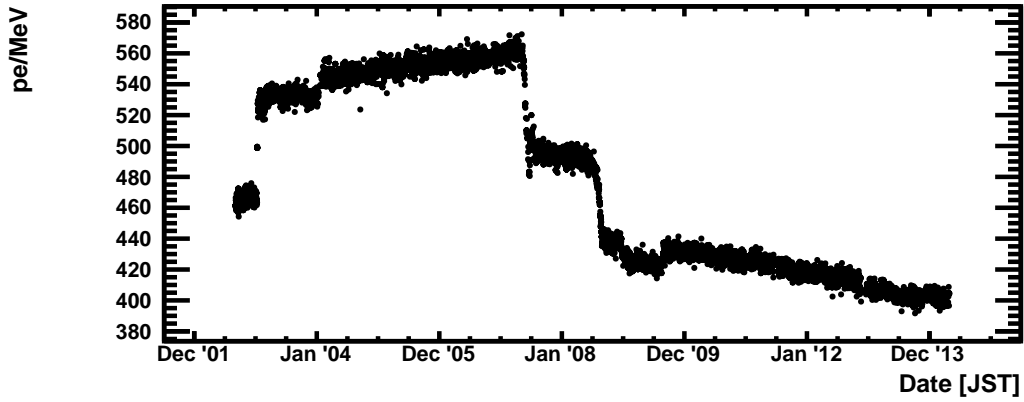


Figure 4.19: Distribution of charge deposition per energy loss dQ/dE in units of p.e./MeV of 1000 cosmic ray muons traversing the ID for a sample run using only the 17-inch PMTs.

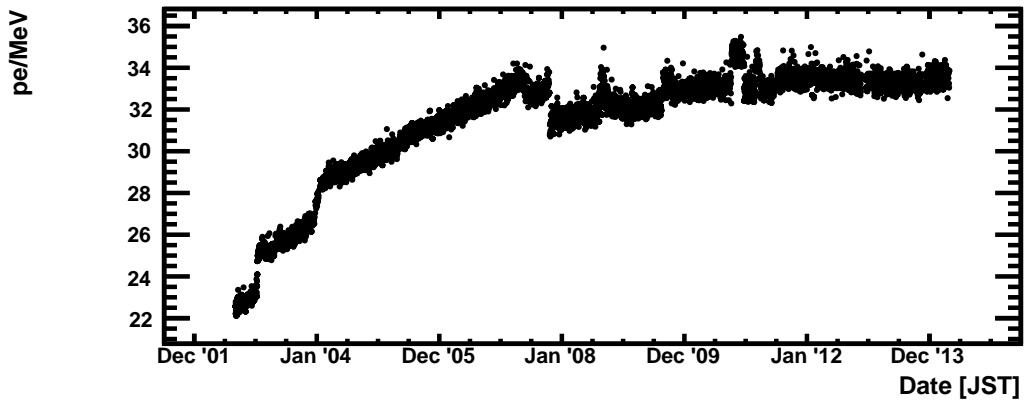
energy loss of the entire muon track inside the ID and the total charge deposit on the 17-inch PMTs. We will use this latter plot as our energy calibration due to the fact that high energy neutrino events that are fully contained within the ID will not always be contained within the LS balloon. Indeed Cherenkov photons from the BO region may contribute to the total charge deposit of the event, and we may under estimate the reconstructed energy if we were to assume that the charge deposition was entirely attributed to photons produced in the LS. There is no clear way to distinguish whether a given photon was produced in the LS or BO, and hence to distinguish how much of the total charge is due to photons produced in the LS or BO. Here we will naively assume contributions from each of the regions to be similar to that of the case of scintillation muons that traverse the entire ID.

4.7 Vertex reconstruction

Lower energy events on the order of a few MeV in KamLAND are highly localized both in space and in time, and are referred to as being *point-like* events. At these energies the event can be estimated to have taken place at a single point in four-dimensional space-time referred to as the *vertex*. The vertex essentially becomes a spatially isotropic source of photons which travel through the LS and BO mediums to eventually reach the PMTs lined around the outer perimeter of the inner detector. PMTs that register one or more photons



(a) 17-inch PMT charge deposition per energy loss of muons in the LS.



(b) 17-inch PMT charge deposition per energy loss of muons in the BO.

Figure 4.20: Shown are the evolution of the 17-inch PMT charge deposition in photoelectrons per MeV of muon energy loss in the (a) LS and (b) BO, both with respect to time in Japan Standard Time (JST).

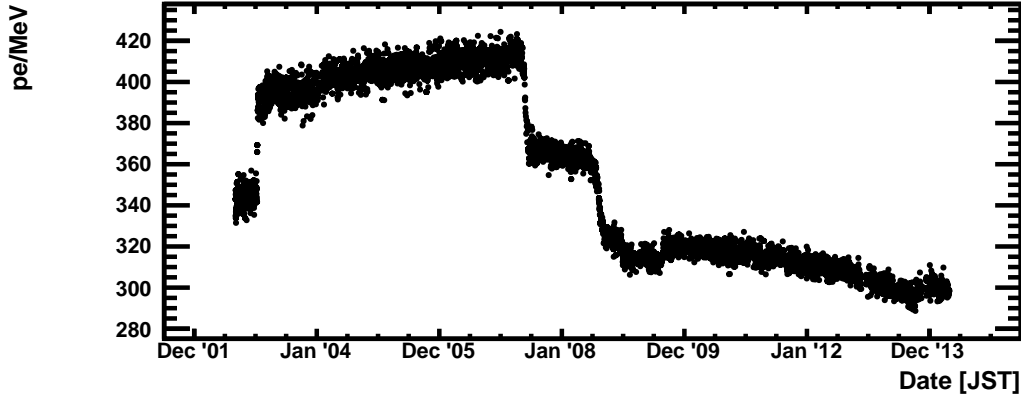


Figure 4.21: 17-inch PMT charge deposition per energy loss of scintillation muons traversing the ID. The energy loss is estimated using the entire muon track length through the LS and BO regions and the total charge deposit associated with the whole track inside the ID.

to induce a useful signal are said to have been *hit*. The information of when these PMT *hits* occur relatively in time is used to estimate the vertex.

The algorithm used for vertex reconstruction is explained below. Suppose an actual physical event took place in the inner detector at a vertex in space-time (t_0, x_0, y_0, z_0) . We would like to find the set of four parameters in space-time that best approximates this vertex. Different PMTs will receive photon hits at different times depending on how far away the vertex was from a given PMT. Taking a test vertex (t, x, y, z) , we can define the time-of-flight subtracted photon emission time t_i for the i -th PMT that received a hit

$$t_i(x, y, z) = t_i^{\text{hit}} - t_i^{\text{flight}}(x, y, z), \quad (4.7.1)$$

where t_i^{hit} is the photon hit-time, and $t_i^{\text{flight}}(x, y, z)$ is the time-of-flight ideally determined by

$$t_i^{\text{flight}}(x, y, z) = \frac{l_i^{\text{LS}}}{\left(\frac{c}{n_{\text{LS}}}\right)} + \frac{l_i^{\text{BO}}}{\left(\frac{c}{n_{\text{BO}}}\right)}, \quad (4.7.2)$$

both for the i -th PMT. Here c is the speed of light in vacuum with l_i^{LS} and l_i^{BO} being the respective photon travel lengths in the LS and BO mediums, both of which can be

determined from the location of the i -th PMT and (x, y, z) . n_{LS} and n_{BO} are respectively the refractive indices for the LS and BO. In practice, the time-of-flight t_i^{flight} is parameterized as

$$t_i^{\text{flight}} = \frac{\sqrt{(x - x_i)^2 + (y - y_i)^2 + (z - z_i)^2}}{\left(\frac{c}{n_{\text{eff}}}\right)}, \quad (4.7.3)$$

where n_{eff} is the effective index of refraction which inclusively represents all processes that may affect the average photon propagation speed in both the LS and BO. Note here that the actual hit-time t_i^{hit} for the i -th hit PMT is dependent on the registered charge on the said PMT due to slewing effects. These effects are corrected for as discussed in Section 4.2.

The vertex is estimated by locating the position (x, y, z) for which the deviation of the distribution of elements in the set of photon-emission times $\{t_i\}$ is minimized. This is accomplished through iteration of different test vertices for (x, y, z) . However, the set does not readily converge due to effects such as the spread in photon emission time of the LS with fast and slow decay time constants of $\tau_{\text{fast}} = 4.0$ ns and $\tau_{\text{slow}} = 8.6$ ns respectively, and the LS absorption-remission processes which may introduce an additional effective time constant on the order of ~ 50 ns.

Despite this problem, it is known that the distribution in the set $\{t_i\}$ is statistically independent from that of the set $\{dt_i/dx\}$. This can be expressed by the covariance $S_{t_i, \frac{dt_i}{dx}}$ of the two distributions being zero:

$$\begin{aligned} 0 = S_{t_i, \frac{dt_i}{dx}} &= \frac{1}{\sum_i w_i} \sum_i w_i (t_i - \langle t_i \rangle) \left(\frac{dt_i}{dx} - \left\langle \frac{dt_i}{dx} \right\rangle \right) \\ &= \frac{1}{\sum_i w_i} \sum_i w_i \left(t_i \frac{dt_i}{dx} \right) - \langle t_i \rangle \left\langle \frac{dt_i}{dx} \right\rangle, \end{aligned} \quad (4.7.4)$$

where

$$\begin{aligned} \frac{dt_i}{dx} &= \frac{d}{dx} \left(t_i^{\text{hit}} - t_i^{\text{flight}}(x, y, z) \right) \\ &= -\frac{d}{dx} \left(t_i^{\text{flight}}(x, y, z) \right) \\ &= \frac{x_i - x}{\left(\frac{c}{n_{\text{eff}}}\right) \sqrt{(x - x_i)^2 + (y - y_i)^2 + (z - z_i)^2}}, \end{aligned} \quad (4.7.5)$$

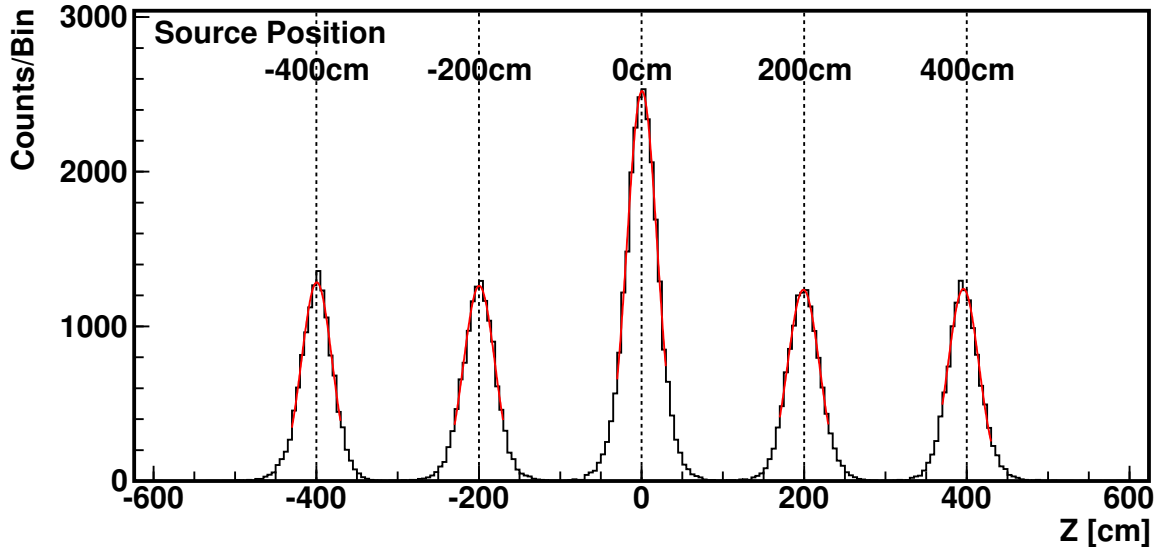


Figure 4.22: Distribution of reconstructed vertices for the ^{60}Co source located at different heights along the Z-axis. The position resolution was found to be around 20 cm with slight biases of on the order of a few centimeters near the top ($z = +400$ cm) and bottom ($z = -400$ cm) of the balloon. Figure taken from [35].

and w_i is a weighting factor that is a function of the photon traveling distance, and i is the index for the i -th hit PMT. Test vertices for (x, y, z) are iterated to find the best position where this condition is satisfied.

Figure 4.22 shows the distribution of reconstructed vertices using a ^{60}Co source placed at various heights along the Z-axis. The reconstruction resolution was found to be generally around 20 cm. The reconstruction biases were also measured with several calibration sources located at varying heights along the Z-axis as shown in Figure 4.23. Sources located within the range of $-5.5 \text{ m} < z < 5.5 \text{ m}$, show a vertex reconstruction bias of less than 5 cm at energies from around 12 MeV (Am-Be source) down to around 1 MeV (^{68}Ge and ^{65}Zn sources). The calibration sources used to measure the performance of the vertex fitter are listed in Section 4.7.

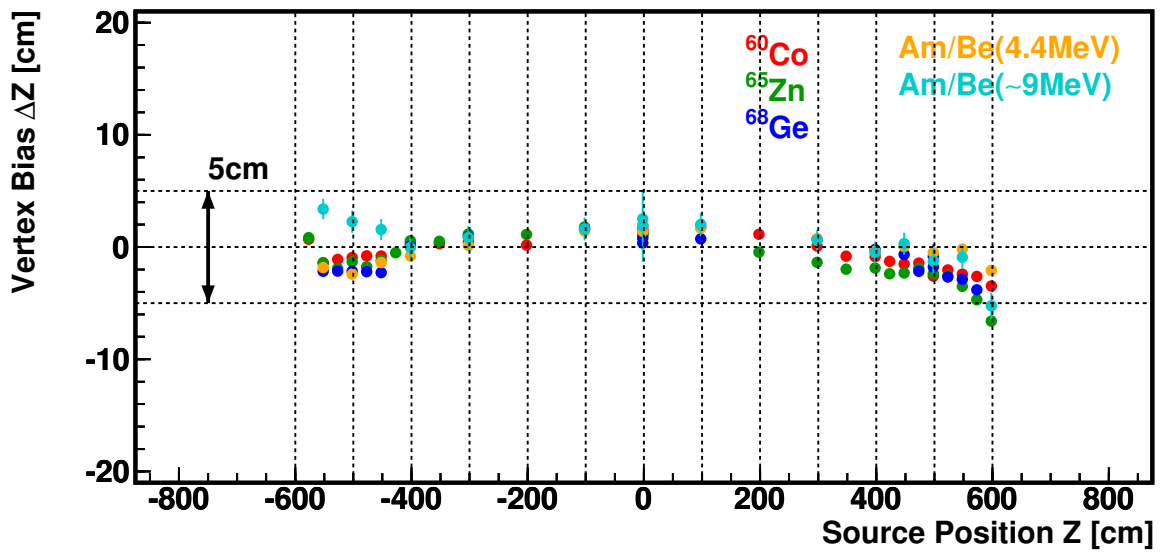


Figure 4.23: Vertex reconstruction bias ΔZ relative to the true source height for the sources ^{60}Co , ^{65}Zn , ^{68}Ge , and Am/Be sources with energies of 4.4 MeV and 9 MeV. The bias was found to be less than 5 cm at energies from around 12 MeV (Am-Be source) down to around 1 MeV (^{68}Ge and ^{65}Zn sources). Figure taken from [35].

Table 4.1: Radioactive sources used for measuring the resolution and bias for vertex reconstruction. Only the dominant decay mode is listed with the half-life denoted by $T_{\frac{1}{2}}$. Data reproduced from [16, 17].

Source	Dominant Decay Mode	Total γ Energy [MeV]
^{60}Co	$T_{\frac{1}{2}}=5.3\text{ yr} \rightarrow ^{60}\text{Ni}^* + e^- (0.317\text{ MeV})$	2.450
	$^{60}\text{Ni}^* \rightarrow ^{60}\text{Ni} + \gamma(1.117\text{ MeV}) + \gamma(1.333\text{ MeV})$	
^{65}Zn	$T_{\frac{1}{2}}=244.0\text{ d} \rightarrow ^{65}\text{Cu} + \gamma(1.116\text{ MeV})$	1.116
^{68}Ge	$T_{\frac{1}{2}}=271.0\text{ d} \rightarrow ^{68}\text{Ga}(0.11\text{ MeV})$	1.022
	$T_{\frac{1}{2}}=67.8\text{ min} \rightarrow ^{68}\text{Zn} + e^+ (1.899\text{ MeV})$	
	$e^+ + e^- \rightarrow \gamma(0.511\text{ MeV}) + \gamma(0.511\text{ MeV})$	
Am-Be	$T_{\frac{1}{2}}=432.6\text{ yr} \rightarrow ^{237}\text{Np} + ^4\text{He}(5.486\text{ MeV}) + \gamma(7.653\text{ MeV})$	12.091
	$^4\text{He} + ^9\text{Be} \rightarrow ^{12}\text{C} + n(\sim 6\text{ MeV}) + \gamma(4.438\text{ MeV})$	

4.8 Neutrino directionality

4.8.1 Overview

One of the disadvantages of neutrino detectors that use a scintillating medium as the target material, such as KamLAND, have in comparison to water-Cherenkov detectors is the inability to discern the direction from which a given detected neutrino came from. This is due to the isotropic production of scintillation light that is emitted from all points of ionization in the scintillating medium. In contrast, Cherenkov light produced in, for example water, is emitted from a charged particle track in the forward direction at the Cherenkov angle (about 45°) with respect to the track direction. An example ring pattern created by PMTs that solely detected Cherenkov photons in the Super-Kamiokande (SK) experiment is shown in Figure 4.24. When there is no other radiation, the Cherenkov photons provide a clean signature that explicitly shows the direction of the charged particle. However, in the presence of scintillation photons, given a large enough number, the earliest among them will partially coincide with the Cherenkov photons both in space and time effectively smearing out the directional information. This effect has led to the conventional view that scintillator detectors are more or less calorimeters in which analysis is solely conducted using the reconstructed event energy. Figure 4.32 shows a diagram depicting the Fermat surface created by the earliest scintillation light that is isotropically emitted from a fully contained lepton track inside the ID.

4.8.2 Neutrino-nucleon interaction

In order to successfully observe dark matter annihilation induced neutrinos, directional information is necessary in order to distinguish those that originate from a gravitational potential well of interest (can be either Earth or Sun) from those coming from other sources. Here we introduce an algorithm to determine the incoming neutrino direction at energies of about 1 GeV and greater. At these relatively high energies, the interaction of the neutrino with its target does not solely occur through the well-known *inverse beta decay* (a type of quasi-elastic scattering process) which KamLAND generally observes at lower energies of a few MeV and involves relatively simple two-body kinematics as shown

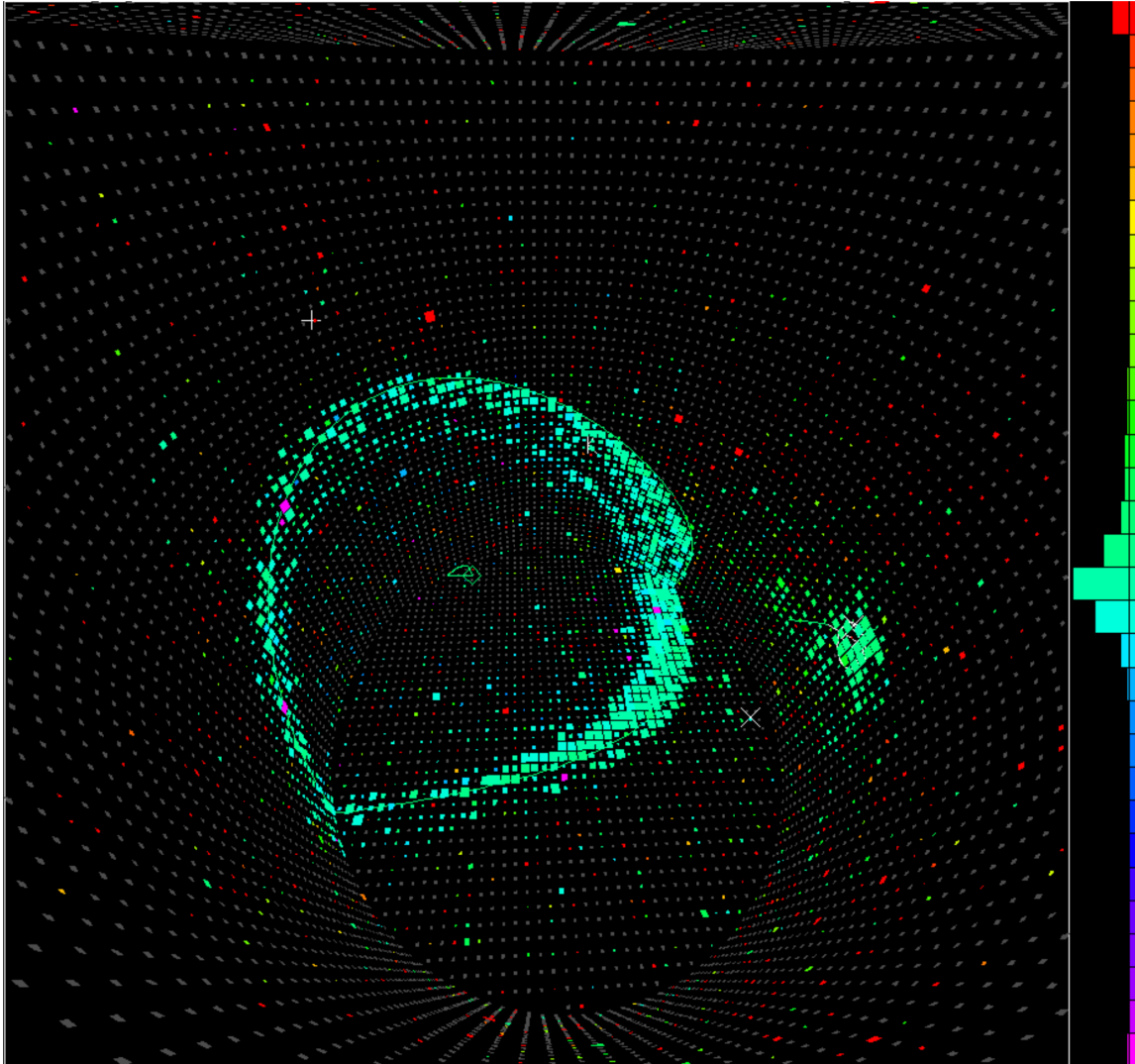


Figure 4.24: Projected circular ring patterns shown in the Super-K event display. The patterns are produced by Cherenkov radiation emitted from a charged particle track in the forward direction at the Cherenkov angle with respect to the track direction. The patterns are used to discern the final-state lepton direction coming from neutrino nucleon interaction thus effectively letting one infer the direction from which the neutrino originated. Figure taken from [76].

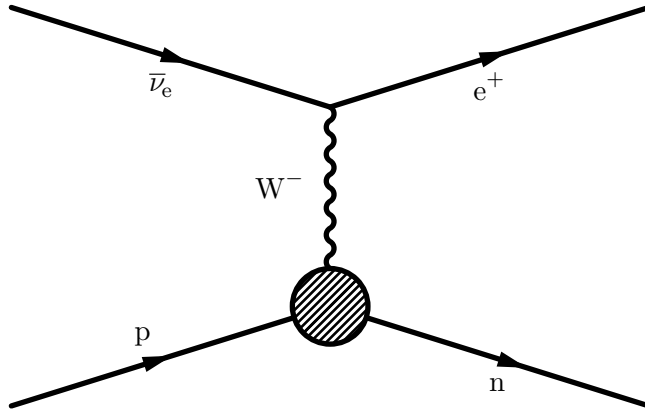


Figure 4.25: The well known IBD process that KamLAND traditionally utilizes to search for electron type anti-neutrinos $\bar{\nu}_e$. The incoming $\bar{\nu}_e$ interacts with a proton p inside of the detector medium through exchange of a W^- boson producing a positron e^+ and a neutron n in the final state.

in Figure 4.25. In contrast, neutrinos with higher energies at the $\sim\text{GeV}$ scale may interact through other processes that have more complicated kinematics with a greater multiplicity in the number of final state particles such as *resonant secondary particle production scattering* processes or *deep inelastic scattering* interactions where the incoming neutrino may interact with individual partons inside of a nucleon that comprises the nucleus. These partons would eventually hadronize in the final state leaving behind a remnant nucleus. Diagrams showing examples of these processes that occur at energies of a few GeV are shown in Figure 4.26.

Figure 4.27 shows the total cross sections for charged current neutrino interaction on target nuclei in the atomic components that constitute the LS ^1H , ^{12}C , ^{14}N , and ^{16}O . The cross sections are shown for the four neutrino flavors of ν_e , $\bar{\nu}_e$, ν_μ , and $\bar{\nu}_\mu$. Cross sections for the same four neutrino flavors to interact through quasi-elastic scattering, resonant production scattering, and deep inelastic scattering on nucleons in ^1H and ^{12}C are respectively shown in Figures 4.28 and 4.29.

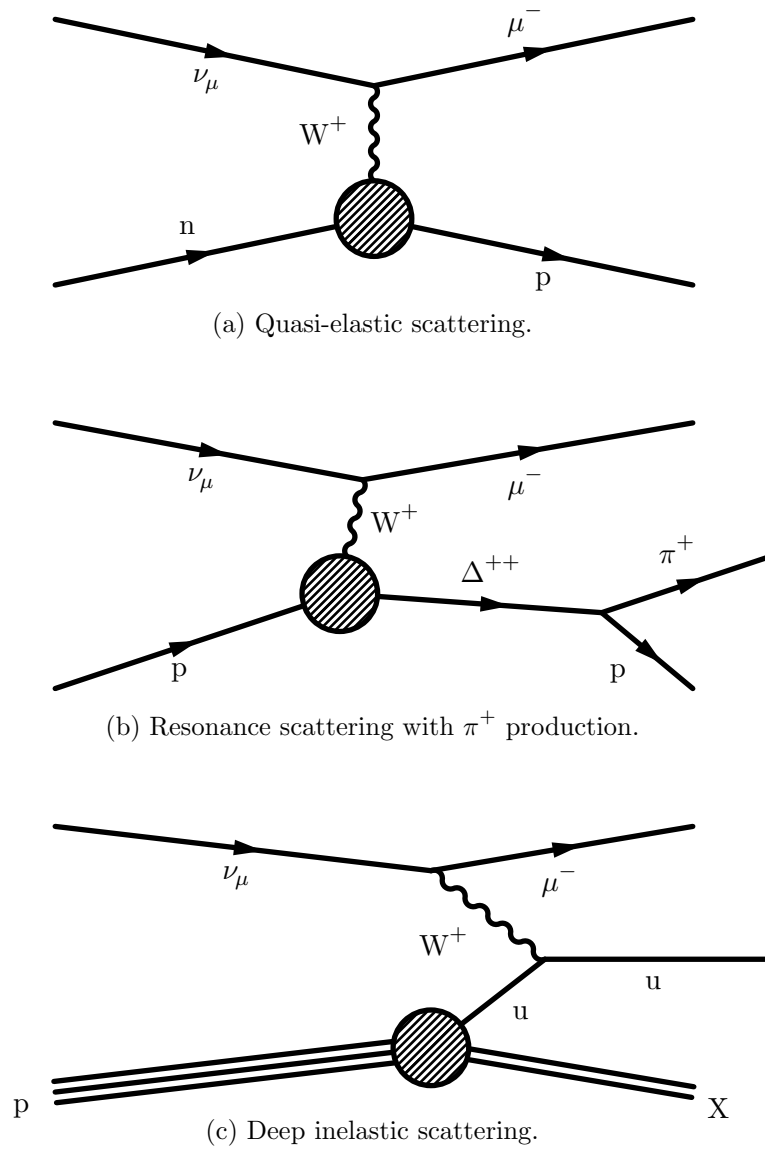
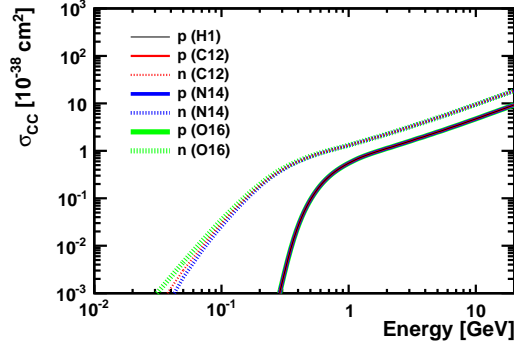
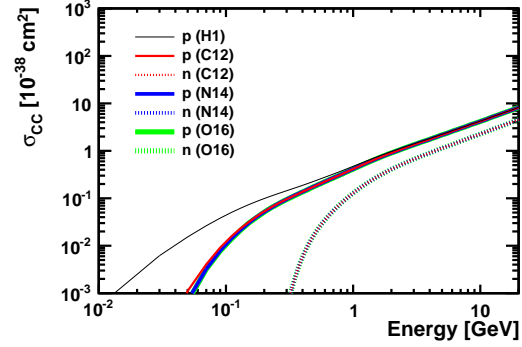


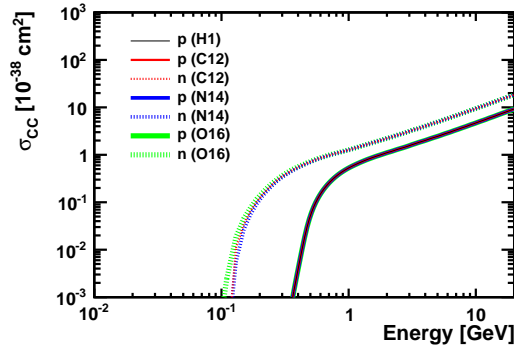
Figure 4.26: Feynman diagrams depicting processes for ν_μ interacting with nucleons p, n. The top figure shows quasi-elastic scattering of ν_μ on n through exchange of a W^+ (a). The middle figure shows a similar interaction on p producing an intermediate Δ^{++} with an extra π^+ in the final state (b). The bottom figure shows an example case where the ν_μ had a high enough energy to interact with an individual parton (in this case a u quark) inside of the p which eventually hadronizes leaving behind the remnant nucleus X (c).



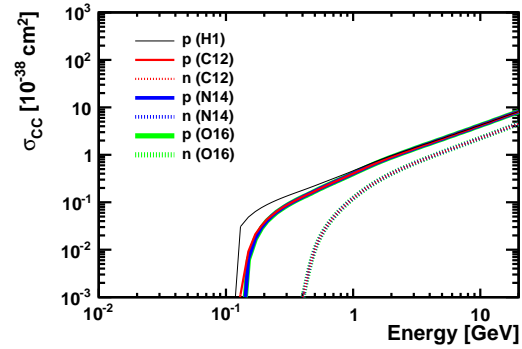
(a) ν_e .



(b) $\bar{\nu}_e$.

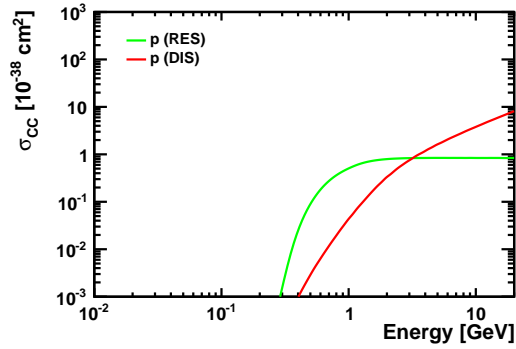


(c) ν_μ .

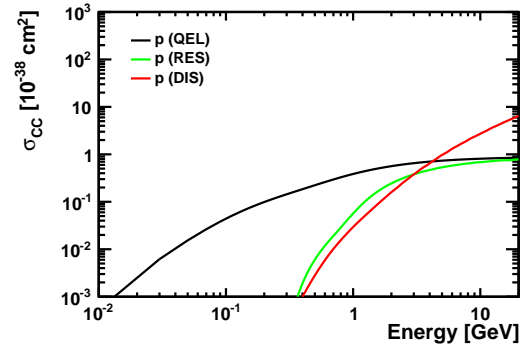


(d) $\bar{\nu}_\mu$.

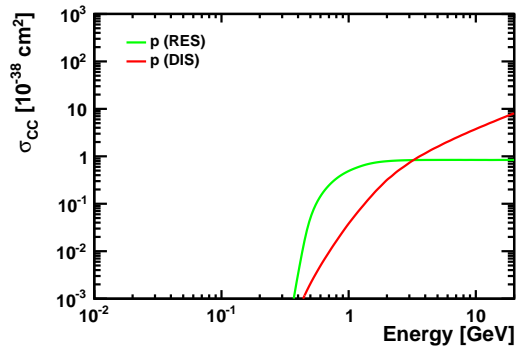
Figure 4.27: Total charged current scattering cross sections σ_{CC} for neutrinos of flavor ν_e (a), $\bar{\nu}_e$ (b), ν_μ (c), and $\bar{\nu}_\mu$ (d) on target nucleons p (proton) and n (neutron). Target nucleons are shown for the four elements that constitute the LS in the Kamioka Liquid Scintillator Antineutrino Detector (KamLAND): ^1H , ^{12}C , ^{14}N , and ^{16}O . Plots reproduced from the Generates Events for Neutrino Interaction Experiments (GENIE) Monte Carlo neutrino event generator [10].



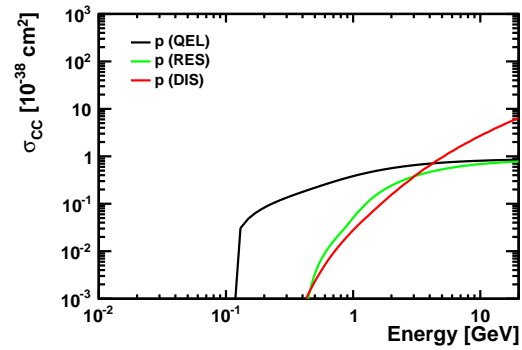
(a) ν_e .



(b) $\bar{\nu}_e$.

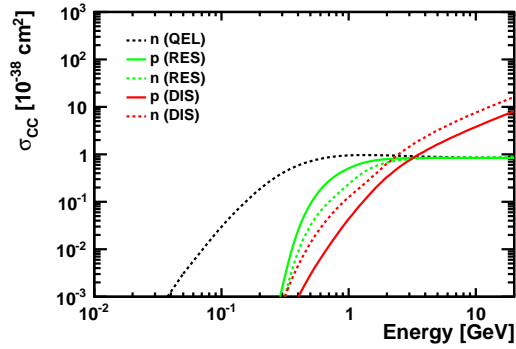


(c) ν_μ .

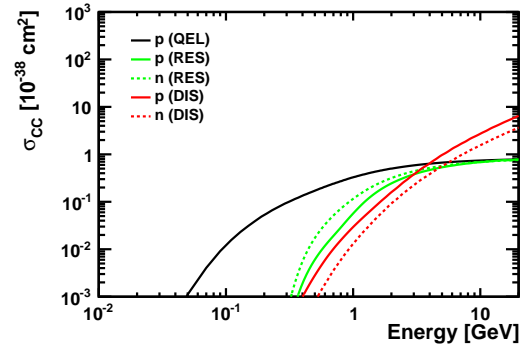


(d) $\bar{\nu}_\mu$.

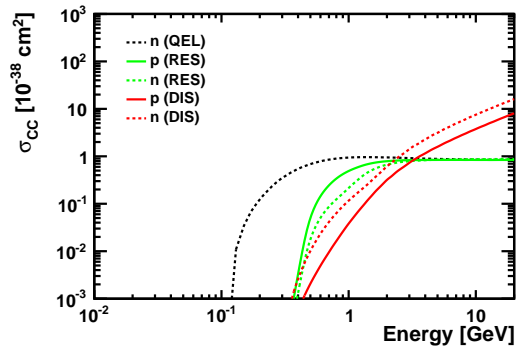
Figure 4.28: Charged current scattering cross sections for ν_e (a), $\bar{\nu}_e$ (b), ν_μ (c), and $\bar{\nu}_\mu$ (d) on proton (p) in Hydrogen nuclei. Cross sections are shown for the three types of scattering processes quasi-elastic scattering (QEL), resonant scattering (RES), and deep inelastic scattering (DIS).



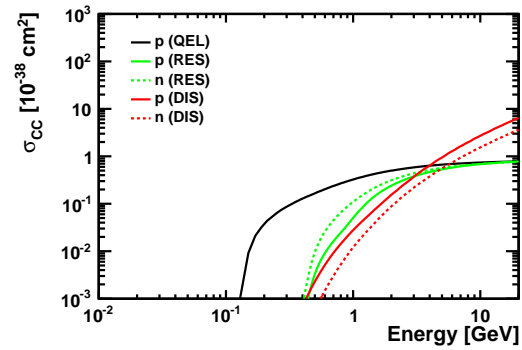
(a) ν_e .



(b) $\bar{\nu}_e$.



(c) ν_μ .



(d) $\bar{\nu}_\mu$.

Figure 4.29: Charged current scattering cross sections for ν_e (a), $\bar{\nu}_e$ (b), ν_μ (c), and $\bar{\nu}_\mu$ (d) on nucleons p (proton) and n (neutron) in Carbon nuclei. Cross sections are shown for the three types of scattering processes quasi-elastic scattering (QEL), resonant scattering (RES), and deep inelastic scattering (DIS).

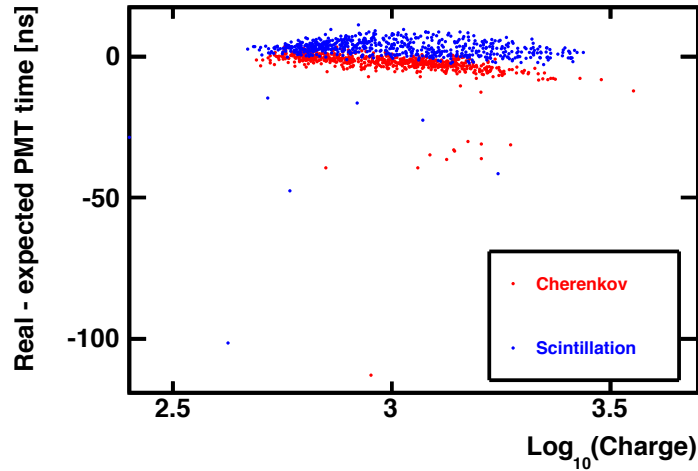


Figure 4.30: PMT first-hit time relative to expected first-hit time versus PMT charge for a single example muon event. The photon hits were classified as being due to Cherenkov or scintillation light depending on whether the position of a given PMT was within the spatial coverage of the Cherenkov cone.

4.8.3 PMT pre-pulsing

The conventional method of detecting photon hits at a PMT is through amplification of the photoelectron signal that is produced by the photocathode through the photoelectric effect. However, there is a small but finite probability that a given photon may tunnel through the photocathode surface and interact directly with the dynode structure inside of the PMT producing a *hit* signal that is appreciably earlier than compared to if the signal had been produced by a photoelectron. This is called PMT pre-pulsing.

The effective number of photons produced per unit energy deposited in the detector is about 8300 photons/MeV, and the number of photons arriving at each PMT monotonically increases with energy deposition in the ID. If the photons are abundant enough, pre-pulsing can be readily observed for example in the case of cosmic ray muon events that have a high photon yield. This is shown in Figure 4.30 depicting the PMT first-hit time relative to the expected first-hit time versus PMT charge for a single sample muon event. The photon hits were categorized as being due to Cherenkov or scintillation light depending on whether the position of a given PMT was within the spatial coverage of the Cherenkov cone calculated

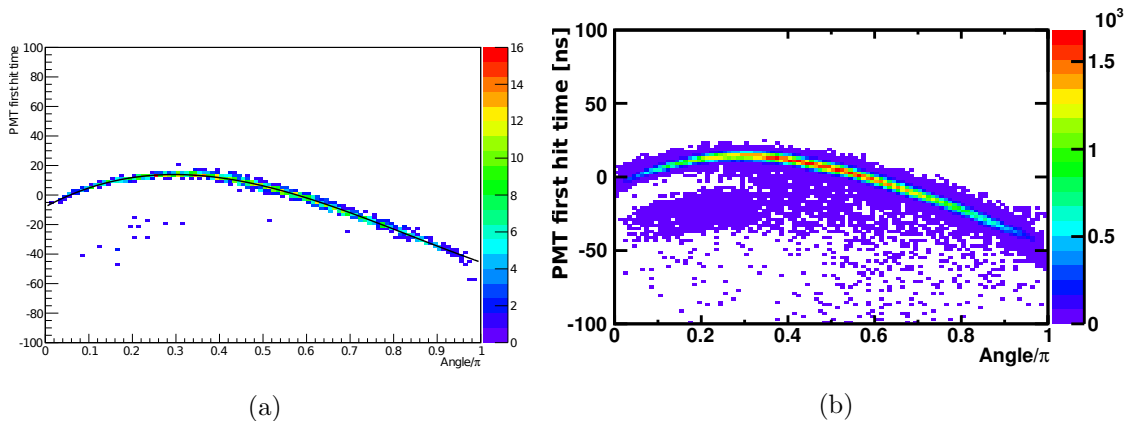


Figure 4.31: Two figures showing PMT pre-pulsing phenomenon in high photon yield cosmic-ray muon events. (a) shows the PMT earliest hit time versus the angle between two vectors. The first being the vector connecting the muon track mid-point and a given PMT, and the other, the vector coinciding with the direction of the muon track. Some abnormally early hit times compared to the majority can clearly be seen. (b) shows an identical plot with 204 muon events overlaid in order to better emphasize the pre-pulsing effect seen at around $0.1 \lesssim \text{angle}/\pi \lesssim 0.3$.

using the Cherenkov angle. In the ideal case the distribution of the data points should be a flat line across all energies. However there are several photons that seem to be arriving distinctly earlier than they should be as shown by the markers below the flat red and blue lines.

These were further confirmed to be due to pre-pulsing and not be caused by random noise or dark hits as demonstrated in Figure 4.31. Data from a single and 204 through-going muon events were examined, and a clear arch can be seen peaking in distribution where the majority of the first-hit photons are concentrated. The abnormally early hits seem to be concentrated at a region of about 20 ns to 40 ns earlier than the expected first-hit times and within angles of around 0π to 0.4π . This is an indicator that the early hits occur most often when the photons arrive at angles near the normal angle with respect to the PMT photocathode surface. The directional orientation of the early hit photons along with the

time scale at which this occurs most prominently is consistent with what is expected for pre-pulsing.

4.8.4 Neutrino directionality algorithm

As seen above, there are many issues associated with extracting the directional information of an incoming neutrino from a given event in the ID. The Cherenkov photons preserve the directional information and can be readily utilized to infer directionality in water-Cherenkov detectors such as Super-Kamiokande, but get smeared out by the earliest scintillation light in LS. At the conventional neutrino energies of around \sim MeV, the interaction cross section is largely dominated by quasi-elastic scattering processes such as inverse beta decay. However, at higher energies of on the scale of \sim GeV, cross sections for interactions with non-trivial kinematics such as resonant particle production scattering and deep inelastic scattering start to rise sharply and take over above a few GeV. The complicated kinematics and high multiplicity of final state particles poses a problem for discerning the neutrino direction. The abundance of photons in large numbers at high energies increases the probability of abnormal PMT hit times necessitating a directional fitter that is robust against such statistical outliers.

Such issues lead us to take a step back and develop a directional technique that views the event as a whole rather than scrutinizing individual final state particle tracks. There are two types of information that can be extracted from a given event through the PMTs. One is the time of photon arrival and the other is the charge. These two pieces of information can be exploited along with the position information of where the PMTs are located by calculating a *center of charge* and *center of time*. Figure 4.32 shows an example diagram where these two points in space are being employed in an extremely simplified case scenario of an event consisting of a single fully contained charged lepton track that originated and terminated entirely inside the ID. The two points can then simply in principle be connected to find the direction of the single lepton track.

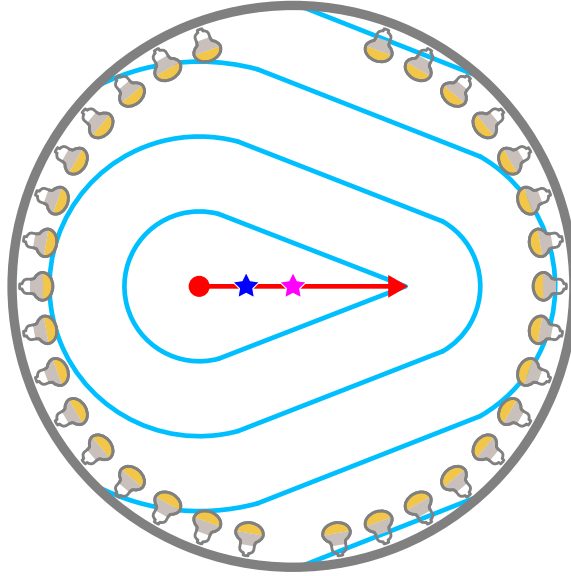


Figure 4.32: Conceptual diagram depicting the simple case scenario of a fully contained straight track of a charged lepton in the spherically shaped KamLAND ID. The red arrow indicates the lepton track where the red dot indicates the beginning of the track and the tip of the arrow, the end of the track. The gray circle represents the spherical stainless steel tank of which the inner surface is aligned with PMTs facing the center of the ID. The light-blue lines represent the three-dimensional surface (Fermat surface) created by the earliest photons emanating from the track, each at subsequently later times as the photons isotropically propagate outward. The Fermat surface can include photons from both Cherenkov and scintillation processes. The *center of the charge* indicated by the magenta colored star will naturally be very close to the middle point of the red lepton track. The *center of time* indicated by the blue colored star lies also along the track, but slightly more biased toward one end of the track.

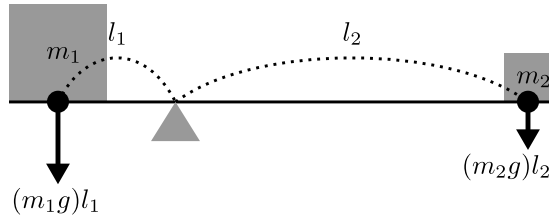


Figure 4.33: Two square block masses m_1 and m_2 on a horizontal plank, each at a respective distance of l_1 and l_2 from the center of gravity. The point of the plank corresponding to the center of gravity is supported by a triangle shaped fulcrum. Gravitational force acting on the two masses, depicted by the downward arrows, creates torque with magnitudes $(m_1g)l_1$ and $(m_2g)l_2$ with respect to the center of gravity. g is the gravitational acceleration constant.

The center of charge and center of time are essentially weighted mean values taken in three-dimensional space with the formula

$$\frac{\sum_i^{N_{\text{PMT}}} w_i \mathbf{x}_i}{\sum_i^{N_{\text{PMT}}} w_i}, \quad (4.8.1)$$

where i indexes all the N_{PMT} number of PMTs that will be used in the calculation, and w_i and \mathbf{x}_i are respectively the corresponding weight and position for the i -th PMT. A question arises here where one can ask what is the proper weight w_i to use in calculating the center of charge or time. To better illuminate the derivation we will first allude to the concept of center of gravity shown in Figure 4.33. The center of gravity is the point in space where the net torque τ_{net} created here by gravitational force acting on masses m_1 and m_2 vanishes,

$$\begin{aligned} \tau_{\text{net}} &= \tau_1 + \tau_2 \\ &= 0, \end{aligned} \quad (4.8.2)$$

where τ_1 and τ_2 are respectively the torque on masses m_1 and m_2 so rewriting the equation gives

$$-(m_1g)l_1 + (m_2g)l_2 = 0. \quad (4.8.3)$$

Dividing both sides of the equation by g , we get

$$-(m_1)l_1 + (m_2)l_2 = 0. \quad (4.8.4)$$

It can be explicitly seen in here where the values inside the parentheses can be regarded as the weight coefficients with regards to the distance. Therefore the correct weight that must be used in calculating the center of gravity is *mass*:

$$w_i = m_i. \quad (4.8.5)$$

We can likewise deduce what the correct weight should be for the center of charge and time. Figure 4.34 shows an analogical diagram to the case of center of gravity, but for the case when there is an isotropic flash of light at some location between two PMTs. First let us look at the center of charge as shown in Figure 4.34a. It is well known that the charge received by a PMT is inversely proportional to the square of the distance of the particular PMT to the origin of the flash of light:

$$q_1 \propto \frac{1}{l_1^2}, \quad q_2 \propto \frac{1}{l_2^2}, \quad (4.8.6)$$

or equivalently

$$\sqrt{q_1} \propto \frac{1}{l_1}, \quad \sqrt{q_2} \propto \frac{1}{l_2}. \quad (4.8.7)$$

Multiplying each relation by its corresponding distance and combining the two contributions, we get

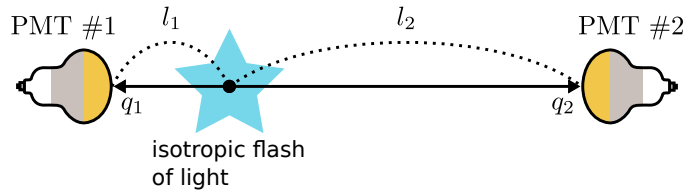
$$-(\sqrt{q_1})l_1 + (\sqrt{q_2})l_2 = 0. \quad (4.8.8)$$

Here we can see the coefficients multiplied with the distances is the square-root of charge. Hence this is the weight to be used in the center of charge:

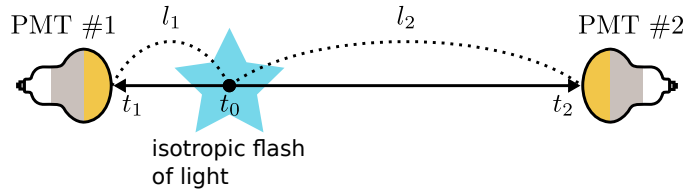
$$w_i = \sqrt{q_i}. \quad (4.8.9)$$

Following a similar logic, we can also derive the weight for the center of time as shown in Figure 4.34b. The arrival time of the earliest photons at a given PMT from the isotropic flash of light is proportional to the distance from the PMT to the origin of the flash

$$\Delta t_1 = \frac{l_1}{c}, \quad \Delta t_2 = \frac{l_2}{c}, \quad (4.8.10)$$



(a) Isotropic flash of light at unequal distances from PMTs #1 and #2. l_i is the distance from the i -th PMT to the origin of the isotropic flash of light depicted by the large blue star. q_i is the total charge accumulated by the i -th PMT.



(b) Isotropic flash of light at unequal distances from PMTs #1 and #2. l_i is the distance of the i -th PMT to the origin of an isotropic flash of light depicted by the large blue star. t_0 is the point in time when the flash occurs with t_i being the time in which the earliest photons from the flash arrive at the i -th PMT.

Figure 4.34: Simplified case scenarios for calculating the center of charge (a) and center of time (b).

where we have defined the lifetime of the photon to be $\Delta t_i \equiv t_i - t_0$, for t_0 being the time of when the flash occurred, t_i the arrival time of the earliest photon at the i -th PMT, and c the constant speed of light in the medium. Dividing both relations by the corresponding photon lifetime Δt , we can combine the two contributions to get

$$-\left(\frac{1}{\Delta t_1}\right)\frac{l_1}{c} + \left(\frac{1}{\Delta t_2}\right)\frac{l_2}{c} = 0, \quad (4.8.11)$$

or equivalently by ignoring the constant c ,

$$-\left(\frac{1}{\Delta t_1}\right)l_1 + \left(\frac{1}{\Delta t_2}\right)l_2 = 0. \quad (4.8.12)$$

Again it is clear here that the coefficients multiplied with the distance is the inverse of time so, although a bit surprising, this is the correct weight to use in the center of time:

$$w_i = \frac{1}{\Delta t_i}, \quad \Delta t_i \equiv t_i - t_0. \quad (4.8.13)$$

Here, one qualification must be made for t_0 in the inverse of time. t_0 is the time at which the first photons from the isotropic flash of light are created in our simple example. This is easy to comprehend in the case of neutrino energies at the \sim MeV scale where the event profile is more or less point-like. However, at energies of around GeV and greater, the profile is no longer point-like but often times elongated due to the longer travel distances of the final state particles. At these higher energies t_0 is more difficult to define and, for the sake of this algorithm, it was defined as the most probable photon emission time if the event were estimated to be point-like using the generic KamLAND vertex fitter used in lower energy analysis. In other words, despite the fact that the profile may not be point-like, the vertex fitter was used to first establish an estimated vertex, which was usually fitted to be somewhere near the middle of the final state lepton track. Once the vertex is fitted, a time-of-flight can be calculated for photons propagating from the hypothetical vertex to each of the PMTs. Then the time-of-flight subtracted earliest PMT hit times were tallied in a histogram to find the most probable peak. Finally this peak was fitted and used to define t_0 .

The process explained here to find t_0 was necessary not only to simplify the algorithm to be able to use a single value for t_0 , but also to make sure that the method

would be robust against statistical outliers such as abnormal PMT hit times due to pre-pulsing explained in Section 4.8.3. This point was crucial in the construction of this technique.

Although the algorithm presented above was developed assuming the event consists entirely of a single particle track, the method is still applicable for multiple tracks in which there is a relatively localized charge deposit and an overall net momentum such as in the case of an event composed of multiple final state particles in a neutrino interaction. This claim will be validated later.

One of the advantages that the technique developed in this section for directionality has in comparison to other techniques is that it is *not* a fitter in the sense that there is no iterative process in the calculation (except for when t_0 is fitted). The entire calculation is merely taking a weighted mean of a few thousand numbers. This is practically instantaneous in terms of CPU time with modern day computing power, and therefore can potentially be employed in on-line real-time analysis. In addition, it can serve as a simple check to validate more complicated techniques that may require more time to conduct off-line.

One of more common approaches taken in directionality algorithms for physics experiments in general is to reconstruct an event image where individual particle tracks associated with an interaction vertex are drawn out in spatial coordinates to better understand it from a visual perspective. An example of this sort of technique will be presented later. However, it is also often the case that these spatial maps take longer to analyze and may even have a degeneracy in the direction of the traveling particle that created the track. In other words, a map of a given particle position integrated through time as the particle moves about, may have difficulties in incorporating directional information. The algorithm shown here can serve as an easy and accurate way to break this degeneracy.

4.8.5 Validation of neutrino directionality

We would like to verify the particle directionality algorithm developed in Section 4.8.4 using the resources presently available. Figure 4.35 shows the agreement of the method with respect to the generic KamLAND muon fitter for 1000 through-going cosmic-ray muon events from a given sample run. There is fairly good agreement between

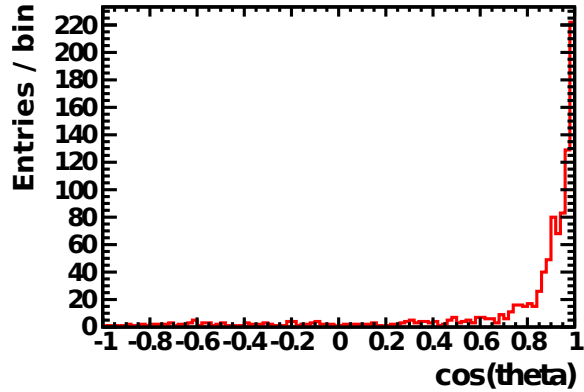


Figure 4.35: Agreement between the neutrino directionality algorithm and the generic KamLAND muon fitter tested against data from 1000 cosmic-ray muon events in a sample run. $\cos(\theta) = 1$ indicates total agreement between the two methods while $\cos(\theta) = -1$ indicates a total disagreement of 180° .

the two techniques, although it must be stated that the muon fitter is generally the more reliable of the two when fitting muon tracks. This was verified through the zenith angle distribution of reconstructed cosmic-ray muon directions, which falls off appropriately at the horizon for the muon fitter but does not vanish cleanly for the directional neutrino algorithm. This is simply attributed to the fact that the muon fitter was specifically designed to fit long muon tracks fully traversing the detector.

Validation with Monte Carlo

The neutrino directionality method was tested in Monte Carlo simulation with the full detector response for neutrino events using the KamLAND Geant4 Simulation (KLG4Sim) and GENIE. Figure 4.36 shows the results for charged current interactions of electron-type neutrinos with Hydrogen and Carbon nuclei in the KamLAND LS and BO. The neutrino direction was reconstructed and compared against the true neutrino direction and plotted with respect to the range of true neutrino energies 0.1 GeV to 5 GeV. The vertical white band below about 500 MeV devoid of any events in Figure 4.36a is due to the fact that the interaction $\nu_e + {}^1\text{H} \xrightarrow{\text{CC}} e^- + (?)$ necessitates multiple positively

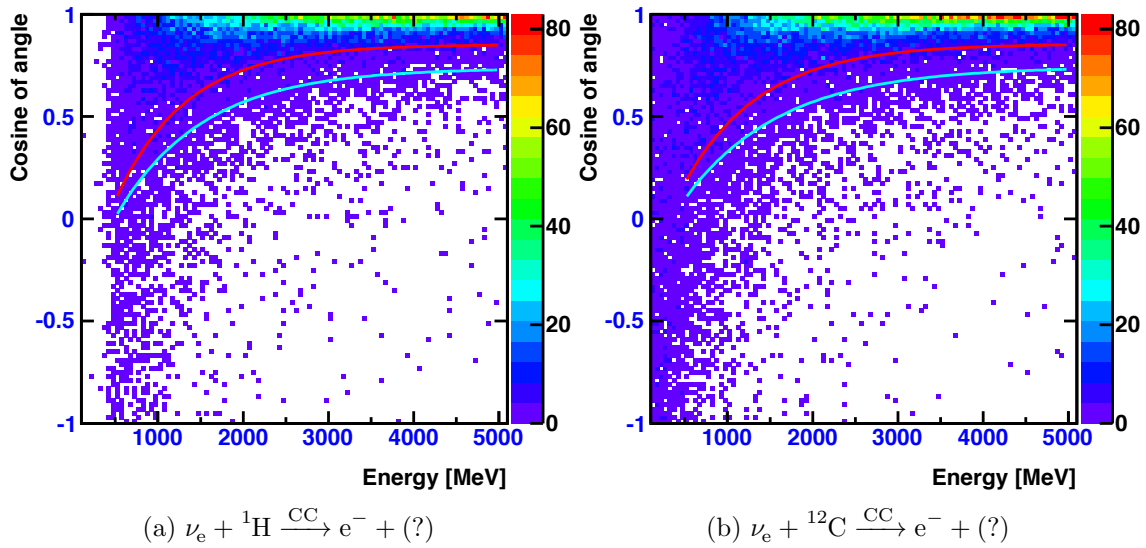


Figure 4.36: Two dimensional histograms showing Monte Carlo simulation results for the agreement between the reconstructed and the true neutrino direction for charged current interactions of ν_e on nuclei (a) ${}^1\text{H}$ and (b) ${}^{12}\text{C}$ in the KamLAND LS. The red and cyan lines respectively indicate the 1σ edge of distribution of the reconstructed neutrino angles and the true final state lepton angles with respect to the true neutrino direction coinciding with $\cos(\theta) = 1$. Note that on average the fitter does better than if one solely analyzed the lepton direction in estimating the neutrino direction. The fitter reaches an improvement of about 10° above 1.5 GeV.

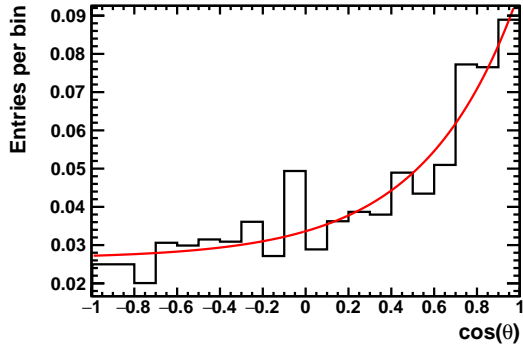
charged final state particles to maintain charge conservation, which only begins to have a non-negligible cross section at higher energies. The reconstructed neutrino direction improves monotonically with energy shown by the red curve indicating the 1σ edge of the distribution of the reconstructed neutrino angles with respect to the true neutrino angle coinciding with $\cos(\theta) = 1$. The cyan curve shows the 1σ edge of the true final state lepton angle and it is clearly seen that the reconstructed neutrino angle is consistently better than this above an energy of 0.5 GeV. The difference reaches an improvement of about $\sim 10^\circ$ at 1.5 GeV and above! The events were selected by requiring the reconstructed vertex to be within a radius of 6 m from the center of the ID, and the simulation was conducted using only ideal fully contained events by excluding events that produced any non-photon particles that traveled outside of a 8.5 m radius.

Neutrino directionality was also tested with Monte Carlo with a more sparse energy resolution but using a wider range of energies and employing a more realistic scenario where the inefficiency of the OD was taken into account. A sample of these results for neutrino energies of 1 GeV, 10 GeV and 100 GeV are shown in Figures 4.37 to 4.40. In order to account for the time dependent OD inefficiency due changing status of the number of dead OD PMTs with respect to time, the results were averaged over the OD PMT statuses of 12 arbitrarily selected runs with numbers 1313, 2001, 3000, 4000, 5005, 6022, 7002, 8000, 9000, 10 000, 11 000 and 12 002. These runs were selected among good runs to be as uniformly distributed as possible throughout the detector live time. The reconstructed directional resolution is seen to clearly worsen at the highest simulated energies of 100 GeV where most of the events will not be fully contained. Those that are falsely perceived to be fully contained will be due to the inefficiency of the OD attributed to the dead OD PMTs and to the thin OD geometry in the vicinity of the detector equator. Events that are falsely identified to be fully contained events will be biased in their directional reconstruction as the full event information is not available to the ID PMTs to interpret.

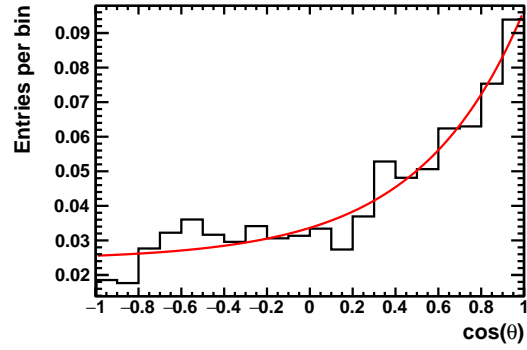
The directional resolution was fitted using a function $f(\cos(\theta))$ of the form

$$f(\cos(\theta)) = f_1(\cos(\theta)) + f_2(\cos(\theta)) \quad (4.8.14)$$

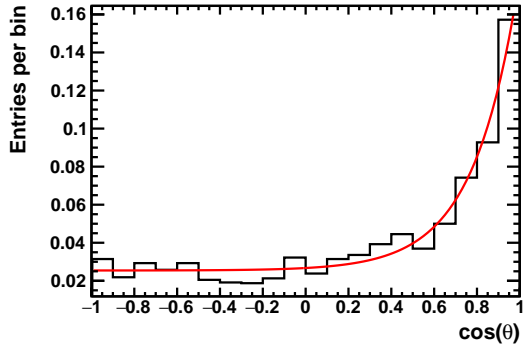
$$= a \times \frac{\kappa}{2 \sinh(\kappa)} \exp(\kappa \cos(\theta)) + b \times \frac{1}{2}, \quad (4.8.15)$$



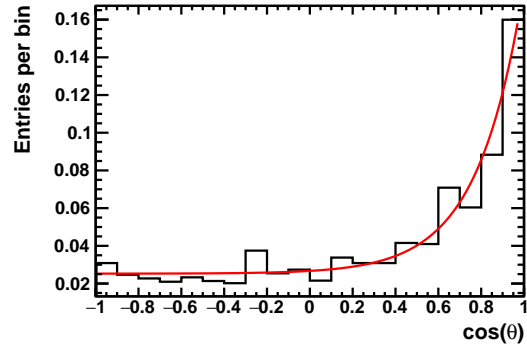
(a) $\nu_e(1 \text{ GeV}) + {}^1\text{H} \xrightarrow{\text{CC}} (?)$



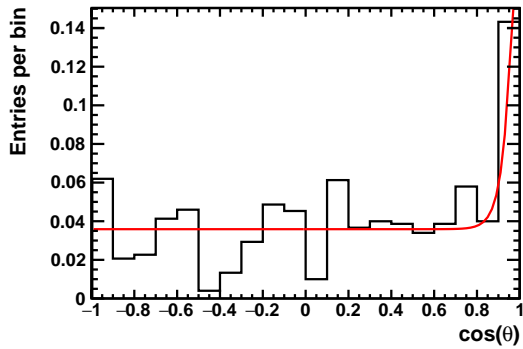
(b) $\nu_e(1 \text{ GeV}) + {}^{12}\text{C} \xrightarrow{\text{CC}} (?)$



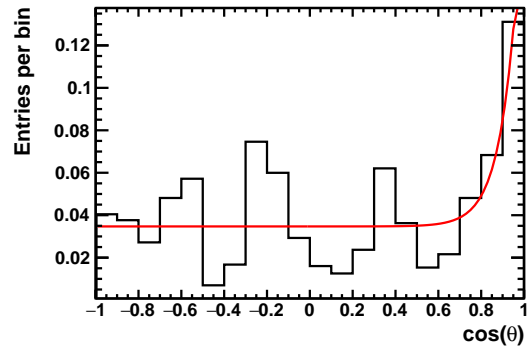
(c) $\nu_e(10 \text{ GeV}) + {}^1\text{H} \xrightarrow{\text{CC}} (?)$



(d) $\nu_e(10 \text{ GeV}) + {}^{12}\text{C} \xrightarrow{\text{CC}} (?)$

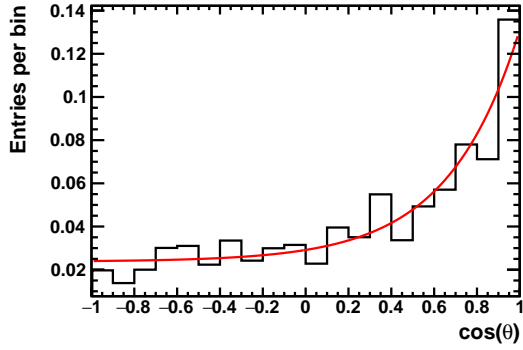


(e) $\nu_e(100 \text{ GeV}) + {}^1\text{H} \xrightarrow{\text{CC}} (?)$

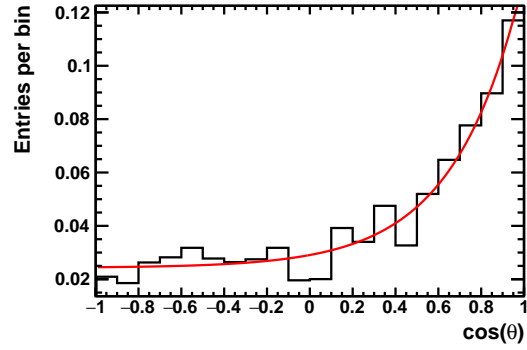


(f) $\nu_e(100 \text{ GeV}) + {}^{12}\text{C} \xrightarrow{\text{CC}} (?)$

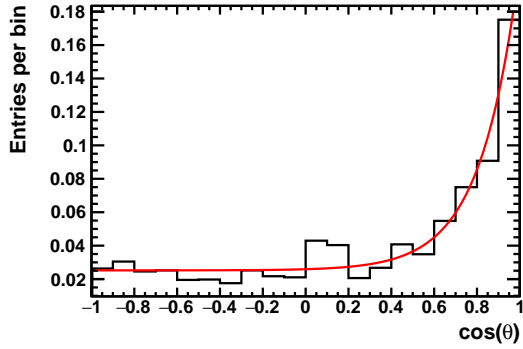
Figure 4.37: Reconstructed directional resolution of ν_e undergoing charged current interaction on ${}^1\text{H}$ and ${}^{12}\text{C}$ nuclei taking into account OD inefficiencies.



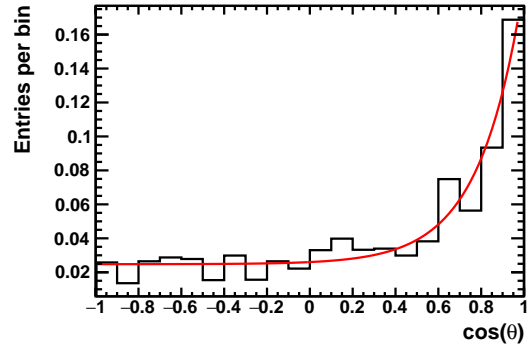
(a) $\bar{\nu}_e(1 \text{ GeV}) + {}^1\text{H} \xrightarrow{\text{CC}} (?)$



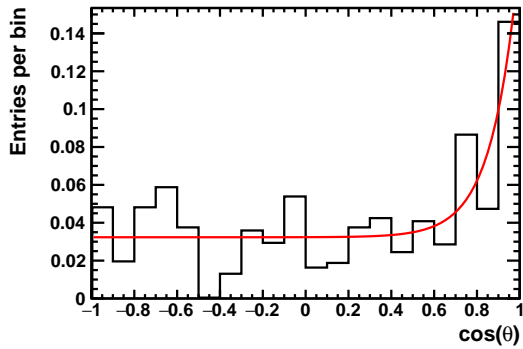
(b) $\bar{\nu}_e(1 \text{ GeV}) + {}^{12}\text{C} \xrightarrow{\text{CC}} (?)$



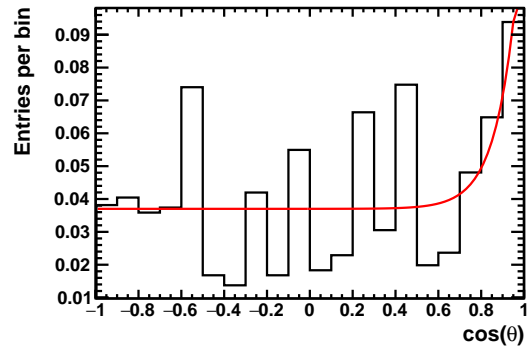
(c) $\bar{\nu}_e(10 \text{ GeV}) + {}^1\text{H} \xrightarrow{\text{CC}} (?)$



(d) $\bar{\nu}_e(10 \text{ GeV}) + {}^{12}\text{C} \xrightarrow{\text{CC}} (?)$

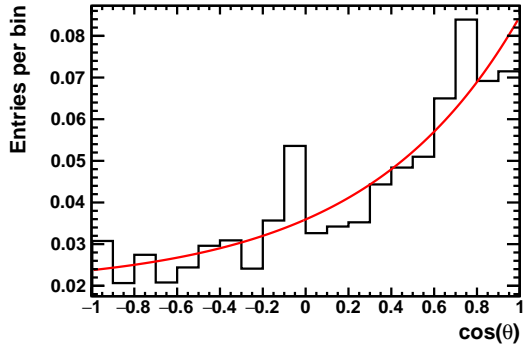


(e) $\bar{\nu}_e(100 \text{ GeV}) + {}^1\text{H} \xrightarrow{\text{CC}} (?)$

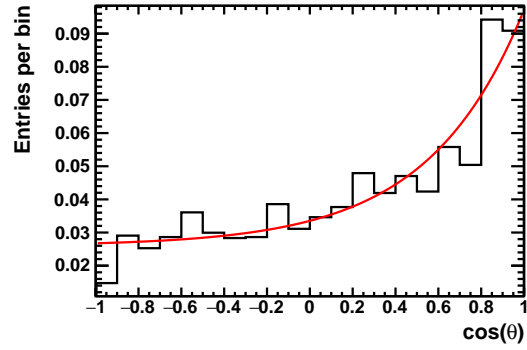


(f) $\bar{\nu}_e(100 \text{ GeV}) + {}^{12}\text{C} \xrightarrow{\text{CC}} (?)$

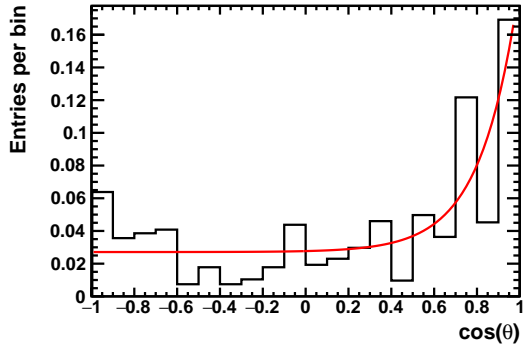
Figure 4.38: Reconstructed directional resolution of $\bar{\nu}_e$ undergoing charged current interaction on ${}^1\text{H}$ and ${}^{12}\text{C}$ nuclei taking into account OD inefficiencies.



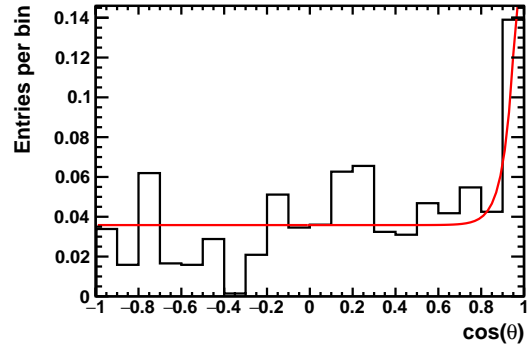
(a) $\nu_\mu(1 \text{ GeV}) + {}^1\text{H} \xrightarrow{\text{CC}} (?)$



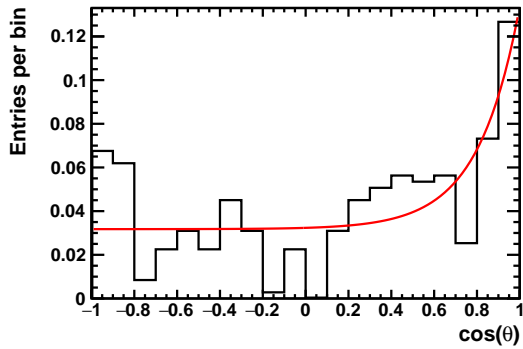
(b) $\nu_\mu(1 \text{ GeV}) + {}^{12}\text{C} \xrightarrow{\text{CC}} (?)$



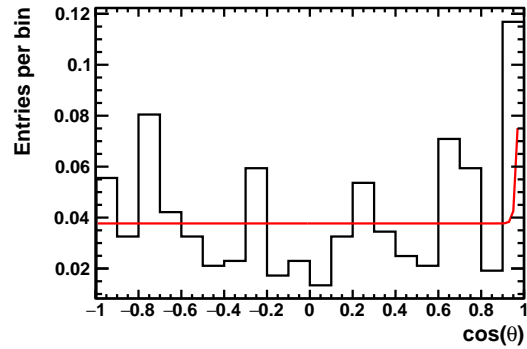
(c) $\nu_\mu(10 \text{ GeV}) + {}^1\text{H} \xrightarrow{\text{CC}} (?)$



(d) $\nu_\mu(10 \text{ GeV}) + {}^{12}\text{C} \xrightarrow{\text{CC}} (?)$

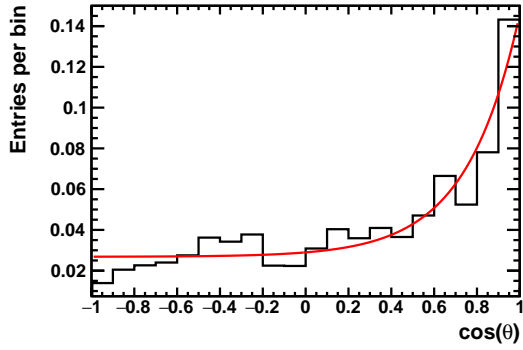


(e) $\nu_\mu(100 \text{ GeV}) + {}^1\text{H} \xrightarrow{\text{CC}} (?)$

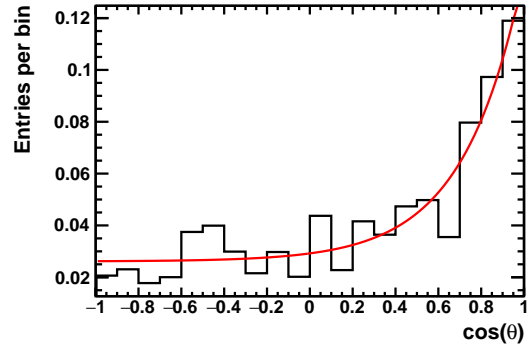


(f) $\nu_\mu(100 \text{ GeV}) + {}^{12}\text{C} \xrightarrow{\text{CC}} (?)$

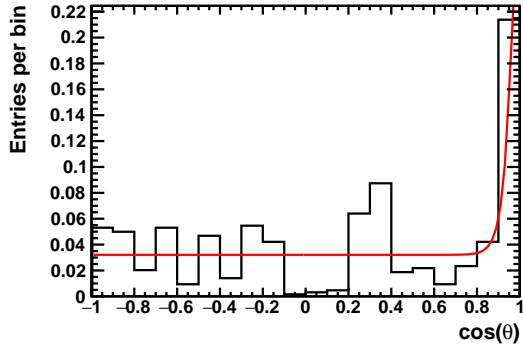
Figure 4.39: Reconstructed directional resolution of ν_μ undergoing charged current interaction on ${}^1\text{H}$ and ${}^{12}\text{C}$ nuclei taking into account OD inefficiencies.



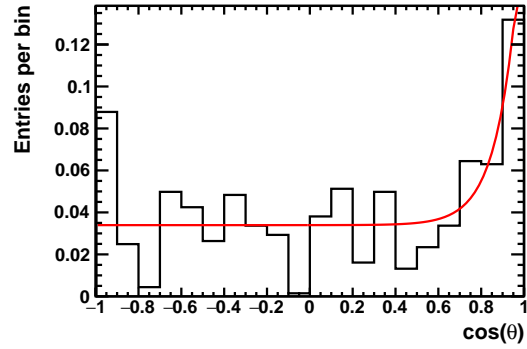
(a) $\bar{\nu}_\mu(1 \text{ GeV}) + {}^1\text{H} \xrightarrow{\text{CC}} (?)$



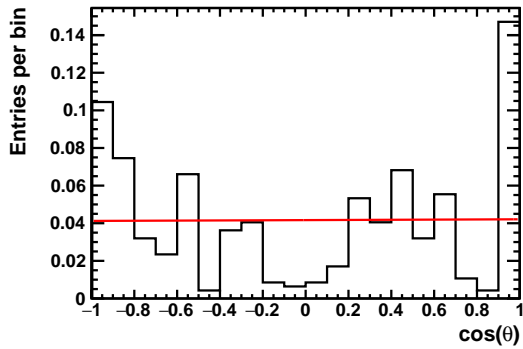
(b) $\bar{\nu}_\mu(1 \text{ GeV}) + {}^{12}\text{C} \xrightarrow{\text{CC}} (?)$



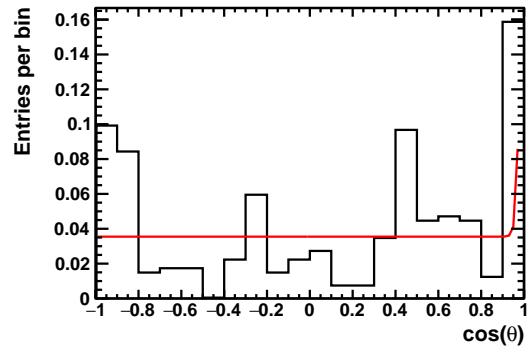
(c) $\bar{\nu}_\mu(10 \text{ GeV}) + {}^1\text{H} \xrightarrow{\text{CC}} (?)$



(d) $\bar{\nu}_\mu(10 \text{ GeV}) + {}^{12}\text{C} \xrightarrow{\text{CC}} (?)$



(e) $\bar{\nu}_\mu(100 \text{ GeV}) + {}^1\text{H} \xrightarrow{\text{CC}} (?)$



(f) $\bar{\nu}_\mu(100 \text{ GeV}) + {}^{12}\text{C} \xrightarrow{\text{CC}} (?)$

Figure 4.40: Reconstructed directional resolution of $\bar{\nu}_\mu$ undergoing charged current interaction on ${}^1\text{H}$ and ${}^{12}\text{C}$ nuclei taking into account OD inefficiencies.

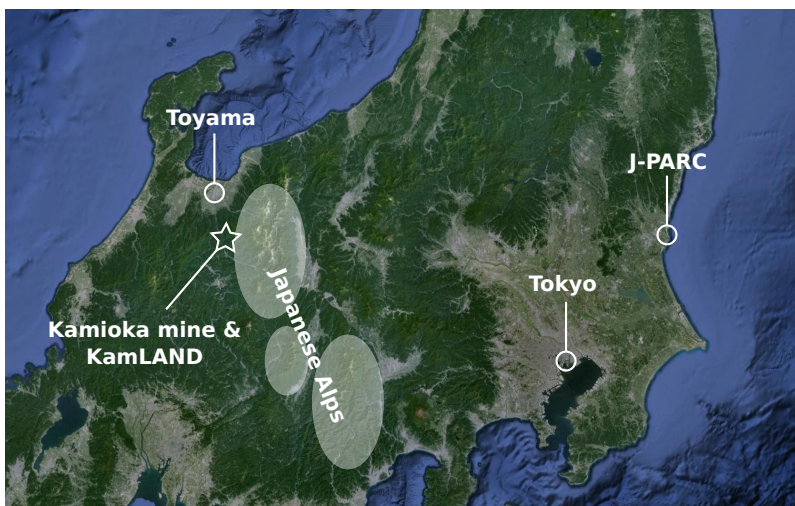


Figure 4.41: Map of central Japan showing the locations of the Japan Proton Accelerator Research Complex (J-PARC) facility and KamLAND. The T2K neutrino beam line runs from J-PARC to the Super-K detector located in the Kamioka mine measuring a baseline distance of about 295 km. Muon-type neutrinos compose the majority flavor in the T2K neutrino beam. Figure created with Google Earth [45].

where the former $f_1(\cos(\theta))$ represents the directional Fisher distribution on the surface of a unit sphere and the latter $f_2(\cos(\theta))$ denotes a flat constant, both with respect to cosine of the polar angle of deviation $\cos(\theta)$ from the true neutrino direction. a and b are the relative normalizations of each of the two distributions.

Validation with data

The only existing directional neutrino source available at present is the Tokai to Kamioka (T2K) neutrino beam line from Tokai to Kamioka. The baseline of this beam is 295 km with the majority of the initial flavor being muon-type neutrinos with a mean energy of about 600 MeV. Figure 4.41 shows a map of the locations of the J-PARC facility and the Kamioka mine where KamLAND is located. Figure 4.42 shows the expected neutrino energy spectrum for different off-axis angles of 0.0° , 2.0° , and 2.5° from the main beam direction. The T2K beam is off-axis at an angle of 2.5° where the mean energy is

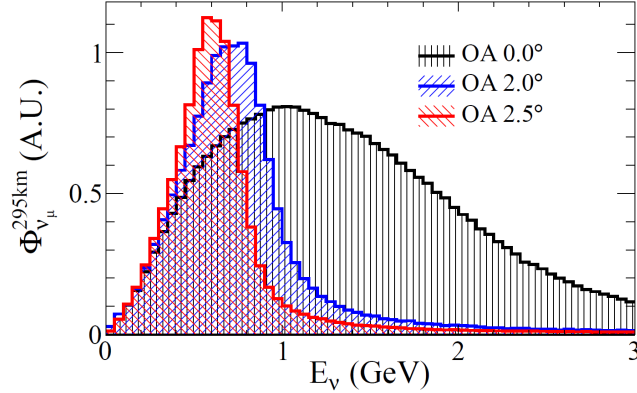


Figure 4.42: Expected neutrino energy spectrum for different off-axis angles of 0.0° , 2.0° , and 2.5° from the main beam direction. The T2K beam is off-axis at an angle of 2.5° where the mean energy is about 600 MeV. [2]

about 600 MeV. Figure 4.43 shows the spectrum for neutrino flavor of ν_μ , $\bar{\nu}_\mu$, ν_e , $\bar{\nu}_e$ at the location of the T2K far detector which is the Super-K detector. Note that all bins here were resized to be 0.1 GeV in width using data available from [59] in which the data was not originally presented with uniform bins. The resizing was done in order to present the data here more clearly and to circumvent issues when using the spectral histograms for fitting. The bin widths at relatively high energies near 5 GeV appear to be larger than those at lower energies, however this is simply due to multiple bins having the same content, and therefore also height, making them indistinguishable from their neighboring bins. This is an inevitable artifact coming from manual resizing of the bins.

The directionality algorithm was tested against data from neutrino events that spill into KamLAND from the T2K neutrino beam line. There are currently 14 observed T2K events of which the neutrino flavors are yet unknown. The events in this sample were selected from the beam spill-time and therefore are essentially background free. Figure 4.44 shows the events with their reconstructed directions compared against the actual direction of the J-PARC facility and simulated angles of outgoing final state muons from ν_μ interactions inside the KamLAND LS. The final state muons were simulated using KLG4Sim and

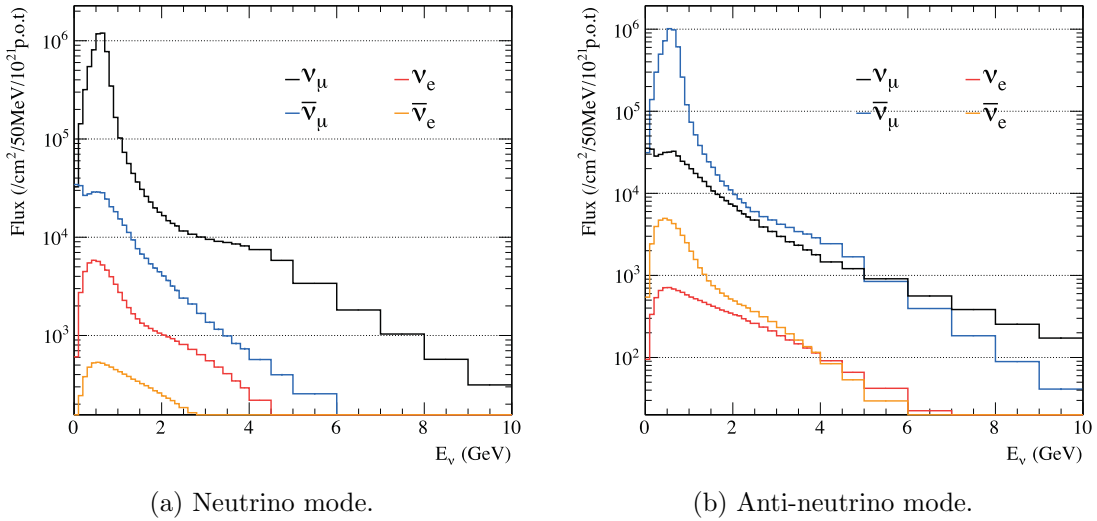


Figure 4.43: Expected neutrino energy spectrum for neutrino flavors ν_μ , $\bar{\nu}_\mu$, ν_e , $\bar{\nu}_e$ at the Super-K detector from the T2K neutrino beam for (a) neutrino mode and (b) anti-neutrino mode. Figure taken from [63].

GENIE. A Kolmogorov-Smirnov (K-S) test conducted on data in Figure 4.44b gives a high p-value of about 0.65 indicating that the initial results are consistent with expectation.

4.9 Track reconstruction and particle identification

4.9.1 Hellgartner's algorithm

Although the neutrino directionality algorithm presented in Section 4.8.4 may be relatively simple and fast in terms of computation time. It is often the case that one may desire to have a visual representation of a given event. A visual image of an event that can reconstruct individual particle tracks may be crucial in developing further techniques to distinguish particle types or extract more desired information about an event.

Here we introduce an algorithm for event imaging that was developed by Dominikus Hellgartner while a graduate student working with the Low Energy Neutrino Astronomy (LENA) detector. First we partition a volume of interest where the neutrino interaction took place into a finite number of voxels essentially creating a three-dimensional grid. The

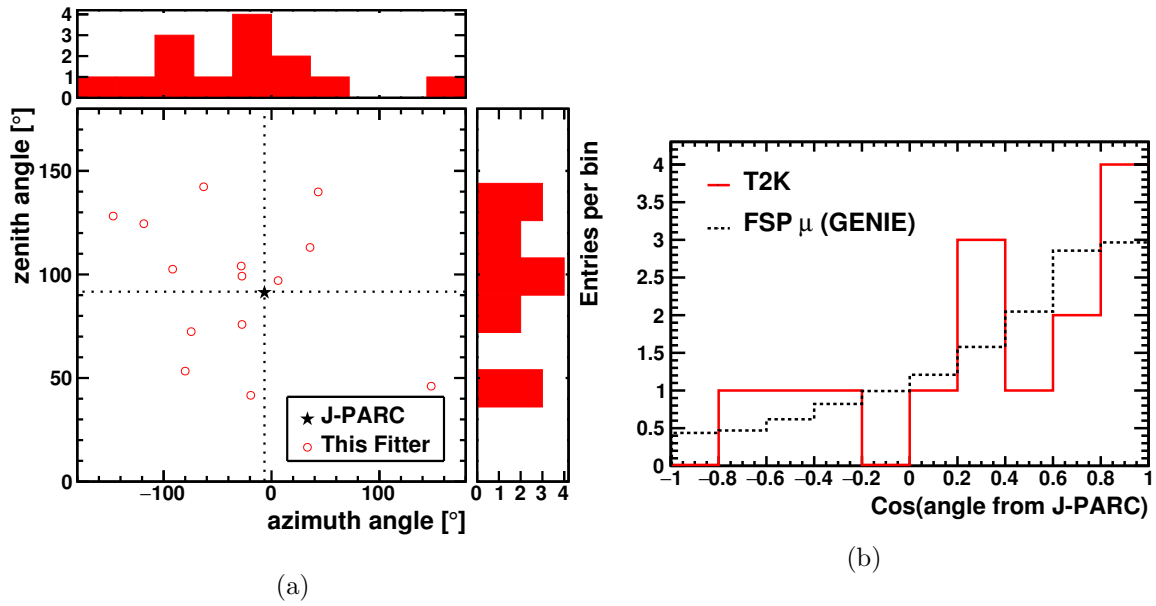


Figure 4.44: 14 neutrino events that spilled into the KamLAND detector from the T2K neutrino beam line. (a) shows the reconstructed direction along with respective histogram projections onto the zenith and azimuthal angles. The direction of J-PARC is depicted by the black star near the middle of the plot. (b) shows the same events with their reconstructed directions compared with the final-state muon angles from ν_μ interactions in the KamLAND LS simulated using KLG4Sim and GENIE. The true direction of J-PARC coincides with $\cos(\theta_{\text{from J-PARC}}) = 1$.

center point of each voxel will have a definite position, say \mathbf{x} . For any given point \mathbf{x} , we can define a function $h(\mathbf{x}, t)$ with respect to all time t such that

$$h(\mathbf{x}, t) \equiv \sum_{i=1}^{N_{\text{PMT}}} \Theta(q_i - q_{\text{threshold}}) \sum_{j=1}^{N_{\gamma}} f(t_{ij} - t_i^{\text{TOF}}, t), \quad (4.9.1)$$

where N_{PMT} is the number of PMTs that will be incorporated into the calculation with N_{γ} , the number of photon hits to utilize per given PMT. Here q_i is the charge of the i -th PMT with $q_{\text{threshold}}$ being the minimum charge for the given PMT to be used in the analysis. t_{ij} is the arrival time of the j -th photon at the i -th PMT, and t_i^{TOF} is the expected photon time-of-flight between the same PMT and point \mathbf{x} . The final term includes a function of both a time interval $t_{ij} - t_i^{\text{TOF}}$, and all time t . This can actually take many forms in order to optimize the final image resolution. Hellgartner chose a bi-polar Gaussian function such that

$$f(\Delta t, t) \propto (t - \Delta t) \exp \left[-\frac{(\Delta t - t)^2}{2\sigma_{\text{tts}}} \right], \quad (4.9.2)$$

where σ_{tts} is the one-sigma edge value of the transit-time-spread distribution of the PMTs. The second term reflects the fact that the timing resolution is modeled by a Gaussian distribution incorporating the PMT transit-time-spread. The first term is an interference term that will be explained in more detail shortly.

Finally, the square of the function is integrated through all time (the square insures that the integration will not vanish due to the bi-polar property) to get a weight $w(\mathbf{x})$ for the given point \mathbf{x} such that

$$w(\mathbf{x}) = \int_{-\infty}^{\infty} |h(\mathbf{x}, t)|^2 dt. \quad (4.9.3)$$

The first term in Equation (4.9.2) is an interference term to maximize the image resolution such that photons arriving at or nearly in coincidence with the expected time-of-flight in comparison to σ_{tts} will constructively interfere where as those that arrive slightly off at time scales on the order of σ_{tts} will destructively interfere. Those that arrive significantly outside of the σ_{tts} range will not contribute significantly to the final result $w(\mathbf{x})$.

This can be done for each voxel point comprising the volume at as fine a voxel spacing as desired. The finite timing resolution of the PMTs is probably the limiting factor

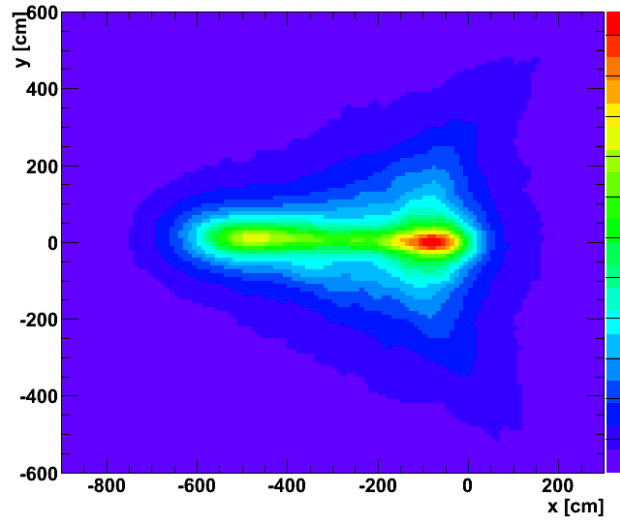
Table 4.2: Parameters used in Hellgartner’s muon event reconstruction simulation studies. Data taken from Hellgartner’s notes.

Parameter	Value
number of PMTs	13 472
PMT diameter	20 inch
Winston cones	none
quantum efficiency (QE)	100 %
light yield	200/MeV
dark noise	0 Hz
PMT resolution function	Gaussian
PMT transit-time spread	$\sigma = 1$ ns
LS	linear alkylbenzene (LAB)

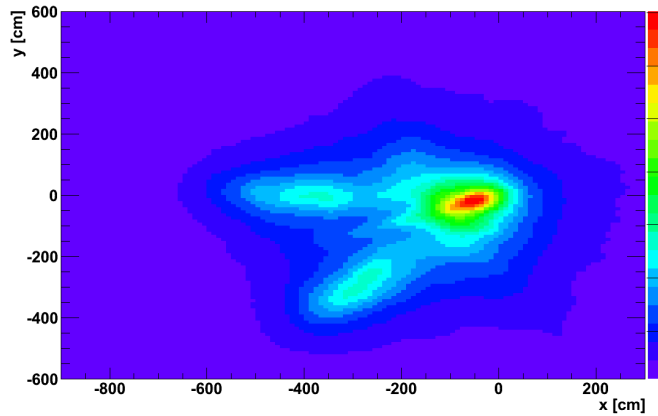
in which the resolution of the resultant image will not improve significantly below voxel spacings of σ_{tts}/c , where c is the speed of light in the medium.

The track image reconstruction algorithm presented in this section was tested by Hellgartner for fully contained muon events in Monte Carlo simulation as shown in Figure 4.45. The studies were done on single and double muon events where the muon kinetic energies were 1 GeV, with a varying number of first photon hits used in the reconstruction. The detector parameters used in Hellgartner’s Monte Carlo simulation are listed in Table 4.2.

This algorithm was also applied in simulated neutrino interactions on target nuclei ^1H , ^{12}C , ^{14}N , and ^{16}O in the KamLAND LS using KLG4Sim and GENIE. An example event where a 2 GeV electron neutrino interacted to produce multiple final-state particles is shown in Figure 4.46. The dotted black line represents the path of an incoming electron-type neutrino while the solid lines represent the final state outgoing particles of which the black line corresponds to a lepton or in this case an electron, the magenta colored line a proton, and the violet colored one a pion. The point at which these lines converge is the interaction vertex which is well estimated by the red high-weight region of the reconstructed Hellgartner color map. Despite the multiple number of final state particles, the general direction of



(a) Event with single 1 GeV muon.



(b) Event with two 1 GeV muons.

Figure 4.45: Results of the Hellgartner track reconstruction for (a) a single 1 GeV muon shot from the origin at $x = 0$, $y = 0$, traveling toward the $-x$ direction using the first three photon hits on each PMT, and (b) a double muon event consisting of two muons both with an energy of 1 GeV shot in the directions $(-1, 0, 0)$ and $(1/\sqrt{2})(-1, -1, 0)$. The first seven photon hits for each PMT were used for the double muon event. Figures taken from Hellgartner's unpublished notes.

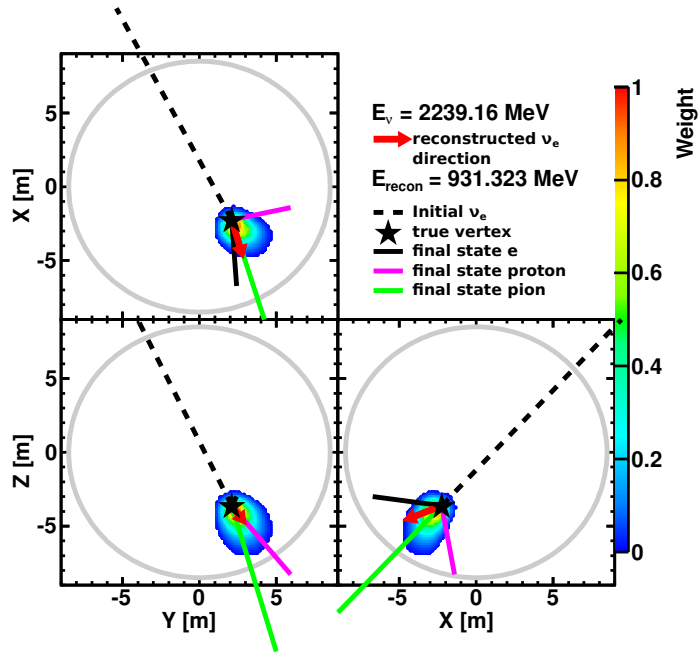


Figure 4.46: Reconstructed three-dimensional image of a simulated 2 GeV ν_e interacting inside the KamLAND ID. The three plots show respective projections of the image onto three orthogonal surfaces of a $9\text{ m} \times 9\text{ m} \times 9\text{ m}$ box that encompasses the ID, with the surfaces folded out to lie flat on this paper. The 8.5 m radius sphere that coincides with the equatorial lines along the PMT glass housings is represented by the gray circle. The initial incoming ν_e is represented by the dotted black line. The final state particles are represented by the solid colored lines. The direction of the solid colored lines coincide with the direction of the initial momentum of the final state particles with their lengths equal in magnitude to the displacement vector tying the given final state particle's production point and stopping point. The interaction vertex is the point indicated by the black star at which the lines representing the initial and final state particles converge. This is well estimated by the high-weight region of the reconstructed Hellgartner color map indicated in red. The red arrow indicates the reconstructed neutrino direction that was derived from connecting the center of time and center of charge.

Table 4.3: Detector parameters used in the KLG4Sim Monte Carlo simulation to study neutrino interactions in the KamLAND LS.

Parameter	Value
number of PMTs	1325 (17 inch), 554 (20 inch)
PMT diameter	17 inch, 20 inch
Winston cones	none
QE	function of γ wavelength (Figure 4.47)
dark noise	0 Hz
PMT resolution function	Gaussian
PMT transit-time spread	$\sigma = 2.283$ ns (17 inch), $\sigma = 4.605$ ns (20 inch)
LS	Dodecane (80.06 wt%), Pseudocumene (19.77 wt%), 2,5-Diphenyloxazole (PPO) (0.17 wt%)

the neutrino is adequately reconstructed by the direction in which the colored blob spreads outward in the correct direction from the red high-weight region. It can also be noted here that although the interaction took place near the edge of the detector in a way such that the PMTs to first receive light are in the direction aligned with that of the incoming neutrino with respect to the interaction vertex and the PMTs to last receive light are in the opposite direction, the correct direction of neutrino is reconstructed successfully. This is likely not the case if the event had been fitted by a straight line-like muon event fitter which may be biased to fit the earliest hit PMTs to be nearer to the vertex in this particular event and the later hit PMTs to be in the direction coinciding with that of the neutrino with respect to the interaction vertex.

The detector parameters for the simulation studies conducted to produce for example Figure 4.46, are listed in Table 4.3, with the PMT QE modeled as shown in Figure 4.47. The QE was modeled as being constant below 370 nm and was extracted from measurements reported by Hamamatsu such that the other contributing factors such as photon attenuation and absorption due to multiple reflections in the PMT glass housing structure are taken out to attempt to model the pure contribution solely from the QE of

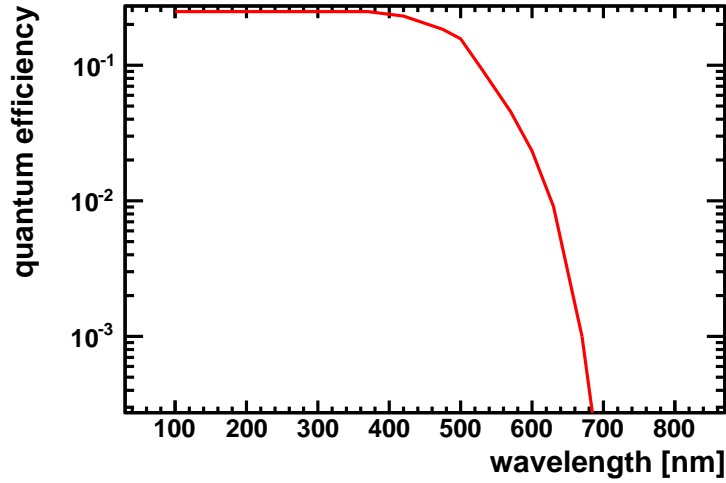


Figure 4.47: QE as a function of photon wavelength used in the KLG4Sim Monte Carlo simulation. The value is modeled as being constant below 370 nm.

the photocathode itself. This was done because QE measurements reported by Hamamatsu are likely to include the mentioned effects that cannot be isolated from the measurements and contribute to the overall effective QE.

The 14 T2K events were also reconstructed using Hellgartner’s algorithm. Figures 4.48 to 4.61 show the reconstructed event images. Although the reconstructed direction of the neutrino cannot be trivially inferred by a visual inspection of the shape of the track shown by the colored region, the reconstruction vertex shown by the empty black star seems to coincide very often with the heavily weighted red colored regions that the algorithm reconstructs. At times, there can possibly be seen separate *arms* coming off from the *main* trajectory that may indicate reconstructed multiplicity of final state particles. The direction away from the J-PARC facility where the neutrino beam originates is indicated by the black arrow, and the reconstructed direction of the event using the *center of time* and *center of charge* technique is indicated by the red arrow. Both arrows have an arbitrary length of 8 m that is projected on the to respective x - y , y - z , and z - x planes. The gray circle indicates the 8.5 m radius optically opaque spherical black sheet that coincides with

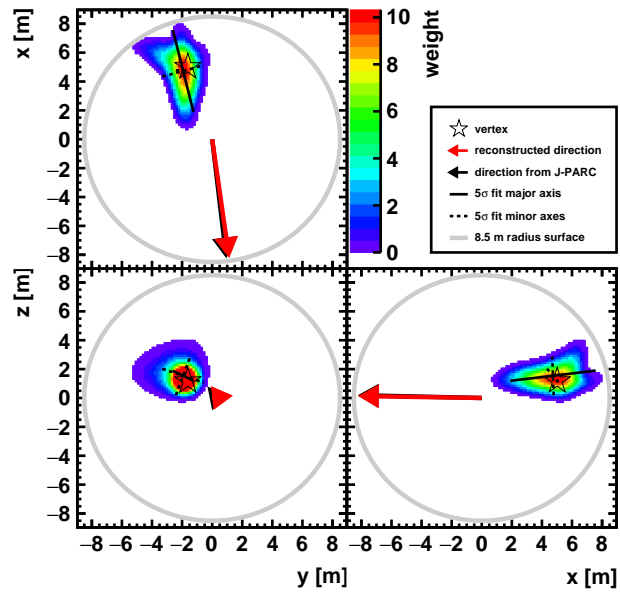


Figure 4.48

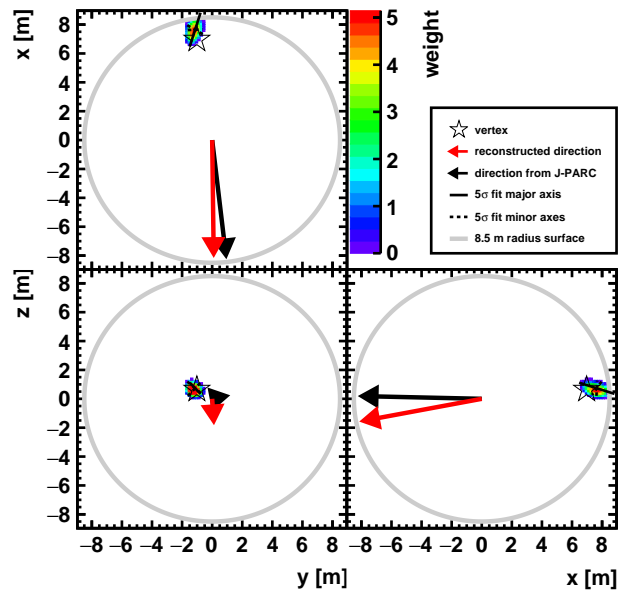


Figure 4.49

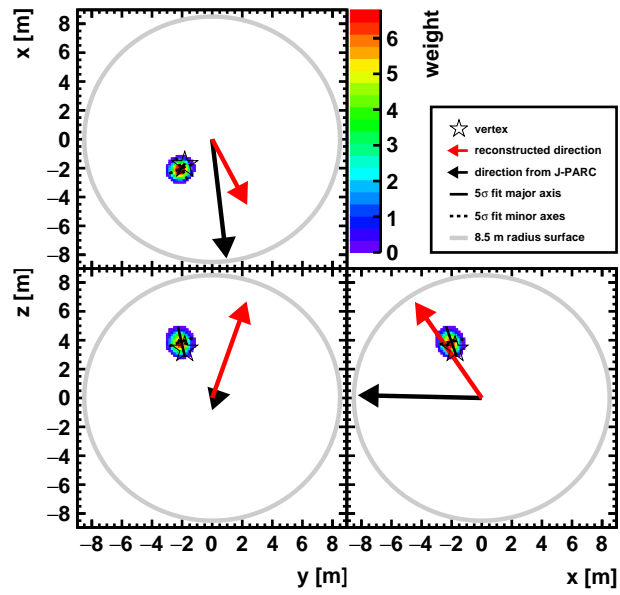


Figure 4.50

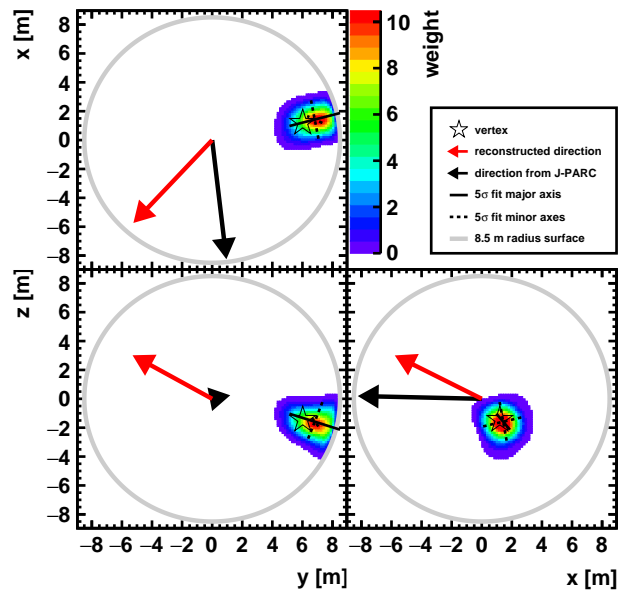


Figure 4.51

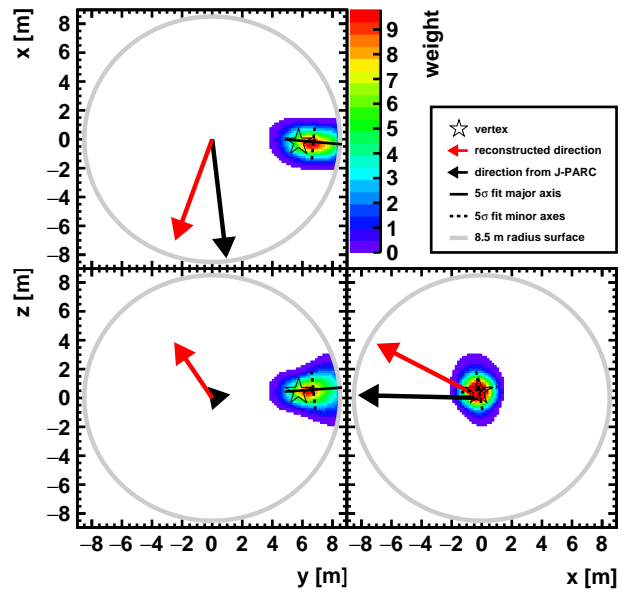


Figure 4.52

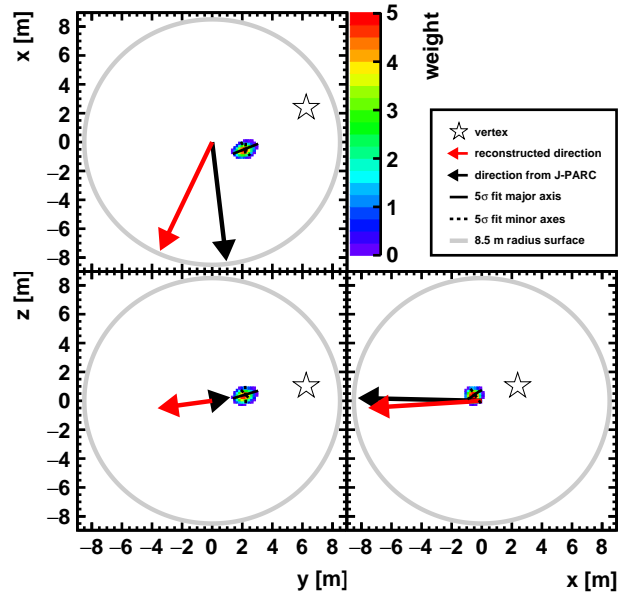


Figure 4.53

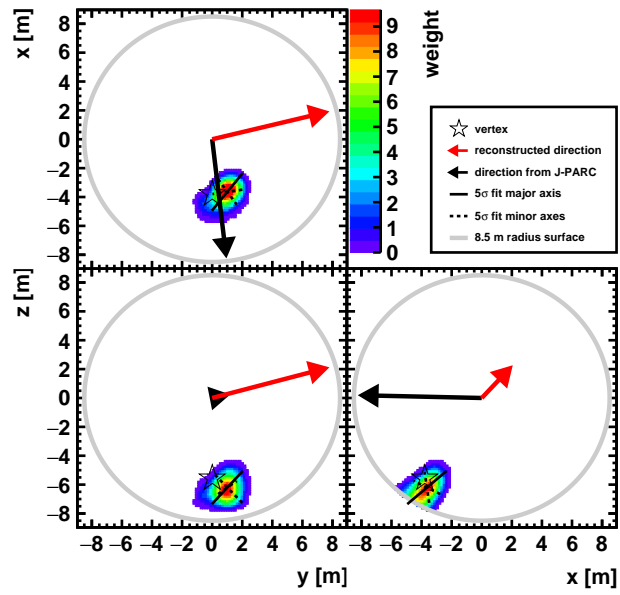


Figure 4.54

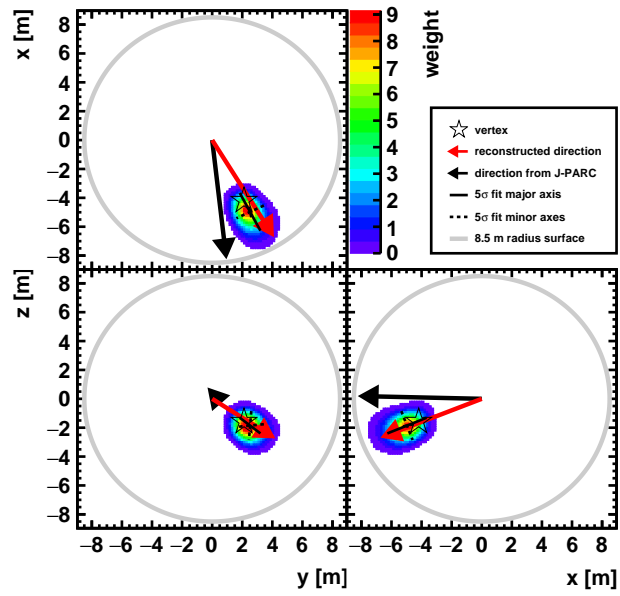


Figure 4.55

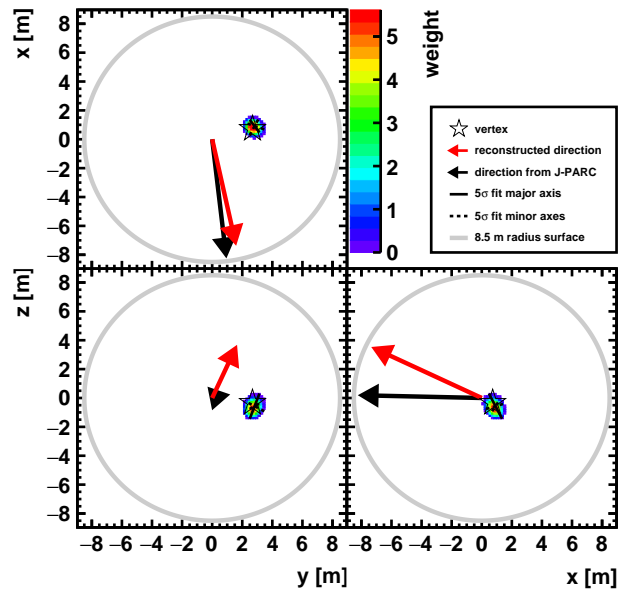


Figure 4.56

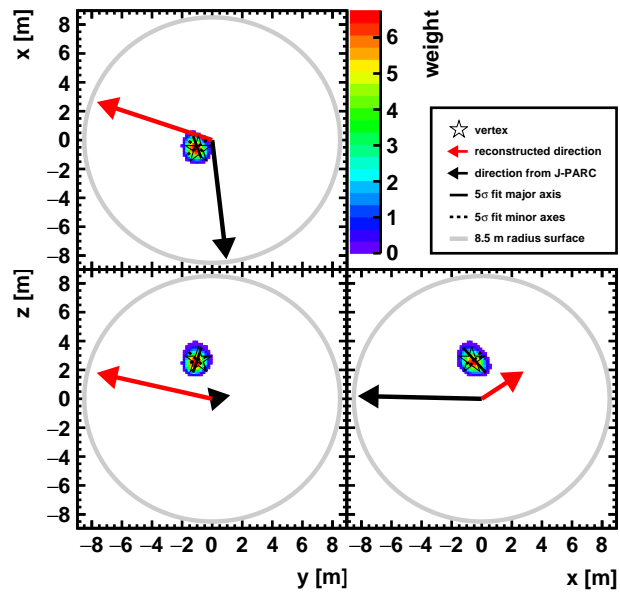


Figure 4.57

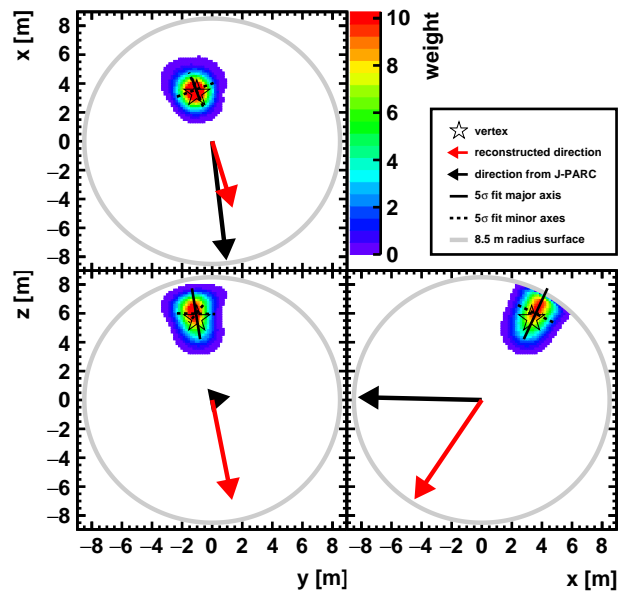


Figure 4.58

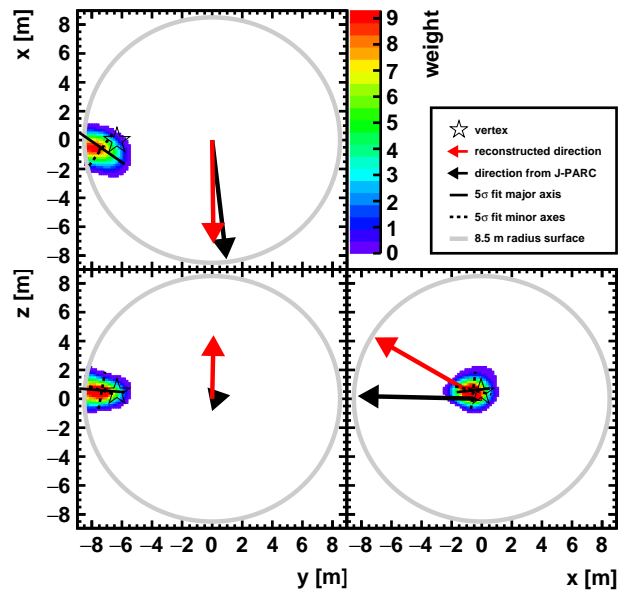


Figure 4.59

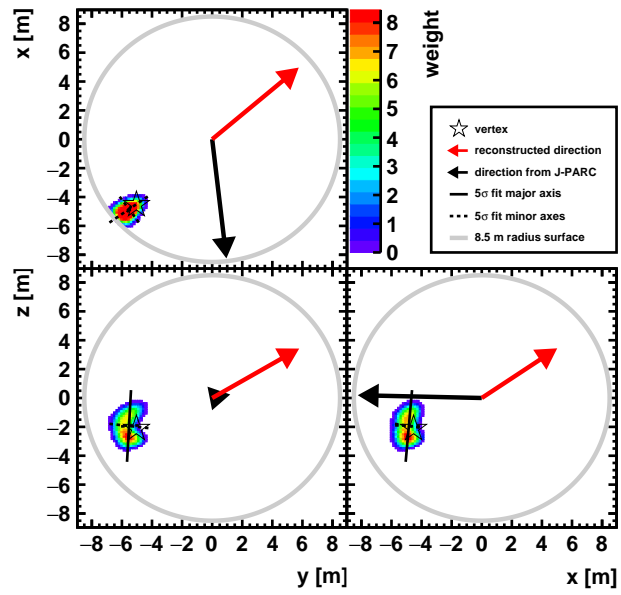


Figure 4.60

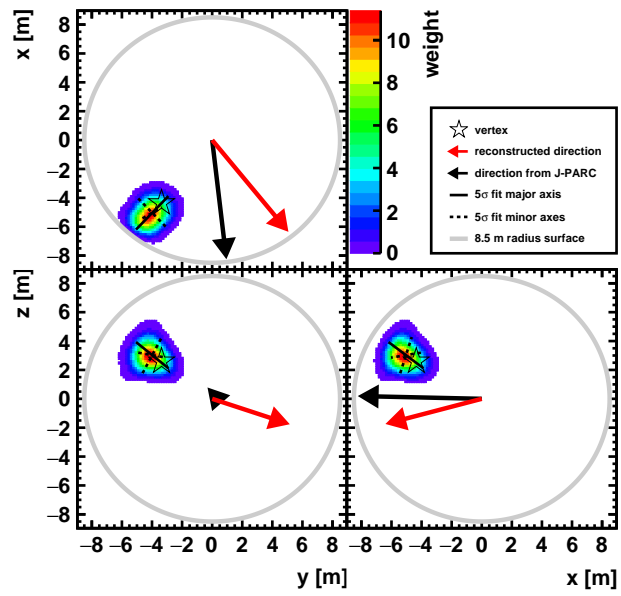


Figure 4.61

the equator of the glass surface of the PMTs. This sheet is what optically defines the ID. Each of the reconstructed event profiles were fitted with an ellipsoid using the principal component analysis (PCA) method. The solid black line running through the reconstructed track profile indicates the major axis of the ellipsoid which covers 5σ of the weighted profile points when they are projected onto the major axis. The dotted black lines indicate the other two minor axes likewise of identical 5σ coverage. This will be explained in more detail in Section 4.9.2 below.

4.9.2 Particle identification

Once a particle track profile can be reconstructed and imaged, its track length and width can be estimated. It is well known that at high energies of above 1 GeV or so, for a given energy, electrons and muons travel different distances inside the LS due to different energy deposition profiles. Electrons are more likely produce electromagnetic showers depositing most of their energies in shorter distances in comparison to muons which tend to produce longer and cleaner minimum ionizing tracks.

The ellipticity f of a track can be defined such that

$$f \equiv \frac{a - b}{a}, \quad (4.9.4)$$

where a and b are defined as the dimensions of a three dimensional ellipsoid as shown in Figure 4.62 that can be fitted to a reconstructed track profile. The parameter b is projected to be relatively large compared to a for a muon-like elongated track traveling in the direction along the z -axis. On the other hand, b will be smaller and possibly more comparable to a for an electron-like shower event profile.

Figure 4.63 shows the fitted ellipticity of tracks produced by 1 GeV mono-energetic leptons e^+ and μ^- simulated in the KamLAND ID using KLG4Sim. There can be seen distinct peaks in the two distributions that correspond to the two lepton flavors, yielding evidence for some particle identification power. It should be mentioned however that due to reconstruction biases that are not yet fully understood near the edge of the ID, an aggressive fiducial volume cut was placed at a radius of 3 m to achieve this result. Due to a lack of fiducial volume in the current KamLAND detector, it is not practical to apply this

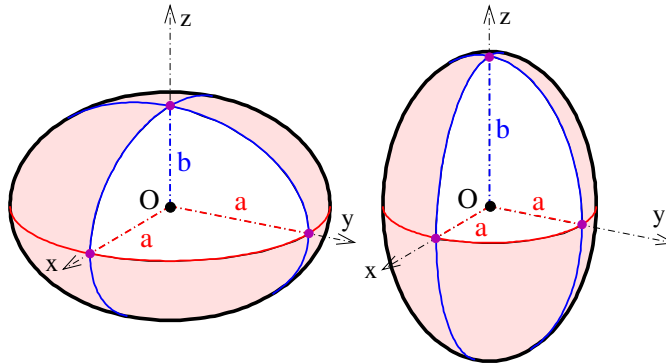


Figure 4.62: Ellipsoids that are symmetric about the z -axis. All of the dimensions of the ellipsoid are identical to a with the exception of only a single dimension along the z -axis being b . Figure reproduced from [5].

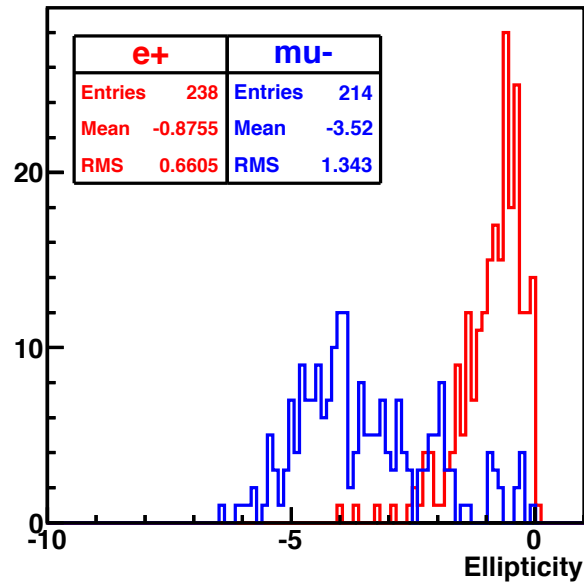


Figure 4.63: Histogram of the fitted ellipticity of 1 GeV mono-energetic positrons and muons simulated in KLG4Sim.

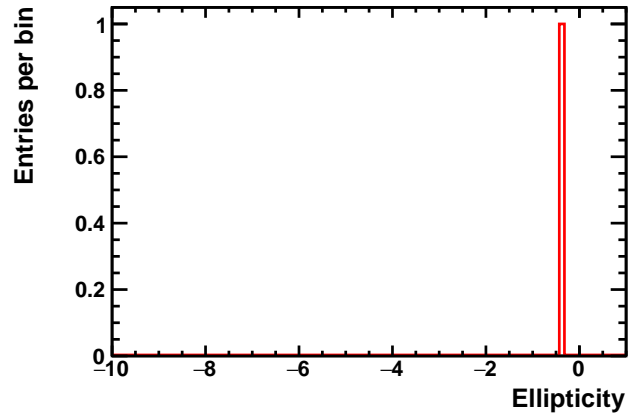


Figure 4.64: Reconstructed ellipticity of the sole fully contained T2K event for which the vertex was reconstructed to be within a 3 m radius fiducial volume.

technique in the present analysis, and possibly a future upgrade of KamLAND with a larger fiducial volume may allow this method to be developed further for practical employment. Figure 4.64 shows the fitted ellipticity for the sole fully contained T2K event for which the vertex was reconstructed to be within a 3 m radius fiducial volume.

Chapter 5

Signal and Background Models

5.1 Atmospheric neutrinos

Neutrinos are naturally produced in abundance in the Earth's atmosphere. These are coined *atmospheric neutrinos* and are the major source of background in the search for neutrinos from dark matter annihilation. The atmosphere encompasses the entire globe and much of the atmospheric neutrinos that reach the Kamioka Liquid Scintillator Antineutrino Detector (KamLAND) will have traveled through some portion of the Earth. At the $\sim\text{GeV}$ energy scale of interest, the neutrinos may very well undergo oscillation through the mechanism explained in Chapter 2 and change their flavor states by the time they reach KamLAND. Figure 5.1 shows a simplified diagram of how a single neutrino produced in the atmosphere at the Earth's surface may travel through the Earth and reach the detector.

Atmospheric neutrinos are created from the interaction of cosmic rays with atomic nuclei in the Earth's atmosphere. Secondary particle showers are produced including many unstable pions and kaons that decay into neutrinos. The dominant neutrino producing decay modes of kaons K^+ or K^- in the atmosphere with their respective branching ratios

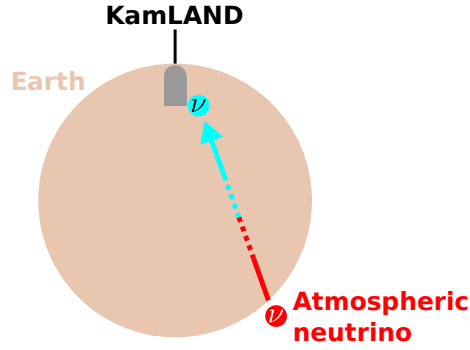
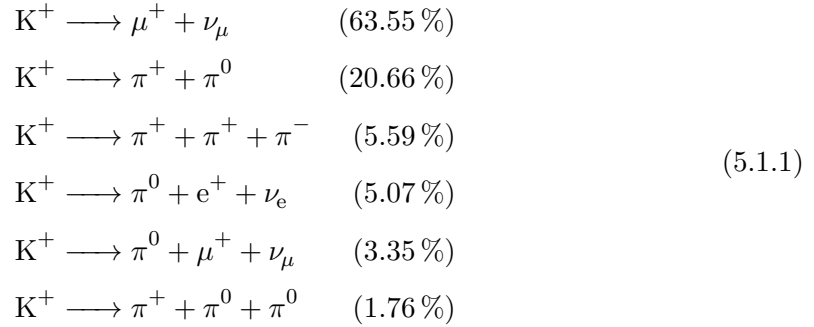
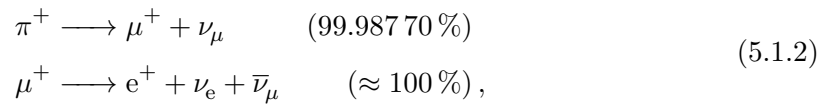


Figure 5.1: Simplified diagram showing the production and detection scheme of atmospheric neutrinos. Neutrinos are produced in abundance in the Earth’s atmosphere around the globe. Some may very well oscillate into different flavor neutrinos or scatter off of nuclei as they travel through the Earth before reaching KamLAND where they can be observed.

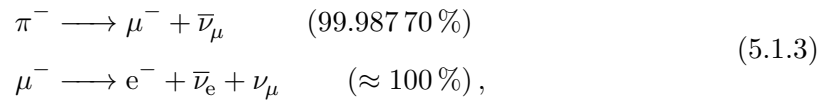
are



with the decay modes for K^- being charge conjugates of the same processes. The mean lifetime of K^+ or K^- is $(1.2380 \pm 0.0021) \times 10^{-8}$ s. The dominant neutrino producing decay modes for the charged pions, π^+ and π^- , are



and



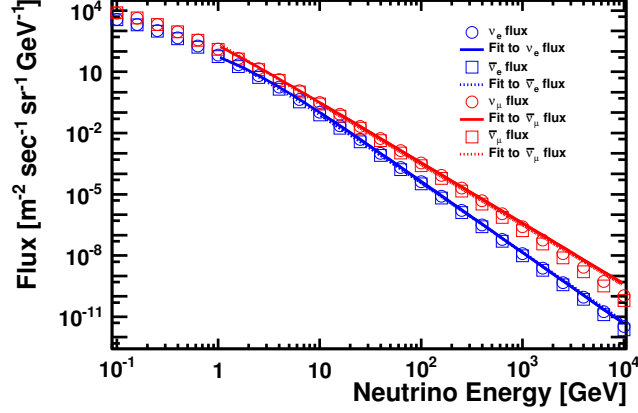


Figure 5.2: The pre-oscillated atmospheric neutrino flux spectrum calculated by Honda et al. [52] averaged over all zenith and azimuthal angles taking into account the effects of the mountain above the detector. The spectrum was fitted with arbitrary curves of the form $f(x) = a(x - b)^c$ for each neutrino flavor shown by the solid and dotted lines.

with a mean lifetime of $(2.6033 \pm 0.0005) \times 10^{-8}$ s for π^+ or π^- and $(2.1969811 \pm 0.0000022) \times 10^{-6}$ s for μ^- or μ^+ . Neutral pions usually decay into non-neutrino products:

$$\begin{aligned} \pi^0 &\longrightarrow \gamma + \gamma && (98.823 \%) \\ \pi^0 &\longrightarrow e^+ + e^- + \gamma && (1.174 \%). \end{aligned} \quad (5.1.4)$$

The flavor ratio r defined by

$$r \equiv \frac{\nu_\mu + \bar{\nu}_\mu}{\nu_e + \bar{\nu}_e} \quad (5.1.5)$$

is approximately $r \approx 2$ and increases with energies above about 2 GeV as more muons with comparatively longer lifetimes begin to survive until they arrive at the ground before decaying.

The atmospheric neutrino production flux at the Kamioka site was modeled using studies conducted by Honda et al. [52]. Figure 5.2 shows the calculated atmospheric neutrino flux spectrum averaged over all zenith and azimuthal angles at the Kamioka site taking into account the effects of the rock overburden of Mt. Ike above the detector. The spectrum was fitted using an arbitrary function of the form $f(x) = a(x - b)^c$ for energies above 1 GeV.

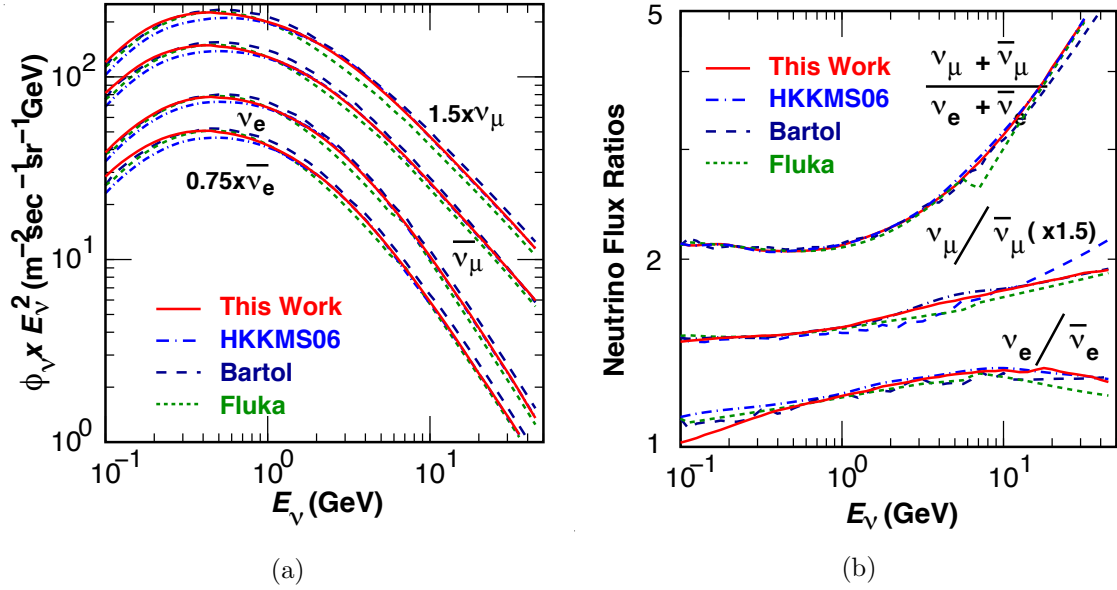


Figure 5.3: Comparison between different models for the atmospheric neutrino flux spectrum averaged over all zenith and azimuthal angles (a) and flavor ratios (b) calculated for the Kamioka site. Calculations by Honda et al. done in 2011 is shown by the solid red line and compared to previous work by the same group done in 2006 indicated by the blue dash-dot lines. The black dashed lines are for studies done by the Bartol group [15], and the green dotted lines for those of the FLUKA group [62]. Figure taken from [53].

Figure 5.3 shows the Honda flux spectrum and flavor ratio calculations released in 2011 compared to past work by the same group and those conducted by other groups. The Honda flux spectrum was averaged over all zenith and azimuthal angles from 0.1 GeV to 32 GeV for Kamioka using their *3-dimensional* calculation scheme.

Figures 5.4 to 5.7 show the neutrino oscillation probabilities for transition between flavors ν_e and ν_μ along with $\bar{\nu}_e$ and $\bar{\nu}_\mu$ for atmospheric neutrinos traveling through the bulk Earth and the lower 20 km of the Earth's atmosphere. The figures with fine resolution corresponds to probabilities independent of detector effects and solely taking into account full three-flavor mixing and matter effects through the Earth which was modeled using the PREM [32] density profile as shown in Figure 2.2 and the 2014 neutrino best fit oscillation and mass parameters shown in Table 2.1. The figures with coarse resolution shows identical plots with the bins adjusted to coincide with the Honda flux bins used in this analysis. The production height of the atmospheric neutrinos was assumed to be constant at 20 km above the surface of the Earth, and the atmosphere was modeled using the 1976 International Standard Atmosphere (ISA).

Figures 5.8 and 5.9 show the Honda atmospheric neutrino flux for detector zenith angles θ with respect to neutrino energy in GeV for the flavors ν_e , $\bar{\nu}_e$, ν_μ , $\bar{\nu}_\mu$. The fluxes shown were averaged over azimuthal angles, and for the two cases of maximum and minimum solar activities. The detector independent atmospheric neutrino fluxes are shown for the pure unoscillated case as well as for the case including full three flavor oscillation with matter effects above 1 GeV. It is worthwhile to note a peculiar but common feature that exists in the pure non-oscillated fluxes. Namely that there appears to be an excess flux observed near the region $\cos(\theta) \approx -0.7$ where θ is the zenith angle and $\log_{10}(E_\nu/\text{GeV}) \approx -0.4$ or equivalently $E_\nu \approx 400 \text{ MeV}$. This is thought to be due to the magnetic latitude of Kamioka where the symmetry between the upward and downward going fluxes only starts to appear at energies above $\sim 1 \text{ GeV}$ when the geomagnetic effects are defeated. This feature is also confirmed by studies conducted by the Super-Kamiokande (SK) collaboration [54, Figure 5].

The effective atmospheric neutrino fluxes after incorporating detector effects are shown with respect to zenith angle in Figure 5.10. The corresponding effective atmospheric

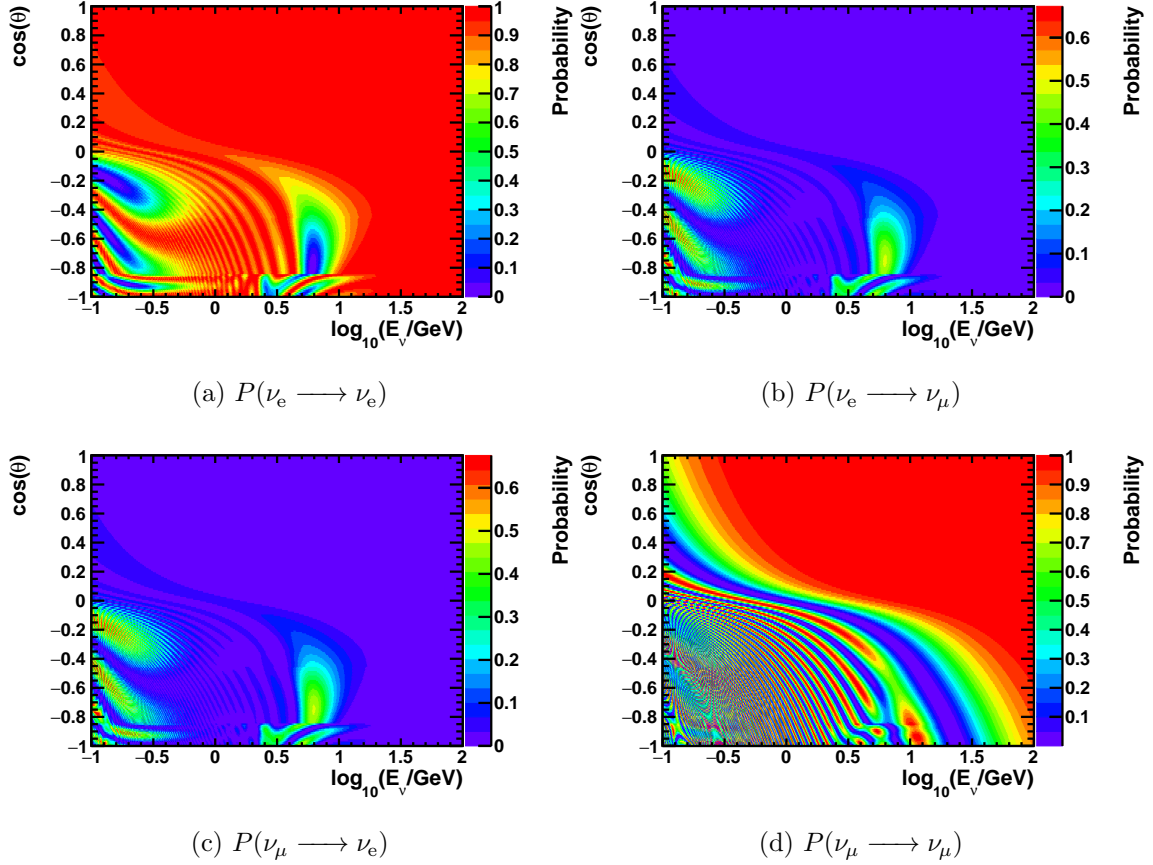


Figure 5.4: The oscillation probability $P(\nu_\alpha \rightarrow \nu_\beta)$ of atmospheric neutrinos between flavors ν_e and ν_μ . Probabilities are shown for cosine of zenith angle θ with respect to the neutrino energy in GeV. Full three-flavor oscillation with matter effects through the Earth is included using the Preliminary Reference Earth Model (PREM) [32] density profile as shown in Figure 2.2 and the 2014 neutrino best fit oscillation and mass parameters shown in Table 2.1. Only pure detector independent oscillation probabilities are shown.

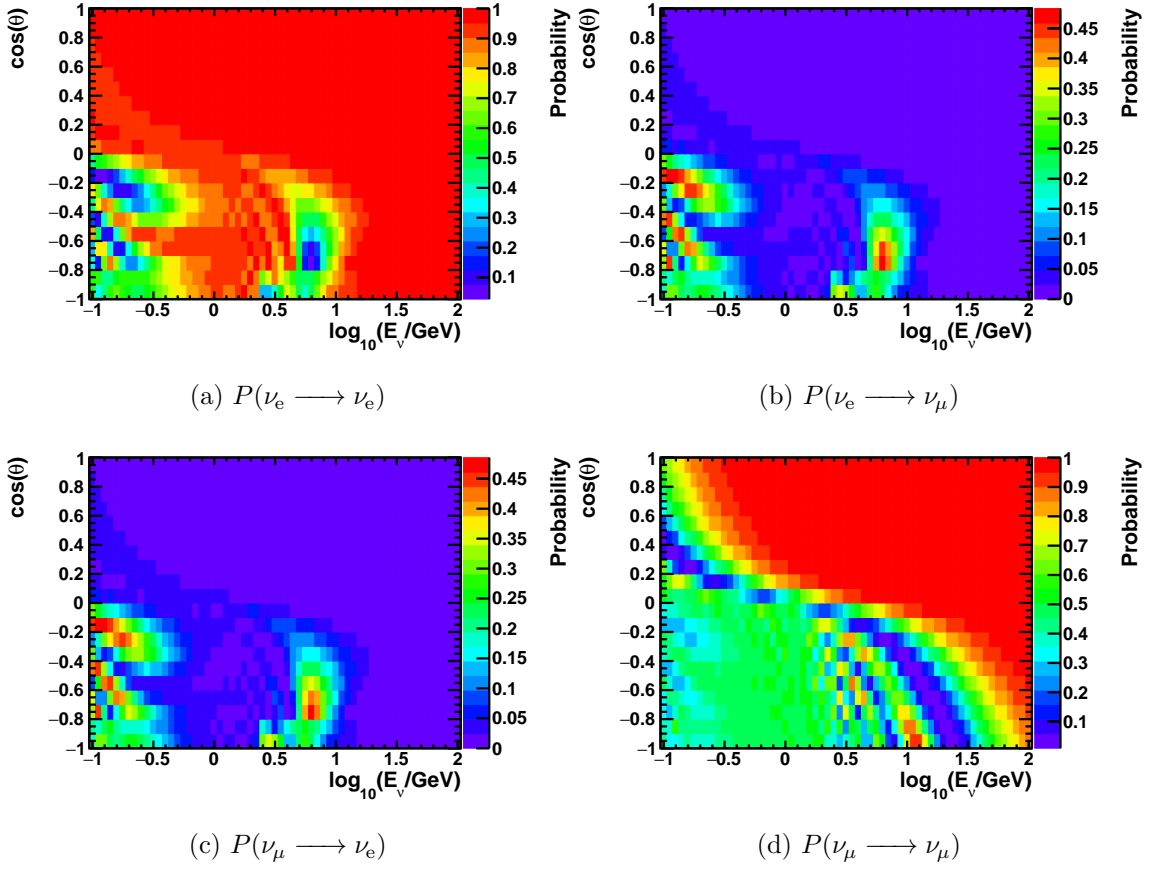


Figure 5.5: The oscillation probability $P(\nu_\alpha \rightarrow \nu_\beta)$ of atmospheric neutrinos between flavors ν_e and ν_μ . Plots are identical to Figure 5.4, however the bins are adjusted to coincide with that of the Honda atmospheric neutrino flux calculations.

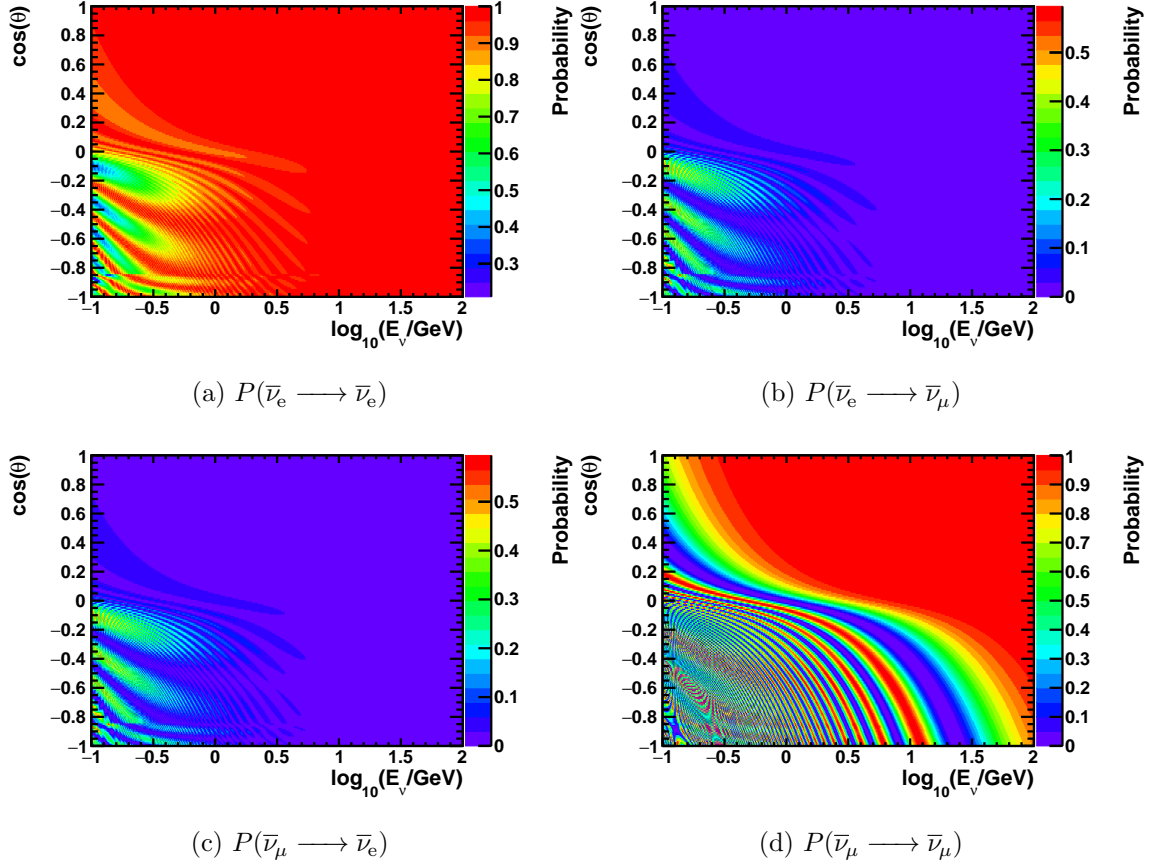


Figure 5.6: The oscillation probability $P(\bar{\nu}_\alpha \rightarrow \bar{\nu}_\beta)$ of atmospheric neutrinos between flavors $\bar{\nu}_e$ and $\bar{\nu}_\mu$. Probabilities are shown for cosine of zenith angle θ with respect to the neutrino energy in GeV. Full three-flavor oscillation with matter effects through the Earth is included using PREM [32] density profile as shown in Figure 2.2 and the 2014 neutrino best fit oscillation and mass parameters shown in Table 2.1. Only pure detector independent oscillation probabilities are shown.

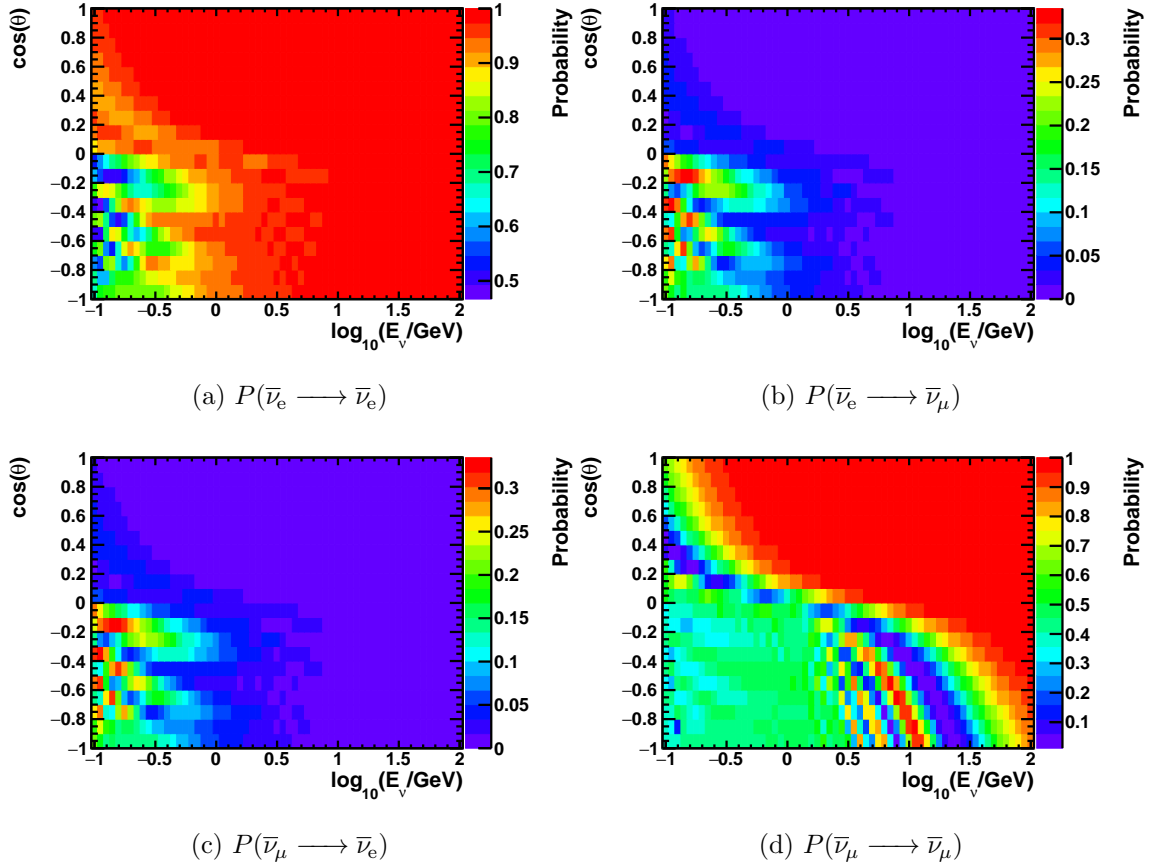


Figure 5.7: The oscillation probability $P(\bar{\nu}_\alpha \longrightarrow \bar{\nu}_\beta)$ of atmospheric neutrinos between flavors $\bar{\nu}_e$ and $\bar{\nu}_\mu$. Plots are identical to Figure 5.6, however the bins are adjusted to coincide with that of the Honda atmospheric neutrino flux calculations.

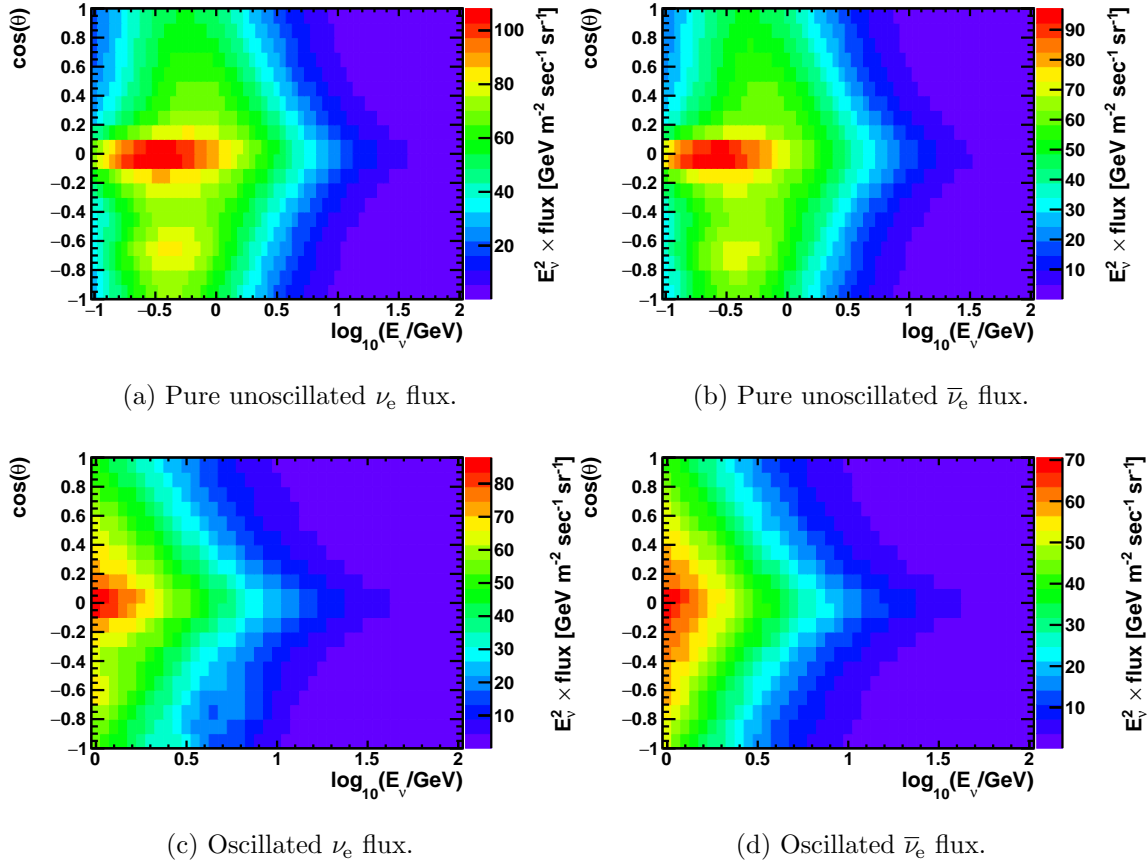


Figure 5.8: Atmospheric neutrino fluxes shown for cosine of zenith angle θ with respect to neutrino energy E_ν in GeV. Plots are for pure unoscillated fluxes for neutrino flavors ν_e (a) and $\bar{\nu}_e$ (b) as well as oscillated fluxes for the same flavors ν_e (c) and $\bar{\nu}_e$ (d) .

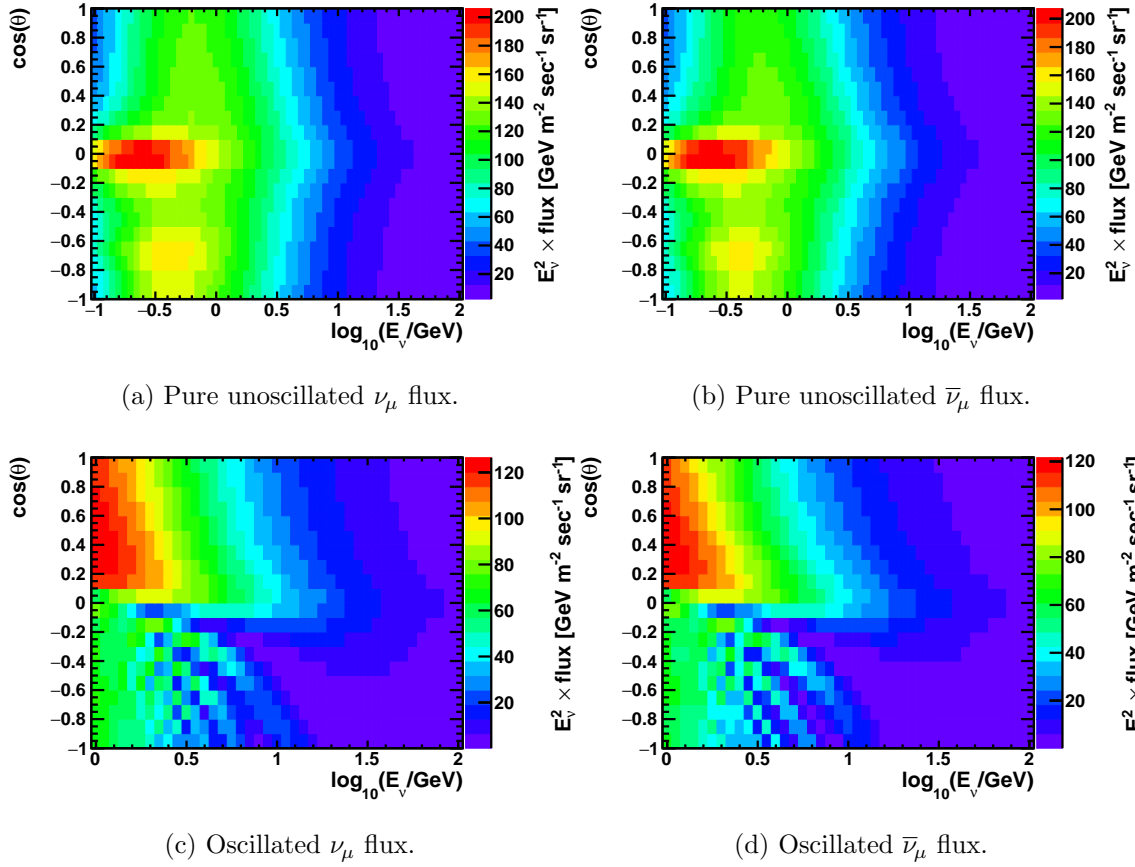


Figure 5.9: Atmospheric neutrino fluxes shown for cosine of zenith angle θ with respect to neutrino energy E_ν in GeV. Plots are for pure unoscillated fluxes for neutrino flavors ν_μ (a) and $\bar{\nu}_\mu$ (b) as well as oscillated fluxes for the same flavors ν_μ (c) and $\bar{\nu}_\mu$ (d) .

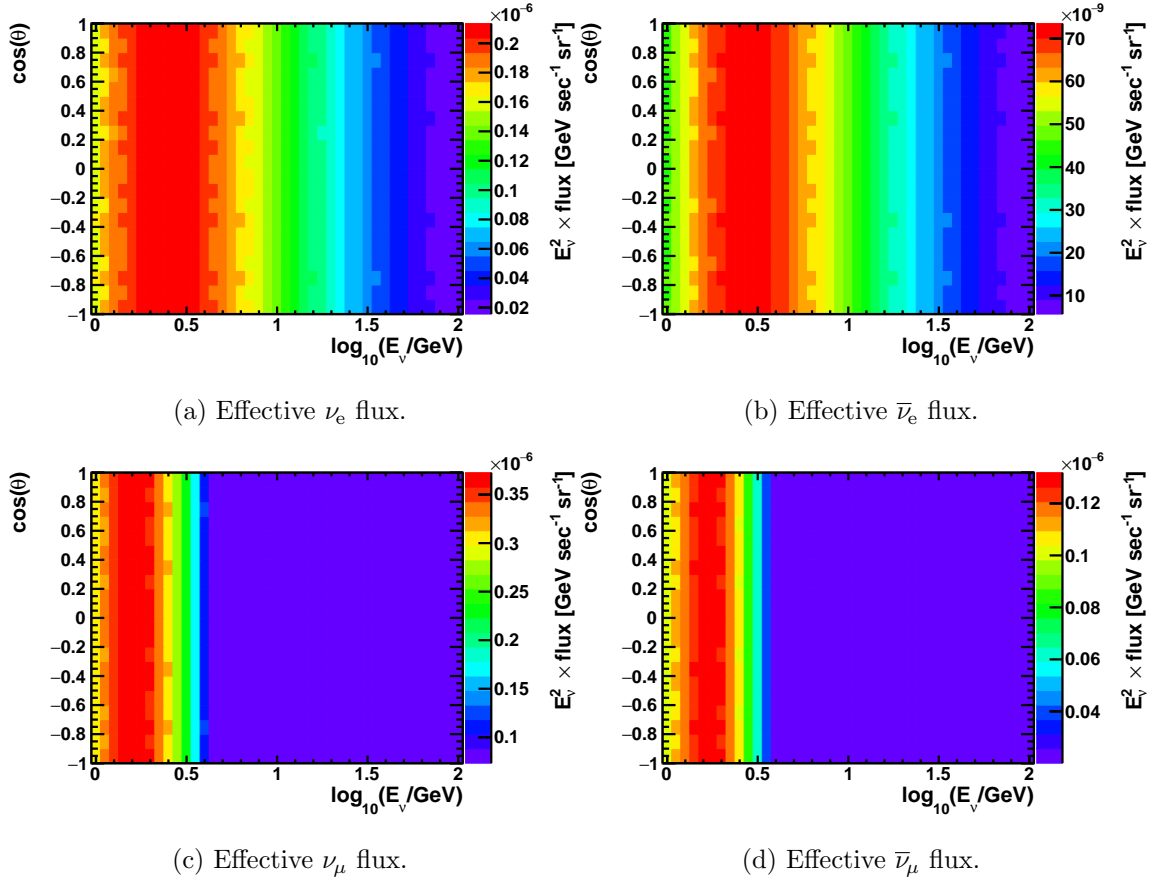


Figure 5.10: Atmospheric neutrino fluxes shown for cosine of polar angle θ from the direction toward the Sun's core with respect to neutrino energy E_ν in GeV. Shown are effective fluxes after taking into account oscillation, matter effects, and detector effects.

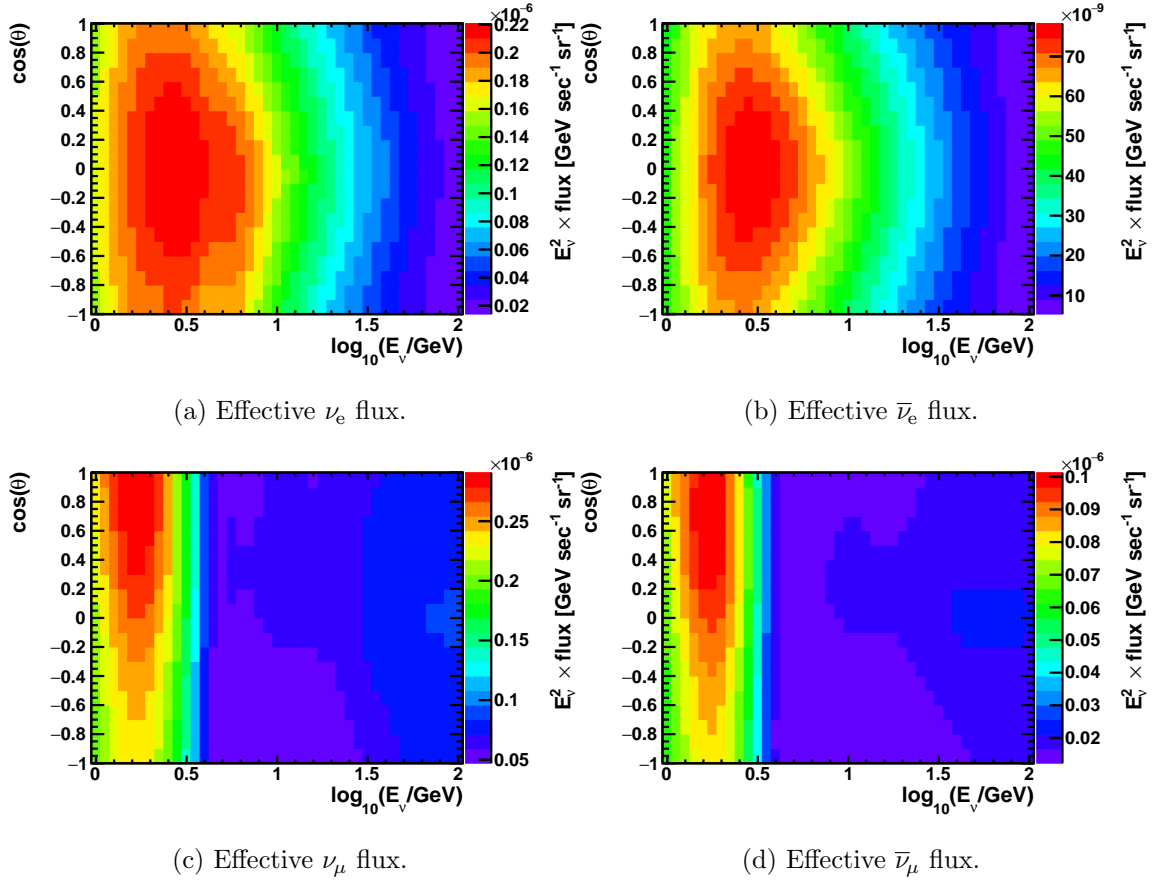


Figure 5.11: Atmospheric neutrino fluxes shown for cosine of zenith angle θ with respect to neutrino energy E_ν in GeV. Shown are effective fluxes after taking into account oscillation, matter effects, and detector effects.

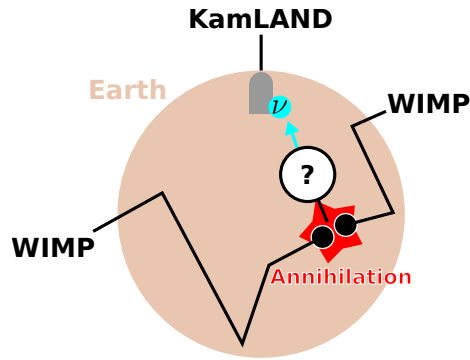


Figure 5.12: Simplified diagram showing the production and detection scheme of WIMP annihilation induced neutrinos. Dark matter particles that are gravitationally captured by the Earth will undergo annihilation at or near the center of the Earth. They are weakly interacting and at energy scales of $\sim\text{GeV}$ will mostly travel unhindered to the surface of the Earth. Some will arrive at the KamLAND detector and be observed.

neutrino fluxes rotated and shown with respect to polar angle from the direction toward the Sun's core are shown in Figure 5.11.

5.2 Weakly interacting massive particle (WIMP) annihilation induced neutrinos from the Sun or Earth

Figure 5.12 shows a simplified diagram depicting the detection scheme of WIMP annihilation induced neutrinos coming from the Earth's core. WIMPs that are gravitationally captured by the Earth will be most populous near the core. WIMPs that annihilate within some channel to effectively create neutrinos will produce some signal that can be observed at the KamLAND detector. Neutrinos which interact weakly will have a low enough scattering cross section with respect to nuclei in the Earth at the energy scale of interest at a few GeV.

WIMPs that are captured in the Earth are in thermal equilibrium with the Earth's core and they will be distributed according to a spherically symmetrical Boltzmann

distribution

$$n(r) = n(0) \exp \left[-\frac{m_X \phi(r)}{kT} \right], \quad (5.2.1)$$

where $n(r)$ is the WIMP number density at some radius r from the core, m_X is the dark matter mass, k is the Boltzmann constant, T is the temperature at the core, and $\phi(r)$ is the gravitational potential inside the body at radius r such that

$$\phi(r) = \int_0^r G_N M(r) \frac{1}{r^2} dr, \quad (5.2.2)$$

where G_N is Newton's gravitational constant, and $M(r)$ is the mass of the body enclosed in the sphere of radius r . The enclosed mass is expressed as

$$M(r) = 4\pi \int_0^r \rho(r) r^2 dr, \quad (5.2.3)$$

where $\rho(r)$ is the density of normal matter at radius r . If we look at only the vicinity of the core, the density of normal matter can be assumed to be constant for approximation purposes such that $\rho(r) = \rho(0)$. We can then explicitly take the integral to get

$$M(r) = \frac{4}{3}\pi\rho(0)r^3. \quad (5.2.4)$$

Inserting this back into the expression for the potential $\phi(r)$, we have

$$\begin{aligned} \phi(r) &= \int_0^r G_N \left(\frac{4}{3}\pi\rho(0)r^3 \right) \frac{1}{r^2} dr \\ &= \frac{4}{3}\pi\rho(0)G_N \int_0^r r dr \\ &= \frac{2}{3}\pi\rho(0)G_N r^2. \end{aligned} \quad (5.2.5)$$

Finally we can write the WIMP density profile $n(r)$ as

$$n(r) = n(0) \exp \left(-\frac{r^2}{r_X^2} \right), \quad (5.2.6)$$

where

$$r_X = \left(\frac{3kT}{2\pi G_N \rho(0) m_X} \right)^{\frac{1}{2}}. \quad (5.2.7)$$

Plugging in the parameters for the Sun $\rho(0)_\odot = 151 \text{ g/cm}^3$, $T_\odot = 15.5 \times 10^6 \text{ K}$, we get

$$r_X \approx 0.03 R_\odot \sqrt{\frac{10 \text{ GeV}}{m_X}}, \quad (5.2.8)$$

which states that the dark matter density is concentrated in the immediate vicinity of the core. The annihilation probability is proportional to $n(r)^2$ so most of the WIMP annihilation induced neutrinos can be approximated to originate from the center of the Sun.

However the situation is different in the case of the Earth. Plugging in the parameters for the Earth $\rho(0)_\oplus = 13.1 \text{ g/cm}^3$, $T_\oplus = 6000 \text{ }^\circ\text{C}$, we see that

$$r_X \approx 0.24 R_\oplus \sqrt{\frac{10 \text{ GeV}}{m_X}}. \quad (5.2.9)$$

The WIMP distribution is considerably more broad relative to the size of the body. For the case of the Earth, it is more likely for WIMP annihilation to take place in locations further away from the core and the approximation for a single common baseline for these neutrinos no longer holds very well.

The WIMP annihilation induced neutrino signal is modeled using the WimpSim [34] Monte Carlo simulation software. Figures 5.13 to 5.18 and Figures 5.19 to 5.24 show the directional flux spectra for neutrino flavors ν_e , $\bar{\nu}_e$, ν_μ , $\bar{\nu}_\mu$ produced from WIMPs (XX) with masses 1 GeV, 10 GeV and 100 GeV annihilating through the sample channels

- $\text{XX} \longrightarrow \nu_e \bar{\nu}_e$
- $\text{XX} \longrightarrow \nu_\mu \bar{\nu}_\mu$
- $\text{XX} \longrightarrow \text{b}\bar{\text{b}}$
- $\text{XX} \longrightarrow \tau^- \tau^+$,

where Figures 5.13 to 5.18 are those for annihilations in the Earth and Figures 5.19 to 5.24 are those for annihilations in the Sun. For the case of flux originating from annihilations in the Earth, a clear distinction can be seen in the angular distribution of neutrino fluxes in which the heavier WIMPs tend to concentrate more near the vicinity of the Earth's core when in equilibrium and hence produce a signal neutrino flux profile that is more peaked in

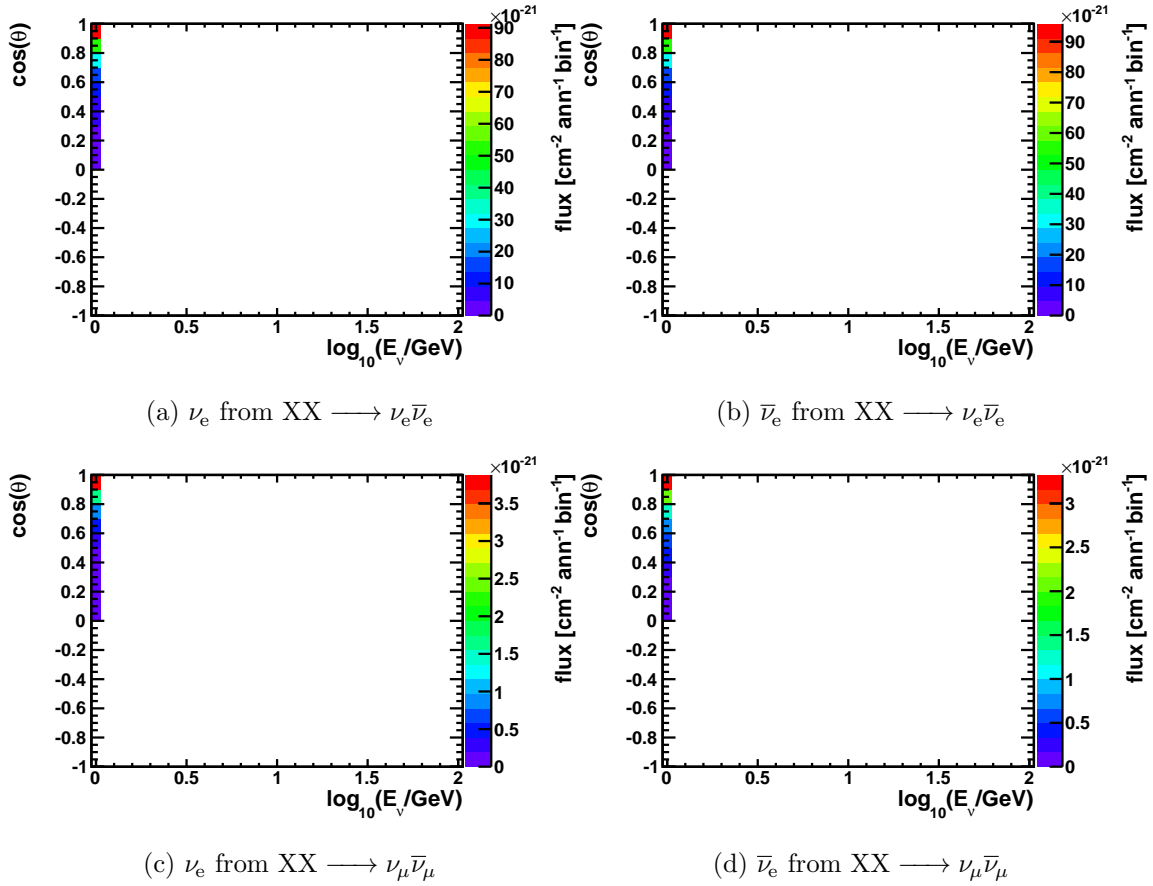


Figure 5.13: Directional spectra for ν_e , $\bar{\nu}_e$ from 1 GeV WIMPs (XX) annihilating in the Earth through sample channels. $\cos(\theta) = 1$ indicates the direction toward the Earth's core.

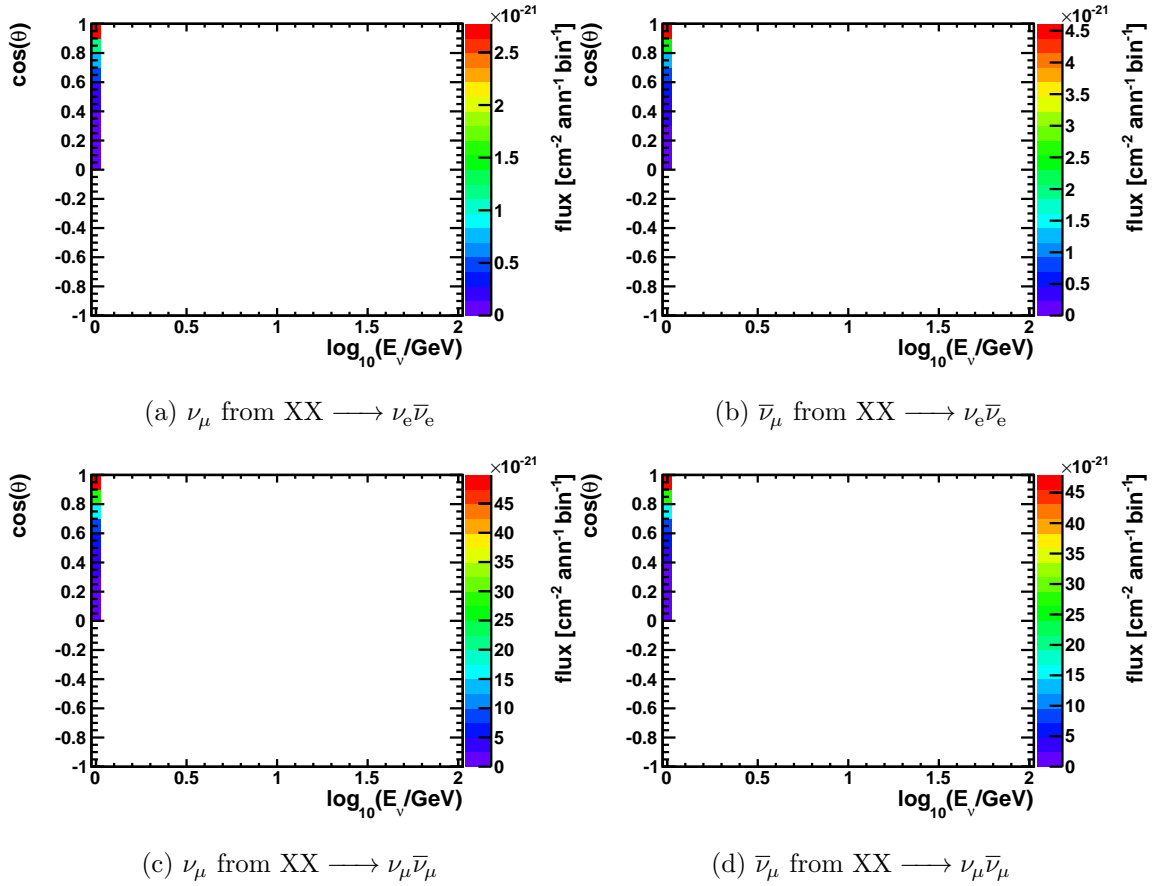


Figure 5.14: Directional spectra for ν_μ , $\bar{\nu}_\mu$ from 1 GeV WIMPs (XX) annihilating in the Earth through sample channels. $\cos(\theta) = 1$ indicates the direction toward the Earth's core.

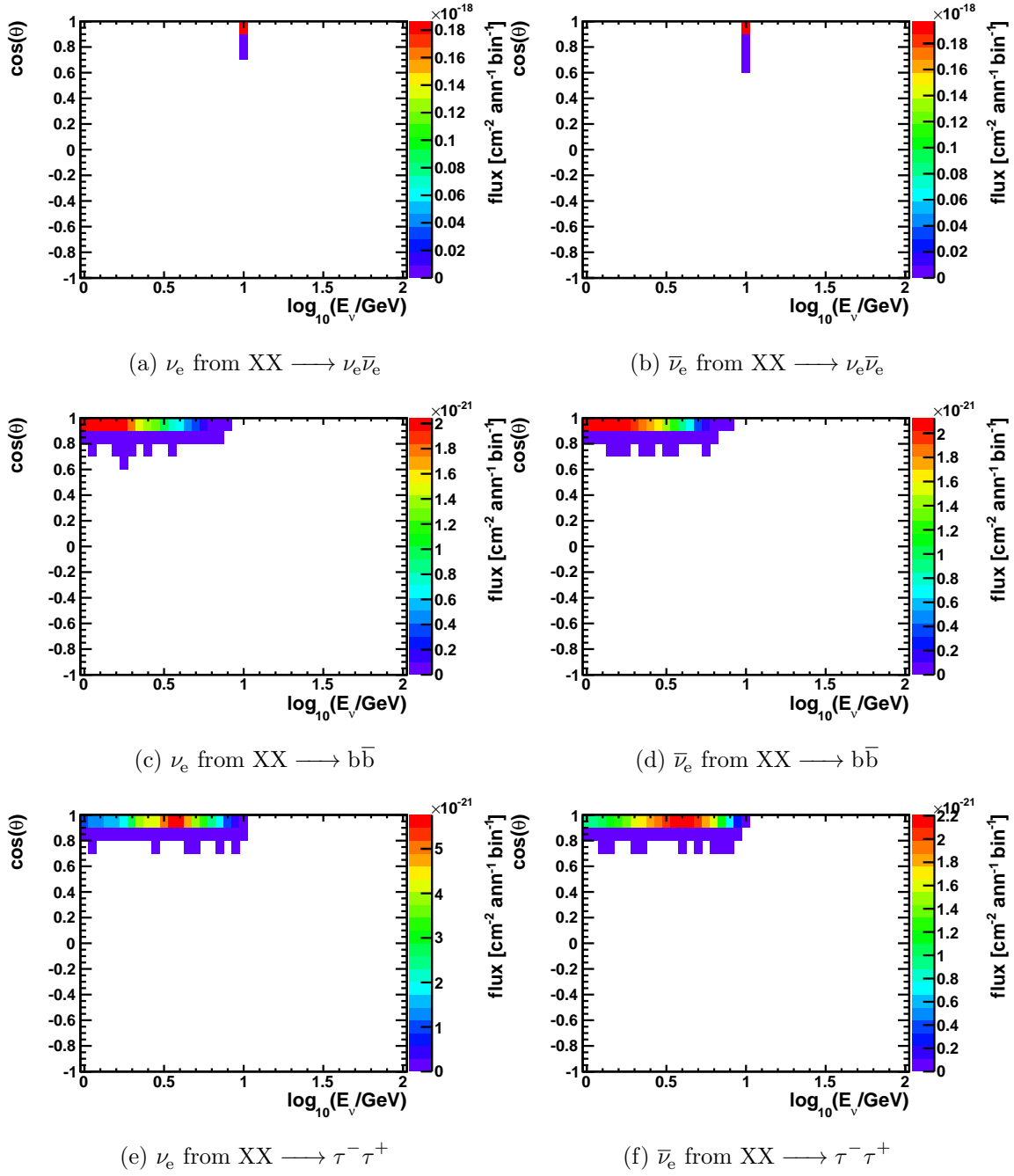


Figure 5.15: Directional spectra for ν_e , $\bar{\nu}_e$ from 10 GeV WIMPs (XX) annihilating in the Earth through sample channels. $\cos(\theta) = 1$ indicates the direction toward the Earth's core.

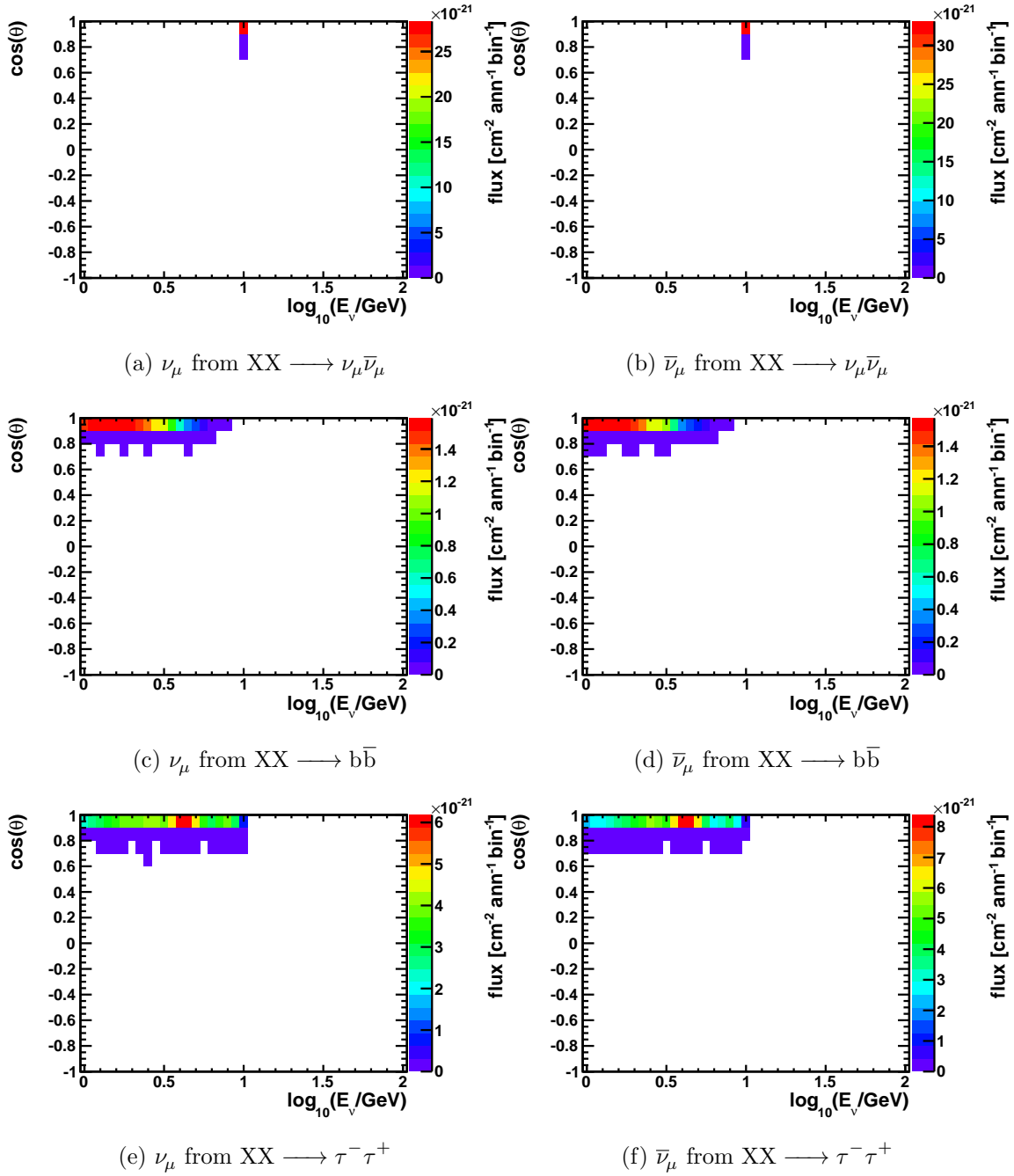


Figure 5.16: Directional spectra for ν_μ , $\bar{\nu}_\mu$ from 10 GeV WIMPs (XX) annihilating in the Earth through sample channels. $\cos(\theta) = 1$ indicates the direction toward the Earth's core.

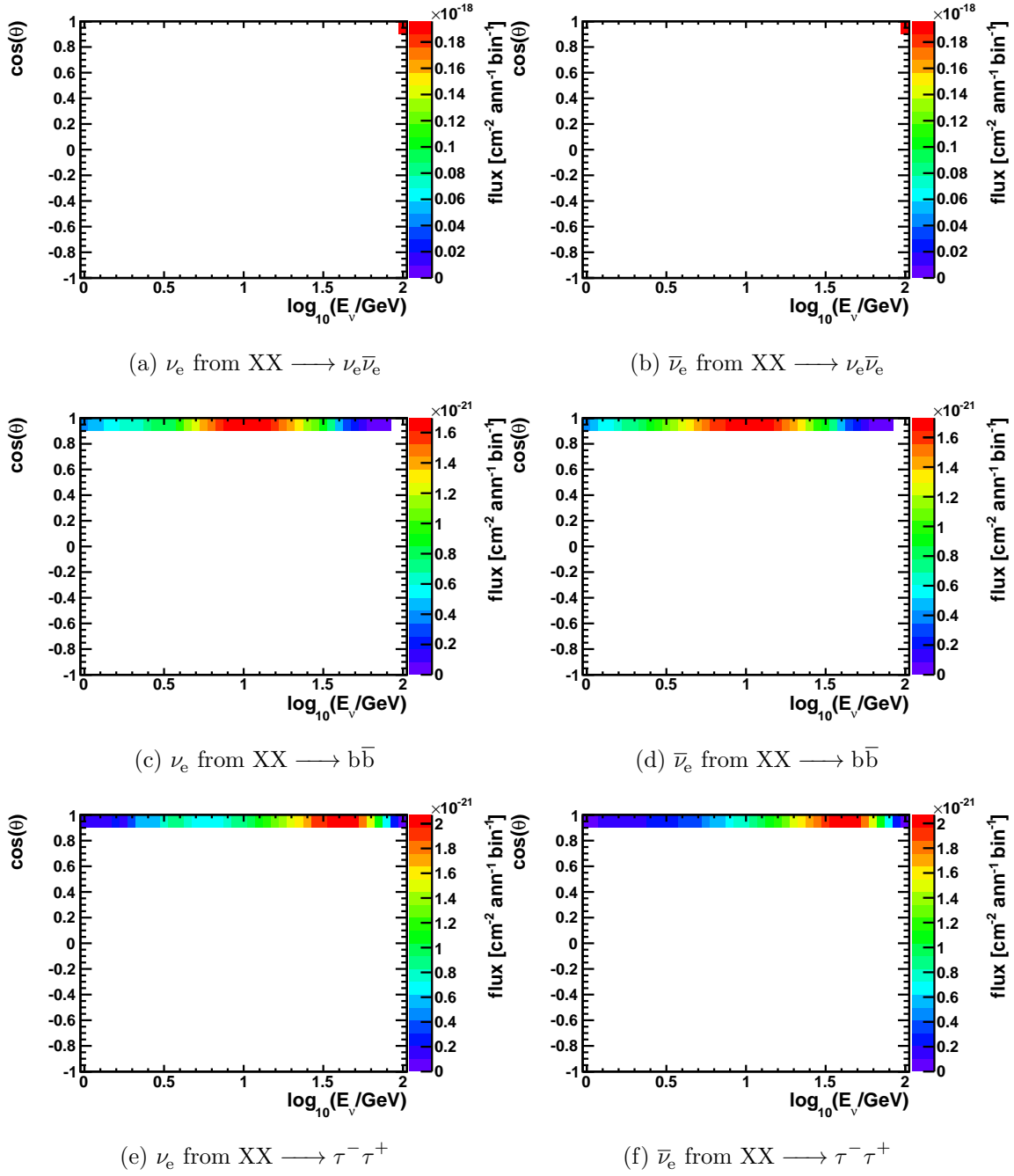


Figure 5.17: Directional spectra for ν_e , $\bar{\nu}_e$ from 100 GeV WIMPs (XX) annihilating in the Earth through sample channels. $\cos(\theta) = 1$ indicates the direction toward the Earth's core.

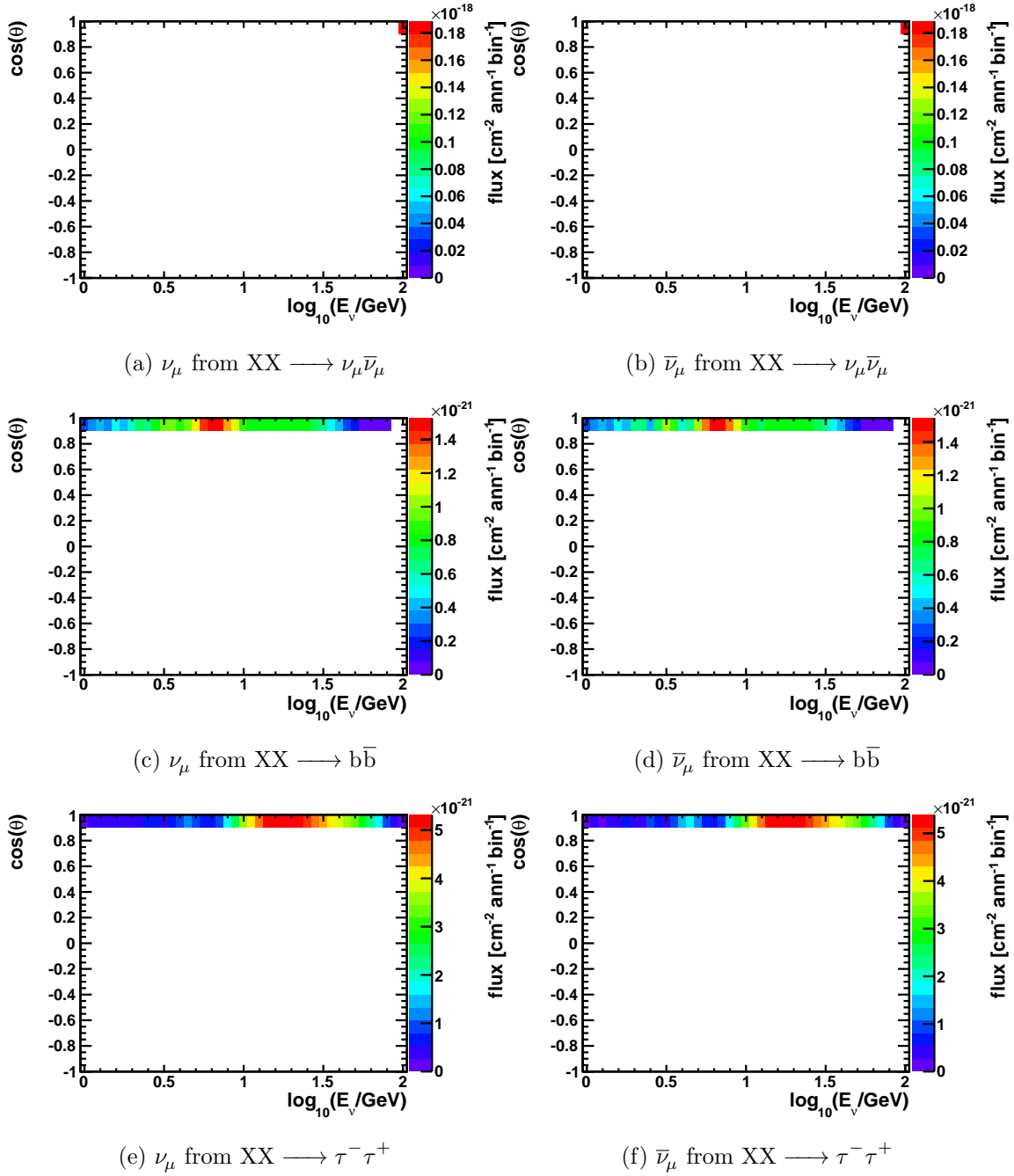


Figure 5.18: Directional spectra for $\nu_\mu, \bar{\nu}_\mu$ from 100 GeV WIMPs (XX) annihilating in the Earth through sample channels. $\cos(\theta) = 1$ indicates the direction toward the Earth's core.

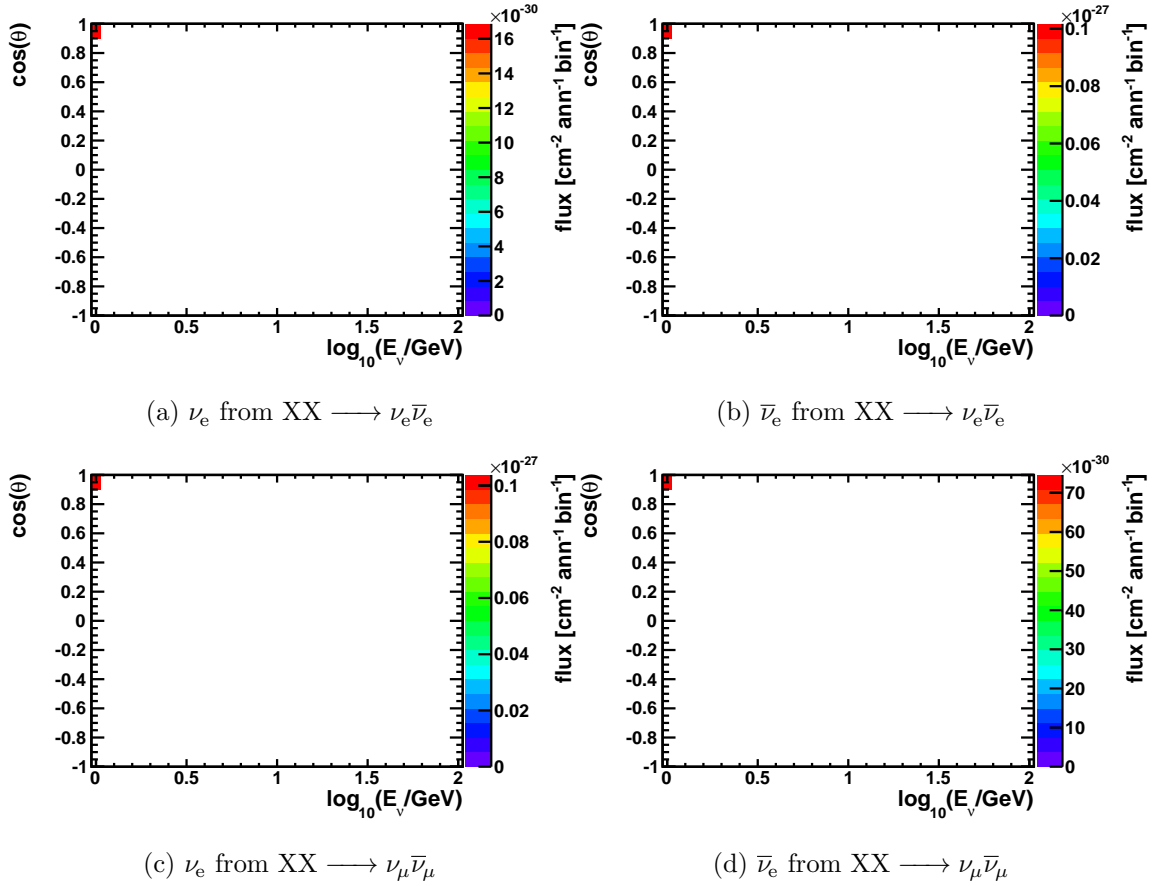


Figure 5.19: Directional spectra for ν_e , $\bar{\nu}_e$ from 1 GeV WIMPs (XX) annihilating in the Sun through sample channels. $\cos(\theta) = 1$ indicates the direction toward the Sun's core.

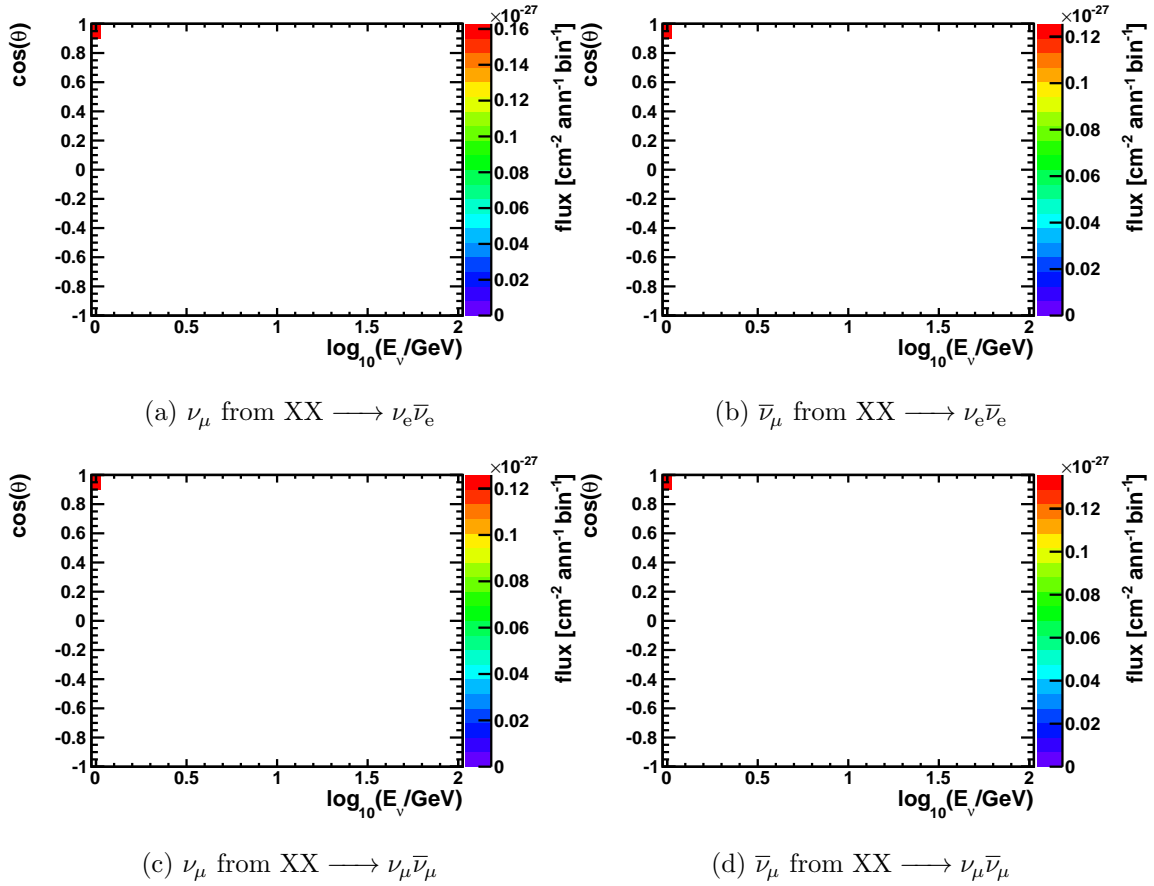


Figure 5.20: Directional spectra for ν_μ , $\bar{\nu}_\mu$ from 1 GeV WIMPs (XX) annihilating in the Sun through sample channels. $\cos(\theta) = 1$ indicates the direction toward the Sun's core.

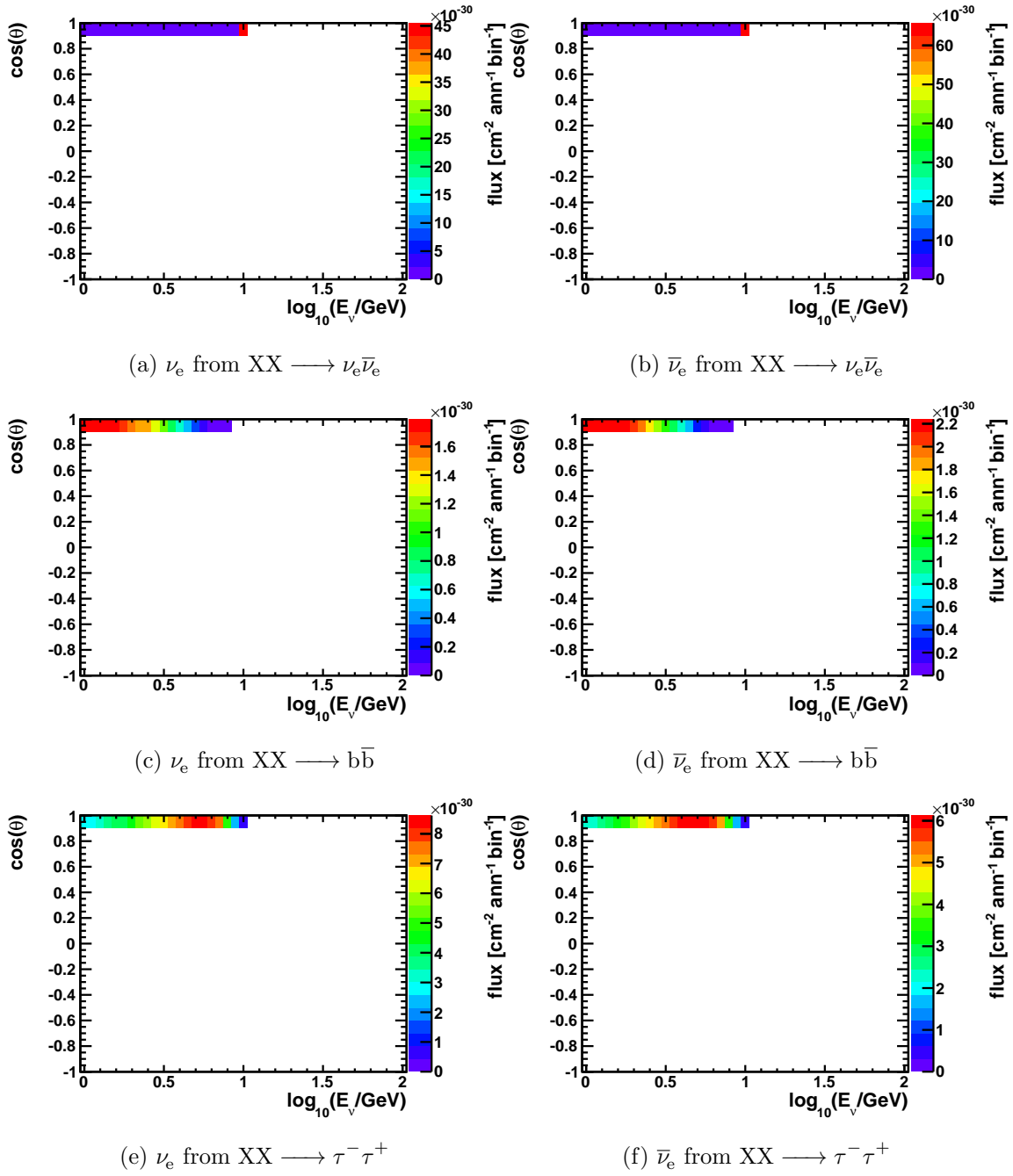


Figure 5.21: Directional spectra for ν_e , $\bar{\nu}_e$ from 10 GeV WIMPs (XX) annihilating in the Sun through sample channels. $\cos(\theta) = 1$ indicates the direction toward the Sun's core.

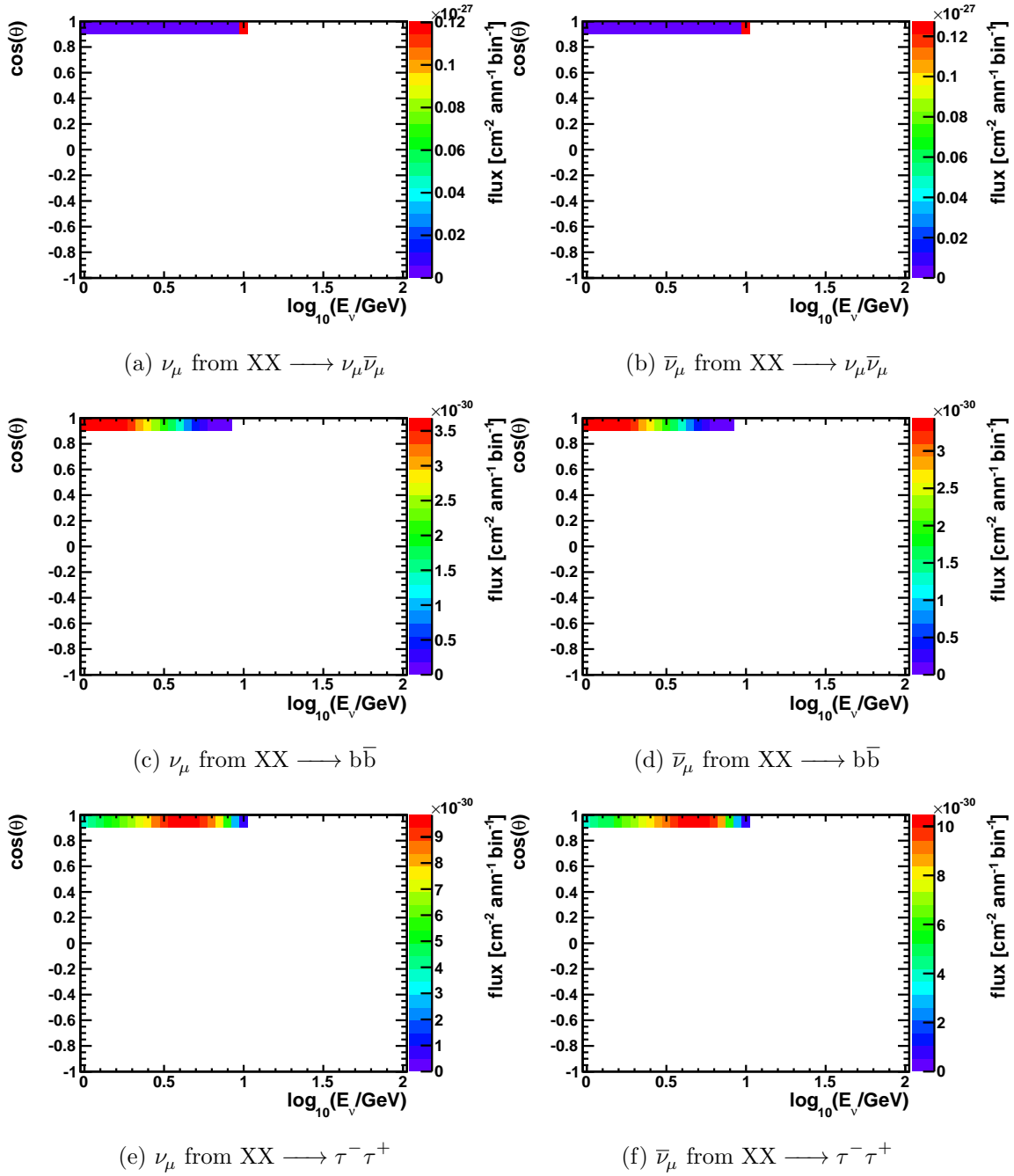


Figure 5.22: Directional spectra for ν_μ , $\bar{\nu}_\mu$ from 10 GeV WIMPs (XX) annihilating in the Sun through sample channels. $\cos(\theta) = 1$ indicates the direction toward the Sun's core.

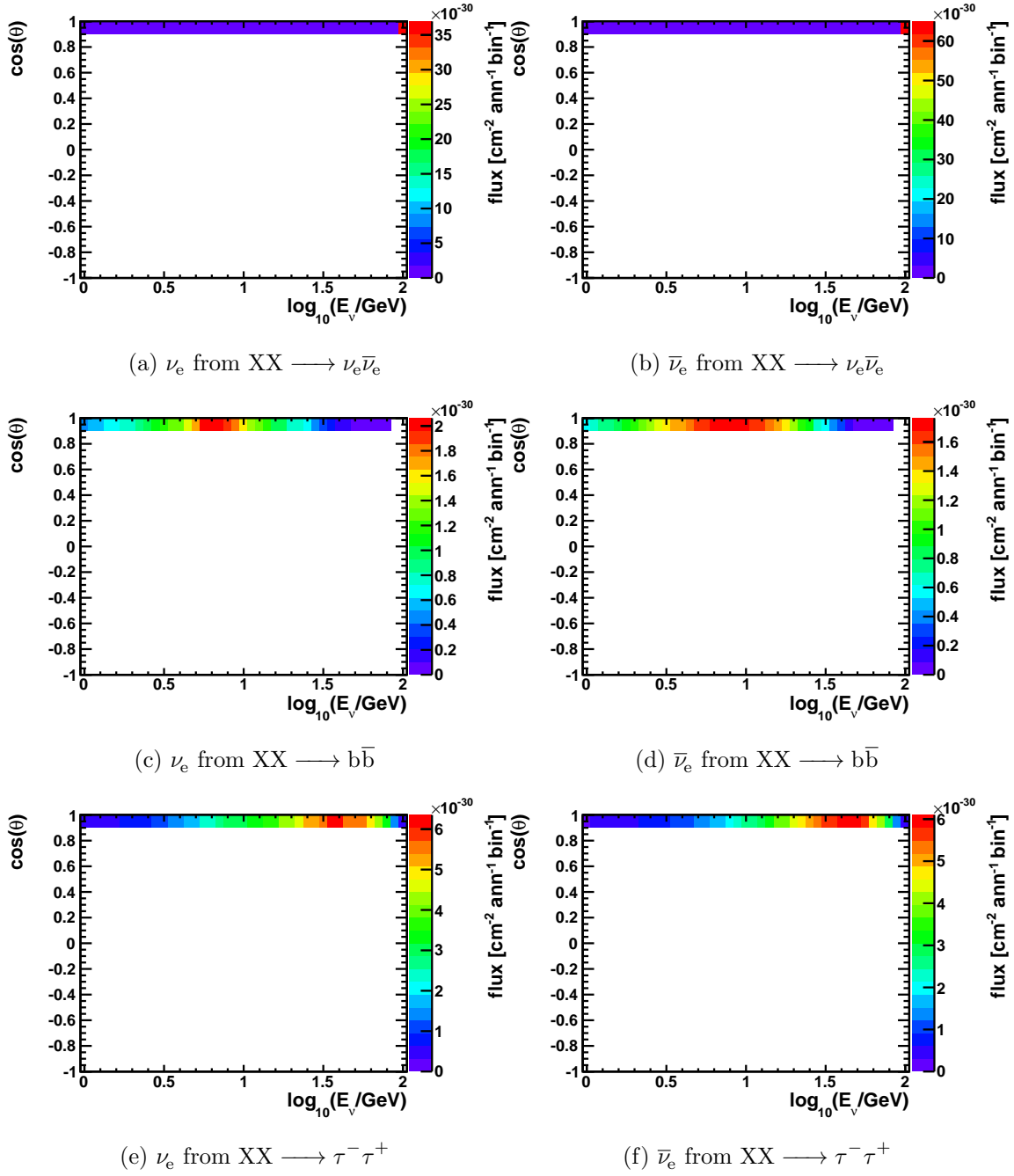


Figure 5.23: Directional spectra for ν_e , $\bar{\nu}_e$ from 100 GeV WIMPs (XX) annihilating in the Sun through sample channels. $\cos(\theta) = 1$ indicates the direction toward the Sun's core.

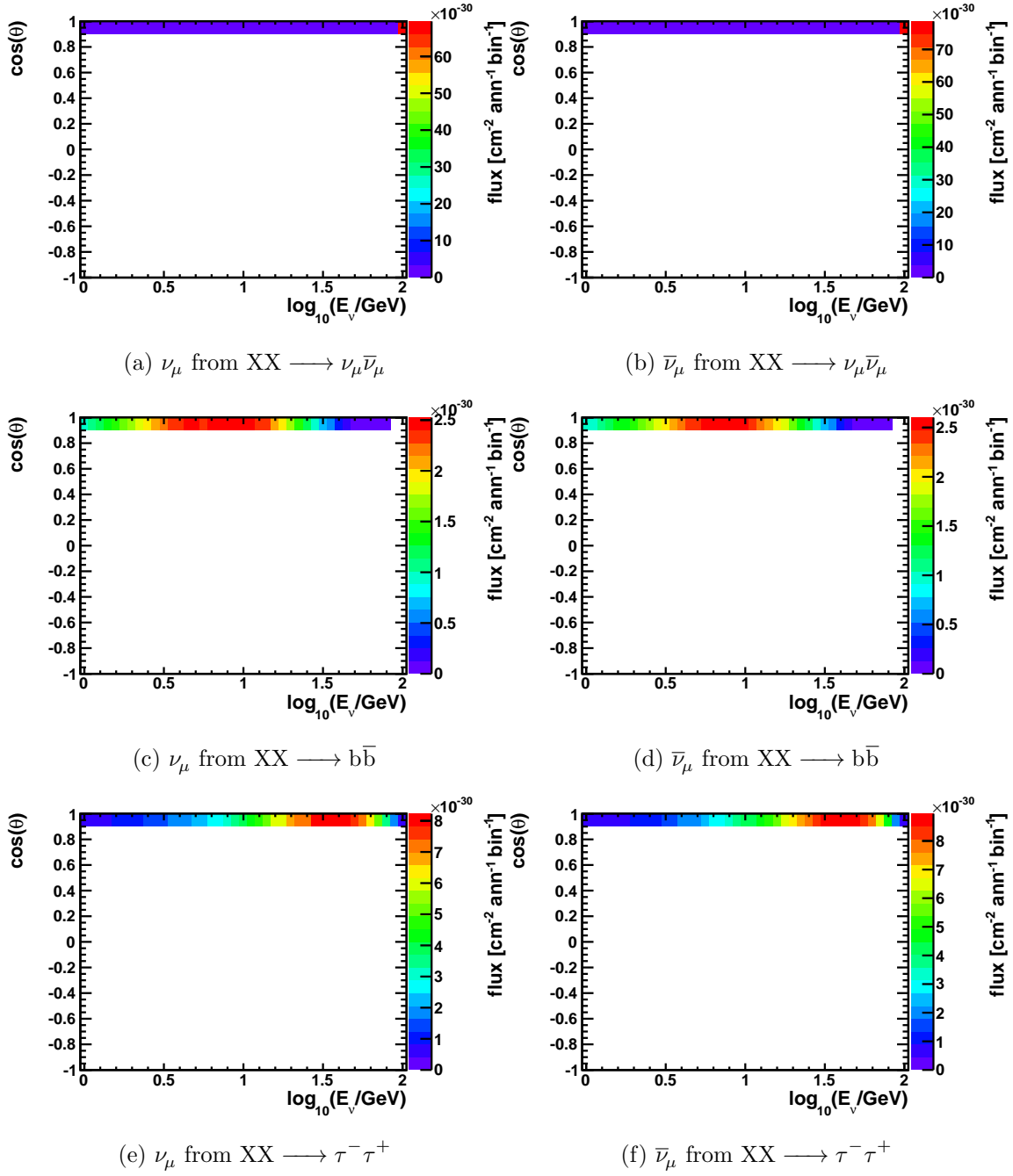


Figure 5.24: Directional spectra for $\nu_\mu, \bar{\nu}_\mu$ from 100 GeV WIMPs (XX) annihilating in the Sun through sample channels. $\cos(\theta) = 1$ indicates the direction toward the Sun's core.

the direction toward the core. On the other hand, this distinction is not so prominent for neutrinos originating from annihilations in the Sun and all three WIMP masses of 1 GeV, 10 GeV and 100 GeV tend to produce signal flux profiles that are more or less similarly peaked in the direction toward the Sun's core.

The corresponding fluxes with detector effects taken into account, such as the efficiency for events to be fully contained, the efficiency for the vertex to be reconstructed within the fiducial volume, and the energy dependent directional resolution, are shown in Figures 5.25 to 5.30 and Figures 5.31 to 5.36 . Details of the detector effects are explained in Section 6.8 and Section 4.8.5.

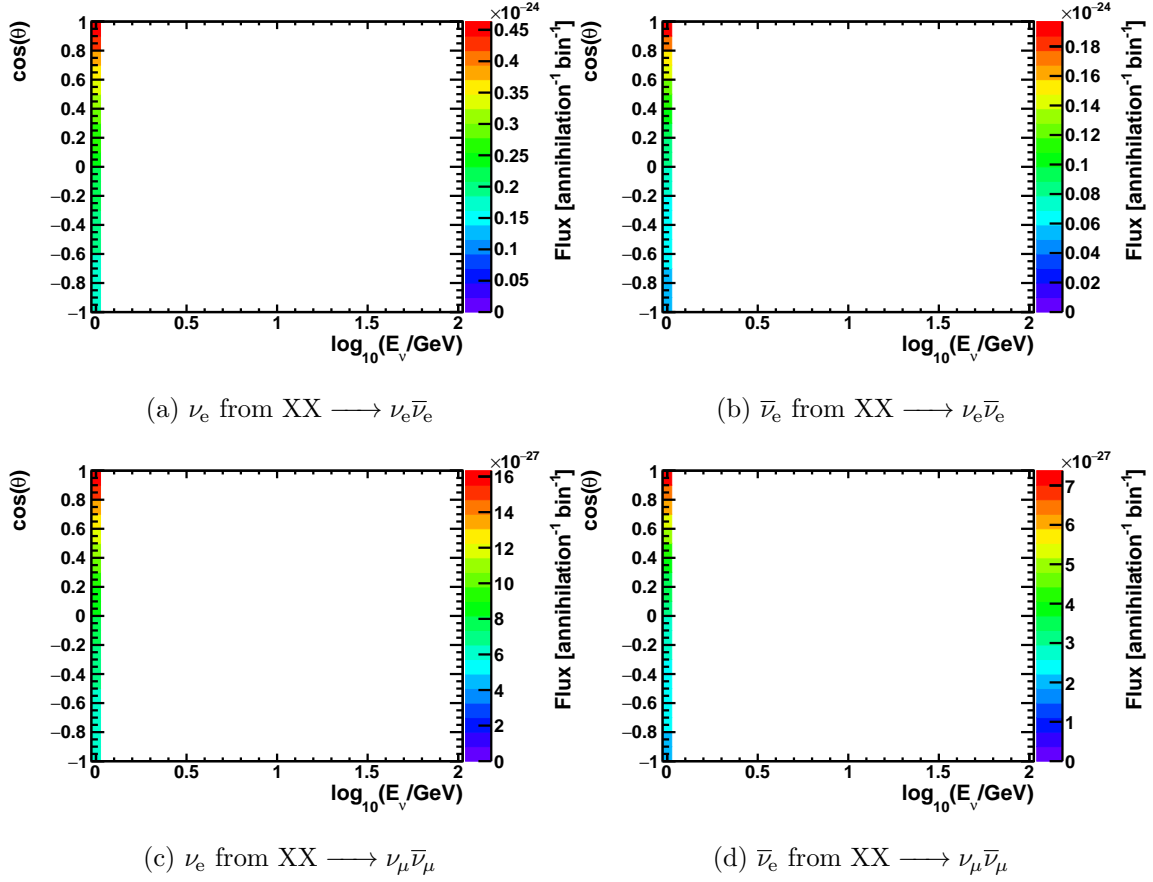


Figure 5.25: Directional spectra for ν_e , $\bar{\nu}_e$ from 1 GeV WIMPs (XX) annihilating in the Earth through sample channels with detector effects taken into account. $\cos(\theta) = 1$ indicates the direction toward the Earth's core.

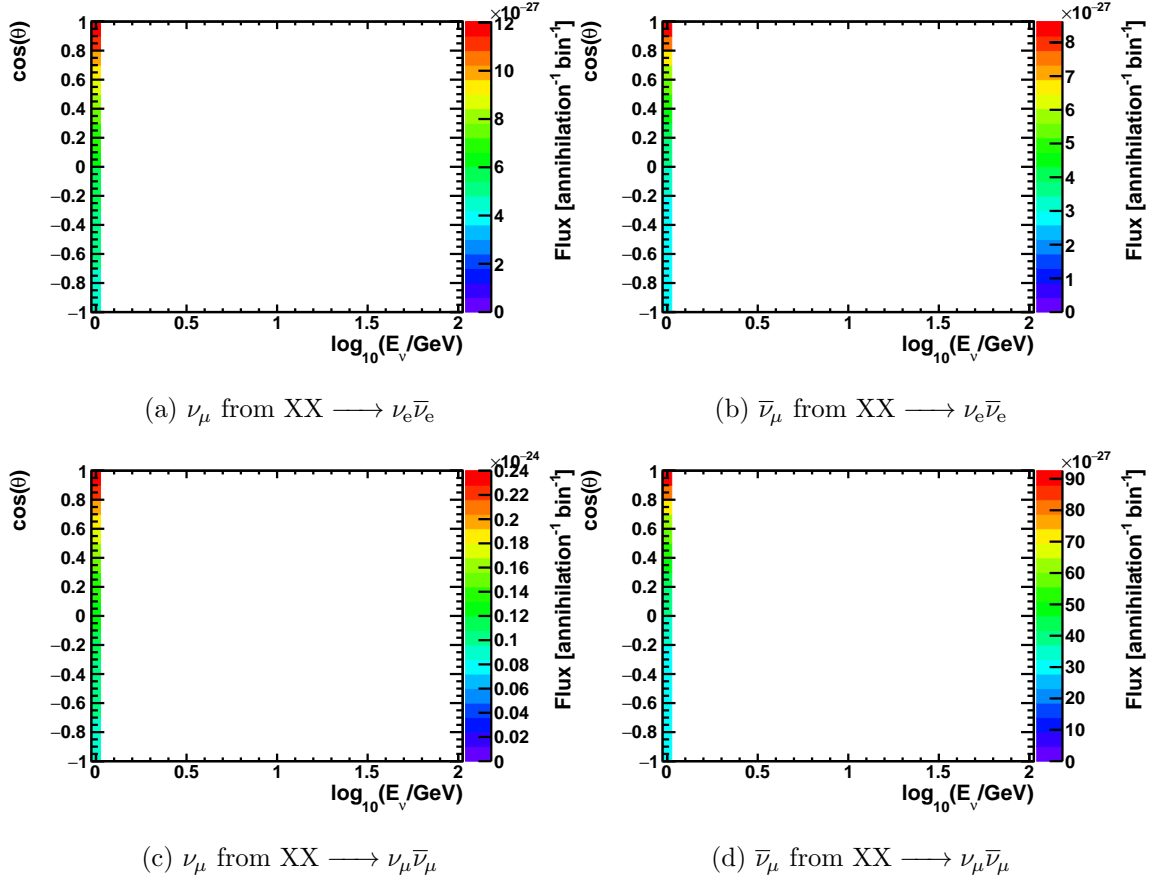


Figure 5.26: Directional spectra for ν_μ , $\bar{\nu}_\mu$ from 1 GeV WIMPs (XX) annihilating in the Earth through sample channels with detector effects taken into account. $\cos(\theta) = 1$ indicates the direction toward the Earth's core.

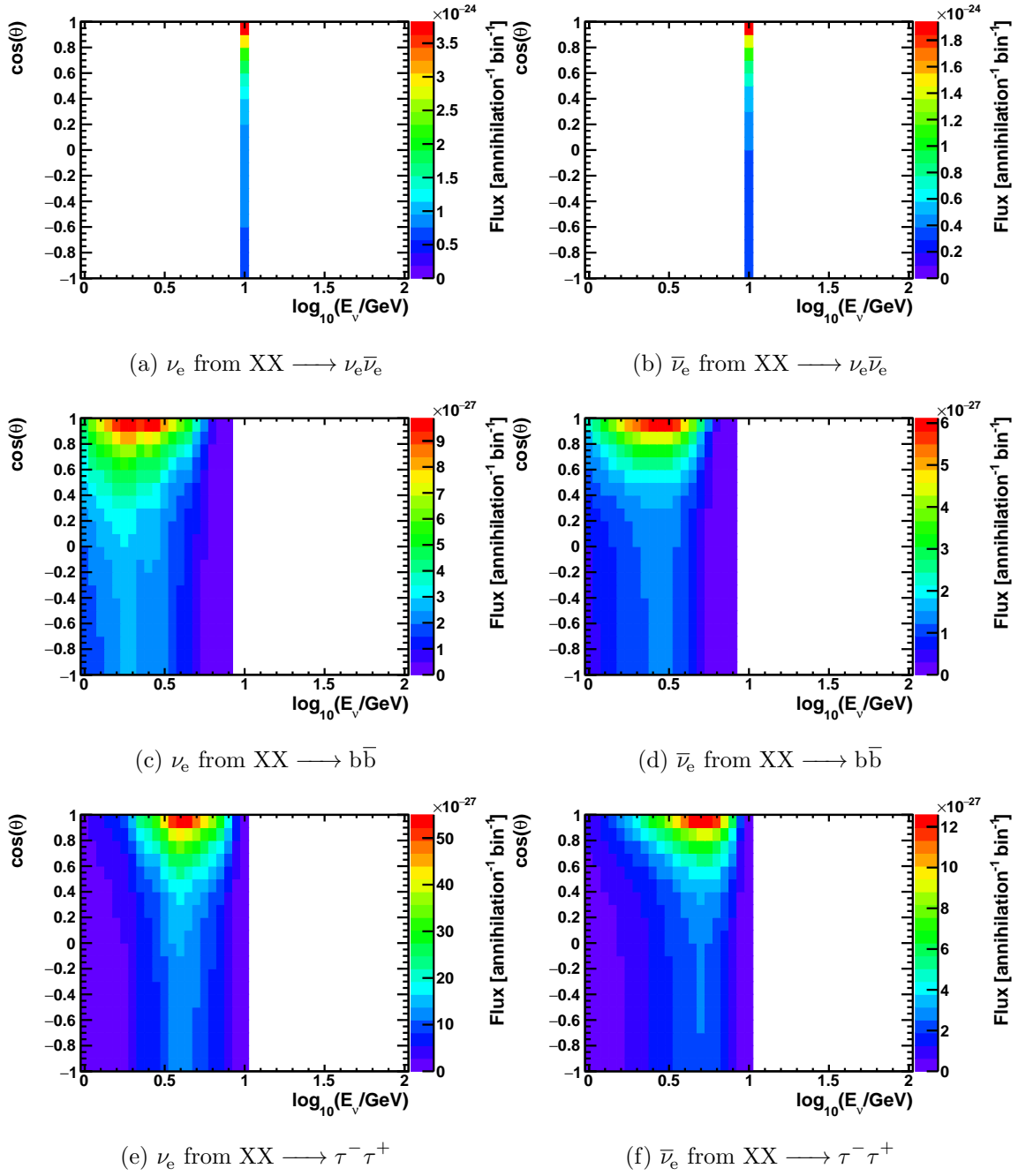


Figure 5.27: Directional spectra for ν_e , $\bar{\nu}_e$ from 10 GeV WIMPs (XX) annihilating in the Earth through sample channels with detector effects taken into account. $\cos(\theta) = 1$ indicates the direction toward the Earth’s core.

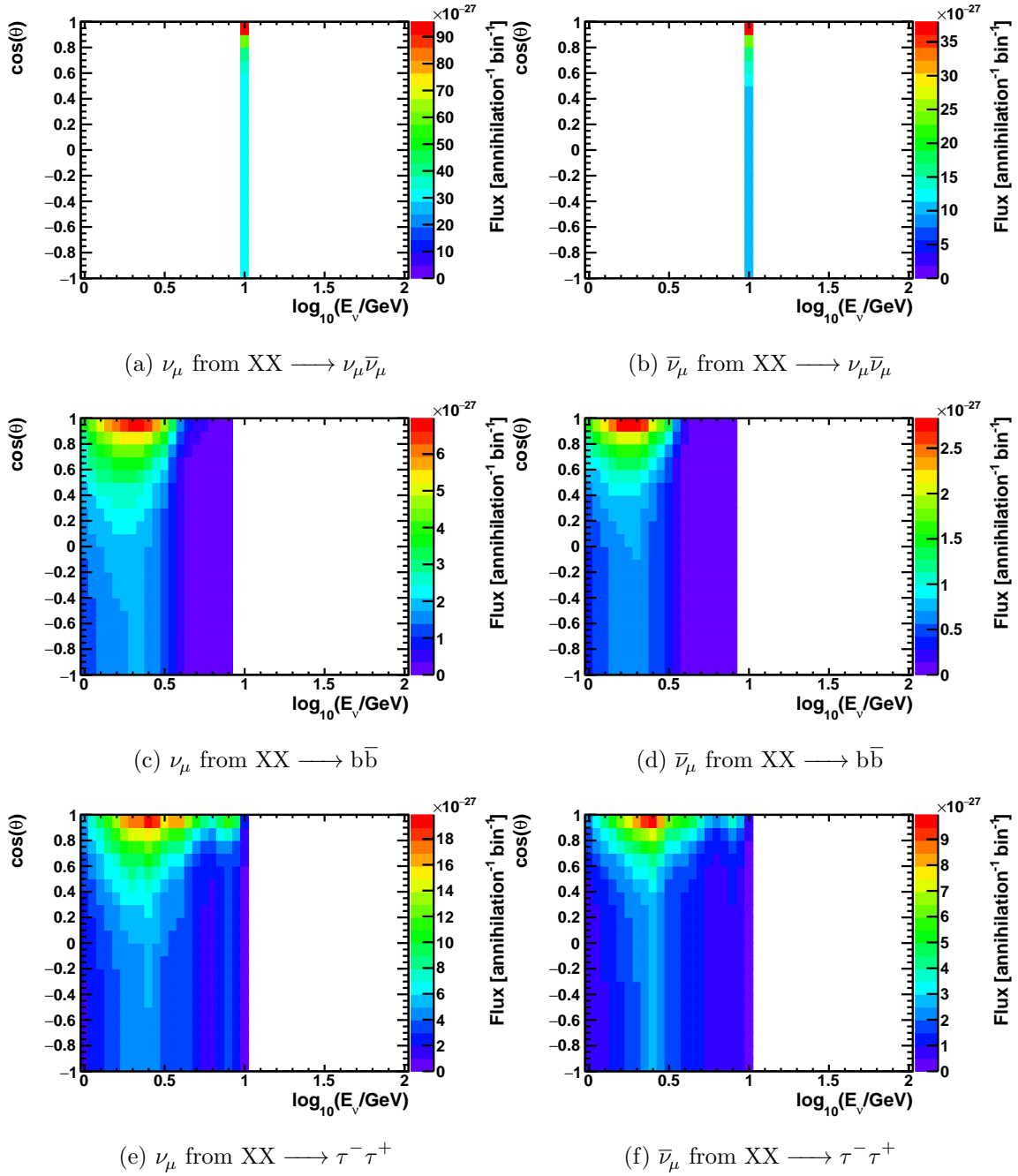


Figure 5.28: Directional spectra for ν_μ , $\bar{\nu}_\mu$ from 10 GeV WIMPs (XX) annihilating in the Earth through sample channels with detector effects taken into account. $\cos(\theta) = 1$ indicates the direction toward the Earth's core.

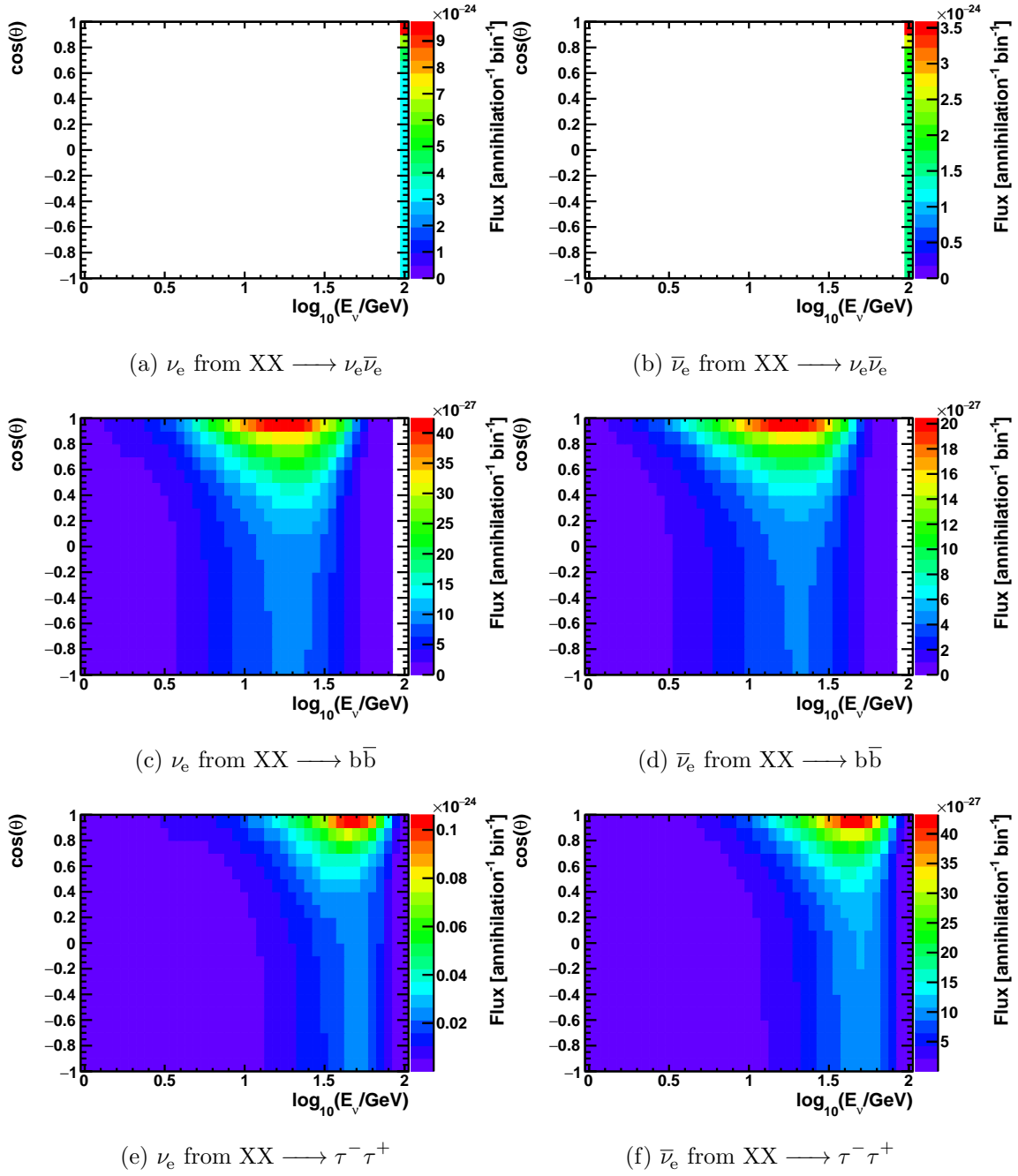


Figure 5.29: Directional spectra for ν_e , $\bar{\nu}_e$ from 100 GeV WIMPs (XX) annihilating in the Earth through sample channels with detector effects taken into account. $\cos(\theta) = 1$ indicates the direction toward the Earth's core.

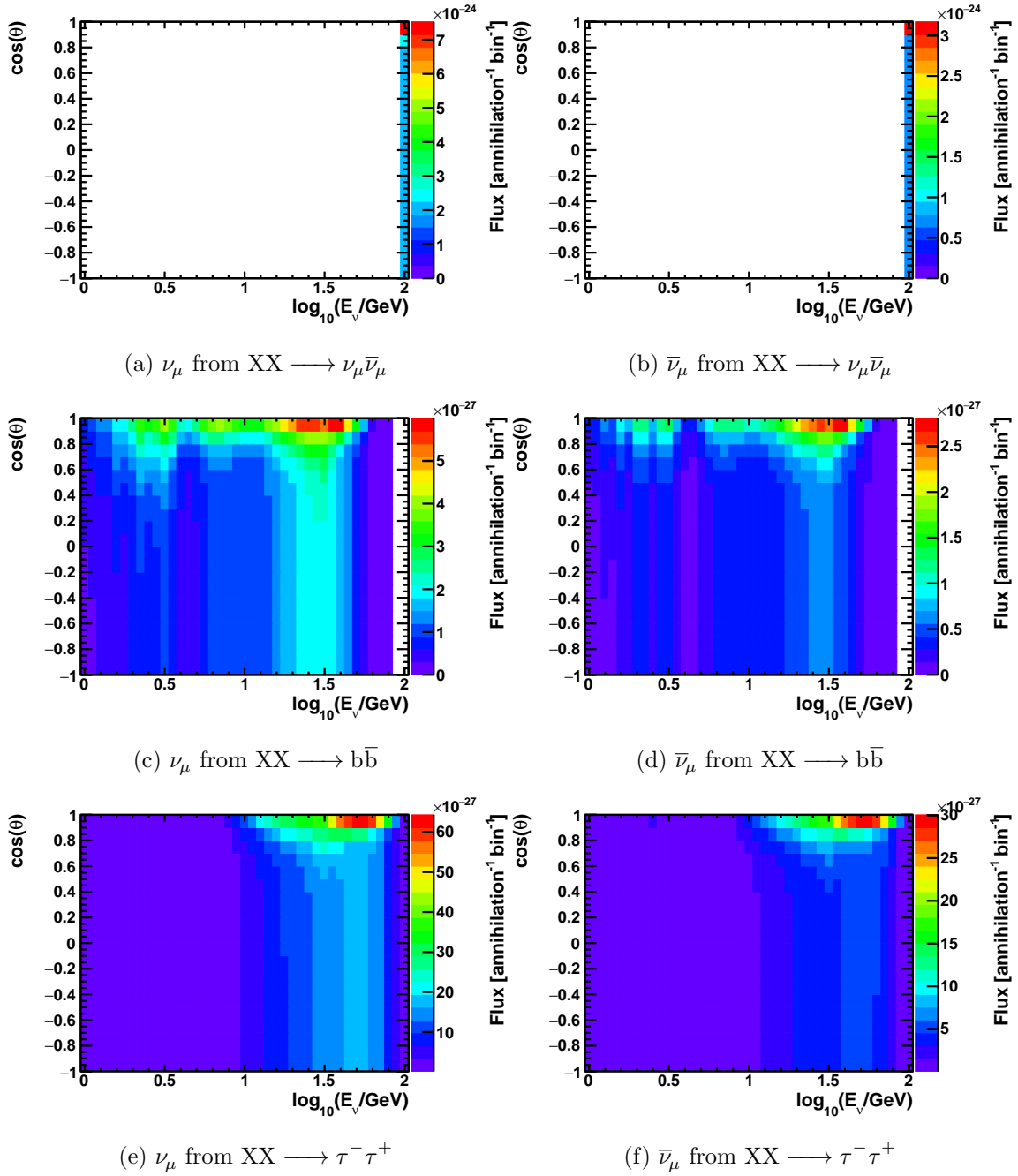


Figure 5.30: Directional spectra for $\nu_\mu, \bar{\nu}_\mu$ from 100 GeV WIMPs (XX) annihilating in the Earth through sample channels with detector effects taken into account. $\cos(\theta) = 1$ indicates the direction toward the Earth's core.

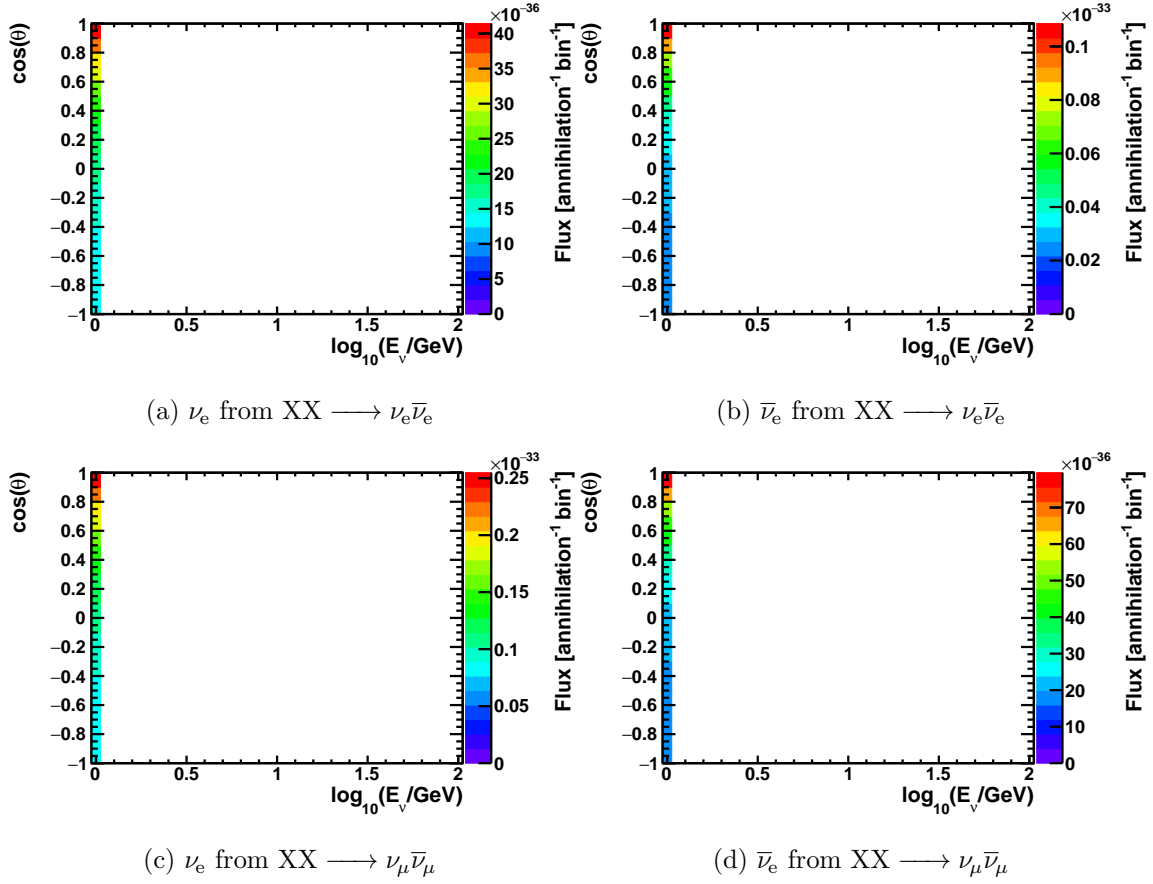


Figure 5.31: Directional spectra for ν_e , $\bar{\nu}_e$ from 1 GeV WIMPs (XX) annihilating in the Sun through sample channels with detector effects taken into account. $\cos(\theta) = 1$ indicates the direction toward the Sun's core.

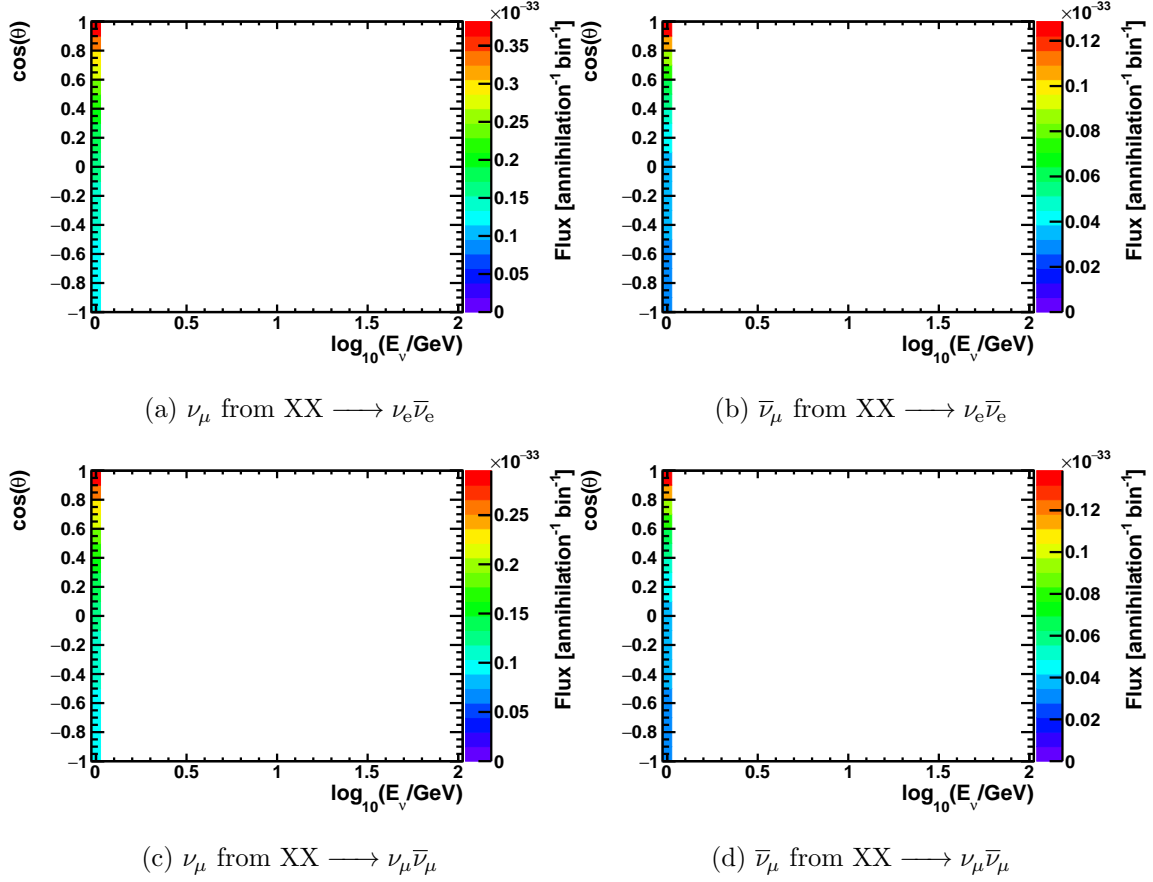


Figure 5.32: Directional spectra for ν_μ , $\bar{\nu}_\mu$ from 1 GeV WIMPs (XX) annihilating in the Sun through sample channels with detector effects taken into account. $\cos(\theta) = 1$ indicates the direction toward the Sun's core.

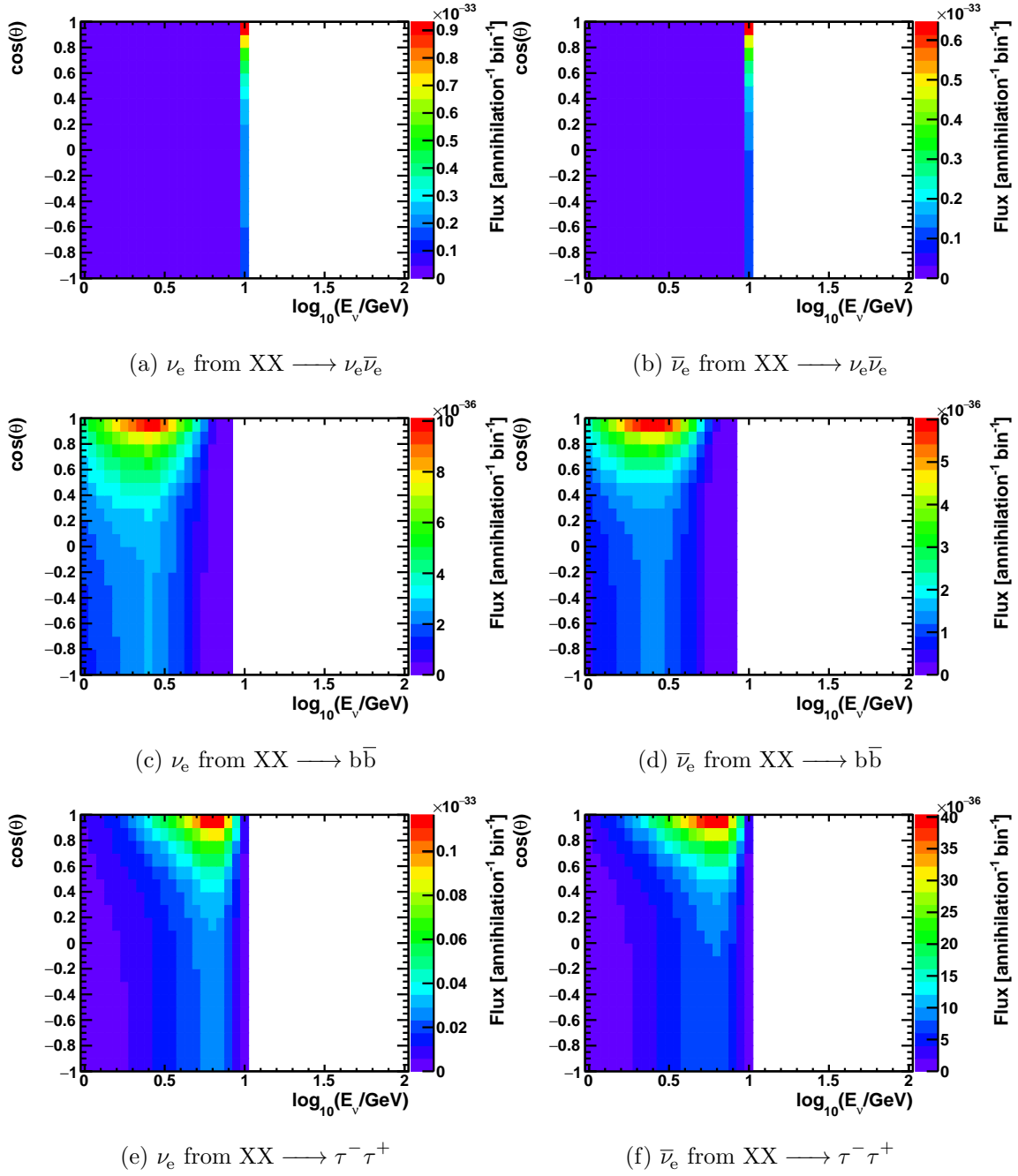


Figure 5.33: Directional spectra for ν_e , $\bar{\nu}_e$ from 10 GeV WIMPs (XX) annihilating in the Sun through sample channels with detector effects taken into account. $\cos(\theta) = 1$ indicates the direction toward the Sun's core.

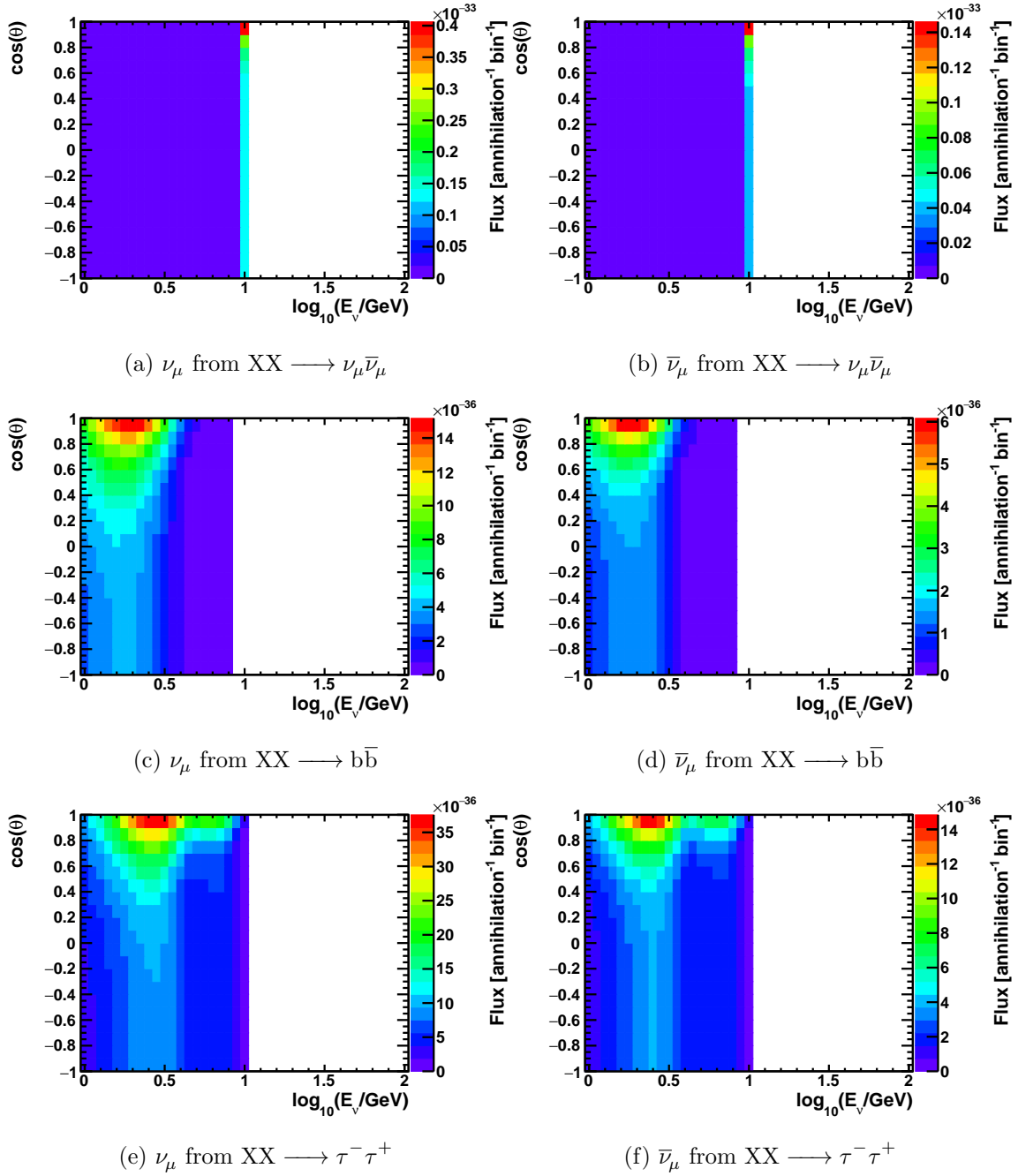


Figure 5.34: Directional spectra for ν_μ , $\bar{\nu}_\mu$ from 10 GeV WIMPs (XX) annihilating in the Sun through sample channels with detector effects taken into account. $\cos(\theta) = 1$ indicates the direction toward the Sun's core.

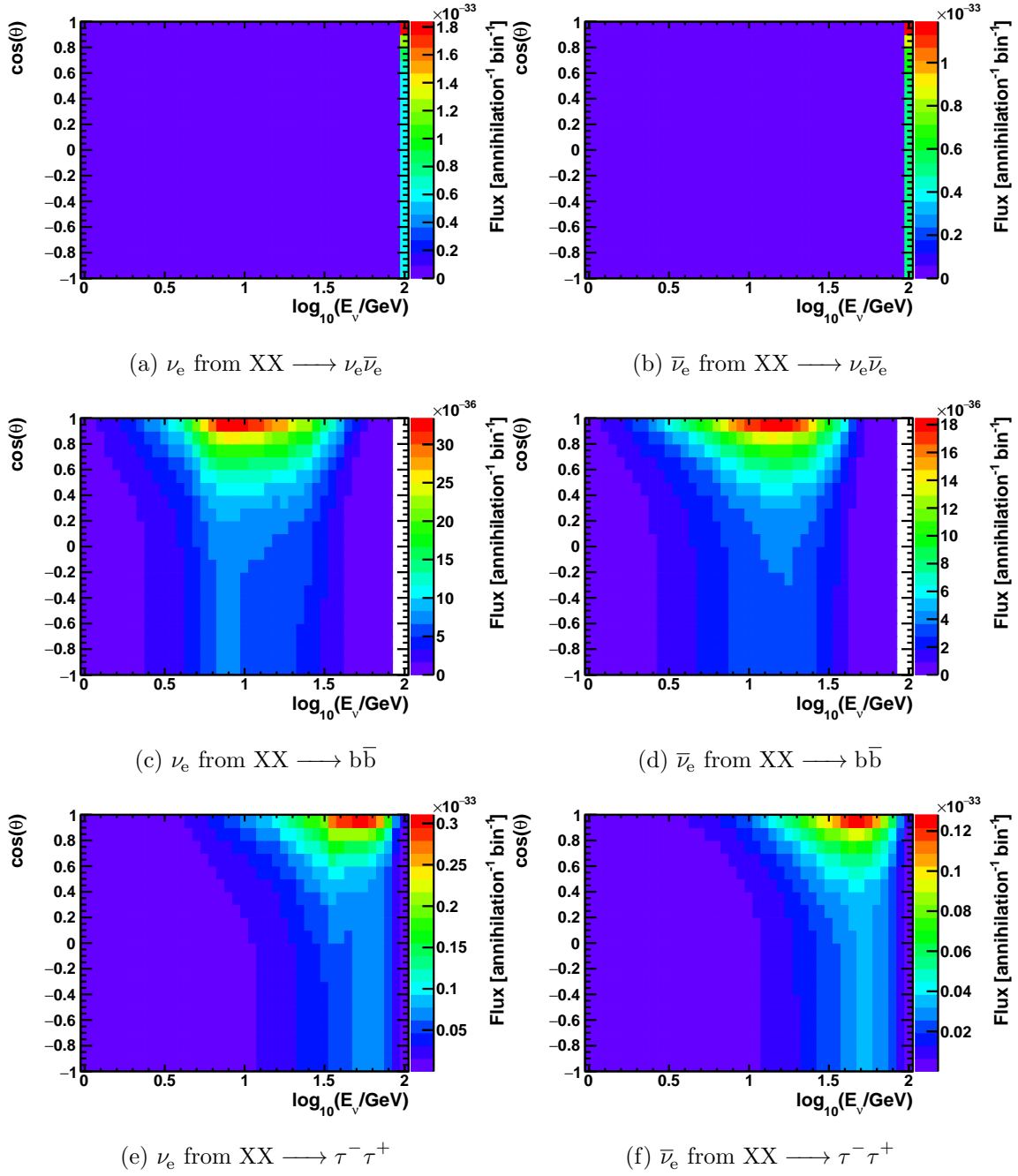


Figure 5.35: Directional spectra for ν_e , $\bar{\nu}_e$ from 100 GeV WIMPs (XX) annihilating in the Sun through sample channels with detector effects taken into account. $\cos(\theta) = 1$ indicates the direction toward the Sun's core.

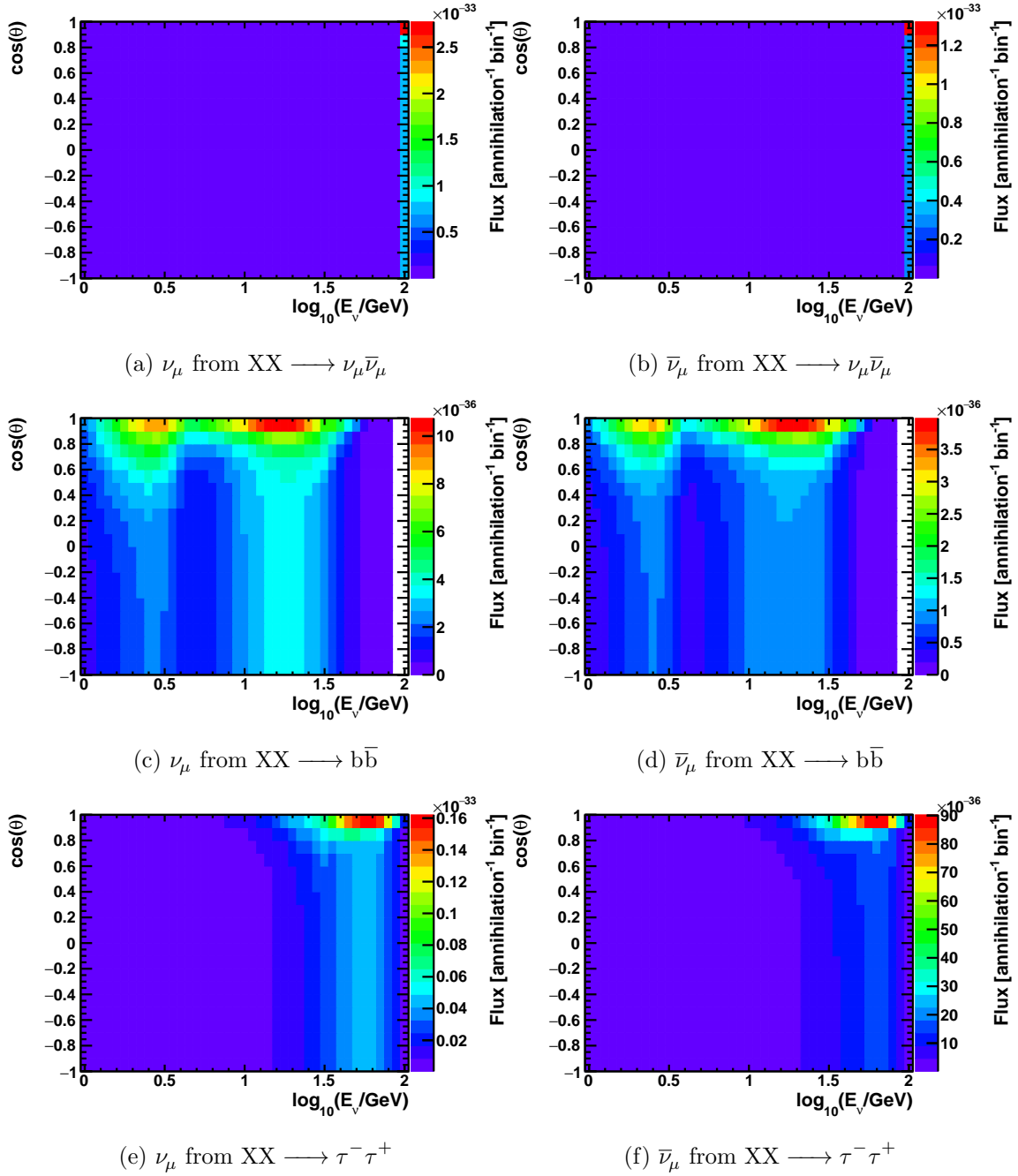


Figure 5.36: Directional spectra for $\nu_\mu, \bar{\nu}_\mu$ from 100 GeV WIMPs (XX) annihilating in the Sun through sample channels with detector effects taken into account. $\cos(\theta) = 1$ indicates the direction toward the Sun's core.

Chapter 6

Analysis

6.1 Event rate equation

Foremost, we use the typical assumption found in literature that the astronomical body in question, be it the Sun or Earth, is in thermal equilibrium with respect to the accumulation of dark matter through the rate of its capture Γ_C and depletion through the annihilation rate Γ_A ,

$$\Gamma_C = 2\Gamma_A. \quad (6.1.1)$$

We can think of this analysis in terms of a bound on the signal event rate at the detector. The signal event rate can be expressed as

$$\text{rate}_{\text{signal}} = \Gamma_A \sum_i \sum_\nu \left[B_i \int_{E_{\text{threshold}}}^{E_X} dE \frac{dN_{i,\nu}(E)}{dE} \frac{\sigma_\nu^{\text{eff}}(E)}{4\pi R^2} \right], \quad (6.1.2)$$

where i is the annihilation channel into some pair of matter and antimatter products, ν is the neutrino flavor, B_i is the branching fraction to annihilation channel i , E is the energy of the neutrino, $N_{i,\nu}$ is the neutrino yield of flavor ν per annihilation for a given channel i , $\sigma_\nu^{\text{eff}}(E)$ is the effective detector cross section for a neutrino of flavor ν and energy E , and R is the distance from the detector to the signal source of interest. The integral can be thought of as being taken from some lower bound energy threshold $E_{\text{threshold}}$ to the weakly interacting massive particle (WIMP) mass E_X . $E_{\text{threshold}}$ is an arbitrary parameter set high enough to exclude as much atmospheric neutrino background as possible while at the

same time being low enough to include neutrinos from WIMP annihilation of which our signal consists. For the sake of this analysis we will examine each annihilation channel i individually and assume that $B_i = 1$ for the channel of interest so Equation (6.1.2) can be simplified as the following for a single channel

$$\text{rate}_{\text{signal}} = \Gamma_A \sum_{\nu} \left[\int_{E_{\text{threshold}}}^{E_X} dE \frac{dN_{\nu}(E)}{dE} \frac{\sigma_{\nu}^{\text{eff}}(E)}{4\pi R^2} \right]. \quad (6.1.3)$$

The location of annihilation and hence neutrino production is most probable at the center of the astronomical body. However there is some finite distribution in this location which may be pronounced, such as in the case of the Earth where the gravitational potential well is not as deep as that of the Sun. Moreover even in the case of the Sun where the location of WIMP annihilation is fairly constrained to be in the vicinity of the Sun's core, the eccentric orbit of the Earth around the Sun and the Earth's rotation itself will induce a varying baseline R by the time the neutrinos reach the detector. Therefore R is strictly speaking, not a constant but varies depending on the given neutrino. In order to take this effect into account, the neutrino yield per unit area $N_{\nu}(E)/(4\pi R^2)$ in Equation (6.1.3) should be replaced by

$$\frac{N_{\nu}(E)}{4\pi R^2} \longrightarrow \iint_{\text{body}} dl \, d\cos(\theta) \frac{\partial^2}{\partial l \, \partial \cos(\theta)} \left(\frac{N_{\nu}(E, l, \theta)}{4\pi l^2} \right), \quad (6.1.4)$$

where l represents the distance of the vector connecting the detector position and point of neutrino origin, and θ the angle of this vector with respect to the axis that runs through the detector and core of the body. The location of neutrino origin is now allowed to vary anywhere in the body and thus we can now rewrite Equation (6.1.3) as

$$\text{rate}_{\text{signal}} = \Gamma_A \sum_{\nu} \left\{ \int_{E_{\text{threshold}}}^{E_X} dE \frac{d}{dE} \left[\iint_{\text{body}} dl \, d\cos(\theta) \frac{\partial^2}{\partial l \, \partial \cos(\theta)} \left(\frac{N_{\nu}(E, l, \theta)}{4\pi l^2} \right) \right] \sigma_{\nu}^{\text{eff}}(E) \right\}. \quad (6.1.5)$$

The effective detector cross section $\sigma_{\nu}^{\text{eff}}(E)$ includes the detector efficiency but this in turn depends on not just the neutrino flavor ν and energy E , but also on the target nucleus that the neutrino interacts with. This is accounted for by the following equation

$$\sigma_{\nu}^{\text{eff}}(E) = \sum_j^{\text{elements}} \sigma_{\nu,j}^{\text{CC}}(E) \mathcal{E}_{\nu,j}(E) N_j^{\text{LS+BO}}, \quad (6.1.6)$$

where the index j runs over the two representative target elements Hydrogen and Carbon, $\sigma_{\nu,j}^{\text{CC}}(E)$ is the charged current scattering cross section for a given combination of neutrino flavor and target element shown in Figure 4.27, $\mathcal{E}_{\nu,j}(E)$ is the detector efficiency for charged current events to be fully contained inside the inner detector (ID) for the same combination of neutrino flavor and target element. This is shown in Figures 6.9 and 6.10. $N_j^{\text{LS+BO}}$ is the total number of target nuclei for element j in both the liquid scintillator (LS) and buffer oil (BO) combined as shown in Equations (6.7.32) and (6.7.33).

In practice the detector will have some finite resolution for reconstructing neutrino directions. We can use the spherical analog of the normal distribution to model this in a simple way and replace the differential neutrino yield with respect to the angle from the body core $\partial N_\nu(E, l, \theta) / \partial \cos(\theta)$ with one that is convolved with the directional resolution of the detector

$$\frac{\partial N_\nu(E, l, \theta)}{\partial \cos(\theta)} \longrightarrow \int_{\phi'=0}^{\phi'=2\pi} d\phi' \int_{\cos(\theta')=-1}^{\cos(\theta')=1} d\cos(\theta') \frac{\partial N_\nu(E, l, \theta')}{\partial \cos(\theta')} \text{psf}_{\text{direction}}(\theta, \theta', \phi, \phi'). \quad (6.1.7)$$

Here $\text{psf}_{\text{direction}}(\theta, \theta', \phi, \phi')$ represents the directional resolution expressed using the Fisher probability point spread density function in spherical coordinates plus a constant flat background

$$\text{psf}_{\text{direction}}(\theta, \theta', \phi, \phi') = \frac{1}{a+b} \left\{ a \times \frac{\kappa_{\nu,j}(E)}{4\pi \sinh(\kappa_{\nu,j}(E))} \exp[\kappa_{\nu,j}(E) \cos(\alpha)] + b \times \frac{1}{4\pi} \right\}, \quad (6.1.8)$$

where we have normalized the function using the respective contributions a and b from each of the two components, and α is the angle between two directions in spherical coordinates (θ, ϕ) and (θ', ϕ') which follows the relation

$$\cos(\alpha) = \sin(\theta) \sin(\theta') \cos(\phi - \phi') + \cos(\theta) \cos(\theta'). \quad (6.1.9)$$

Here both θ and θ' are polar angles with respect to the direction toward the body core, and ϕ and ϕ' are the respective azimuthal angles in the spherical coordinate system set by the astronomical body in question. $\kappa_{\nu,j}(E) \in [0, \infty)$, which depends on the neutrino type ν , the target element j , and the neutrino energy E , is a directional resolution parameter such that $\kappa_{\nu,j}(E) = 0$ represents the worst resolution possible with $\text{psf}_{\text{direction}}(\theta, \theta', \phi, \phi')$ being

entirely spherically symmetric, and $\kappa_{\nu,j}(E) = \infty$ being that for the case of infinitely good resolution where the point spread density function becomes a delta function in spherical coordinates $\text{psf}_{\text{direction}}(\theta, \theta', \phi, \phi') = \delta(\cos(\theta) - \cos(\theta'))\delta(\phi - \phi')$. Sample plots showing this function fitted to Monte Carlo simulations for energies of 1 GeV, 10 GeV and 100 GeV are shown in Figures 4.37 to 4.40.

In summary, all the above contributions to the signal event rate equation would give us the penultimate formula

$$\text{rate}_{\text{signal}} = \Gamma_A \sum_{\nu} \left[\int_{E_{\text{threshold}}}^{E_X} dE \frac{dN_{\nu}^{\text{detected}}(E)}{dE} \right], \quad (6.1.10)$$

where the sum runs over the different neutrino flavors $\nu = \nu_e, \bar{\nu}_e, \nu_{\mu}, \bar{\nu}_{\mu}$, and $\frac{dN_{\nu}^{\text{detected}}(E)}{dE}$ represents the energy spectrum of successfully detected neutrinos of a given flavor ν in the detector

$$\frac{dN_{\nu}^{\text{detected}}(E)}{dE} = \sigma_{\nu}^{\text{eff}}(E) \frac{dN_{\nu}^{\text{flux}}(E)}{dE} \quad (6.1.11)$$

Here $N_{\nu}^{\text{flux}}(E)$ is the neutrino yield flux in units of counts per unit area at the detector per dark matter annihilation taking into account contributions from annihilations at all locations inside the astronomical body,

$$N_{\nu}^{\text{flux}}(E) = \iint_{\text{body}} dl \, d\cos(\theta) \frac{\partial}{\partial l} \left[\frac{1}{4\pi l^2} \frac{\partial N_{\nu}^{\text{flux profile}}(E, l, \theta)}{\partial \cos(\theta)} \right]. \quad (6.1.12)$$

Here we will call $N_{\nu}^{\text{flux profile}}(E, l, \theta)$ the neutrino *flux profile* and it is the location (l, θ) dependent contribution to the total neutrino flux $N_{\nu}^{\text{flux}}(E)$. $\frac{\partial N_{\nu}^{\text{flux profile}}(E, l, \theta)}{\partial \cos(\theta)}$ is a convolution of the true angular neutrino flux profile $\frac{\partial N_{\nu}^{\text{true flux profile}}(E, l, \theta)}{\partial \cos(\theta)}$ with the directional resolution of the detector represented by the point spread function on a spherical surface $\text{psf}_{\text{direction}}(\theta, \theta', \phi, \phi')$ for some given baseline l ,

$$\begin{aligned} \frac{\partial N_{\nu}^{\text{flux profile}}(E, l, \theta)}{\partial \cos(\theta)} = & \\ & \int_{\phi'=0}^{\phi'=2\pi} d\phi' \int_{\cos(\theta')=-1}^{\cos(\theta')=1} d\cos(\theta') \frac{\partial N_{\nu}^{\text{true flux profile}}(E, l, \theta')}{\partial \cos(\theta')} \text{psf}_{\text{direction}}(\theta, \theta', \phi, \phi'), \end{aligned} \quad (6.1.13)$$

where we have used the fact that the point spread function is symmetric with respect to interchange of directions,

$$\text{psf}_{\text{direction}}(\theta, \theta', \phi, \phi') = \text{psf}_{\text{direction}}(\theta', \theta, \phi', \phi). \quad (6.1.14)$$

The point spread resolution functions for neutrino directionality $\text{psf}_{\text{direction}}$ is defined to be

$$\text{psf}_{\text{direction}}(\theta, \theta', \phi, \phi') = \frac{1}{a+b} \left\{ a \times \frac{\kappa_{\nu,j}(E)}{4\pi \sinh(\kappa_{\nu,j}(E))} \exp[\kappa_{\nu,j}(E) \cos(\alpha)] + b \times \frac{1}{4\pi} \right\}, \quad (6.1.15)$$

where a and b are relative contributions of each of the two terms, and

$$\cos(\alpha) = \sin(\theta) \sin(\theta') \cos(\phi - \phi') + \cos(\theta) \cos(\theta'). \quad (6.1.16)$$

The detector efficiency for a given neutrino flavor ν and energy E is given by

$$\sigma_{\nu}^{\text{eff}}(E) = \sum_j^{\text{elements}} \sigma_{\nu,j}^{\text{CC}}(E) \mathcal{E}_{\nu,j}(E) N_j^{\text{LS+BO}}, \quad (6.1.17)$$

where the index j runs over the two representative target elements Hydrogen and Carbon, $\sigma_{\nu,j}^{\text{CC}}(E)$ is the charged current scattering cross section for a given combination of neutrino flavor and target element, $\mathcal{E}_{\nu,j}(E)$ is the detector efficiency for charged current events to be fully contained inside the ID for the same combination of neutrino flavor and target element. $N_j^{\text{LS+BO}}$ is the total number of target nuclei for element j in both the LS and BO combined.

6.2 Statistical methods for setting upper limits

There exist two main methods for statistical analysis in assessing the results of a physics experiments and determining the validity of and also the parameters included in a hypothesized model. These are called the *Bayesian* and *frequentist* methods. The two methods both utilize the concept of probability to quantify estimates of parameters and hence some hypothesis that the experimenter is interested in determining. However, they are completely different in the way that probability itself is interpreted. The frequentist method interprets probability of events as the limit of the relative frequency of its occurrence

in a large number of trials. On the other hand, the Bayesian method interprets probability as a quantity we assign to represent our state of knowledge or degree of *belief* regarding the phenomenon of interest. From the frequentist point of view, a hypothesis or parameter value is tested without being assigned a probability. The hypothesis is simply either true or false and never in between, and a parameter that describes some phenomenon of nature is determined to be some value even if the experimenter may not at present know what it is. On the other hand, the Bayesian point of view incorporates the experimenter's degree of belief in the form of a probability for the hypothesis to be true or a parameter to hold some value. An interesting feature of the Bayesian method is that a *prior* belief regarding the hypothesis or parameter is required before the particular experiment is conducted and this is *updated* by the result of the experiment to yield a posterior probability. The posterior probability represents the new belief that the experimenter assigns to the hypothesis or parameter which was determined through new knowledge gained by conducting the experiment.

6.2.1 The frequentist method

According to the frequentist, a parameter that describes a certain model, say θ is estimated using the so called *confidence interval* in the case that the parameter is a scalar value or *confidence region* in the case the parameter is a vector. We will assume here that the parameter is a scalar value such that $\theta = \theta$ for the sake of simplicity and relevance to our present analysis. The confidence interval is a set of the possible values of θ for which if a large number of multiple identical trials of the experiment were conducted, each giving its own confidence interval, some fraction of intervals would include or as is coined in the literature *cover* the true value of the parameter. If this fraction of inclusion or *coverage probability* is $1 - \alpha$, the *confidence level* of the interval is said to be $1 - \alpha$. This popular method is known as the *Neyman construction* [65].

Figure 6.1 shows a diagram depicting the construction process. Each supposed value of θ is associated with a distinct range of values for the possible outcome of the experiment x defined by the range $x_1 < x < x_2$. Multiple hypothetical experiments for the given θ would yield results within this interval with a probability of $1 - \alpha$. The union of all such intervals for all values of θ form what is known as the confidence belt $D(\alpha)$.

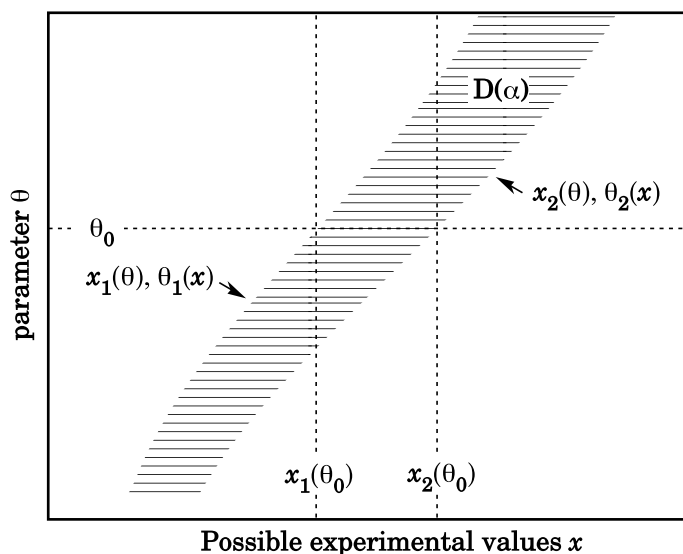


Figure 6.1: Neyman construction of the confidence interval. Figure taken from [36].

If the true value of the parameter were say $\theta = \theta_0$, the associated interval in x would be $x_1(\theta_0) < x < x_2(\theta_0)$ and if we obtained an experimental result of some $x = x_0$ within this region, the resulting confidence interval for θ would be the set of all values of θ such that their corresponding line segment $(x_1(\theta), x_2(\theta))$ is intercepted by a vertical line created by $x = x_0$. This would become the confidence interval $(\theta_1(x_0), \theta_2(x_0))$. It is important to note that the interpretation of probability in the frequentist approach requires that a single confidence interval once determined in such a way either does or does not cover the true value of the model parameter θ_0 , and that there is never a probability for this. The confidence level of $1 - \alpha$ refers to the coverage probability that is only defined for multiple such intervals resulting from multiple experimental trials if they were to be conducted.

An interesting feature of the Neyman construction is that although the line segment $(x_1(\theta), x_2(\theta))$ for a given θ is constrained to include the measurable value x with a probability of $P(x_1(\theta) < x < x_2(\theta)) = 1 - \alpha$, the exact values of $x_1(\theta)$ and $x_2(\theta)$ is not uniquely determined and one is relatively free to adjust these values as long as $P(x_1(\theta) < x < x_2(\theta))$ is conserved. One popular prescription for determining the interval limits in x is the so called *Feldman and Cousins* [37] method. Here for a given θ the interval

in x is assigned to be the set of x 's that have the highest likelihood ratio

$$\lambda(x) = \frac{P(x|\theta)}{P(x|\hat{\theta})}, \quad (6.2.1)$$

where $\hat{\theta}$ is the model parameter among all possible θ that maximizes $P(x|\theta)$ for the value of x in question.

In the case that we are interested in setting only a confidence limit instead of a confidence interval, the probability excluded outside of either x_1 or x_2 and hence θ_1 or θ_2 can be set to zero. For example in the case of Poisson statistics where we are interested in setting an upper limit, we can set $x_1 = 0$ and hence $\theta_1 = 0$.

6.2.2 The Bayesian method

Suppose the result of some experiment is characterized by a vector of data \mathbf{x} , and the probability distribution of \mathbf{x} depends on some unknown model parameters $\boldsymbol{\theta}$ that we are interested in. The experimenter's knowledge regarding $\boldsymbol{\theta}$ after conducting the experiment is summarized by the posterior belief probability distribution function (PDF) $p(\boldsymbol{\theta}|\mathbf{x})$ for a given experimental result \mathbf{x} . This can be obtained using Bayes' theorem

$$p(\boldsymbol{\theta}|\mathbf{x}) = \frac{P(\mathbf{x}|\boldsymbol{\theta})\pi(\boldsymbol{\theta})}{\int P(\mathbf{x}|\boldsymbol{\theta}')\pi(\boldsymbol{\theta}') d\boldsymbol{\theta}'}, \quad (6.2.2)$$

where $P(\mathbf{x}|\boldsymbol{\theta}) = L(\boldsymbol{\theta}|\mathbf{x})$ is the likelihood function of the model parameters $\boldsymbol{\theta}$ evaluated after the given experimental data \mathbf{x} is obtained. $\pi(\boldsymbol{\theta})$ is the *prior* PDF for $\boldsymbol{\theta}$. The denominator in Equation (6.2.2) plays the role of normalization to establish $p(\boldsymbol{\theta}|\mathbf{x})$ as a probability with respect to $\boldsymbol{\theta}$.

There is no predetermined *rule* that dictates the functional form for the prior $\pi(\boldsymbol{\theta})$ and it is often taken as a flat distribution with respect to $\boldsymbol{\theta}$ along with additional constraints provided by physical common sense. This represents the experimenter's complete lack of knowledge regarding the parameter or hypothesis to be tested. For example in a counting experiment where the result is reported in a number of events, the prior $\pi(\mu)$ with respect to the average number of events μ can be constructed to be flat in the non-zero region and

uniformly zero otherwise in the unphysical negative region

$$\pi(\mu) = \begin{cases} 1 & \text{if } \mu \geq 0 \\ 0 & \text{if } \mu < 0 \end{cases}. \quad (6.2.3)$$

In this way it is attempted to fabricate a prior that reflects the objective position of the experimenter before the experiment is conducted. However, this is not so trivial a matter as it would seem because a flat PDF in θ is not necessarily flat in some nonlinear function of θ , and then it can be argued, for which metric is the experimenter to profess his objective lack of knowledge in? There have been attempts to rectify this problem by finding priors that are invariant with respect to parameter transformation in the case that the prior distribution is a continuously differentiable function of the parameters [56]. This is called the Jeffreys prior which for the case of the mean μ of a Poisson distribution is

$$\pi(\mu) = \frac{1}{\sqrt{\mu}}. \quad (6.2.4)$$

A derivation of this is given in Appendix C.

Additionally there are arguments stressing that the Bayesian method is naturally designed to incorporate the belief of the experimenter and that it is absurd to invent a prior attempting to circumvent this. This is the subject of philosophical controversy and discussions are divided between two groups of proponents; *objective* Bayesians who claim the existence and utility of *objective* priors, and *subjective* Bayesians who regard that a prior necessarily represent a subjective judgment that cannot be rigorously justified [86]. A resolution of this controversy is beyond the scope of this discussion and we will simply employ the most commonly accepted priors mentioned in the Particle Data Group (PDG) guide lines.

To obtain an upper limit on the average number of signal events s , the total number of events observed follows the Poisson distribution

$$P(n|s) = \frac{(s+b)^n}{n!} e^{-(s+b)}, \quad (6.2.5)$$

where b is the mean number of background events and therefore $s+b$ is the mean number of total events. An upper limit of the signal mean s_{up} at a confidence level of $1 - \alpha$ can be

calculated by the following

$$1 - \alpha = \int_{-\infty}^{s_{\text{up}}} p(s|n) \, ds = \frac{\int_{-\infty}^{s_{\text{up}}} P(n|s)\pi(s) \, ds}{\int_{-\infty}^{\infty} P(n|s)\pi(s) \, ds}, \quad (6.2.6)$$

where if a flat prior such as that shown in Equation (6.2.3) is used, the lower limit of integration is essentially $s = 0$.

6.3 WIMP-nucleon cross section bound calculation

The annihilation rate of dark matter Γ_A is related to its capture rate Γ_C which is ultimately related to the dark matter-nucleon scattering cross section σ_{XN} . Under the condition that dark matter accumulation in an astronomical body is in equilibrium, this can be expressed as

$$\Gamma_A = \frac{1}{2}\Gamma_C = \frac{1}{2}\sigma_{XN}C_0, \quad (6.3.1)$$

where we have defined C_0 to be the dark matter capture rate per unit dark matter-nucleon scattering cross section which is a function of the dark matter mass m_X such that

$$C_0(m_X) \equiv \frac{\Gamma_C(m_X)}{\sigma_{XN}}. \quad (6.3.2)$$

Any dependence on the cross section is effectively canceled out in the numerator and denominator on the right-hand side of Equation (6.3.2), and therefore $C_0(m_X)$ can simply be derived by calculating the capture rate for some arbitrary cross section value say $\sigma_{XN} = 1 \times 10^{-40} \text{ cm}^2$ as shown in Figures 1.8 and 1.9 and tabulated in Tables 1.3 and 1.4.

We would like to place an upper bound on the dark matter-nucleon cross section at some arbitrary confidence level. It is common in the field to choose a confidence level of 90% so we will follow likewise. The expression for the cross section σ_{XN} can be derived from Equation (6.3.1) and Equation (6.1.10) in Section 6.1 such that

$$\sigma_{XN} = \frac{2}{C_0(m_X)} \frac{\text{rate}_{\text{signal}}}{\left[\sum_{\nu} \int_{E_{\text{threshold}}}^{E_X} dE \frac{dN_{\nu}^{\text{detected}}(E)}{dE} \right]}, \quad (6.3.3)$$

where the sum is over the neutrino flavors $\nu = \nu_e, \bar{\nu}_e, \nu_{\mu}, \bar{\nu}_{\mu}$, and $\frac{dN_{\nu}^{\text{detected}}(E)}{dE}$ is the spectrum of successfully detected neutrinos, E_X is the dark matter mass energy, and $E_{\text{threshold}}$ is the

lower energy threshold of our analysis. If we define b to be the upper bound of the signal event rate ($\text{rate}_{\text{signal}}$) at a confidence level of 90%, we can express the corresponding upper bound on the cross section σ_{XN} as

$$\sigma_{XN} < \sigma_{XN}^{\text{bound}}(m_X) = \frac{2}{C_0(m_X)} \frac{b}{\left[\sum_{\nu} \int_{E_{\text{threshold}}}^{E_X} dE \frac{dN_{\nu}^{\text{detected}}(E)}{dE} \right]}. \quad (6.3.4)$$

The upper bound $\sigma_{XN}^{\text{bound}}(m_X)$ is not only dependent on the dark matter mass m_X , but also on the dark matter annihilation channel which was initially assumed to be some arbitrary but given channel at the beginning of this discussion. The different annihilation channels that will be included in this analysis are the following nine channels.

- $XX \longrightarrow \nu_e \bar{\nu}_e$
- $XX \longrightarrow \nu_{\mu} \bar{\nu}_{\mu}$
- $XX \longrightarrow \nu_{\tau} \bar{\nu}_{\tau}$
- $XX \longrightarrow \tau^{-} \tau^{+}$
- $XX \longrightarrow gg$
- $XX \longrightarrow b\bar{b}$
- $XX \longrightarrow c\bar{c}$
- $XX \longrightarrow s\bar{s}$
- $XX \longrightarrow u\bar{u}$

6.4 Event selection

6.4.1 Run selection

Before individual neutrino event candidates are selected, the valid runs in which the events are to be searched for must be determined. The analysis in this work utilizes

both the ID 17-inch and 20-inch photomultiplier tubes (PMTs). However both types are not always available for use. For example a high-voltage supply unit that was responsible for only the 20-inch PMTs might have malfunctioned for a given run and it may have been the case that all 20-inch PMTs were off-line at the time or vice-versa. Additionally, in a given run individual PMTs or their signal channels may be unsuitable for use in data analysis for a variety of reasons as explained in Section 4.5. In order to utilize as much live time as possible the following run selection criteria was applied for this study. The condition of all PMTs are checked for all runs and valid runs are selected based on the available number of healthy PMTs of a given type in the particular run. The majority of the ID 17-inch PMTs must be usable in a valid run. If the majority of ID 20-inch PMTs are also healthy in a given run, they will be included in the analysis. If most or all of them are unsuitable for use, they will be left out of the run and analysis will continue using just the 17-inch PMTs for the single run. A separate energy calibration is applied to each individual run to be able to account for the varying number of PMTs being used.

6.4.2 Noise event rejection

Noise events are non-physical events characterized by their abnormal PMT hit time distribution. In a typical physical event, much of the PMT hit times are distributed within a time window of about 100 ns which is the characteristic live time of photons within the ID when taking into account effects from LS decay times and photon absorption and reemission processes. On the other hand non-physical noise events do not exhibit this feature. The corresponding hit time distribution is more randomly spread out in time and there is no correlation among PMT hit times. In order to reject these non-physical events, we introduce a parameter n_{100} which represents the number of PMT hits within a 100 ns time window. For any given event this 100 ns time window is moved about in such a way as to contained the maximum number of hits possible. This parameter is used in conjunction with the total number of PMT hits n_{hit} in the event to effectively reject noise events that are identified using the following criterion,

$$n_{100} \leq \frac{n_{\text{hit}} + 50}{2}. \quad (6.4.1)$$

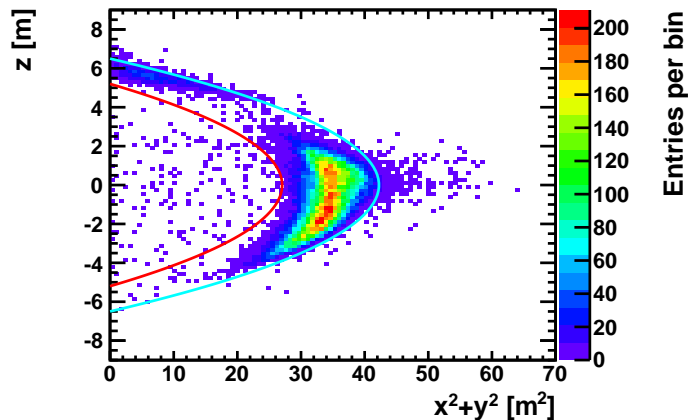


Figure 6.2: Scatter histogram of reconstructed event vertices with respect to the uniform phase space of the detector coordinates z versus $x^2 + y^2$. The red curve indicates a cut at a radius of 5.2 m of which the volume inside defines the fiducial volume of the analysis. The cyan line indicates the edge of the 6.5 m radius balloon which holds the KamLAND LS.

This cut essentially places a bound on how spread out the PMT hit time distribution is allowed to be and is used extensively in the low-energy analysis. We will employ the same noise event rejection criterion in our high-energy analysis.

6.4.3 Fiducial volume selection

Figure 6.2 shows the reconstructed vertices of candidate neutrino events with reconstructed energies of 1 GeV and above. The detector was originally employing magnetic coordinates where the y -axis points toward magnetic north, and the x -axis points in the direction rotated 90° clockwise from magnetic north. The z -axis is taken to be pointing directly overhead forming a right handed Cartesian coordinate system. All PMT positions and hence the coordinate system in which all reconstruction takes place in utilizes these coordinate. The vertices are shown with respect to the square of the radial distance $x^2 + y^2$ from the z -axis in order to preserve a flat spatial phase space. Neutrinos interact weakly and hence their reconstructed vertices should be populated in a uniform manner. A spherical fiducial volume cut was placed at a radius of 5.2 m within which the vertices seem to be

relatively uniform. This is designated by the red curve. The cyan curve indicates the edge of the 6.5 m radius LS containing balloon. An extremely large cluster of events can be seen between the two curves at the equatorial region and at the top of the detector near the chimney. These are attributed to cosmic ray muon induced background events that were not excluded by the outer detector (OD) cut due to inefficiencies of the OD near the equator and chimney regions. The inefficiency near the equator is due to two factors. The first is that the radial distance between the stainless steel tank that houses the ID and the cavern wall that defines the OD closes down to about 1 m at its narrowest point which effectively reduces the Cherenkov photon producing track length in the OD near this region. The latter is that there are no OD PMTs placed directly at the equator due to space constraints and the nearest located PMTs above and below the equator have their photo-sensitive photocathode faces facing toward the z -axis and not toward the equator. These two factors make the production and collection of Cherenkov light relatively more difficult in comparison to other regions of the OD. The asymmetric distribution of the excess cluster of vertices near the equator with respect to the plane $z = 0$ can be attributed to a symmetric OD inefficiency convolved with an *asymmetric* cosmic-ray muon distribution which is characterized by a fall off approximately in proportion to $\cos^n(\theta)$ where $n \sim 4$ for zenith angles $\theta \lesssim 70^\circ$ and approaching a relatively constant value with respect to θ for larger zenith angles up to the direction toward the horizon $70^\circ \lesssim \theta < 90^\circ$. The inefficiency at the chimney region is simply attributed to the fact that there are no OD PMTs at this region due to the physical presence of the chimney itself.

6.4.4 Vertex *point-likeness* estimation using χ_{time}^2

For MeV scale energy neutrino events there is typically a linear correlation between the time a given PMT receives its first photon hit and the distance from the PMT to the vertex where the photons were emitted. An example event showing this is presented in Figure 6.3. The event *point-likeness* can be parameterized by the reduced χ_{time}^2 value fitted using the expected and actual first photon hit times. In the case of an idealized point vertex with an isotropic emission of photons, this parameter will likely yield a very small value. In

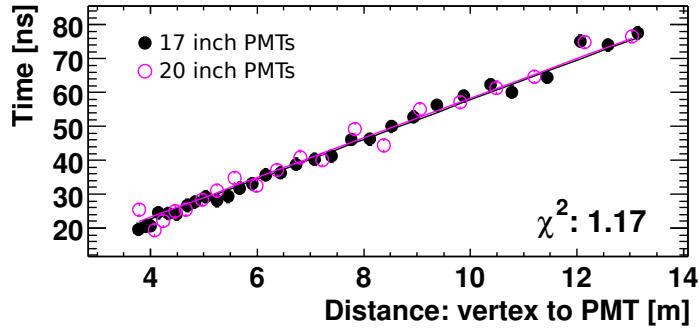


Figure 6.3: Linear correlation between the first photon hit time on a PMT and the distance between the vertex and the PMT for a sample low energy neutrino event from run 2446, event 10 151 512. Here the reduced χ^2 is fitted to be 1.17, and in general vertices that are more or less point-like yield a χ^2 value of less than 2. Figure reproduced from [74].

this particular sample event the value was fitted to be 1.17, and in general vertices that are more or less point-like yield results below 2.

However for events with energies on the scale of a GeV, the vertex may distort greatly from that of a *point* if at all a vertex can be defined. Indeed for neutrino interactions at high energies the event profile may be better characterized by *tracks* similar to those seen in bubble chamber particle detectors. Nonetheless the point-likeness test can be used to exclude the most extreme non-point-like events which will most likely be due to cosmic ray muons that draw out elongated track profiles.

Figure 6.4 shows the point-likeness of reconstructed vertices parameterized by χ_{time}^2 versus the radial distance from the detector center for our high energy candidate events in this analysis. The plot is shown with respect to the cube of the radial distance in order to preserve a uniform spatial phase space. The vertical red line indicates the extent of the fiducial volume due to the radial cut placed at $r = 5.2$ m. The fitter is seen to saturate at around $\chi_{\text{time}}^2 > 40$ so a cut was placed at $\chi_{\text{time}}^2 = 40$ indicated by the horizontal red line. The events excluded above this red line are attributed to be background events due to cosmic-ray muons.

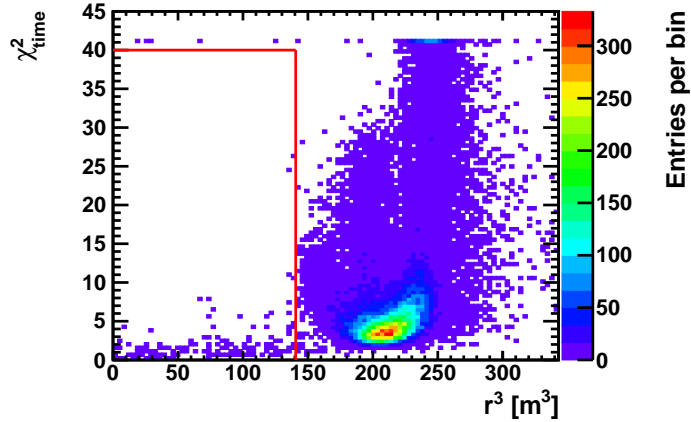


Figure 6.4: χ_{time}^2 representing the point-likeness of event vertices versus the cube of the radial distance from the detector center r^3 . The vertical red line indicates the extent of the fiducial volume due to the cut placed at $r = 5.2$ m. The horizontal red line indicates a cut placed at χ_{time}^2 above which the fitter is seen to saturate. Events with $\chi_{\text{time}}^2 \geq 40$ are attributed to be background cosmic-ray muon events.

6.4.5 Reconstructed energy of candidate events

Figure 6.5 shows the reconstructed energy spectrum of candidate neutrino events. The black line indicates a total of 41 697 candidates that passed the reconstruction energy criterion of ≥ 1 GeV. Among these, the stacked red and green filled histograms both represent the candidates wherein the vertex was reconstructed to be within the spherical fiducial volume $r < 5.2$ m. The former totaling 175 events had a point-likeness parameter χ_{time}^2 within the cut of $\chi_{\text{time}}^2 < 40$. These are defined as our final atmospheric neutrino event candidates. The latter comprised of only 5 events is attributed to cosmic-ray muon background events where despite the vertex being reconstructed within the fiducial volume $r < 5.2$ m, the events had a point-likeness parameter outside of the designated cut such that $\chi_{\text{time}}^2 \geq 40$.

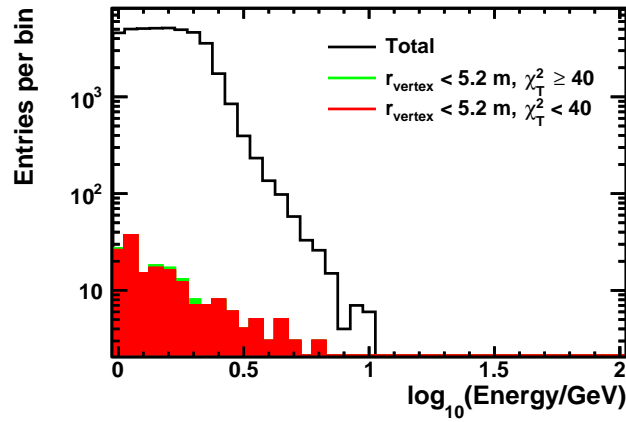


Figure 6.5: Stacked histogram of the reconstructed energy spectrum of candidate events. The black line indicates the total number of candidates selected solely by the reconstructed energy criteria of ≥ 1 GeV. The green filled histogram corresponds to candidates with vertex locations inside the 5.2 m radius fiducial volume, but with a point-likeness parameter of $\chi_{\text{time}}^2 \geq 40$. The red filled histogram corresponds to the final residual candidates to be used in this analysis with vertices located within the fiducial volume $r < 5.2$ m and with point-likeness parameters yielding $\chi_{\text{time}}^2 < 40$.

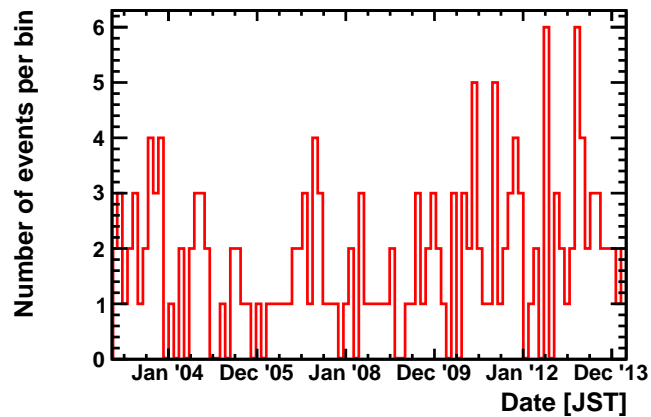


Figure 6.6: Atmospheric neutrino event distribution with respect to time.

6.4.6 Event distribution with respect to time

Figure 6.6 shows the time distribution of candidate atmospheric neutrino events. Shown are only event with reconstructed energies above 1 GeV that satisfy the background cuts explained in Section 6.4.5.

6.5 Fitting data to the model

After the event selection is completed through employing the various cuts detailed in Section 6.4, the directionality of the events were reconstructed using the method explained in Section 4.8.4. The directional distribution of this data was then fitted to the modeled net distribution of background atmospheric neutrinos summing over the four relevant flavors in this analysis $\nu_e, \bar{\nu}_e, \nu_\mu, \bar{\nu}_\mu$, taking into account the respective flavor and energy dependent directional resolution and detection efficiencies for events to be fully contained in the ID. Here we ignore the contribution from the detection of tau flavor neutrinos ν_τ and $\bar{\nu}_\tau$. The detectable flux contribution from charged current interactions of tau flavor neutrinos is relatively low as the mass of the tau lepton is 1.78 GeV, and thus the neutrino energy threshold for tau lepton production through interactions in the detector is approximately 3.5 GeV. Most of the atmospheric neutrino flux contribution comes from energies below this value as seen in Figure 5.2.

The angular distribution for WIMP annihilation induced neutrino flux originating from inside the Earth and Sun, along with the net distribution of backgrounds associated with atmospheric neutrinos is shown in Figures 6.7 and 6.7. Here $\cos(\theta) = 1$ indicates the direction toward the Earth or Sun's core. The modeled signal distribution for 1 GeV mass WIMP annihilation induced neutrinos through the annihilation channel $XX \longrightarrow \nu_e \bar{\nu}_e$ indicated by the red histogram is fitted identically to zero, but is artificially normalized to 30 events in order to be visible to the reader. The total background model distribution is depicted by the black histogram and the individual contributions by the respective neutrino flavors $\nu_e, \bar{\nu}_e, \nu_\mu, \bar{\nu}_\mu$ are indicated by the colored dotted histograms.

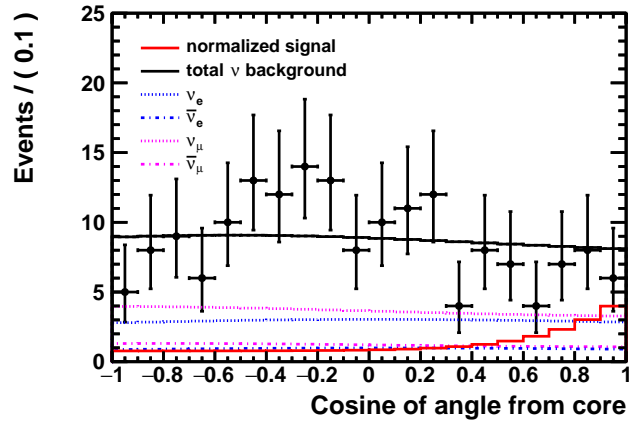


Figure 6.7: Angular distribution of signal and background neutrino model fitted to data for dark matter annihilation induced neutrinos originating from within the Earth. The angle is with respect to the direction toward the Earth’s core. The signal model distribution for 1 GeV mass WIMPs through annihilation channel $XX \rightarrow \nu_e \bar{\nu}_e$ indicated by the red histogram is fitted identically to zero, but is normalized to 30 events to be visible to the reader. The respective atmospheric neutrino flux contributions are shown by the dotted colored histograms. The total model flux is shown by the solid black histogram which is fitted to the data represented by the black dot markers with error bars.

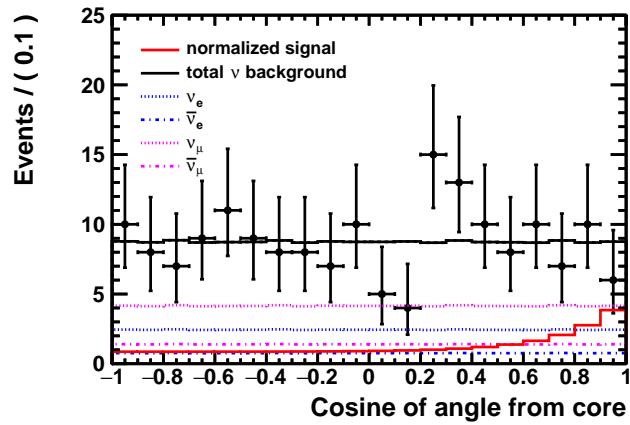


Figure 6.8: Angular distribution of signal and background neutrino model fitted to data for dark matter annihilation induced neutrinos originating from within the Sun. The angle is with respect to the direction toward the Sun’s core. The signal model distribution for 1 GeV mass WIMPs through annihilation channel $XX \rightarrow \nu_e \bar{\nu}_e$ indicated by the red histogram is fitted identically to zero, but is normalized to 30 events to be visible to the reader. The respective atmospheric neutrino flux contributions are shown by the dotted colored histograms. The total model flux is shown by the solid black histogram which is fitted to the data represented by the black dot markers with error bars.

6.6 Live time calculation

Any period of time during which the detector cannot collect useful data for whatever reason, or the data taken is rendered useless due to any analysis criteria is considered to be *dead time*. On the other hand, periods during which useful data *can* be taken and the detector is sensitive to neutrino detection is considered to be *live time*. It is one of the crucial objectives of a data taking experiment, especially one that is designed to observe rare events such as those of neutrinos, to increase the total live time as much as possible in order to collect statistics and make a precise measurement. There are a few components to calculating the total live time of an experiment.

- **run time**

The time period of data taking for a given run. This is defined as the time interval between the first and last events in the ensemble of events of the given run.

- **dead time**

The period of time within which data is not or cannot be taken or is taken but the data is not useful for analysis.

- **veto time**

The period of time that is vetoed due to background event rejection.

- **live time**

The period of time within a given run in which the experiment is sensitive to neutrino detection. This is defined as

$$(\text{live time}) = (\text{run time}) - (\text{dead time}) - (\text{veto time}). \quad (6.6.1)$$

6.6.1 Dead time

Dead time is classified into four categories.

- **bad run**

A run where the quality of the data taken is not usable. For example the number of bad 17-inch PMT channels in the ID is too high or they are clustered together in

close spatial proximity due to some problem with the high-voltage supply or other issue with the electronics. These can be filtered out by an abnormally low trigger rate of either low energy events or muon events. In this case, the whole duration of the entire run contributes to the overall total dead time.

- **bad period (half-bad run)**

A run in which some part of the run satisfies the condition to be a bad run.

- **trigger dead period**

The trigger module may be busy processing other data and not be able to function properly for the current incoming data. During these intermittent periods of time, data cannot be processed and thus contributes to the overall total dead time.

- **noisy period**

Muon events are usually accompanied by subsequent multiple noise events occurring within a time window of $150\ \mu\text{s}$ due to transient ringing in the front-end electronics (FEE). If a similar clustering of noise events is observed without any apparent preceding muon event, it may be an indication that a muon event did in fact take place but was missed due to dead time. A missing muon event is tagged by a cluster of noise events within a 1 ms time window where no preceding muon event was observed. In this case, the entire 1 ms duration contributes to the dead time.

6.6.2 Veto time

Cosmic ray muons are a major source of background for high energy neutrino analysis in KamLAND. They are tagged by the criteria explained in Section 4.4.1. A 2 ms period of veto time is applied following all muon events regardless of the identified muon classification. This contributes a certain amount of dead time to the experiment which is summarized in Section 4.4.4.

6.6.3 Live time

The live time of each run is calculated using its run time, dead time, and veto times. The total run time from run number 1330 on September 6, 2002 to run number 12474 on April 30, 2014 is 3280.7 days. The total live time during this period is 3238.6 days, and the total veto time due to background muon event rejection is 7.7 days.

6.7 Number of target nuclei

In order to calculate the total detector cross section for neutrino interactions in the Kamioka Liquid Scintillator Antineutrino Detector (KamLAND), we must first know the number of valid targets. The conventional approach taken when conducting analysis at low energies on the order of \sim MeV, is to calculate the number of targets in the given fiducial volume set by the particular analysis, and take the ratio of this value versus the total number of possible targets in the active detector volume. However, in this analysis, although the reconstruction vertex is constrained to be within a spherical fiducial volume of radius 5.2 m, the reconstructed vertex itself may be ill defined due to the extended event profile at high energies on the order of \sim GeV.

In order to circumvent this problem, we will define the valid targets to be the total number of target nuclei inside the entire active detector volume defined by the ID. This assumes that any neutrinos that interact with nuclei outside of the ID will *not* be fully contained and any efficiencies related to the 5.2 m radius spherical fiducial volume will be accounted for by placing the cut on vertices reconstructed using simulated events in the KamLAND Geant4 Simulation (KLG4Sim).

Here we would like to estimate the total number of target Hydrogen and Carbon nuclei in the ID. Although there also exists minute traces of Nitrogen and Oxygen, we will ignore these components because their contribution is minimal as shown in Table 3.2.

Let us first estimate the number of targets in the LS. The problem here is that the LS volume and density, and therefore also the total mass and number of target elements at the in situ temperature of 11.5 °C, is not known. We will begin with the measured temperature dependence of the LS density, $\alpha = 7.41 \times 10^{-4} \text{ g}/(\text{cm}^3 \text{ K})$, as shown in Table 3.1.

This is assumed to be constant with respect to the relatively small variations in temperature of $|\Delta T| < 5^\circ\text{C}$ discussed here and follows the relation for density ρ such that

$$\rho = \rho_0 - \alpha\Delta T, \quad (6.7.1)$$

where ρ_0 is the initial density. A volumetric thermal expansion of ΔV for liquids under a constant pressure follows a generic form such that

$$\beta = \frac{1}{V_0} \frac{\Delta V}{\Delta T}, \quad (6.7.2)$$

or equivalently

$$V = V_0 (1 + \beta\Delta T), \quad (6.7.3)$$

where β is the volumetric expansion coefficient, V_0 is the initial volume, and the current volume is $V = V_0 + \Delta V$. Expressing the density in terms of the volume, we get

$$\rho = \frac{M}{V} \quad (6.7.4)$$

$$= \frac{M}{V_0 (1 + \beta\Delta T)} \quad (6.7.5)$$

$$\simeq \frac{M}{V_0} (1 - \beta\Delta T) \quad (6.7.6)$$

$$= \rho_0 - \beta\rho_0\Delta T, \quad (6.7.7)$$

where we have assumed $\beta\Delta T \ll 1$. Comparing Equations (6.7.1) and (6.7.7) gives us the relation between β and α ,

$$\beta = \frac{\alpha}{\rho_0}. \quad (6.7.8)$$

Now that we know the thermal volumetric expansion coefficient β with respect to the density dependence on temperature α , we can estimate the total mass of the KamLAND LS $M_{11.5^\circ\text{C}}^{\text{LS}}$ at the in situ temperature of 11.5°C by the following.

$$M_{11.5^\circ\text{C}}^{\text{LS}} = \rho_{11.5^\circ\text{C}}^{\text{LS}} V_{11.5^\circ\text{C}}^{\text{LS}} \quad (6.7.9)$$

$$= \left\{ \rho_{15^\circ\text{C}}^{\text{LS}} - \alpha^{\text{LS}} (11.5^\circ\text{C} - 15^\circ\text{C}) \right\} \times \quad (6.7.10)$$

$$\left\{ V_{12.45^\circ\text{C}}^{\text{LS}} \left[1 + \beta^{\text{LS}} (11.5^\circ\text{C} - 12.45^\circ\text{C}) \right] \right\}$$

$$= 917 \text{ t}, \quad (6.7.11)$$

where we have used

$$\beta^{\text{LS}} = \frac{\alpha^{\text{LS}}}{\rho_{12.45^\circ\text{C}}^{\text{LS}}} \quad (6.7.12)$$

$$= \frac{\alpha^{\text{LS}}}{\rho_{15^\circ\text{C}}^{\text{LS}} - \alpha^{\text{LS}} (12.45^\circ\text{C} - 15^\circ\text{C})} \quad (6.7.13)$$

$$= 9.51 \times 10^{-4} / \text{K}. \quad (6.7.14)$$

Here we have calculated the LS mass as a function of measured values at their respective temperatures as shown in Table 3.1. Comparing the estimated LS mass $M_{11.5^\circ\text{C}}^{\text{LS}}$ and Table 3.2, we can estimate the actual number of Hydrogen and Carbon nuclei, $N_{\text{Hydrogen}}^{\text{LS}}$ and $N_{\text{Carbon}}^{\text{LS}}$ respectively, in the KamLAND LS as

$$N_{\text{Hydrogen}}^{\text{LS}} = \frac{M_{11.5^\circ\text{C}}^{\text{LS}}}{1000 \text{ t}} \times 8.47 \times 10^{31} = 7.77 \times 10^{31}, \quad (6.7.15)$$

$$N_{\text{Carbon}}^{\text{LS}} = \frac{M_{11.5^\circ\text{C}}^{\text{LS}}}{1000 \text{ t}} \times 4.30 \times 10^{31} = 3.94 \times 10^{31}. \quad (6.7.16)$$

On the other hand, the total number of targets in the BO can be estimated using the following method. The volume of the BO $V_{10.7^\circ\text{C}}^{\text{BO}}$ at the in situ temperature of 10.7°C is

$$V_{10.7^\circ\text{C}}^{\text{BO}} = V_{11.85^\circ\text{C}}^{\text{BO}} \left[1 + \beta^{\text{BO}} (10.7^\circ\text{C} - 11.85^\circ\text{C}) \right], \quad (6.7.17)$$

where

$$\beta^{\text{BO}} = \frac{\alpha^{\text{BO}}}{\rho_{11.85^\circ\text{C}}^{\text{BO}}}. \quad (6.7.18)$$

The BO itself is a mixture of 53 % Dodecane and 47 % isoparaffin by volume. The respective number of targets atoms for Hydrogen and Carbon in the two components can be calculated by their respective densities and molecular masses. At the in situ temperature of 10.7°C , the best overall BO density is measured to be 0.78033 g/cm^3 and the density of Dodecane at this temperature can be linearly extrapolated using its known densities at 15°C and 20°C shown in Table 3.4, namely 0.7526 g/cm^3 and 0.7487 g/cm^3 respectively such that

$$\rho_{\text{Dodecane}, 10.7^\circ\text{C}}^{\text{BO}} = 0.7560 \text{ g/cm}^3. \quad (6.7.19)$$

The density of isoparaffin, however, is ill defined due to the fact that isoparaffin itself is a mixture of a variety of alkanes (saturated hydrocarbon chain molecules) of distinct numbers

of Carbon atoms and therefore distinct molecular masses and densities. We can estimate an *average* density of isoparaffin by using the densities of the overall BO mixture and that of the Dodecane component along with the relative volumetric contributions of Dodecane and isoparaffin,

$$\rho_{10.7^\circ\text{C}}^{\text{BO}} = \left(0.53 \times \rho_{\text{Dodecane},10.7^\circ\text{C}}^{\text{BO}}\right) + \left(0.47 \times \rho_{\text{isoparaffin},10.7^\circ\text{C}}^{\text{BO}}\right) \quad (6.7.20)$$

or equivalently

$$\rho_{\text{isoparaffin},10.7^\circ\text{C}}^{\text{BO}} = \frac{1}{0.47} \left(\rho_{10.7^\circ\text{C}}^{\text{BO}} - 0.53 \times \rho_{\text{Dodecane},10.7^\circ\text{C}}^{\text{BO}}\right). \quad (6.7.21)$$

Finally we can use the molecular mass of Dodecane u_{Dodecane} to derive the target count for Dodecane alone, while using the best representative number of Carbon atoms in isoparaffin molecules of 15 and the corresponding molecular mass of $u_{\text{isoparaffin}}$ to estimate the target count for isoparaffin. The molecular masses are

$$u_{\text{Dodecane}} = 12\bar{A}_{\text{Carbon}} + 26\bar{A}_{\text{Hydrogen}}, \quad (6.7.22)$$

$$u_{\text{isoparaffin}} = 15\bar{A}_{\text{Carbon}} + 32\bar{A}_{\text{Hydrogen}}, \quad (6.7.23)$$

where

$$\bar{A}_{\text{Hydrogen}} = 1.00784, \quad (6.7.24)$$

$$\bar{A}_{\text{Carbon}} = 12.0107, \quad (6.7.25)$$

are the averages of the relative atomic masses of Hydrogen and Carbon which can be derived from Table B.1. The number of Hydrogen or Carbon nuclei $N_{10.7^\circ\text{C}}^{\text{BO}}$ in the BO at the in situ temperature of 10.7°C is

$$N_{10.7^\circ\text{C}}^{\text{BO}} = \left(a \times N_{\text{Dodecane},10.7^\circ\text{C}}^{\text{BO}}\right) + \left(b \times N_{\text{isoparaffin},10.7^\circ\text{C}}^{\text{BO}}\right) \quad (6.7.26)$$

$$= a \left\{ N_{\text{A}} \frac{V_{\text{Dodecane},10.7^\circ\text{C}}^{\text{BO}} \times \rho_{\text{Dodecane},10.7^\circ\text{C}}^{\text{BO}}}{u_{\text{Dodecane}}} \right\} + \quad (6.7.27)$$

$$b \left\{ N_{\text{A}} \frac{V_{\text{isoparaffin},10.7^\circ\text{C}}^{\text{BO}} \times \rho_{\text{isoparaffin},10.7^\circ\text{C}}^{\text{BO}}}{u_{\text{isoparaffin}}} \right\}$$

where a and b are the numbers of nuclei respectively for Dodecane and isoparaffin molecules. Namely these values are 26 and 32 respectively for the case of Hydrogen, and 12 and 15 respectively for that of Carbon. Here $N_{\text{Dodecane},10.7^\circ\text{C}}^{\text{BO}}$ and $N_{\text{isoparaffin},10.7^\circ\text{C}}^{\text{BO}}$ are the numbers of target nuclei, $V_{\text{Dodecane},10.7^\circ\text{C}}^{\text{BO}}$ and $V_{\text{isoparaffin},10.7^\circ\text{C}}^{\text{BO}}$ are the projected volumes of the two BO components at the in situ temperature, and N_A is the Avogadro constant. The projected volumes are

$$V_{\text{Dodecane},10.7^\circ\text{C}}^{\text{BO}} = 0.53 \times V_{10.7^\circ\text{C}}^{\text{BO}}, \quad (6.7.28)$$

$$V_{\text{isoparaffin},10.7^\circ\text{C}}^{\text{BO}} = 0.47 \times V_{10.7^\circ\text{C}}^{\text{BO}}, \quad (6.7.29)$$

where $V_{10.7^\circ\text{C}}^{\text{BO}}$ is shown in Equation (6.7.17).

The number of Hydrogen and Carbon nuclei $N_{\text{Hydrogen}}^{\text{BO}}$ and $N_{\text{Carbon}}^{\text{BO}}$ respectively in the BO are

$$N_{\text{Hydrogen}}^{\text{BO}} = 1.28 \times 10^{32}, \quad (6.7.30)$$

$$N_{\text{Carbon}}^{\text{BO}} = 5.95 \times 10^{31}, \quad (6.7.31)$$

and the combined total number of Hydrogen and Carbon nuclei in both the LS and BO, $N_{\text{Hydrogen}}^{\text{LS+BO}}$ and $N_{\text{Carbon}}^{\text{LS+BO}}$ respectively are

$$N_{\text{Hydrogen}}^{\text{LS+BO}} = 2.06 \times 10^{32}, \quad (6.7.32)$$

$$N_{\text{Carbon}}^{\text{LS+BO}} = 9.89 \times 10^{31}. \quad (6.7.33)$$

6.8 Detector efficiency for events to be fully contained

The detector efficiency for neutrino events to be fully contained inside the ID for low energy neutrino events on the scale of an $\sim\text{MeV}$ is relatively simple to calculate. The reason for this is because low energy events are relatively localized in a more or less point-like profile, and therefore the efficiency can simply be estimated as the ratio of the fiducial volume with respect to the total active detector volume. On the other hand, neutrino events on a much larger energy scale such as those on the order of $\sim\text{GeV}$ and above are no longer localized, and may be better characterized by track-like or multiple track-like profiles that

are drawn out by final state particles emerging from the neutrino interaction point. This complicates the reconstruction of the vertex and the reconstructed vertex itself is no longer a sufficient parameter that can best describe the spatial profile of the event. Moreover it may be the case that an event for which the reconstructed vertex lies within the ID may no longer be fully contained inside the ID if final state particle tracks extend out of the ID into the OD. This needs to be accounted for in the estimation of the efficiency. At high energies for an event to be fully contained with a reconstructed vertex that lies within some predefined fiducial volume is now a non-trivial function of the event profile, neutrino energy, neutrino flavor, and target nuclei.

In order to study this in more detail, the efficiency was simulated in KLG4Sim using neutrinos of different flavors and energies interacting with target elements in the ID. The efficiency $e(L)$ with respect to track length L was fitted using the following function,

$$e(L) = \begin{cases} \frac{R'^3}{R^3} & \text{if } L < 2(R - R') \\ \frac{3}{4\pi R^3} \left[\int_0^{S(L,R,R')} 2 \left(\sqrt{R^2 - r^2} - \frac{L}{2} \right) 2\pi r \, dr \right. \\ \quad \left. + \int_{S(L,R,R')}^{R'} 2 \left(\sqrt{R'^2 - r^2} \right) 2\pi r \, dr \right] & \text{if } \begin{cases} 2(R - R') \leq L \text{ and} \\ L < 2\sqrt{R^2 - R'^2} \end{cases} \\ \frac{3}{4\pi R^3} \int_0^{\sqrt{R^2 - (L/2)^2}} 2 \left(\sqrt{R^2 - r^2} - \frac{L}{2} \right) 2\pi r \, dr & \text{if } 2\sqrt{R^2 - R'^2} \leq L \end{cases}, \quad (6.8.1)$$

or explicitly taking the integrals and expanding to get an equivalent expression

$$e(L) = \begin{cases} \frac{R'^3}{R^3} & \text{if } L < 2(R - R') \\ \left[\begin{aligned} & \left[\frac{3}{64} \frac{L^3}{R^3} - \frac{3}{8} \frac{L}{R} + \frac{3}{4} \frac{R}{L} - \frac{3}{8} \frac{LR'^2}{R^3} - \frac{3}{2} \frac{R'^2}{LR} + \frac{3}{4} \frac{R'^4}{LR^3} \right. \\ & - \frac{1}{64} \frac{(L^4 + 8L^2R^2 + 16R^4 - 8L^2R'^2 - 32R^2R'^2 + 16R'^4)^{\frac{3}{2}}}{L^3R^3} \\ & + \frac{1}{64} \frac{(L^4 - 8L^2R^2 + 16R^4 + 8L^2R'^2 - 32R^2R'^2 + 16R'^4)^{\frac{3}{2}}}{L^3R^3} \\ & \left. + 1 \right] \end{aligned} \right. & \text{if } \begin{cases} 2(R - R') \leq L \text{ and} \\ L < 2\sqrt{R^2 - R'^2} \end{cases} \\ \frac{1}{16} \frac{L^3}{R^3} - \frac{3}{4} \frac{L}{R} + 1 & \text{if } 2\sqrt{R^2 - R'^2} \leq L \end{cases} \quad (6.8.2)$$

Here $S(L, R, R') = \sqrt{R^2 - \frac{(R^2 - R'^2 + (L/2)^2)^2}{L^2}}$, $R = 8.5$ m, and $R' = 5.2$ m. The particle track length L was then parameterized with respect to the neutrino energy E in units of GeV through the functional forms $L(E) = a(E + b)$ for the case of ν_μ or $\bar{\nu}_\mu$ interactions, and $L = a(\log_{10} E + b)$ for the case of ν_e or $\bar{\nu}_e$ interactions. Here a and b are the two floating parameters to be fitted. This efficiency fitting function was derived by imposing the joint condition for the fiducial volume cut and for events to be fully contained. In other words, the fitting function was derived by imposing two conditions. First that the reconstructed vertex must lie within a spherical fiducial volume of radius $R' = 5.2$ m, and second that the entire event profile must lie within a spherical ID volume of radius $R = 8.5$ m. Here we have simplified the calculations by making two assumptions. One that the entire event profile is a single straight line segment of length $L(E)$ representative of the single final state lepton track in a charged-current interaction, and another that the reconstructed vertex would coincide with the mid-point of the line segment. Although the assumptions employed were naive in the sense that a real muon track would have a finite ionization track width, which may be even more pronounced in the case of an electromagnetic shower produced by a final state electron or positron, one can see that the constructed function reproduces to some degree the general efficiency trends shown by Monte Carlo simulations

in Figures 6.9 and 6.10. Here we would like to note that in the actual efficiency fit, the constructed efficiency fit function was scaled and adjusted by

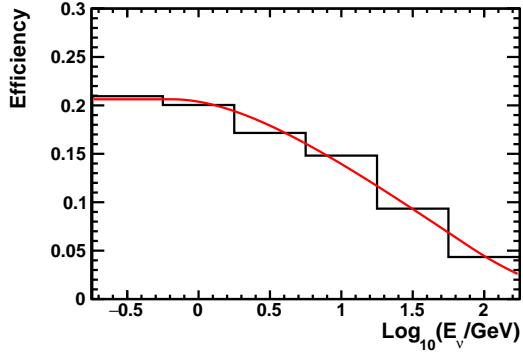
$$\mathcal{E}(E) = \alpha(e(E) + \beta), \quad (6.8.3)$$

where α and β are fitted values within the ranges $0 < \alpha < 1$ and $0 < \beta < 1$. The scaled efficiency fit function $\mathcal{E}(E)$ was ultimately used in the actual implementation of the fit with a total of four floating parameters a , b , α and β . The scaling and adjusting was done because the two extreme cases of the efficiency vanishing at high energies, and flattening out to a constant value R'^3/R^3 at low energies, are never observed within simulation. It is reasonable to expect this feature to also exist in the actual experiment as extreme cases that may be possible in idealized situations are rarely reflected in the experimental data.

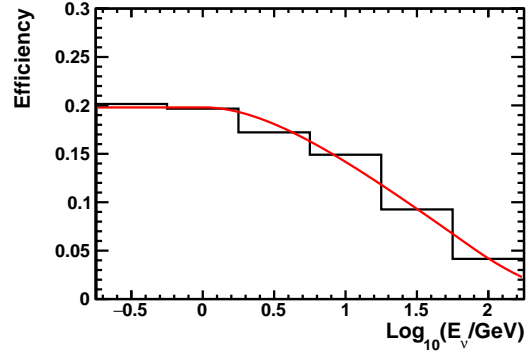
6.9 WIMP-nucleon cross section bounds

Using the fitted number of neutrino events from WIMP annihilation in Section 6.5, along with the calculated detector live time in Section 6.6.3, and the signal event rate equation derived in Equation (6.1.10), we can place an upper limit to the WIMP-nucleon cross section at a desired level of statistical confidence. It is common in the literature of the field to cite a confidence level of 90 % so we follow convention.

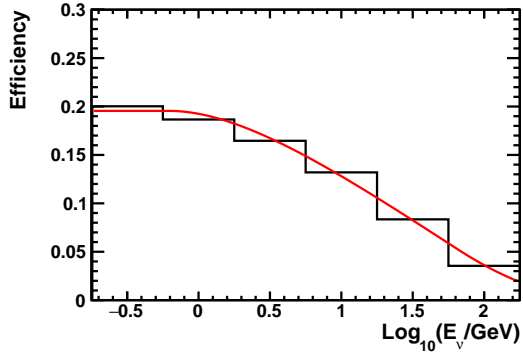
Figures 6.11 and 6.12 show the *spin independent* WIMP-nucleon scattering cross section upper bounds at a confidence level of 90 % for different WIMP annihilation channels when searching for annihilation induced neutrino signals from the Earth and Sun. Also shown are expected signal regions published by the experiments CoGeNT [1], CDMS [6], CRESST [11,27] and DAMA/LIBRA [21,71], along with recently published bounds from the Super-Kamiokande (SK) collaboration in 2015 looking for a signal solely from the Sun [29] and other various experiments. The oscillatory behavior in the varying upper bounds for the case of the Earth is due to resonances in WIMP capture from impedance matching to various elements in the composition of the Earth. Similar corresponding features in the capture rate can be seen in Figure 1.8. The first dip enhancement in the cross section is due to ^{16}O . The second to the elements ^{24}Mg , ^{28}Si , and ^{32}S . The last enhancement is due to ^{56}Fe and ^{58}Ni .



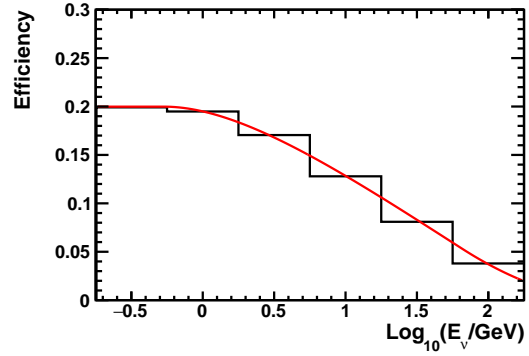
(a) $\nu_e + {}^1\text{H} \xrightarrow{\text{CC}} (?)$.



(b) $\nu_e + {}^{12}\text{C} \xrightarrow{\text{CC}} (?)$.

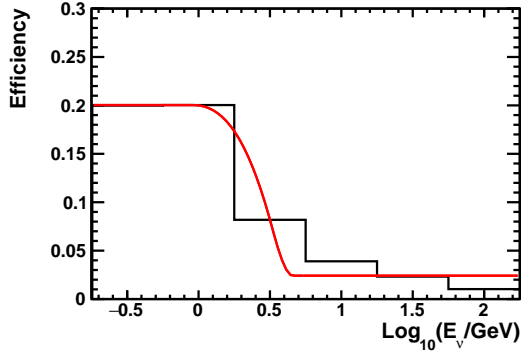


(c) $\bar{\nu}_e + {}^1\text{H} \xrightarrow{\text{CC}} (?)$.

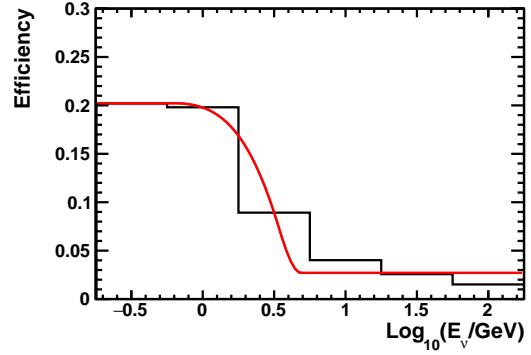


(d) $\bar{\nu}_e + {}^{12}\text{C} \xrightarrow{\text{CC}} (?)$.

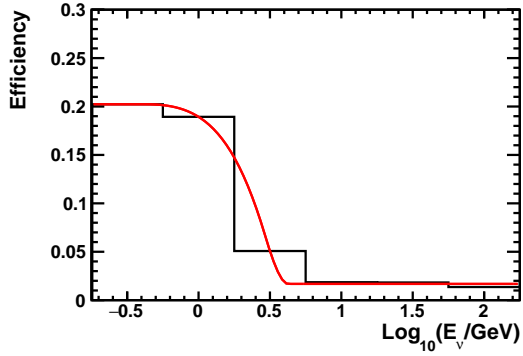
Figure 6.9: Simulated detector efficiency for fully contained events for the case of ν_e and $\bar{\nu}_e$ interacting through charged current interaction with ${}^1\text{H}$ and ${}^{12}\text{C}$ nuclei. Plots are shown with respect to neutrino energy E_ν in units of GeV.



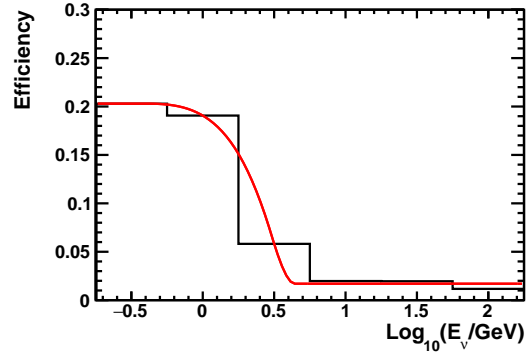
(a) $\nu_\mu + {}^1\text{H} \xrightarrow{\text{CC}} (?)$



(b) $\nu_\mu + {}^{12}\text{C} \xrightarrow{\text{CC}} (?)$



(c) $\bar{\nu}_\mu + {}^1\text{H} \xrightarrow{\text{CC}} (?)$



(d) $\bar{\nu}_\mu + {}^{12}\text{C} \xrightarrow{\text{CC}} (?)$

Figure 6.10: Simulated detector efficiency for fully contained events for the case of ν_μ and $\bar{\nu}_\mu$ interacting through charged current interaction with ${}^1\text{H}$ and ${}^{12}\text{C}$ nuclei. Plots are shown with respect to neutrino energy E_ν in units of GeV.

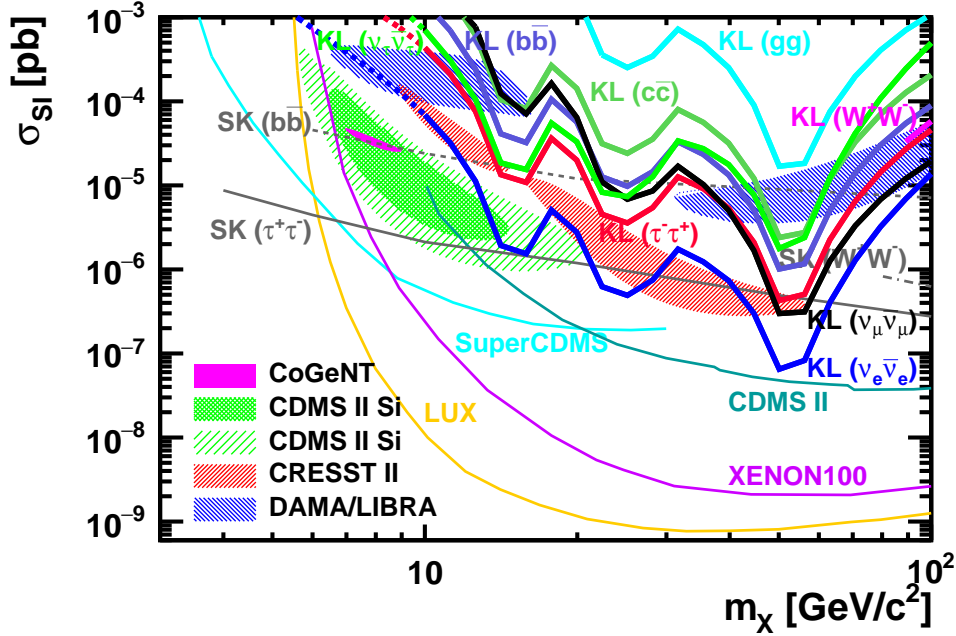


Figure 6.11: WIMP-nucleon spin independent scattering cross section upper bounds at 90 % confidence level for WIMP annihilation in the Earth. Thick colored lines show the 90 % C.L. upper bounds placed by this work assuming the various WIMP annihilation channels indicated. The extension of these bounds below a mass of 10 GeV indicated by the thick dotted colored lines are placed assuming that WIMP evaporation does not take place and our assumption for equilibrium of WIMP accumulation in the Earth still holds at lower masses. Also shown are the claimed signal regions from various experiments: CoGent [1] (magenta filled region, 90 % C.L.); CDMS II Si [6, 8] (green hatched region, 68 % and 90 % C.L.); CRESST [11, 27] (red hatched region, 95.45 % C.L.); DAMA/LIBRA [21, 71] (blue hatched region, 99.7 % C.L.). Other bounds from experiments include: LUX [9] (orange line, 90 % C.L.); XENON100 [12] (violet line, 90 % C.L.); CDMS II [6, 8] (dark green line, 90 % C.L.); SuperCDMS [7] (cyan line, 90 % C.L.); Super Kamiokande by looking for annihilations in the Sun [29] (gray lines, 90 % C.L.).

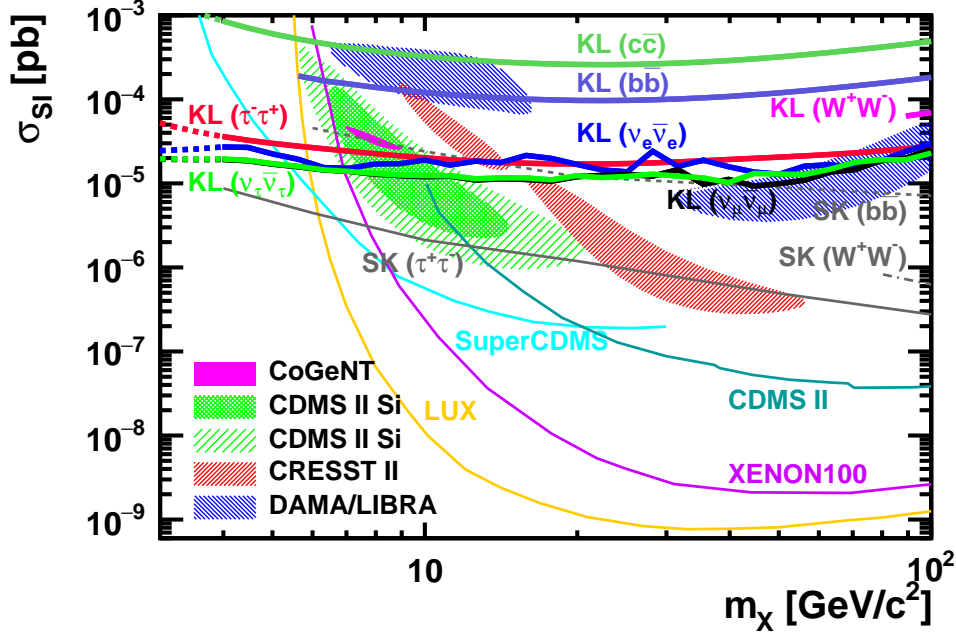


Figure 6.12: WIMP-nucleon spin independent scattering cross section upper bounds at 90 % confidence level for WIMP annihilation in the Sun. Thick colored lines show the 90 % C.L. upper bounds placed by this work assuming the various WIMP annihilation channels indicated. The extension of these bounds below a mass of 4 GeV indicated by the thick dotted colored lines are placed assuming that WIMP evaporation does not take place and our assumption for equilibrium of WIMP accumulation in the Sun still holds at lower masses. Also shown are the claimed signal regions from various experiments: CoGent [1] (magenta filled region, 90 % C.L.); CDMS II Si [6, 8] (green hatched region, 68 % and 90 % C.L.); CRESST [11, 27] (red hatched region, 95.45 % C.L.); DAMA/LIBRA [21, 71] (blue hatched region, 99.7 % C.L.). Other bounds from experiments include: LUX [9] (orange line, 90 % C.L.); XENON100 [12] (violet line, 90 % C.L.); CDMS II [6, 8] (dark green line, 90 % C.L.); SuperCDMS [7] (cyan line, 90 % C.L.); Super Kamiokande [29] (gray lines, 90 % C.L.).

The lower extent in WIMP mass of the validity of these results is bounded by the threshold below which WIMP evaporation must be taken into account and the equilibrium condition for WIMP accretion in the body that we have assumed for this analysis no longer holds. This is depicted by the extensions of our bounds indicated by the dotted lines below 10 GeV for the case of the Earth and 4 GeV for the case of the Sun. These show purely energetically allowed cases if the condition of equilibrium still were to hold.

Figure 6.13 shows the *spin dependent* WIMP-proton scattering cross section upper bounds at a confidence level of 90 % for various WIMP annihilation channel when searching for annihilation induced neutrino signals from solely the Sun. The shown expected signal region corresponds to results published by DAMA/LIBRA [21, 71] in 2010 assuming WIMP coupling to only protons. Therefore this exclusion result assumes the composition of the Sun is pure Hydrogen. Although the power of exclusion is not as strong as that of Super-K, the signal claimed region is well excluded by a number of annihilation channels at a confidence level of 90 %.

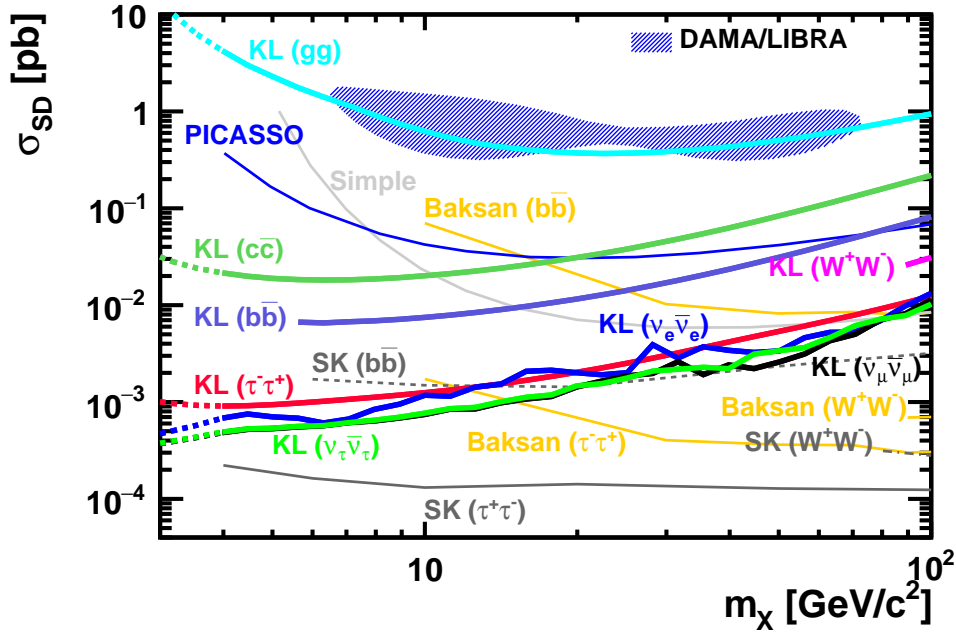


Figure 6.13: WIMP-proton spin dependent scattering cross section upper bounds at 90 % confidence level for WIMP annihilations in the Sun. Thick colored lines show the 90 % C.L. upper bounds placed by this work assuming the various WIMP annihilation channels indicated. The extension of these bounds below a mass of 4 GeV indicated by the thick dotted colored lines are placed assuming that WIMP evaporation does not take place and our assumption for equilibrium of WIMP accumulation in the Earth still holds at lower masses. Also shown is the claimed signal region from DAMA/LIBRA [21, 71] (blue hatched region, 5σ C.L.) assuming WIMP coupling to only protons. Other bounds from experiments include: Super Kamiokande [29] (gray lines, 90 % C.L.); Baksan [26] (orange line, 90 % C.L.); PICASSO [13] (blue line, 90 % C.L.); SIMPLE [38] (light gray line).

Chapter 7

Summary and Discussion

7.1 Summary

As shown in Figures 6.11 to 6.13 in Section 6.9, we have successfully placed bounds on the *spin dependent* and *spin independent* dark matter-nucleon cross sections respectively for capture in the Sun and Earth. We have considering a variety of dark matter annihilation channels:

- $XX \longrightarrow \nu_e \bar{\nu}_e$
- $XX \longrightarrow \nu_\mu \bar{\nu}_\mu$
- $XX \longrightarrow \nu_\tau \bar{\nu}_\tau$
- $XX \longrightarrow \tau^- \tau^+$
- $XX \longrightarrow gg$
- $XX \longrightarrow b\bar{b}$
- $XX \longrightarrow c\bar{c}$
- $XX \longrightarrow s\bar{s}$
- $XX \longrightarrow u\bar{u}$.

The data used for this analysis was taken from September 6, 2002 through April 30, 2014 with a total live time of 3253.0 days. The range of dark matter masses analyzed in this work ranges from 1 GeV to 100 GeV taking into account dark matter evaporation constraints for light dark matter capture in the Sun and Earth. The weakly interacting massive particle (WIMP) annihilation induced neutrino signal flux spectrum was simulated using the WimpSim Monte Carlo simulation program. This is shown in Figures 5.13 to 5.18 and Figures 5.19 to 5.24 where we show the directional flux spectra for neutrino flavors ν_e , $\bar{\nu}_e$, ν_μ , $\bar{\nu}_\mu$ produced from WIMP annihilation with sample masses 1 GeV, 10 GeV and 100 GeV annihilating through the sample channels

- $XX \longrightarrow \nu_e \bar{\nu}_e$
- $XX \longrightarrow \nu_\mu \bar{\nu}_\mu$
- $XX \longrightarrow b \bar{b}$
- $XX \longrightarrow \tau^- \tau^+$.

The atmospheric neutrino background was modeled using work conducted by [52] shown in Figures 5.8 and 5.9. The full three-flavor neutrino oscillation probabilities taking into account the Mikheyev-Smirnov-Wolfenstein (MSW) effect as the neutrinos travel from inside the Sun or Earth to the Kamioka Liquid Scintillator Antineutrino Detector (KamLAND) were modeled using DarkSUSY [43], the 2014 best fit oscillation parameters [36], and the Preliminary Reference Earth Model (PREM) [32]. The compositional, mass, electron, and neutron density models that were used for the Sun and Earth are shown in Figures 2.1 and 2.2. The neutrino-nucleus interactions were modeled using the Generates Events for Neutrino Interaction Experiments (GENIE) Monte Carlo neutrino event generator [10]. We show a summary of the interaction cross sections for the relevant elements in KamLAND in Figures 4.27 to 4.29. The detector response such as event selection efficiency and directional resolution of reconstructed neutrino events were simulated using the KamLAND Geant4 Simulation (KLG4Sim). The directional resolution is summarized in Figure 4.36 for neutrino flavors $\bar{\nu}_e$ and ν_μ for energies between 100 MeV to 5 GeV.

7.2 Future outlook

The work presented here is a first attempt to employ directional event reconstruction at high energies on the scale of a GeV and above in a scintillator neutrino detector. KamLAND with a fiducial volume of 1 kt is at present the largest scintillator detector in the world. However, in comparison to some established Cherenkov detectors such as Super-Kamiokande (SK) and the IceCube Neutrino Observatory (IceCube), KamLAND is a relatively small detector in volume, and although the limits placed on the dark matter-nucleon cross section in this work suffer from a lack of fiducial volume, it is the hope of the author that this work can be utilized and developed further in a future endeavor for the next generation scintillator neutrino detector that can deploy larger fiducial volumes.

Some of the issues behind the restriction to smaller fiducial scintillator detector volumes have been related with cost of deployment, environmental safety issues, and physical impracticalities involved with scaling to large sizes. Scintillator is relatively expensive to manufacture as a detector medium in comparison to water, for example as used by the Super-K detector or utilizing a natural media such as ice in the South Pole in the case of IceCube. In addition, neutrino detectors are usually placed deep underground to take advantage of ample shielding of overburden from unwanted external backgrounds such as cosmic rays and their byproducts. Underground facilities housing these detectors require special chemical safety precautions and regulations for personnel working in confined spaces in an underground environment, with one of these being a strict limit on how much flammable material can be brought in and stored in a single location. This effectively limits the size of the detector that can be constructed. Furthermore, there exist physical reasons why large scintillator neutrino detectors are difficult to build. In purified water, the optical attenuation length at a typical wavelength that matches the region of good photomultiplier tube (PMT) quantum efficiency (QE) response of about 400 nm is on the order of 10^2 m [40], whereas that for scintillator is closer to ~ 10 m. The difference is roughly an order of magnitude implying that in order to build a scintillator detector similar in volume to the current Super-K detector, an increase in the attenuation length to that similar of water is desired.

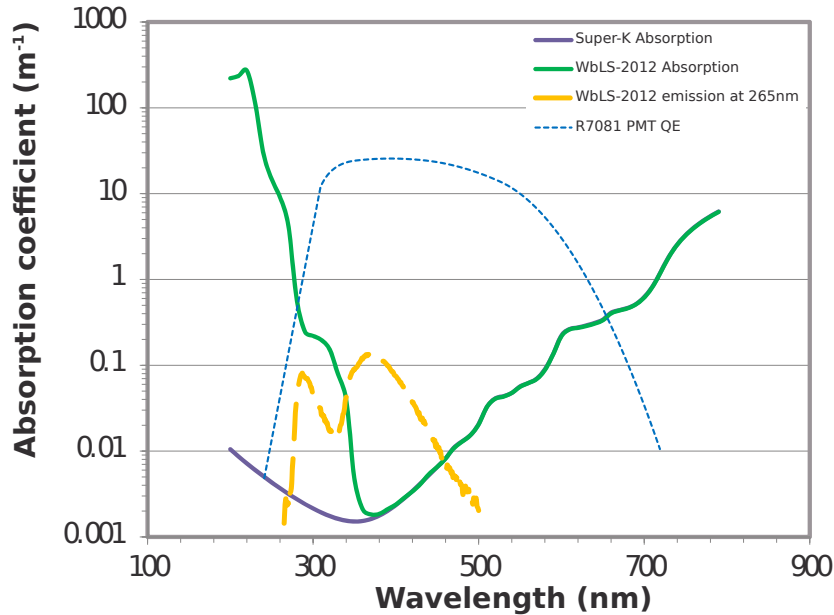


Figure 7.1: Projected absorption coefficient achievable by the WbLS in comparison to that of purified water in Super-K. Also shown is the relative QE curve of Hamamatsu PMT model R7081. Figure reproduced from [88].

Recent efforts in the development of the water-based liquid scintillator (WbLS) [89] holds promise to overcome exactly these issues pertaining to scaling scintillator detectors. Figure 7.1 shows the projected absorption coefficient expected to be achieved in comparison to purified water used in Super-K. Also shown in the figure is the emission spectrum of WbLS and the relative QE curve of an example Hamamatsu PMT model. The typical cost of conventional liquid scintillator (LS) is currently around \$2k per tonne or \$50 M to \$70 M per 50 kt [87]. Development of the WbLS is aimed at reducing the production cost in large volumes on the scale of ~ 50 kt and above, as well as increasing the safety of the detector medium. Table 7.1 shows the NFPA 704 flammable material safety rating of the LS used in existing and proposed neutrino experiments, all of which are combustible if not flammable.

Table 7.1: NFPA safety ratings for LS used in existing or proposed neutrino experiments. Table reproduced from [87].

Experiment	Liquid scintillator (LS)	NFPA 704 flammability rating
Borexino	Pseudocumene	~ 3
LENS	linear alkylbenzene (LAB)/Pseudocumene	1/3
Daya Bay	LAB	1
SNO+	LAB	1
Reno	LAB	1
Double-CHOOZ	20 % PXE + 80 % Dodecane	1 to 2
KamLAND	20 % Pseudocumene + 80 % Dodecane	2 to 3
NOvA	5 % Pseudocumene + 95 % mineral oil	1 to 2
LENA	PXE/LAB/Dodecane	1/1/2

With the advent of the WbLS, larger scintillator detectors will become cheaper and easier to build and it is expected that the work presented here will become more relevant with larger fiducial volumes. Furthermore, as photosensors with better timing resolutions compared to that of PMTs employed today become readily available with possibly on the order of ~ 100 ps and below, the event reconstruction tools described in this work will greatly benefit and potentially be able to start discerning individual final state particle tracks. The new Large Area Picosecond Photodetector (LAPPD) photo detector currently being developed is an example of upcoming technology with this sort of capability.

The significance of the work presented here lies in the development and application of a novel neutrino analysis technique at GeV scale energies to extract directional and possibly flavor discrimination information for scintillator neutrino detection with available data. Directional reconstruction of neutrinos in scintillator detectors is largely still in its stage of infancy undergoing active research, and flavor discrimination has previously not been thought possible. Application of tools utilizing these methods in a physics analysis is unprecedented, and it is the hope of the author that this work can further contribute to

the development of these techniques in the future for more improved analyses and a wider range of applications in scintillator neutrino detection.

7.3 Issues with high energy particle simulations in scintillator

One of the main challenges of conducting high energy analyses using scintillator such as the LS in KamLAND is the computational power required to simulate the detector response of physics events that produce an extremely large number of optical photons. Some of these photons will be those included in Cherenkov radiation but the majority will be due to scintillation. Geant4 simulations that are responsible in handling the detector response are relatively inefficient at propagating photons in media due to the particle tracking methods employed. With an excessive number of photons to propagate, single events can take on the order of hours to simulate and batches of simulations can take on the order of up to months when attempting to accumulate enough statistics to be used in a decent analysis.

In order to circumvent this problem, photons depending on whether they were of Cherenkov radiation or scintillation were selectively turned on or off in specific volumes of the detector. This was done while also preserving the evolution of the pseudorandom number generator for non-photon particles to be identical whether photons were or were not produced in a given volume. In other words, the reproducibility of non-photon tracks were guaranteed regardless of the response of the medium. In this analysis, the neutrino event candidates were required to be fully contained in order to be able to reconstruct their full energies. Fully contained events in KamLAND are defined to be events in which less than a total of five outer detector (OD) PMTs register any photon hits. Monte Carlo events vertices that were uniformly distributed in the inner detector (ID) volume were first pre-screened for those that satisfy this criterion while only producing Cherenkov photons in the OD and no photons in the ID. Once a set of such events were collected, they were subsequently re-simulated using the full photon output of both Cherenkov radiation and scintillation throughout the whole detector. In this way, simulation time was drastically

reduced, especially for the higher energy events, while being able to determine the efficiency for detecting fully contained events.

Recently there have been efforts to handle photon simulations of large numbers by exploiting video game technology, namely by employing graphics processing units (GPUs) for general purpose computing. One such example is the Chroma project [61] which cites speed improvements of a factor of 200 [73] compared to the case of conducting the same photon simulation using Geant4. The resources to utilize this particular technology was not available when our work was conducted. However, it is thought that employing tools such as these to improve processing speeds will be vital for future endeavors in high energy Monte Carlo simulations with a large number of photons.

Chapter 8

Conclusion

We have successfully developed and applied a directional neutrino analysis method for high energy GeV scale neutrinos in scintillator using data taken at the Kamioka Liquid Scintillator Antineutrino Detector (KamLAND) totaling a live time of 3253.0 days. We have also applied reconstruction techniques to image the topology of neutrino events in scintillator and tested this using actual events induced by the Tokai to Kamioka (T2K) neutrino beam. Imaging the topology may enable lepton flavor discrimination although this will require more study using larger statistics of neutrinos with energies above ~ 1 GeV.

The techniques mentioned above were employed to conduct an indirect dark matter search by looking for an excess in the dark matter annihilation induced neutrino signal originating from astronomical bodies such as the Sun and Earth. No significant excess above background was found to exist and we have used this null result to place a 90% confidence level upper limits to the *spin dependent* and *spin independent* dark matter-nucleon cross sections as shown in Figures 6.11 to 6.13 using the following possible dark matter annihilation channels.

- $XX \longrightarrow \nu_e \bar{\nu}_e$
- $XX \longrightarrow \nu_\mu \bar{\nu}_\mu$
- $XX \longrightarrow \nu_\tau \bar{\nu}_\tau$
- $XX \longrightarrow \tau^- \tau^+$

- $XX \longrightarrow gg$
- $XX \longrightarrow b\bar{b}$
- $XX \longrightarrow c\bar{c}$
- $XX \longrightarrow s\bar{s}$
- $XX \longrightarrow u\bar{u}$

The bounds deduced in this work are weaker than those found using detectors with larger fiducial volumes compared to KamLAND. However, the significance of this work lies in the development of a novel directional analysis technique using high energy $\sim\text{GeV}$ scale neutrinos in liquid scintillator (LS), and the unprecedented application of this in a physics result. Furthermore the reconstructed directional resolution of neutrinos in scintillator is suggested to be better than that of solely using the Cherenkov radiation from the final state lepton of a neutrino event by an order of $\sim 10^\circ$ in this energy regime.

As LS technologies advance and production costs decrease, it is inevitable in the near future that scintillator neutrino detectors will increase in size, and the demand for more analysis techniques to study neutrinos from a wider range of perspectives will grow. It is the hope of the author that the work presented here can make a meaningful contribution.

Appendix A

Friedmann Equations

In cosmology, the Friedmann equations describe the expansion of space in a homogeneous and isotropic universe within the context of general relativity. They were derived by Alexander Friedmann in 1922 from Einstein's field equations of gravitation for the Friedmann-Lemaître-Robertson-Walker (FLRW) metric assuming a perfect fluid of mass density ρ and pressure p . Dark matter regardless of its form, must contribute to the total mass density of the universe and be governed by the Friedmann equations consistent with any other type of mass. This enables us to estimate a *natural* dark matter density that is consistent with a locally flat universe.

Here we will briefly cover the derivation of the Friedmann equations. The metric of any space-time can be written in its general form as

$$ds^2 = \sum_{\alpha=0}^3 \sum_{\beta=0}^3 g_{\alpha\beta} dx^\alpha dx^\beta, \quad (\text{A.0.1})$$

where Greek letters, e.g. $\alpha, \beta, \gamma, \dots$, will signify variables that can be any number from the set $\{0, 1, 2, 3\}$. Here x^α with $\alpha = 0, 1, 2, \text{ or } 3$ are some coordinates of space-time, and the coefficients $g_{\alpha\beta}$ are in general functions of these coordinates such that $g_{\alpha\beta} = g_{\alpha\beta}(x^0, x^1, x^2, x^3)$. These coefficients are the components of what is called the metric tensor.

A more illuminating form of this metric equation can be written by explicitly distinguishing the time coordinate with respect to the other three spatial coordinates by

setting $t = x^0$ which gives

$$ds^2 = -\alpha c^2 dt^2 + \sum_{i=1}^3 \beta_i dx^i dt + \sum_{i=1}^3 \sum_{j=1}^3 \gamma_{ij} dx^i dx^j, \quad (\text{A.0.2})$$

where Roman letters, e.g. i, j, k, \dots , that appear as superscripts or subscripts in this section will signify variables that can be any number from the set $\{1, 2, 3\}$. Here t is the *global time* coordinate and the constant c is the speed of light in vacuum extracted out from the coefficient of dt^2 .

A common assumption made here is the *cosmological principle* which states that the universe is homogeneous and isotropic with respect to the distribution of matter on a large enough scale, i.e., that the universe when seen from a sufficiently large scale has no preference for a particular observer. This implies that α and β depend only on time. Among the various coordinate systems for which this is possible, we can choose one for which α is a constant and simply redefine the time coordinate so that $dt' = \sqrt{\alpha} dt$ effectively absorbing α into the time coordinate. Rewriting the equation gives

$$ds^2 = -c^2 dt^2 + \sum_{i=1}^3 \beta_i dx^i dt + \sum_{i=1}^3 \sum_{j=1}^3 \gamma_{ij} dx^i dx^j. \quad (\text{A.0.3})$$

Furthermore, the isotropy of the universe implies $\beta_i = 0$ because if this were not the case, we could do the substitution $x^i \rightarrow -x^i$ and the form of expression above would change.

These modifications lead to the result

$$ds^2 = -c^2 dt^2 + dl^2, \quad (\text{A.0.4})$$

where

$$dl^2 = \sum_{i=1}^3 \sum_{j=1}^3 \gamma_{ij} dx^i dx^j. \quad (\text{A.0.5})$$

dl^2 expressed in spherical coordinates can be written as

$$dl^2 = a(t)^2 \left(d\Psi^2 + \sin^2 \Psi \left(d\theta^2 + \sin^2 \theta d\phi^2 \right) \right), \quad (\text{A.0.6})$$

where $a(t)$ is called the *scale factor* and Ψ, θ, ϕ are the three spatial coordinates that correspond to x^1, x^2, x^3 in *comoving coordinates*. The line element dl^2 can be thought

of as the squared value of an infinitesimal distance on a three dimensional surface of a hypersphere also known as a β -sphere or *glome*. This surface has a constant curvature implied by the term $\sin^2 \Psi$ and is locally flat as can be seen by making the substitution $\Psi = r/a(t)$, where r is the radial distance in spatial coordinates, and taking the limit $r \rightarrow 0$ which yields

$$dl^2 = dr^2 + r^2 \left(d\theta^2 + \sin^2 \theta d\phi^2 \right). \quad (\text{A.0.7})$$

This is the familiar metric form of a three-dimensional Euclidean space in polar coordinates. On the other hand, there can also exist other types of manifolds with constant curvature such as those expressed by

$$dl^2 = a(t)^2 \left(d\Psi^2 + \Psi^2 \left(d\theta^2 + \sin^2 \theta d\phi^2 \right) \right), \quad (\text{A.0.8})$$

and

$$dl^2 = a(t)^2 \left(d\Psi^2 + \sinh^2 \Psi \left(d\theta^2 + \sin^2 \theta d\phi^2 \right) \right). \quad (\text{A.0.9})$$

In fact, these three metric forms shown in Equations (A.0.6), (A.0.8) and (A.0.9) can be respectively rewritten in the following forms,

$$dl^2 = a(t)^2 \left(\frac{d\chi^2}{1 - \chi^2} + \chi^2 \left(d\theta^2 + \sin^2 \theta d\phi^2 \right) \right) \quad (\text{A.0.10})$$

where $\chi = \sin \Psi \in [0, 1]$,

$$dl^2 = a(t)^2 \left(d\chi^2 + \chi^2 \left(d\theta^2 + \sin^2 \theta d\phi^2 \right) \right) \quad (\text{A.0.11})$$

where $\chi = \Psi \in [0, +\infty)$, and

$$dl^2 = a(t)^2 \left(\frac{d\chi^2}{1 + \chi^2} + \chi^2 \left(d\theta^2 + \sin^2 \theta d\phi^2 \right) \right) \quad (\text{A.0.12})$$

where $\chi = \sinh \Psi \in [0, +\infty)$. Furthermore, they can be consolidated into a single expression

$$dl^2 = a(t)^2 \left(\frac{d\chi^2}{1 - k\chi^2} + \chi^2 \left(d\theta^2 + \sin^2 \theta d\phi^2 \right) \right), \quad k \in \{-1, 0, +1\}, \quad (\text{A.0.13})$$

with the proper respective domains of χ so as to preserve the necessary condition $dl^2 \geq 0$. The universe is called *closed* if $k = 1$, *open* if $k = -1$, and *flat* if $k = 0$. Open and flat

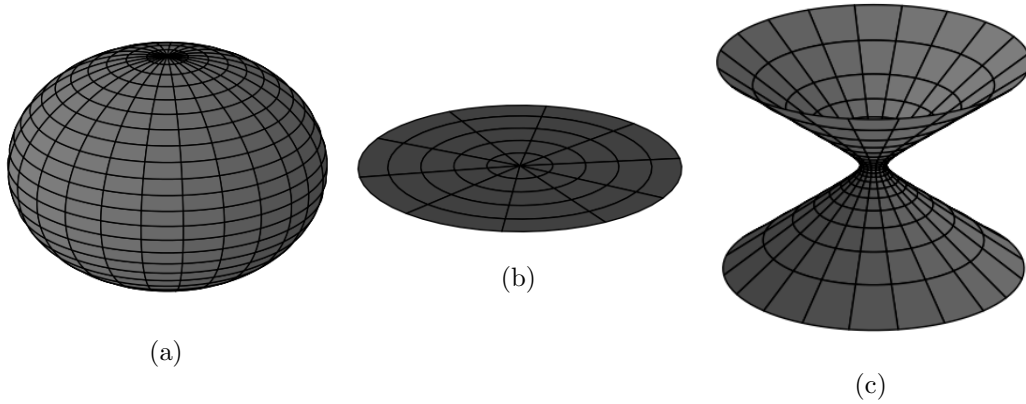


Figure A.1: Two-dimensional analog of the 3 different types of metric spaces with constant curvatures. (a) shows the analog of a closed universe, (b) shows the analog of a flat universe, and (c) shows the analog of an open universe.

universes have infinite volume, whereas closed universes have finite volume. Two dimensional analogs to these three types of universes are shown in Figure A.1. Equations (A.0.4) and (A.0.13) can be combined to derive the so called Friedmann-Lemaître-Robertson-Walker (FLRW) metric

$$ds^2 = -c^2 dt^2 + a(t)^2 \left(\frac{d\chi^2}{1 - k\chi^2} + \chi^2 (d\theta^2 + \sin^2 \theta d\phi^2) \right). \quad (\text{A.0.14})$$

It is clear that only four of the 16 coefficients $g_{\alpha\beta}$ that comprise the metric tensor are non-zero and they are

$$g_{tt} = -c^2, \quad (\text{A.0.15a})$$

$$g_{\chi\chi} = \frac{a(t)^2}{1 - k\chi^2}, \quad (\text{A.0.15b})$$

$$g_{\theta\theta} = a(t)^2 \chi^2, \quad (\text{A.0.15c})$$

$$g_{\phi\phi} = a(t)^2 \chi^2 \sin^2 \theta, \quad (\text{A.0.15d})$$

with the rest being

$$g_{\alpha\beta} = 0, \quad \text{for } \alpha \neq \beta. \quad (\text{A.0.15e})$$

Here we introduce the Einstein field equation which gives the relation amongst the coordinates of four dimensional space-time

$$R_{\alpha\beta} - \frac{1}{2}g_{\alpha\beta}R + g_{\alpha\beta}\Lambda = \frac{8\pi G}{c^4}T_{\alpha\beta} , \quad (\text{A.0.16})$$

where $R_{\alpha\beta}$ is the Ricci curvature tensor

$$R_{\alpha\beta} = R^{\delta}_{\alpha\delta\beta} , \quad (\text{A.0.17})$$

and

$$R^{\delta}_{\alpha\beta\gamma} = \frac{\partial}{\partial x^{\beta}}\Gamma^{\delta}_{\alpha\gamma} - \frac{\partial}{\partial x^{\gamma}}\Gamma^{\delta}_{\alpha\beta} + \Gamma^{\delta}_{\beta\lambda}\Gamma^{\lambda}_{\alpha\gamma} - \Gamma^{\delta}_{\gamma\lambda}\Gamma^{\lambda}_{\alpha\beta} . \quad (\text{A.0.18})$$

The Γ tensors are the so called Christoffel symbols of the first kind $\Gamma_{\alpha\beta\gamma}$, and of the second kind $\Gamma^{\alpha}_{\beta\gamma}$, respectively defined by

$$\Gamma_{\alpha\beta\gamma} = \frac{1}{2} \left(\frac{\partial g_{\alpha\beta}}{\partial x^{\gamma}} + \frac{\partial g_{\alpha\gamma}}{\partial x^{\beta}} - \frac{\partial g_{\beta\gamma}}{\partial x^{\alpha}} \right) , \quad (\text{A.0.19})$$

$$\Gamma^{\alpha}_{\beta\gamma} = g^{\alpha\rho}\Gamma_{\rho\beta\gamma} . \quad (\text{A.0.20})$$

In addition, $\Lambda = 8\pi(G/c^2)\rho_{\text{vac}}$ is the cosmological constant with ρ_{vac} being the energy density of vacuum, and $G \approx 6.674 \text{ N m}^2/\text{kg}^2$ is Newton's gravitational constant.

Substituting Equation (A.0.15) into Equation (A.0.16), we can derive two independent equations which are known as the *Friedmann equations*

$$\frac{\dot{a}^2 + kc^2}{a^2} = \frac{8\pi G\rho + \Lambda c^2}{3} , \quad (\text{A.0.21})$$

$$\frac{\ddot{a}}{a} = -\frac{4\pi G}{3} \left(\rho + \frac{3p}{c^2} + \frac{\Lambda c^2}{3} \right) . \quad (\text{A.0.22})$$

Appendix B

Isotopes and Natural Abundances

Table B.1: Isotopes and natural abundances relevant to the liquid scintillator (LS) in the Kamioka Liquid Scintillator Antineutrino Detector (KamLAND).

Atomic number (Z)	Mass number (A)	Name	Symbol	Mass of atom (u)	Abundance (%)
1	1	Hydrogen	^1H	1.007 825	99.9885
	2	Deuterium	^2H	2.014 102	0.0115
	3	Tritium	^3H	3.016 049	—
6	12	Carbon	^{12}C	12.000 000	98.93
	13		^{13}C	13.003 355	1.07
	14		^{14}C	14.003 242	—
7	14	Nitrogen	^{14}N	14.003 074	99.636
	15		^{15}N	15.000 109	0.364
8	16	Oxygen	^{16}O	15.994 915	99.757
	17		^{17}O	16.999 132	0.038
	18		^{18}O	17.999 160	0.205

Appendix C

Bayesian Priors

The Bayesian approach to estimating or setting a confidence limit to a model parameter of interest, say θ necessarily involves incorporating a so called *prior* probability distribution function (PDF) of the parameter. This reflects the experimenter's subjective degree of belief or state of knowledge regarding θ before conducting the experiment. After the experiment is conducted, the resulting data is used to *update* the experimenter's degree of belief and is summarized by the *posterior* PDF of the parameter.

In physics, it is common to attempt to use a prior that is flat in the allowed physical regions and zero everywhere else. These types of priors are constructed in order to represent the experimenter's complete lack of knowledge or unbiased objective point of view regarding the model prior to conducting the experiment. An example is the case of a counting experiment where the result of the experiment is reported in number of events observed. The average number of observed events, say θ is the parameter of the model we would like to estimate, and the data obtained by the experiment will follow Poisson statistics. In such a case, a flat prior $\pi(\theta)$ can be constructed to be

$$\pi(\theta) = \begin{cases} 1 & \text{if } \theta \geq 0 \\ 0 & \text{if } \theta < 0 \end{cases}, \quad (\text{C.0.1})$$

so that it represents our completely unbiased lack of knowledge in the physically allowed region and zero otherwise.

However, such a flat prior is deemed to be controversial because the experimenter has already decided on a particular metric in which the parameter is to be flat in by the time the prior is constructed. In order to circumvent this problem, there have been attempts to resolve this ambiguity in choice of metric by deriving so called non-informative or *objective* priors from a set of defined rules in such a way as to render the choice of metric irrelevant. One such prior for the case Poisson statistics is

$$\pi(\theta) = \begin{cases} \frac{1}{\theta} & \text{if } \theta \geq 0 \\ 0 & \text{if } \theta < 0 \end{cases} \quad (\text{C.0.2})$$

postulated by Jeffreys [57]. It was motivated by the idea that the shape of $\pi(\theta)$ is invariant with respect to power transformations such that $d\theta/\theta \propto d\theta^n/\theta^n$. Another similar and popular prior that was postulated is

$$\pi(\theta) = \begin{cases} \frac{1}{\sqrt{\theta}} & \text{if } \theta \geq 0 \\ 0 & \text{if } \theta < 0 \end{cases}. \quad (\text{C.0.3})$$

This can be derived by the more general formula also derived by Jeffreys.

$$\pi(\theta) \propto \sqrt{\det \mathcal{I}(\theta)}, \quad (\text{C.0.4})$$

where $\mathcal{I}(\theta)$ is the Fisher information which is defined as

$$\mathcal{I}(\theta) = E \left[\left(\frac{\partial}{\partial \theta} \log P(x|\theta) \right)^2 \right] = \int \left(\frac{\partial}{\partial \theta} \log P(x|\theta) \right)^2 P(x|\theta) dx. \quad (\text{C.0.5})$$

The derivation is explicitly shown by substituting $P(x|\theta) = \theta^x e^{-\theta}/x!$ in Equation (C.0.5):

$$\begin{aligned}
\mathcal{I}(\theta) &= E \left[\left(\frac{\partial}{\partial \theta} \log P(x|\theta) \right)^2 \right] \\
&= E \left[\left(\frac{\partial}{\partial \theta} \log \left(\frac{\theta^x e^{-\theta}}{x!} \right) \right)^2 \right] \\
&= E \left[\left(\frac{\partial}{\partial \theta} (x \log \theta - \theta - \log x!) \right)^2 \right] \\
&= E \left[\left(\frac{x}{\theta} - 1 \right)^2 \right] \\
&= E \left[\frac{x^2}{\theta^2} - 2 \frac{x}{\theta} + 1 \right] \\
&= \frac{1}{\theta^2} (\theta^2 + \theta) - 2 \frac{1}{\theta} (\theta) + 1 \\
&= \frac{1}{\theta},
\end{aligned} \tag{C.0.6}$$

such that Equation (C.0.4) now reads

$$\pi(\theta) \propto \sqrt{\det \mathcal{I}(\theta)} = \sqrt{\det \left(\frac{1}{\theta} \right)} = \frac{1}{\sqrt{\theta}}. \tag{C.0.7}$$

The form of Equation (C.0.4) has the key feature that it is invariant with respect to any re-parameterization of the prior as long as the new parameter is continuously differentiable with respect to the old parameter and vice-versa. This can be explicitly shown for example in the case if θ is a scalar and its prior is denoted as $\pi_\theta(\theta)$ such that

$$\pi_\theta(\theta) \propto \sqrt{\mathcal{I}(\theta)}. \tag{C.0.8}$$

Now let this prior be re-parametrized in such a way that the old parameter θ is a function of some new parameter φ and vice-versa such that $\theta = \theta(\varphi)$ and $\varphi = \varphi(\theta)$. Then we can

utilize the chain rule to find the new prior $\pi_\varphi(\varphi)$ with respect to the new parameter φ

$$\begin{aligned}
\pi_\varphi(\varphi) &= \pi_\theta(\theta) \left| \frac{d\theta}{d\varphi} \right| \\
&\propto \sqrt{\mathcal{I}(\theta) \left(\frac{d\theta}{d\varphi} \right)^2} \\
&= \sqrt{E \left[\left(\frac{d \log L}{d\theta} \right)^2 \right] \left(\frac{d\theta}{d\varphi} \right)^2} \\
&= \sqrt{E \left[\left(\frac{d \log L}{d\theta} \frac{d\theta}{d\varphi} \right)^2 \right]} \\
&= \sqrt{E \left[\left(\frac{d \log L}{d\varphi} \right)^2 \right]} \\
&= \sqrt{\mathcal{I}(\varphi)},
\end{aligned} \tag{C.0.9}$$

where $L = L(\theta(\varphi)|x)$ is the likelihood function of θ or φ when x is given. We find that the new prior with respect to the new variable achieved through re-parameterization of the old variable retains its functional form. This is called *Jeffreys invariance*. To prove the Jeffreys invariance when the parameter is not a scalar but a vector, the proof is slightly more complicated but follows a similar procedure.

Appendix D

NFPA Flammability Rating

Table D.1: NFPA 704 safety rating codes for flammable material.

Code	Description
0	Materials that will not burn under typical fire conditions (e.g. Carbon tetrachloride), including intrinsically noncombustible materials such as concrete, stone and sand (Materials that will not burn in air when exposed to a temperature of 820 °C (1500 °F) for a period of 5 minutes).
1	Materials that require considerable preheating, under all ambient temperature conditions, before ignition and combustion can occur (e.g. mineral oil). Includes some finely divided suspended solids that do not require heating before ignition can occur. Flash point at or above 93.3 °C (200 °F).
2	Must be moderately heated or exposed to relatively high ambient temperature before ignition can occur (e.g. diesel fuel) and multiple finely divided suspended solids that do not require heating before ignition can occur. Flash point between 37.8 °C to 93.3 °C (100 °F to 200 °F).
3	Liquids and solids (including finely divided suspended solids) that can be ignited under almost all ambient temperature conditions (e.g. gasoline, acetone). Liquids having a flash point below 22.8 °C (73 °F) and having a boiling point at or above 37.8 °C (100 °F), or having a flash point between 22.8 °C to 37.8 °C (73 °F to 100 °F).
4	Will rapidly or completely vaporize at normal atmospheric pressure and temperature, or is readily dispersed in air and will burn readily (e.g. acetylene, propane, liquid hydrogen). Includes pyrophoric substances. Flash point below 22.8 °C (73 °F).

Glossary

1976 International Standard Atmosphere A mathematical model of the Earth's atmosphere established in 1976 of how the pressure, temperature, density, and viscosity of the Earth's atmosphere change over a wide range of altitudes or elevations. 149

2,5-Diphenyloxazole (PPO) The primary scintillating fluor used in the KamLAND liquid scintillator (LS). Its chemical composition is $C_{15}H_{11}NO$. 41, 133, 250

Buffer oil (BO) The region between the liquid scintillator (LS) containing balloon and the spherical stainless steel tank on which the photomultiplier tubes (PMTs) are mounted is filled with non-scintillating mineral oil in order to isolate the liquid scintillator (LS) region from backgrounds associated with the photomultiplier tubes (PMTs) and peripheral components of the detector. This is coined the buffer oil. xii, xiv, 41, 44, 74, 93, 188

CDMS The CDMS experiment is a series of experiments designed directly to detect particle dark matter in the form of weakly interacting massive particles (WIMPs) using an array of semiconductor detectors at millikelvin temperatures. 215, 243

Cherenkov radiation Also known as VavilovCherenkov radiation, an electromagnetic radiation emitted when a charged particle (such as an electron) passes through a dielectric medium at a speed greater than the phase velocity of light in that medium. vii, 94, 227, 230

CoGeNT The CoGeNT dark matter experiment is a direct search for signals from interactions of dark matter particles in a low-background germanium detector located at

Soudan Underground Laboratory in Soudan, Minnesota, USA. The CoGeNT Experiment uses a single, 440-gram, high-purity germanium crystal cooled to liquid nitrogen temperatures in its measurements. 215, 243, 244

Comoving coordinates In cosmology, a comoving coordinate system is system of coordinates fixed with respect to the overall Hubble flow of the universe, so that a given galaxy's location in comoving coordinates does not change as the Universe expands. This allows distances and locations in an expanding homogeneous and isotropic cosmology to be related solely in terms of the scale factor. 232, 244

CRESST The CRESST experiment is a search for WIMP dark matter particles via their elastic scattering off nuclei. The nuclei are in the absorber of a cryogenic detector, capable of detecting the small energy of the recoiling nucleus which has been hit by an incoming WIMP. 215, 244

DAMA/LIBRA The DAMA/LIBRA experiment is a particle detector experiment designed to detect dark matter using the direct detection approach, by using a scintillation detector to search for weakly interacting massive particles (WIMPs) in the galactic halo. The experiment aims to find an annual variation of the number of detection events, caused by the variation of the velocity of the detector relative to the dark matter halo as the Earth orbits the Sun. It is located at the Laboratori Nazionali del Gran Sasso in Italy. 215, 220, 244

Dark matter A hypothetical kind of matter that cannot be seen with telescopes but accounts for most of the matter in the universe. The existence and properties of dark matter are inferred from its gravitational effects on visible matter, on radiation, and on the large-scale structure of the universe. Dark matter has not been detected directly, making it one of the greatest mysteries in modern astrophysics. vii, ix, xiii, 1–3, 5–9, 12–15, 18–20, 86, 102, 145, 159, 160, 186, 189, 195, 196, 204, 205, 231, 243–245, 247

DarkSUSY A simulation package written in fortran for calculations related with supersymmetric dark matter. 223

Deep inelastic scattering A name given to a process used to probe the insides of hadrons (particularly the baryons, such as protons and neutrons), using electrons, muons and neutrinos. 104, 107, 108, 111

Dodecane Also known as dihexyl, bihexyl, adakane 12 or duodecane, is a liquid alkane hydrocarbon with the chemical formula $\text{CH}_3(\text{CH}_2)_{10}\text{CH}_3$ (or $\text{C}_{12}\text{H}_{26}$), an oily liquid of the paraffin series. It has 355 isomers. It is used as a solvent, distillation chaser, and scintillator component. 41, 42, 44, 46, 133, 210–212, 226

Free-streaming length The average distance traveled by a dark matter particle before falling into a potential well. 7

Friedmann-Lemaître-Robertson-Walker (FLRW) metric An exact solution of Einstein's field equations of general relativity; it describes a homogeneous, isotropic expanding or contracting universe that may be simply connected or multiply connected. 231, 234

Galaxy rotation curve The rotation curve (also known as a velocity curve) of a disc galaxy where the position of the constituent stars are characterized by a disc-like shape, is a plot of the magnitude of the orbital velocities of the visible stars or gas with respect to their radii measured from the galactic center. 1

Geant4 Geant is an acronym for *GEometry ANd Tracking*. Geant4 is a software platform for developing Monte Carlo programs to simulate the passage of particles through matter. 227, 228

Generates Events for Neutrino Interaction Experiments (GENIE) A comprehensive Monte Carlo neutrino event generator supported and developed by an international collaboration of scientists. 106, 223

Hamamatsu Hamamatsu Photonics K.K. is a Japanese manufacturer of optical sensors (including photomultiplier tubes), electric light sources, and other optical devices and their applied instruments for scientific, technical and medical use. 133, 134, 225

IceCube Neutrino Observatory The IceCube Neutrino Observatory (or simply IceCube) is a neutrino telescope constructed at the AmundsenScott South Pole Station in Antarctica. Its thousands of sensors are distributed over a cubic kilometer of volume under the Antarctic ice. 224

Inverse beta decay (IBD) A broad term that refers to a physical process related to beta decay. In the context of neutrino physics, it refers to the particular process $\bar{\nu}_e + p \longrightarrow e^+ + n$, where the electron anti-neutrino undergoes quasi-elastic scattering off a proton to emit a positron and neutron. This is the dominant process searched for when analyzing MeV energy scale neutrinos in KamLAND. xiv, 84, 102, 111

Japan Proton Accelerator Research Complex (J-PARC) A high intensity proton accelerator facility located at the Tokai campus of the Japan Atomic Energy Agency (JAEA). J-PARC uses high intensity proton beams to create high intensity secondary beams of neutrons, hadrons, and neutrinos. xv, 125, 251

Japan Standard Time (JST) The standard timezone in Japan. It is 9 hours ahead of UTC, i.e., it is UTC+09:00. There is no daylight saving time in Japan. 96

Kamioka Liquid Scintillator Antineutrino Detector (KamLAND) An underground neutrino detection experiment located at the Kamioka Observatory, an underground science facility near Toyama, Japan. The analysis conducted in the work here utilizes neutrino data collected using this detector. vii, 39, 106, 145, 208, 223, 229, 236, 247

Kamioka Observatory The Kamioka Observatory, Institute for Cosmic Ray Research (Kamioka Uchū Soryūshi Kenkyū Shisetsu) is a neutrino physics laboratory located underground in the Mozumi Mine of the Kamioka Mining and Smelting Company near the Kamioka section of the city of Hida in Gifu Prefecture, Japan. xiii, xv, xvi, 38, 40, 42, 58, 125, 147–149

Kevlar A specific para-aramid synthetic fiber developed by DuPont in 1965. Typically it is spun into ropes or fabric sheets and has a high tensile strength-to-weight ratio; approximately five times stronger than steel on an equal weight basis. 41

Kolmogorov-Smirnov (K-S) test In statistics, the K-S test is a nonparametric test of the equality of continuous, one-dimensional probability distributions that can be used to compare a sample with a reference probability distribution (one-sample K-S test), or to compare two samples (two-sample K-S test). 127

Large Area Picosecond Photodetector A new photosensor based on microchannel plate technology currently being developed. The sensor modules are ~ 10 inch \times ~ 10 inch in photosensitive area and only ~ 1 inch thick while expected to have an extremely high timing resolution of on the order of ~ 100 ps resulting in a spatial resolution of ~ 1 cm. 226

Linear alkylbenzene (LAB) A family of organic compounds with the formula $C_6H_5C_nH_{2n+1}$. Typically n lies between 10 and 16. It is a popular liquid scintillator (LS) with good optical transparency (≈ 20 m), high light yield, low amount of radioactive impurities, and a high flash point (140°C). 130, 226

Liquid scintillator (LS) A scintillating material in liquid form. the Kamioka Liquid Scintillator Antineutrino Detector (KamLAND) uses an in-house developed custom scintillator in a liquid form as its neutrino detection medium. xii, xiv, 41, 67, 93, 188, 225, 226, 230, 236, 243, 247, 252

Low Energy Neutrino Astronomy (LENA) detector A liquid scintillator (LS) neutrino detector with a mass of about 50 kt. Its cylindrical shaped tank is about 100 meters in height and 30 meters in diameter. The detector is designed to study low energy neutrinos originated by supernova explosions, and the interior of the Sun and Earth. vii, 127

Massive astrophysical compact halo object (MACHO) Any kind of astronomical body that might explain the apparent presence of dark matter in galaxy halos. A

massive astrophysical compact halo object (MACHO) is a body composed of normal baryonic matter, which emits little or no radiation and drifts through interstellar space unassociated with any planetary system. MACHOs may include black holes, neutron stars, brown dwarfs or rogue planets that orbit a given galaxy directly. 8, 248

Meter water equivalent (mwe) A typical unit used in underground physics experiments to indicate the actual ability of the overburden to shield the experiment from cosmic rays regardless of the materials it may consist of. 38, 72

Mikheyev-Smirnov-Wolfenstein (MSW) effect Often also referred to as *matter effect*, the Mikheyev-Smirnov-Wolfenstein (MSW) effect is a particle physics process which can act to modify neutrino oscillations in matter. 24, 31, 223, 248

Modified Newtonian dynamics (MOND) A theory that proposes a modification of Newton's laws to account for observed properties of galaxies in which the velocities of the constituent stars were observed to be larger than expected based on Newtonian mechanics. Created in 1983 by Israeli physicist Mordehai Milgrom. 8, 251

Neutral density (ND) filter In photography and optics, a neutral density filter is a filter that reduces or modifies the intensity of all wavelengths or colors of light equally, giving no changes in hue or color rendition. 68, 248

Neutrino oscillation A quantum mechanical phenomenon whereby a neutrino created with a specific lepton flavor (electron, muon, or tau) can later be measured to have a different flavor. The probability of measuring a particular flavor for a neutrino varies periodically as it propagates through space thus the term oscillation. xvi, 23, 24, 27, 28, 30, 31, 145, 149, 154–157, 223, 248, 251, 252

NFPA 704 Standard System for the Identification of the Hazards of Materials for Emergency Response. A health safety standard maintained by the U.S.-based National Fire Protection Association. In this standard the flammability of a given material is coded on a scale of 0 through 4 using the criteria shown in Appendix D. xi, 226, 241

Particle Data Group An international collaboration of particle physicists that compiles and reanalyzes published results related to the properties of particles and fundamental interactions. Web page: <http://pdg.lbl.gov/>. 194

Photoelectron (pe) The electrons emitted when photons interact with metals such as the photocathode surface aligning the inner surface of a photomultiplier tube (PMT) vacuum housing. xiv, 71

Photomultiplier tube (PMT) Vacuum tubes that are extremely sensitive to light in various ranges in the electromagnetic spectrum. The models deployed in KamLAND are specifically sensitive near the shorter wavelength of the visible spectrum at around 400 nm. These detectors multiply the current produced by incident light by as much as 100 million times (i.e., 160 dB), in multiple dynode stages, enabling individual photons to be detected when the incident flux of light is very low. x, xiii, xiv, 224, 245, 249, 252

Preliminary reference Earth model (PREM) A one-dimensional model representing the average Earth properties as a function of planetary radius. It includes a table of Earth properties, including elastic properties, attenuation, density, pressure, and gravity, as a function of planetary radius [32]. 31, 150, 223

Principal component analysis A statistical procedure that uses an orthogonal transformation to convert a set of observations of possibly correlated variables into a set of values of linearly uncorrelated variables called principal components. This transformation is defined in such a way that the first principal component has the largest possible variance (that is, accounts for as much of the variability in the data as possible), and each succeeding component in turn has the highest variance possible under the constraint that it is orthogonal to the preceding components. 142

Protogalaxy In physical cosmology, a protogalaxy, which could also be called a *primeval galaxy*, is a cloud of gas which is forming into a galaxy. 7, 249

Pseudocumene A liquid hydrocarbon $C_6H_3(CH_3)_3$ isomeric with mesitylene and cumene that is found in coal tar and petroleum. Also known as 1,2,4-trimethyl-benzene. In

KamLAND it is used as a solvent for the 2,5-Diphenyloxazole (PPO) solute. 41, 42, 46, 133, 226

Pulsed dye laser A dye laser is a laser which uses an organic dye as the lasing medium, usually as a liquid solution. Compared to gases and most solid state lasing media, a dye can usually be used for a much wider range of wavelengths, often spanning 50 nm to 100 nm or more. The wide bandwidth makes them particularly suitable for tunable lasers and pulsed lasers. 67

P-value In statistics, the p-value is a function of the observed sample results (a statistic) that is used for testing a statistical hypothesis. The p-value is the probability of obtaining the observed sample results, or "more extreme" results, when the null hypothesis is actually true 127

Quantum efficiency The incident photon to converted photoelectron ratio often quoted in percentage. xiii, xv, 50, 130, 224

Quasi-elastic scattering A term that designates a limiting case of inelastic scattering, characterized by energy transfers being small compared to the incident energy of the scattered particles. 102, 104, 107, 108, 111

Resonance In particle physics, a Resonance is the peak located around a certain energy found in differential cross sections of scattering experiments. These peaks are associated with subatomic particles (such as nucleons, delta baryons, upsilon mesons) and their excitations. 104, 107, 108, 111, 250

Robust association of massive baryonic objects (RAMBO) In astronomy, a robust association of massive baryonic objects (RAMBO) is a dark cluster made of brown dwarfs or white dwarfs. 8, 250

Scale factor In cosmology, the scale factor is a function of the age of the universe and represents the relative expansion of the universe with respect to some time of reference. It relates the *proper distance* which changes as the universe expands to the *comoving*

distance which is a constant. Any two points in the universe which have a distance between them of $d(t)$ at some point in time t is related to the scale factor $a(t)$ by $d(t) = a(t)d_0$, where d_0 is the distance at some reference time t_0 . It is customary to set t_0 to the present age of the universe (13.798 ± 0.037 Gyr), so $a(t_0) \equiv 1$. 11, 232, 244, 250, 251

Scintillator A material that exhibits scintillation the property of luminescence when excited by ionizing radiation. Luminescent materials, when struck by an incoming particle, absorb its energy and scintillate, (i.e., re-emit the absorbed energy in the form of light). vii, xi, 94, 227, 230, 247

Super-Kamiokande (SK) A water-Cherenkov neutrino observatory located under Mount Ike in the Kamioka zinc mine about 100 m from the location of KamLAND. The observatory was designed to search for proton decay, study solar and atmospheric neutrinos, and keep watch for supernovae in the Milky Way Galaxy. xviii, 102, 111, 149, 215, 224, 251

Tensor-vector-scalar gravity (TeVeS) A relativistic generalization of modified Newtonian dynamics (MOND) theory developed by Jacob Bekenstein in 2004. 8

Tokai to Kamioka (T2K) A particle physics experiment that is the second generation follow up to the K2K experiment, a similar long baseline neutrino oscillation experiment. The Japan Proton Accelerator Research Complex (J-PARC) facility produces an intense off-axis beam of muon neutrinos. The beam is directed towards the Super-Kamiokande (SK) detector, which is 295 km away. The main goal of T2K is to measure the oscillation of ν_μ to ν_e and to measure the value of θ_{13} , one of the parameters of the Pontecorvo-Maki-Nakagawa-Sakata matrix. xv, 125, 229

Transit-time spread The variation in the times of occurrence of a stated point on the output current pulses arising from the application of delta light pulses to the entrance window of the device. 51, 130

Tyvek A brand of commercial synthetic material owned by DuPont created from high-density polyethylene fibers. It is known for being light weight, tear resistant, having

excellent chemical resistance and a high optical reflectivity of approximately 90% in the visible spectrum that drops by 10% to 20% in the near UV [41]. 47, 48

Voxel A value on a regular grid in three-dimensional space. Voxel is a portmanteau for *volume* and *pixel* where pixel is a combination of *picture* and *element*. 127, 129, 130

Water-based liquid scintillator (WbLS) A new liquid scintillator in development to be used in future neutrino detectors. This new material aims to facilitate detector scalability by circumventing issues related to cost and safety while retaining desirable high photon yield properties of conventional pure liquid scintillator. 225

WimpSim A Monte Carlo simulation code that calculates the annihilation of weakly interacting massive particles (WIMPs) inside the Sun or the Earth, collects all the neutrinos that emerge and let these propagate out of the Sun/Earth to the detector including neutrino interactions and neutrino oscillations in a fully consistent three-flavor way. 160, 223

Winston cone A non-imaging light collector in the shape of an off-axis parabola of revolution with a reflective inner surface. It concentrates the light passing through a relatively large entrance aperture through a smaller exit aperture. The collection of incoming rays is maximized by allowing off-axis rays to make multiple reflections before reaching the exit aperture. Winston cone are used to concentrate light from a large area onto a smaller photo-detector or photomultiplier tube (PMT). 130, 133

Bibliography

- [1] Craig E Aalseth, Phillip Spencer Barbeau, J Colaresi, JI Collar, J Diaz Leon, James E Fast, NE Fields, Todd W Hossbach, Andrea Knecht, Marek S Kos, et al. CoGeNT: A search for low-mass dark matter using p-type point contact germanium detectors. *Physical Review D*, 88(1):012002, 2013.
- [2] K. Abe et al. T2K neutrino flux prediction. *Phys. Rev.*, D87(1):012001, 2013. [Addendum: Phys. Rev.D87,no.1,019902(2013)].
- [3] S Abe, S Enomoto, K Furuno, Y Gando, H Ikeda, K Inoue, Y Kibe, Y Kishimoto, M Koga, Y Minekawa, et al. Production of radioactive isotopes through cosmic muon spallation in KamLAND. *Physical Review C*, 81(2):025807, 2010.
- [4] R. Adam et al. Planck 2015 results. I. Overview of products and scientific results. 2015.
- [5] Ag2gaeh. Spheroid with coordinate axes. <https://commons.wikimedia.org/wiki/File:Ellipsoid-rot-ax.svg>, October 2015. Accessed: 2016-01-10.
- [6] R Agnese, Z Ahmed, AJ Anderson, S Arrenberg, D Balakishiyeva, R Basu Thakur, DA Bauer, J Billard, A Borgland, D Brandt, et al. Silicon detector dark matter results from the final exposure of CDMS II. *Physical Review Letters*, 111(25):251301, 2013.
- [7] R Agnese, Alan J Anderson, M Asai, D Balakishiyeva, R Basu Thakur, DA Bauer, J Beaty, J Billard, A Borgland, MA Bowles, et al. Search for low-mass weakly

- interacting massive particles with SuperCDMS. *Physical review letters*, 112(24):241302, 2014.
- [8] Z Ahmed, CDMS collaboration, et al. Results from the final exposure of the CDMS II experiment. *arXiv preprint arXiv:0912.3592*, 2009.
- [9] DS Akerib, HM Araujo, X Bai, AJ Bailey, J Balajthy, S Bedikian, E Bernard, A Bernstein, A Bolozdynya, A Bradley, et al. First results from the LUX dark matter experiment at the Sanford Underground Research Facility. *Physical Review Letters*, 112(9):091303, 2014.
- [10] C. Andreopoulos, A. Bell, D. Bhattacharya, F. Cavanna, J. Dobson, et al. The GENIE Neutrino Monte Carlo Generator. *Nucl.Instrum.Meth.*, A614:87–104, 2010.
- [11] Godehard Angloher, M Bauer, I Bavykina, A Bento, C Bucci, C Ciemniak, G Deuter, F von Feilitzsch, D Hauff, P Huff, et al. Results from 730 kg days of the CRESST-II dark matter search. *The European Physical Journal C*, 72(4):1–22, 2012.
- [12] E Aprile, M Alfonsi, K Arisaka, F Arneodo, C Balan, L Baudis, B Bauermeister, A Behrens, P Beltrame, K Bokeloh, et al. Dark matter results from 225 live days of XENON100 data. *Physical review letters*, 109(18):181301, 2012.
- [13] S Archambault, E Behnke, P Bhattacharjee, S Bhattacharya, X Dai, M Das, A Davour, F Debris, N Dhungana, J Farine, et al. Constraints on low-mass WIMP interactions on ^{19}F from PICASSO. *Physics Letters B*, 711(2):153–161, 2012.
- [14] Walter H Barkas and Martin J Berger. Tables of energy losses and ranges of heavy charged particles. *Studies in Penetration of Charged Particles in Matter, National Academy of Sciences–National Research Council, Publication*, 1133:103, 1964.
- [15] GD Barr, TK Gaisser, Paolo Lipari, Simon Robbins, and T Stanev. Three-dimensional calculation of atmospheric neutrinos. *Physical Review D*, 70(2):023006, 2004.
- [16] M.-M. Bé, V. Chisté, C. Dullieu, E. Browne, C. Baglin, V. Chechev, N. Kuzmenko, R. Helmer, F. Kondev, D. MacMahon, and K.B. Lee. *Table of Radionuclides*,

volume 3 of *Monographie BIPM-5*. Bureau International des Poids et Mesures, Pavillon de Breteuil, F-92310 Sèvres, France, 2006.

- [17] M.-M. Bé, V. Chisté, C. Duiieu, X. Mougeot, V.P. Chechev, F.G. Kondev, A.L. Nichols, X. Huang, and B. Wang. *Table of Radionuclides*, volume 7 of *Monographie BIPM-5*. Bureau International des Poids et Mesures, Pavillon de Breteuil, F-92310 Sèvres, France, 2013.
- [18] Kenneth G Bell. *Uranium and other trace elements in petroleum and rock asphalts*. United States Atomic Energy Commission, United States Geological Survey, United States Government Printing Office, 1960.
- [19] L. Bergström. Non-baryonic dark matter: observational evidence and detection methods. *Reports on Progress in Physics*, 63:793–841, May 2000.
- [20] J Beringer. 31. passage of particles through matter. Technical report, Technical report, Particle Data Group, 2013.
- [21] R Bernabei, P Belli, F Cappella, R Cerulli, CJ Dai, A d'Angelo, HL He, A Incicchitti, HH Kuang, XH Ma, et al. New results from DAMA/LIBRA. *The European Physical Journal C*, 67(1-2):39–49, 2010.
- [22] G. Bertone, D. Hooper, and J. Silk. Particle dark matter: evidence, candidates and constraints. *Phys. Rep.*, 405:279–390, January 2005.
- [23] Hans Bichsel. Stopping power and ranges of fast ions in heavy elements. *Physical Review A*, 46(9):5761, 1992.
- [24] Samoil M Bilenky, J Hošek, and ST Petcov. On the oscillations of neutrinos with Dirac and Majorana masses. *Physics Letters B*, 94(4):495–498, 1980.
- [25] Mattias Blennow, Joakim Edsjö, and Tommy Ohlsson. Neutrinos from WIMP annihilations obtained using a full three-flavor Monte Carlo approach. *Journal of Cosmology and Astroparticle Physics*, 2008(01):021, 2008.

- [26] MM Boliev, SV Demidov, OV Suvorova, et al. Search for muon signal from dark matter annihilations in the Sun with the Baksan Underground Scintillator Telescope for 24.12 years. *Journal of Cosmology and Astroparticle Physics*, 2013(09):019, 2013.
- [27] Andrew Brown, Sam Henry, Hans Kraus, and Christopher McCabe. Extending the CRESST-II commissioning run limits to lower masses. *Physical Review D*, 85(2):021301, 2012.
- [28] B. J. Carr, K. Kohri, Y. Sendouda, and J. Yokoyama. New cosmological constraints on primordial black holes. *Phys. Rev. D*, 81(10):104019, May 2010.
- [29] K Choi, K Abe, Y Haga, Y Hayato, K Iyogi, J Kameda, Y Kishimoto, M Miura, S Moriyama, M Nakahata, et al. Search for neutrinos from annihilation of captured low-mass dark matter particles in the sun by Super-Kamiokande. *Physical review letters*, 114(14):141301, 2015.
- [30] C. J. Copi, D. N. Schramm, and M. S. Turner. Big-Bang Nucleosynthesis and the Baryon Density of the Universe. *Science*, 267:192–199, January 1995.
- [31] Masaru Doi, T Kotani, H Nishiura, K Okuda, and E Takasugi. Cp violation in Majorana neutrinos. *Physics letters B*, 102(5):323–326, 1981.
- [32] Adam M Dziewonski and Don L Anderson. Preliminary reference earth model. *Physics of the earth and planetary interiors*, 25(4):297–356, 1981.
- [33] Gernot Eder. *Nuclear forces*. MIT press, 1968.
- [34] J. Edsjö. WimpSim neutrino Monte Carlo.
<http://www.fysik.su.se/~edsjo/wimpsim/>.
- [35] Sanshiro Enomoto. *Neutrino geophysics and observation of geo-neutrinos at KamLAND*. PhD thesis, 2005.
- [36] K. A. Olive et al. 2014 review of particle physics, January 2014.

- [37] Gary J Feldman and Robert D Cousins. Unified approach to the classical statistical analysis of small signals. *Physical Review D*, 57(7):3873, 1998.
- [38] M Felizardo, TA Girard, Thomas Morlat, AC Fernandes, AR Ramos, JG Marques, Andreas Kling, Joel Puibasset, M Auguste, D Boyer, et al. Final analysis and results of the phase II SIMPLE dark matter search. *Physical review letters*, 108(20):201302, 2012.
- [39] DV Forero, M Tortola, and JWF Valle. Global status of neutrino oscillation parameters after Neutrino-2012. *Physical Review D*, 86(7):073012, 2012.
- [40] S Fukuda, Y Fukuda, T Hayakawa, E Ichihara, M Ishitsuka, Y Itow, T Kajita, J Kameda, K Kaneyuki, S Kasuga, et al. The Super-Kamiokande detector. *Nuclear Instruments and Methods in Physics Research Section A: Accelerators, Spectrometers, Detectors and Associated Equipment*, 501(2):418–462, 2003.
- [41] J. O. Gichaba. Measurement of Tyvek reflective properties for the Pierre Auger project. Master’s thesis, University of Mississippi, 1998.
- [42] P. Gondolo, J. Edsjö, P. Ullio, L. Bergstrom, M. Schelke, and E.A. Baltz. DarkSUSY. <http://www.fysik.su.se/~edsjo/darksusy/>.
- [43] Paolo Gondolo, Joakim Edsjö, Piero Ullio, Lars Bergström, Mia Schelke, and Edward A Baltz. DarkSUSY: Computing supersymmetric dark matter properties numerically. *Journal of Cosmology and Astroparticle Physics*, 2004(07):008, 2004.
- [44] M Concepción González-García and Yosef Nir. Neutrino masses and mixing: evidence and implications. *Reviews of Modern Physics*, 75(2):345, 2003.
- [45] Google. Google Earth V7.1.4.1529, April 2013.
- [46] A. Gould. Resonant enhancements in weakly interacting massive particle capture by the earth. *ApJ*, 321:571–585, October 1987.
- [47] A. Gould. Gravitational diffusion of solar system WIMPs. *ApJ*, 368:610–615, February 1991.

- [48] Donald E Groom, Nikolai V Mokhov, and Sergei I Striganov. Muon stopping power and range tables 10 MeV–100 TeV. *Atomic Data and Nuclear Data Tables*, 78(2):183–356, 2001.
- [49] Hamamatsu. Development of 20-inch PMT.
http://www.hamamatsu.com/us/en/technology/projects/20inch_pmt/index.html.
Accessed: 2016-01-23.
- [50] Hamamatsu. Large photocathode area photomultiplier tubes.
http://www.hamamatsu.com/resources/pdf/etd/LARGE_AREA_PMT_TPMH1286E.pdf.
Accessed: 2016-01-23.
- [51] M. R. S. Hawkins. The case for primordial black holes as dark matter. *MNRAS*, 415:2744–2757, August 2011.
- [52] M. Honda, M. Sajjad Athar, T. Kajita, K. Kasahara, and S. Midorikawa. Atmospheric neutrino flux calculation using the NRLMSISE-00 atmospheric model. *Phys. Rev. D*, 92:023004, Jul 2015.
- [53] M. Honda, T. Kajita, K. Kasahara, and S. Midorikawa. Improvement of low energy atmospheric neutrino flux calculation using the JAM nuclear interaction model. *Phys. Rev. D*, 83(12):123001, June 2011.
- [54] Morihiro Honda, T Kajita, K Kasahara, and S Midorikawa. New calculation of the atmospheric neutrino flux in a three-dimensional scheme. *Physical Review D*, 70(4):043008, 2004.
- [55] ICRU. Stopping powers for electrons and positrons. *ICRU report 37*, 1984.
- [56] H. Jeffreys. An Invariant Form for the Prior Probability in Estimation Problems. *Proceedings of the Royal Society of London Series A*, 186:453–461, September 1946.
- [57] Harold Jeffreys. *The theory of probability*. OUP Oxford, 1998.
- [58] Marc Kamionkowski. Possible relics from new physics in the early universe: Inflation, the cosmic microwave background, and particle dark matter. 1998.

- [59] Brian Kirby. *Measurement of an Off-Axis Neutrino Beam Energy Spectrum*. PhD thesis, UNIVERSITY OF BRITISH COLUMBIA (Vancouver), 2012.
- [60] P Langacker, ST Petcov, G Steigman, and S Toshev. Implications of the Mikheyev-Smirnov-Wolfenstein (MSW) mechanism of amplification of neutrino oscillations in matter. *Nuclear Physics B*, 282:589–609, 1987.
- [61] Anthony LaTorre and Stan Seibert. Chroma: Ultra-fast photon Monte Carlo. <http://chroma.bitbucket.org/>. Accessed: 2016-01-23.
- [62] Paolo Lipari. The east–west effect for atmospheric neutrinos. *Astroparticle Physics*, 14(3):171–188, 2000.
- [63] Tsuyoshi Nakaya and Robert K Plunkett. Neutrino oscillations with the MINOS, MINOS+, T2K, and NOvA experiments. *New Journal of Physics*, 18(1):015009, 2016.
- [64] NASA. Astronomy picture of the day. http://www.hamamatsu.com/us/en/technology/projects/20inch_pmt/index.html.
- [65] Jerzy Neyman. *A selection of early statistical papers of J. Neyman*. University of California Press Berkeley, CA, 1967.
- [66] Planck Collaboration, P. A. R. Ade, N. Aghanim, M. I. R. Alves, C. Armitage-Caplan, M. Arnaud, M. Ashdown, F. Atrio-Barandela, J. Aumont, H. Aussel, and et al. Planck 2013 results. I. Overview of products and scientific results. *A&A*, 571:A1, November 2014.
- [67] Joel R. Primack. *Dark matter and structure formation*. 1997.
- [68] Derek Raine. *An introduction to the science of cosmology*. Institute of Physics Pub, Bristol Philadelphia, 2001.
- [69] V. C. Rubin and W. K. Ford, Jr. Rotation of the Andromeda Nebula from a Spectroscopic Survey of Emission Regions. *ApJ*, 159:379, February 1970.

- [70] V. C. Rubin, W. K. J. Ford, and N. . Thonnard. Rotational properties of 21 SC galaxies with a large range of luminosities and radii, from NGC 4605 /R = 4kpc/ to UGC 2885 /R = 122 kpc/. *ApJ*, 238:471–487, June 1980.
- [71] Christopher Savage, Graciela Gelmini, Paolo Gondolo, and Katherine Freese. Compatibility of DAMA/LIBRA dark matter detection with other searches. *Journal of Cosmology and Astroparticle Physics*, 2009(04):010, 2009.
- [72] David N. Schramm and Michael S. Turner. Big bang nucleosynthesis enters the precision era. *Rev.Mod.Phys.*, 70:303–318, 1998.
- [73] Stan Seibert. Chroma: A fast photon simulation for particle physics with PyCUDA. <http://on-demand.gputechconf.com/gtc/2013/presentations/S3304-Particle-Physics-With-PyCUDA.pdf>. Accessed: 2016-01-23.
- [74] Itaru Shimizu. An evidence for spectral distortion of reactor anti-neutrinos and a study of three flavor neutrino oscillation. *Doctor Thesis, Tohoku University*, 2004.
- [75] Joseph Silk. *The Big Bang: the creation and evolution of the universe*. W.H. Freeman, San Francisco, 1980.
- [76] Snipview. Neutrino. <http://www.snipview.com/q/Neutrino>, July 2015.
- [77] Christian Spiering. Towards high-energy neutrino astronomy. In *From Ultra Rays to Astroparticles*, pages 231–263. Springer, 2012.
- [78] Rudolph M Sternheimer. The density effect for the ionization loss in various materials. *Physical Review*, 88(4):851, 1952.
- [79] F Suekane, T Iwamoto, H Ogawa, O Tajima, H Watanabe, et al. An overview of the KamLAND 1-kiloton liquid scintillator. *arXiv preprint physics/0404071*, 2004.
- [80] Osamu Tajima. *Development of liquid scintillator for a large size neutrino detector*. PhD thesis, Masters thesis, Tohoku University, 2000.

- [81] Osamu Tajima. *Measurement of Electron Anti-Neutrino Oscillation Parameters with a Large Volume Liquid Scintillator Detector, KamLAND*. PhD thesis, Ph. D. thesis, Tohoku University, 2003.
- [82] Mark Trodden and Sean M. Carroll. TASI lectures: Introduction to cosmology. pages 703–793, 2004.
- [83] M. Umemura and S. Ikeuchi. Formation of subgalactic objects within two-component dark matter. *ApJ*, 299:583–592, December 1985.
- [84] N. Vittorio and J. Silk. Fine-scale anisotropy of the cosmic microwave background in a universe dominated by cold dark matter. *ApJ*, 285:L39–L43, October 1984.
- [85] Hiroko Watanabe. *Comprehensive Study of Anti-neutrino Signals at KamLAND*. PhD thesis, Tohoku University, 2011.
- [86] Jon Williamson. Bruno de Finetti. philosophical lectures on probability. collected, edited, and annotated by Alberto Mura. translated by Hykel Hosni. Synthese Library; 340. *Philosophia Mathematica*, page nkp019, 2009.
- [87] M Yeh. Water-based liquid scintillator.
<https://indico.fnal.gov/getFile.py/access?contribId=18&sessionId=11&resId=2&materialId=slides&confId=3356>. Accessed: 2016-01-19.
- [88] M Yeh. Water-based liquid scintillator and isotope loadings.
<http://underground.physics.berkeley.edu/WbLS/slides/WbLS-Yeh.pdf>.
Accessed: 2016-01-18.
- [89] M Yeh, S Hans, W Beriguete, R Rosero, L Hu, RL Hahn, MV Diwan, DE Jaffe, SH Kettell, and L Littenberg. A new water-based liquid scintillator and potential applications. *Nuclear Instruments and Methods in Physics Research Section A: Accelerators, Spectrometers, Detectors and Associated Equipment*, 660(1):51–56, 2011.